Electron microscopy studies of Y-, Sc- and Zr-doped $Ba_{0.5}Sr_{0.5}Co_{0.8}Fe_{0.2}O_{3-\delta}$ ceramics for oxygen separation membranes

Zur Erlangung des akademischen Grades eines
DOKTORS DER NATURWISSENSCHAFTEN
von der Fakultät für Physik
des Karlsruher Instituts für Technologie (KIT)

genehmigte
DISSERTATION
von

Dipl.-Phys. Matthias Simon Meffert

aus Pforzheim

Tag der mündlichen Prüfung: 11. Nov. 2016

Referentin: Prof. Dr. D. Gerthsen

Korreferentin: Prof. Dr.-Ing. E. Ivers-Tiffée

angefertigt am
Laboratorium für Elektronenmikroskopie (LEM)
Karlsruher Institut für Technologie (KIT)

CONTENTS

Acronyms

$(BS)_{0.95}CF$	$(Ba_{0.5}Sr_{0.5})_{0.95}(Co_{0.8}Fe_{0.2})O_{3-\delta}$
$(BS)_{1.05}CF$	$(Ba_{0.5}Sr_{0.5})_{1.05}(Co_{0.8}Fe_{0.2})O_{3-\delta}$
ADF	annular dark-field
ALCHEMI	atom location by channeling enhanced microanalysis
Ba	element barium
BCO	$Ba_{n+1}Co_nO_{3n+3}(Co_8O_8)$ $(n \geq 2)$
BF	bright-field
BSCF	$(Ba_{0.5}Sr_{0.5})(Co_{0.8}Fe_{0.2})O_{3-\delta}$
BSCF10Y	$(Ba_{0.5}Sr_{0.5})(Co_{0.8}Fe_{0.2})_{0.9}Y_{0.1}O_{3-\delta}$
BSCF1Y	$(Ba_{0.5}Sr_{0.5})(Co_{0.8}Fe_{0.2})_{0.99}Y_{0.01}O_{3-\delta}$
BSCF3Sc	$(Ba_{0.5}Sr_{0.5})(Co_{0.8}Fe_{0.2})_{0.97}Sc_{0.03}O_{3-\delta}$
BSCF3Y	$(Ba_{0.5}Sr_{0.5})(Co_{0.8}Fe_{0.2})_{0.97}Y_{0.03}O_{3-\delta}$
BSCF3Zr	$(Ba_{0.5}Sr_{0.5})(Co_{0.8}Fe_{0.2})_{0.97}Zr_{0.03}O_{3-\delta}$
BSCFSc	$(Ba_{0.5}Sr_{0.5})(Co_{0.8}Fe_{0.2})_{1-x}Sc_xO_{3-\delta}$ $(x > 0)$
BSCFY	$(Ba_{0.5}Sr_{0.5})(Co_{0.8}Fe_{0.2})_{1-x}Y_xO_{3-\delta}$ $(x > 0)$
BSCFZr	$(Ba_{0.5}Sr_{0.5})(Co_{0.8}Fe_{0.2})_{1-x}Zr_xO_{3-\delta}$ $(x > 0)$
BSE	backscattered electron
CBED	convergent beam electron diffraction
c-BSCF	cubic phase of BSCF
CCD	charge-coupled device
CL	camera length
Co	element cobalt
DF	dark-field
DFT	density functional theory
DOS	density of states
ECR	electrical conductivity relaxation

EDXS	energy dispersive X-ray spectroscopy
EELS	electron energy loss spectroscopy
ELNES	energy loss near edge fine structure
EV	eigenvalue
EXELFS	extended energy loss near edge fine structure
Fe	element iron
FEG	field-emission gun
FOLZ	first order Laue zone
GB	grain boundary
HAADF	high-angle annular dark-field
h-BSCF	2H hexagonal phase of BSCF
HRTEM	high-resolution transmission electron microscopy
HS	high spin
HT	microscope high tension
HOLZ	higher order Laue zone
IS	intermediate spin
LS	low spin
LSC	$La_{0.6}Sr_{0.4}CoO_{3-\delta}$
LSC_{RP}	$(La,Sr)_{2-x}Co_{1+x}O_{4\pm\delta}$
MIEC	mixed ionic and electronic conductor
NIPALS	non-linear iterative partial least squares
O	element oxygen
PC	principal component
PCA	principal component analysis
PE	primary electron
SAED	selected area electron diffraction
Sc	element scandium

SCF	$SrCo_{0.8}Fe_{0.2}O_{3-\delta}$
SE	secondary electron
SEM	scanning electron microscopy
SI	spectrum image
SNR	signal-to-noise ratio
Sr	element strontium
STEM	scanning transmission electron microscopy
TEM	transmission electron microscopy
TM	transition metal
VLM	visible light microscopy
wPCA	weighted principal component analysis
XRD	X-ray diffraction
ZL	zero-loss
Zr	element zirconium
ZOLZ	zero order Laue zone

SYMBOLS

$10Dq$	octahedral ligand splitting parameter
A	grain area
$A(u)$	aperture function
a, b, c	lattice parameters
α	convergence half-angle
α_j	excitation amplitude
$B(u)$	aberration function
β	collection half-angle
$b^{(j)}(\vec{k}, \vec{r})$	Bloch wave function
b_{rms}	impact parameter
C	covariance matrix
$C_g^{(j)}$	Bloch wave coefficient corresponding to scattering vector $\vec{g}$
χ_{Fe}	Fe white-line ratio
$\chi(u)$	function containing the aberration terms
C_i	concentration of element i
C_s	spherical aberration coefficient
D^*, D_{chem}	tracer, chemical diffusion coefficient
d_0	most probable grain diameter
d	grain diameter
D_{50}	mass median diameter
d_c	critical diameter
δ	oxygen vacancy concentration
Δ	Gaussian broadening of $L_{2,3}$ white-line
ΔE	electron loss energy
Δf	defocus value

d_{hkl}	distance between adjacent (hkl) lattice planes
$\bar{d}$	average grain diameter
d_m^n, $d_{m,0}^n$	initial, final grain diameter
$\frac{\mathrm{d}\sigma}{\mathrm{d}\Omega}$	differential cross-section
$E(u)$	envelope function
e	elementary charge ($e = 1.602\times10^{-19}C$)
E_0	electron energy
E_A	activation energy
E_F	Fermi level
e_g, t_{2g}	high energy, low energy d-orbitals in an octahedral environment
ε_0	vacuum permittivity ($\varepsilon_0 = 8.854\times10^{-12}\frac{F}{m}$)
η_i	formal valence state of element i
F	Faraday constant ($F = 96485.3\,\frac{C}{mol}$)
$f(d)$	probability density function of log-normal distribution
γ	thermodynamic factor
$\gamma^{(j)}$	eigenvalue
$\vec{g}_{hkl}$	scattering vector
$H(u)$	contrast transfer function
ħ	reduced Planck constant
hkl	Miller indices
I_{BG}	EELS background intensity
I_i	X-ray line intensity
$I_{L_{2,3}}$	$L_{2,3}$ white-line intensity
I_m	image intensity
I_t	total transmitted beam intensity
I_{ZL}	intensity of zero-loss peak
J_{O_2}	oxygen flux

k^*, k_{chem}	tracer, chemical surface exchange coefficient
K	electron wave vector inside the crystal
$\vec{k}_0$	incident electron wave vector
K_0	constant
$k_{A,B}$	microscope specific Cliff-Lorimer-factor for elements A, B
$\vec{k}^{(j)}$	wave vector of the Bloch wave j
k_x	scattering parameter
$\tilde{L}$	loading matrix
L	membrane thickness
λ_i	eigenvalue associated with the eigenvector $\vec{p}_i$
λ	electron wavelength
λ_p	mean free path for plasmon scattering
L_C	characteristic membrane thickness
m	relativistic electron mass
μ	mean value
N	number of X-ray counts
n, c	number of spectra, number of spectrum channels
p_{O_2}	oxygen partial pressure
p'_{O_2}, p''_{O_2}	oxygen partial pressure on membrane feed, permeate side
$\vec{p}_i$	eigenvector corresponding to the eigenvalue λ_i
Ψ_0	incident electron wave
Ψ_e	exit electron wave function
ψ	electron wave function
Q	activation energy for grain growth
R	gas constant ($R = 8.314\ \frac{J}{K\ mol}$)
$R_{A/B}$	double intensity ratio of element A and B
R_i	ionic radius of i-type ion

$\tilde{S}$	score matrix
S	spin state
s_g	excitation error
σ_i	inelastic ionization cross-section of element i
σ_{el}, σ_{ion}	intrinsic electronic, ionic conductivity
σ	standard deviation
$\tilde{\sigma}$	electron interaction constant
T	temperature
t	sample thickness
t_a	effective acquisition time
τ_{Co}	Co white-line distance
θ_{hkl}	Bragg angle
θ	scattering angle
T_s	sintering temperature
t_s	sintering time
t_{tol}	Goldschmidt tolerance factor
$\langle u^2 \rangle$	mean square thermal displacement factor
u	spatial frequency
$V_{\vec{g}}$	Fourier coefficient corresponding to $\vec{g}$
$V(\vec{r})$	crystal potential
V_z	potential projected in z-direction
w, v	fit parameters
X	spectrum collection data matrix
$\bar{X}_r$	filtered spectrum collection data matrix
$Y_{L_{2,3}}$	Lorentzian broadening of $L_{2,3}$ white-line
Z	atomic number

1 INTRODUCTION

The production of pure oxygen currently covers an amount of 120 billion m³ per year (standard conditions) and a growth rate of about 5.5 % with the biggest consumers found in steel and chemical industry [1]. Nowadays, pure oxygen is mainly synthesized by cryogenic distillation which requires huge amounts of energy due to extremely low temperatures and high pressure involved in the process and with no prospect of significant improvement in efficiency in the future [2]. Ceramic-based membrane materials are considered a viable alternative to replace cryogenic methods as they exhibit considerable oxygen conductivity. Suitable materials can transport oxygen ions and electronic charge carriers through a gas-tight membrane at elevated temperatures simultaneously. This can considerably improve energy efficiency and oxygen purity especially if there is an abundance of waste heat. Due to its exceptional high oxygen permeability over a wide temperature range (600 – 900 °C), the cubic perovskite $(Ba_{0.5}Sr_{0.5})(Co_{0.8}Fe_{0.2})O_{3-\delta}$ (BSCF) is one of the most promising candidates. However, there are some significant drawbacks preventing the broad application of BSCF, especially in the desired intermediate temperature range between 600 and 800 °C. The most pressing matter involves the decomposition of the oxygen-conducting cubic phase [3] which is strongly connected to the temperature-induced change of the Co-valence state. The Co-valence state increases with decreasing temperature, and the accompanied reduction of ionic radius leads to the formation of secondary phases, essentially blocking the movement of oxygen ions. As the perovskite structure is flexible regarding elemental substitutions, doping with fixed valence transition metals such as yttrium, scandium or zirconium was performed within this thesis with the goal of suppressing the decomposition of the oxygen-conducting cubic phase. This was studied by electron microscopic and spectroscopic techniques. Another issue of BSCF involves its low tolerance towards CO_2 or sulfur-containing atmospheres because these reduce considerably oxygen surface exchange by the formation of secondary phases. Hence, surface coating with the chemically stable compound $La_{0.6}Sr_{0.4}CoO_{3-\delta}$ was also investigated in this thesis.

Electron microscopic instrumentation has been substantially improved during the past decade. However, methodological developments and a deep understanding of the interaction of electrons and solids are still necessary to extract specific materials properties or information from noisy data sets. Of particular interest in this work are the lattice positions of substitutional elements. Especially for intermediate-sized ions

like yttrium, the question arises if they are incorporated on their intended lattice site. Hence, lattice sites of substitutional elements were determined experimentally in this work. An advanced electron microscopic technique, ALCHEMI (atom location by channeling enhanced microanalysis) [4], can be used for this purpose which is based on the inhomogeneous localization of Bloch waves under suitably chosen excitation conditions. Atoms on lattice sites with a high Bloch wave intensity are more likely to be ionized and, therefore, generate element specific X-rays in radiative recombination processes. If the Bloch wave localization in the crystal lattice is precisely known, changes in characteristic X-ray intensity for different Bloch wave localizations can be used to derive element specific site occupancies.

Nowadays it has become possible to acquire huge, spatially resolved spectrum datasets. One of the big advantages is the possibility to analyze features after acquisition since the full spectroscopic information is present for each individual pixel. This is especially important for complex material systems like custom-tailored perovskites because there is usually no á priori information available on relevant features. However, the acquisition of such large data sets is accompanied by extremely low counting statistics which makes the identification of weak features difficult. Multivariate statistical methods have the potential to recover spectral information without sacrificing lateral resolution. In this work, the potential gains and limits of multivariate statistics are systematically investigated on experimentally acquired X-ray spectroscopic data.

In the BSCF material system, Co is not only responsible for its superior oxygen conductivity but also for the decomposition in the intermediate temperature range since the valence state of Co changes easily. Therefore, the Co-valence state is of great interest for the deeper understanding of the material system with respect to improving its long-time stability. Electron energy loss spectroscopy (EELS) of the Co-$L_{2,3}$ ionization edges is usually applied to extract the Co-valence state. However, the established techniques cannot be applied in BSCF due to the superposition of Ba-$M_{4,5}$ and Co-$L_{2,3}$ white-lines. This was used as base for the development of a new methodical concept for reliable characterization of the Co-valence state in BSCF.

This thesis is divided into four main parts each one focusing on specific aspects. In Chapter 2, the fundamentals of membrane materials especially the investigated BSCF system are presented. Furthermore, the electron microscopic techniques utilized within this thesis are introduced. Chapter 3 focuses on methodological aspects concerned with noise reduction and feature recovery in large spectrum data sets using the multivariate

method principal component analysis. The background of ALCHEMI is outlined in Chapter 4 which is used to determine the lattice sites of yttrium and scandium substitutional elements in the BSCF matrix. The impact of different dopants on the BSCF microstructure is presented in Chapter 5. Various annealing treatments were performed to extend the knowledge about secondary phase formation and the related degradation process. Furthermore, the role of fabrication parameters on microstructure is discussed. To further enhance membrane performance and surface stability, coating with functional materials was examined.

2 FUNDAMENTALS

The first part of the following chapter focuses on the fundamentals of oxygen separation membranes with an emphasis on the most prominent material composition $(Ba_{0.5}Sr_{0.5})(Co_{0.8}Fe_{0.2})O_{3-\delta}$ (BSCF) and the inherent decomposition of the cubic BSCF phase in the application-relevant temperature range. The state of literature is reviewed regarding degradation of the ionic and electronic conductivity and approaches to stabilize the material system for long-time operation. Additionally, future prospects of further enhancing permeation properties by functional layers are presented. The second part deals with the fundamental working principles of scanning and/or transmission electron microscopy (SEM, TEM, STEM). The main focus is set on techniques which are relevant for this thesis like energy dispersive X-ray spectroscopy (EDXS) and electron energy loss spectroscopy (EELS). For an extended overview of the topic, the book by WILLIAMS & CARTER [5], as well as the books by REIMER AND KOHL [6,7], are strongly recommended. For analytical electron microscopy the reader is suggested to study the books by EGERTON [8] and SCOTT [9].

2.1 Oxygen separation membranes

Dense ceramics are considered as highly attractive materials regarding their application for membrane materials. Since ceramic membranes operate on the principle of ionic transport rather than molecular diffusion, a high selectivity can be achieved as long as there is no direct connection between both membrane sides. In these materials, oxygen vacancies are responsible for ion conductivity with thermally activated hopping of oxygen ions between unoccupied sites as the basic principle of movement. For oxygen conducting materials, the barrier for oxygen migration should be below 1 eV [10]. Materials with promising oxygen conducting properties are mainly complex oxides like perovskites (ABO_3), fluorites (AO_2), brownmillerites ($A_2B_2O_5$), pyrochlores ($A_2B_2O_7$), orthorhombic K_2NiF_4-types (A_2BO_4), $Sr_4Fe_{6-x}Co_xO_{13}$ phases and several intergrowth compounds like, e.g., Ruddlesden-Popper phases ($A_{n-1}A'_2B_nO_{3n+1}$, $n \geq 1$) [11,12]. Nevertheless, perovskite compounds are regarded most attractive due to their high tolerance towards oxygen non-stoichiometry, making them excellent ionic conductors. As most perovskites can conduct electrons and ions, no electrical feedback circuit is needed for electrical charge compensations which make them highly efficient. Electronic conductivity in these so-called mixed ionic and electronic conductors (MIEC) is provided by transition metals like cobalt, chromium, titanium or iron. Due to

their ionic nature, the oxygen non-stoichiometry is mainly governed by the oxidation states of the cations and can, therefore, be easily influenced by introducing charge defects in the form of dopant elements.

2.1.1 Oxygen transport process

The main driving force of oxygen transport is an oxygen chemical potential gradient within the membrane realized by applying a high oxygen partial pressure on the feed side p'_{O_2} and a low partial pressure on the permeate side p''_{O_2}. As mentioned earlier charge compensation is provided by simultaneous migration of oxygen ions and electrons in opposite directions. For thick membranes migration of oxygen ions is limited by bulk diffusion. Bulk diffusion can be described by the Wagner equation [13] as shown in Equation 1.

$$J_{O_2} = -\frac{RT}{4^2F^2}\frac{1}{L}\int_{\ln p'_{O_2}}^{\ln p''_{O_2}} \frac{\sigma_{el}\sigma_{ion}}{\sigma_{el}+\sigma_{ion}} d\ln p_{O_2} \qquad (1)$$

Hereby, R denotes the gas constant, F the Faraday constant, σ_{el}/σ_{ion} the intrinsic electronic/ionic conductivity, T the operating temperature and L the membrane thickness. For many MIECs the electronic conductivity σ_{el} surpasses the ionic conductivity σ_{ion} by several orders of magnitude making ionic transport the rate-determining factor in bulk diffusion. In order to get a high oxygen flux, free parameters can be adjusted. A high temperature and oxygen partial pressure gradient can enhance the oxygen flux significantly. However, they are only adjustable in a small parameter range, since several limitations like phase stability or economic viability have to be considered.

Some MIECs already contain a high concentration of oxygen vacancies at room temperature. However, oxygen conduction will only occur at high temperatures (typically above 300 °C) due to high activation energies [14]. As the oxygen flux is inversely proportional to the membrane thickness, membranes should be produced as thin as possible without introducing direct gas pathways between both sides. However, for thin membranes, the oxygen flux cannot be increased significantly by further reducing the thickness because oxygen transport will be limited by surface exchange kinetics. The membrane thickness where oxygen flux changes from diffusion-controlled to surface-controlled is called characteristic length L_C. If the p_{O_2} gradient across the ceramic membrane is small and $\sigma_{el} \gg \sigma_{ion}$, the characteristic length can be expressed

as a fraction of tracer diffusion coefficient D^* and tracer surface exchange coefficient k^* [15] as written in Equation 2.

$$L_C = \frac{D^*}{k^*} \tag{2}$$

The tracer coefficients D^* and k^* are linked to their chemical coefficient counterparts D_{chem} and k_{chem} by the thermodynamic factor γ according to the relation $k_{chem} = \gamma k^*$ and $D_{chem} = \gamma D^*$. For most MIEC perovskites the characteristic thickness ranges from a few nanometers to up to several millimeters depending on the material composition, temperature and oxygen partial pressure gradient [13,16]. Yet, most MIECs have L_C values from 0.1 to 1 mm whereas materials with dominating ionic conductivity have large values around 10 mm [17]. Surface exchange on the feed side can be described by the following steps: Adsorption of oxygen molecules from the gas phase, dissociation of oxygen molecules, charge transfer between oxygen and membrane material and incorporation in the crystal lattice. For oxygen excorporation on the permeate side, the steps will follow the reverse order. For surface exchange limited permeation, the Wagner equation can be modified as followed.

$$J_{O_2} = -\frac{RT}{4^2F^2}\frac{1}{L + 2L_C}\int_{\ln P'_{O_2}}^{\ln P''_{O_2}} \frac{\sigma_{el}\sigma_{ion}}{\sigma_{el} + \sigma_{ion}} d \ln P_{O_2} \tag{3}$$

2.1.2 MIEC perovskite materials

As mentioned earlier, the perovskite structure with ABO_3 stoichiometry is the most common structure for MIEC materials. An ideal perovskite crystallizes in cubic symmetry and $Pm\bar{3}m$ space group. The unit cell is depicted in Figure 1(a) and shows that the lattice consists of two cubic cation sublattices (A: green, B: blue) which are relatively shifted towards each other by half of the length of the unit cell's diagonal with the B-site centered in an oxygen octahedron. Hence, B-site cations are 6-fold and A-site cations 12-fold coordinated by oxygen anions. If one considers ions to be solid spheres and closely packed, the lattice parameter a can be written as a function of the ionic radii R_A, R_B and R_O in different ways; the line parallel to the edge B-O-B and the diagonal A-O-A (cf. Equation 4). The mismatch between these two can be used as an indicator for the distortion and, therefore, the stability of crystal structures in the form of the well-established Goldschmidt tolerance factor t_{tol} [18].

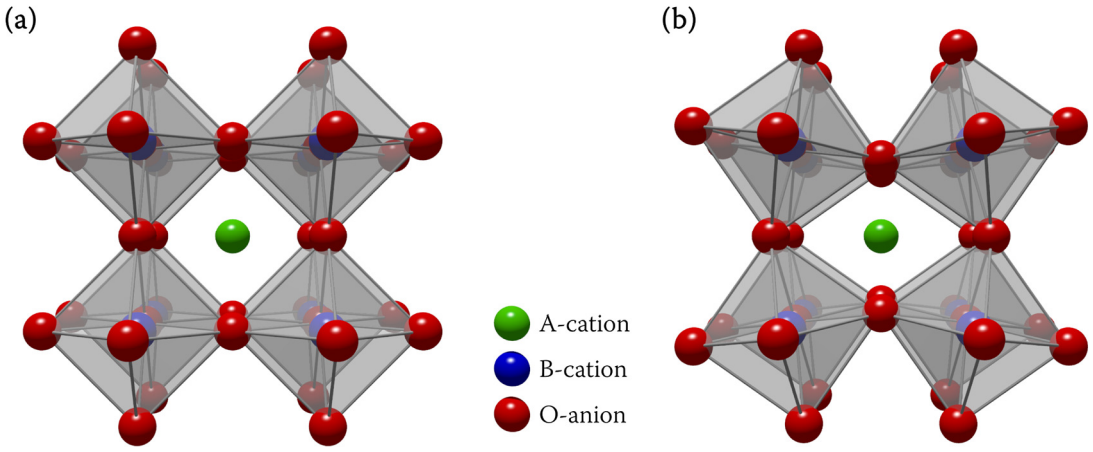

Figure 1. (a) Ideal cubic perovskite ABO_3 structure and (b) example of tilted oxygen octahedrons due to a low tolerance factor.

$$t_{tol} = \frac{a_{A-O-A}}{a_{B-O-B}} = \frac{R_A + R_O}{\sqrt{2}R_B + \sqrt{2}R_O} \tag{4}$$

Even though one would expect that ideal cubic perovskites require a tolerance factor close to unity, cubic perovskites can be found as low as 0.8 depending on numerous parameters [19]. In principle, any deviation will deform the crystal structure and lower the symmetry. It has been suggested that in most cases lowering of symmetry is caused by tilted oxygen octahedrons [20,21] as depicted in Figure 1(b). If the A-cation is too small to occupy the available free space ($t_{tol} \ll 1$) the oxygen octahedrons will tilt in order to fill up empty space. Materials with $t_{tol} \ll 1$ will tend towards orthorhombic or rhombohedral phases [19,22]. Compositions with tolerance factors $t_{tol} > 1$ often form hexagonal phases containing face-sharing octahedrons. For MIEC it has been reported that a tolerance factor close to unity provides best conductivity [23,24].

Many MIEC perovskites are either $A^{IV}B^{II}O_3$, $A^{II}B^{IV}O_3$ or $A^{III}B^{III}O_3$ compounds. As the perovskite structure is quite flexible regarding (partial) elemental substitution charge defects can be introduced into the material by replacing some cations by ions with different valence state. As usually cations with a high valence state are replaced by low-valent cations, charge defects are balanced by introducing oxygen vacancies to fulfill the electrical neutrality criterion. The oxygen vacancy concentration is often referred to as δ which is usually added to the compound formula in the following way: $ABO_{3-\delta}$. As described earlier, these oxygen vacancies provide migration paths for oxygen anions, leading to improved ionic conductivity. Hence, a high oxygen non-stoichiometry is desirable in most materials. However, in many compounds a high δ value is

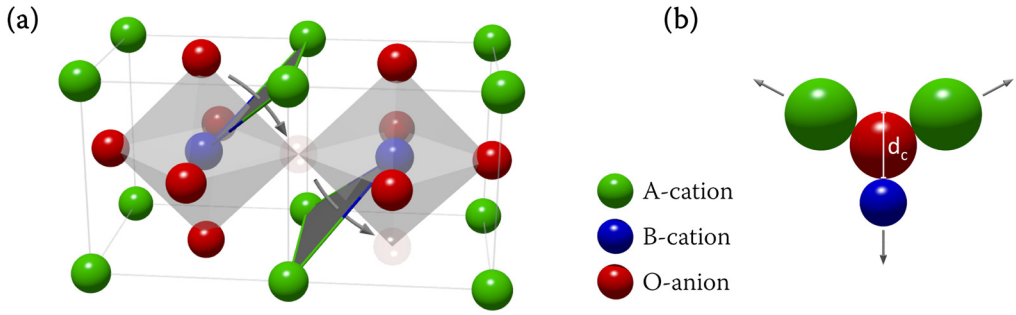

Figure 2. (a) Scheme of oxygen migration path in MIEC perovskites. For the sake of clarity, the sphere radii are depicted much smaller than expected from the ionic radii. (b) Front view of cation triangle A-B-A where oxygen ions have to diffuse through.

accommodated with structural instabilities, namely phase changes into vacancy-ordered phases with low oxygen conductivity; e.g. the cubic phase of $SrCo_{0.8}Fe_{0.2}O_{3-\delta}$ decomposes by precipitation of a vacancy-ordered brownmillerite phases at 0.1 atm and 1020 K. Although the oxygen vacancy concentration in brownmillerite phases is quite high ($\delta = 0.5$), the oxygen conductivity is low because vacancies are trapped in tetrahedral layers and, therefore, immobile [25–31]. The oxygen non-stoichiometry generally increases with increasing temperature because oxygen defects are thermally activated. As a result, redox cations will provide charge neutrality by adjusting their oxidation state.

Electronic conductivity in MIEC is closely connected to the multivalent nature of the B-site cations. In most cases, transition metals with partly unoccupied $3d$-orbitals provide electron conduction due to a covalent overlap between $3d$-orbitals and oxygen $2p$-orbitals. These B-O-B bonds can transfer charges by using the so-called Zener double exchange process as noted below [32–34].

$$B^{n+}-O^{2-}-B^{(n-1)+} \rightarrow B^{(n-1)+}-O^{-}-B^{(n-1)+} \rightarrow B^{(n-1)+}-O^{2-}-B^{n+}$$

In addition to the oxygen vacancy concentration, oxygen permeability is strongly governed by the activation energy of oxygen migration E_A. It is assumed that oxygen ions take a path along the $\langle 110 \rangle$ edge of the oxygen octahedron to propagate to the next vacant anion site. In order to reach the adjacent anion site, they need to pass through a saddle point, a triangle formed by two A-site and one B-site cations [33,35] as indicated in Figure 2(a). Based on the assumption of rigid spheres, a critical diameter d_c can be derived which motivates the change in activation energies for various compounds. Hereby d_c describes the maximum size of an ion to pass through the critical triangle

[33,36]. However, other empirical parameters were identified like lattice free volume, lattice polarizability and average metal-oxygen binding energy having an equally important role regarding E_A.

Simulations of $LaBO_3$ compounds have revealed deviations from the direct path for oxygen moving to adjacent vacancies. Simulated anions travel along a curved path with the saddle point shifted away from the B-site [37–39] which is illustrated in Figure 2(a). Furthermore, simulations suggest a significant displacement in the range of 0.1 Å for the cations in the saddle-point. As depicted in Figure 2(b) the cations move away from the oxygen anion to provide sufficient space for oxygen movement. Hence, the relationship between critical diameter d_c and activation energy is often loosened by the fact that most crystals cannot be approximated by classical rigid sphere models.

2.1.3 The compound BSCF

Perovskites containing transition metals on the B-site are long known for their high electrical conductivity. By introducing low-valence A-site elements, oxygen vacancies could be introduced into several systems to get ionic conductivity. Beginning from 1985 TERAOKA ET AL. [14,40,41] systematically investigated various compounds related to the La-Sr-Co-Fe system with a general material stoichiometric formula of $A_{1-x}A'_xCo_{1-y}B_yO_3$ (A = La, Pr, Nd, Sm, Gd; A' = Sr, Ca, Ba, Na; B = Co, Mn, Fe, Ni, Cu, Cr). The highest permeability among these synthesized compounds was achieved for $SrCo_{0.8}Fe_{0.2}O_{3-\delta}$ (SCF) as the substitution of La^{3+} by Sr^{2+} promotes the generation of oxygen vacancies. However, several research groups reported thermodynamical instabilities of the oxygen-conducting cubic perovskite phase at low temperatures and low oxygen partial pressures. As cubic SCF decomposes into an oxygen vacancy-ordered brownmillerite phase, the oxygen flux, as well as the mechanical strength, is drastically reduced [25–31,42]. By substituting Sr with the larger Ba ion the phase stability could be noticeably enhanced along with an increase in oxygen permeability. This was traced back to the suppression of higher valence states (Co^{4+} and Fe^{4+}) for the B-site cations [3,43]. In contrast to SCF no evidence for oxygen vacancy ordering was found [44]. In addition, many researchers have outlined the high power density for using this material as solid oxide fuel cell cathode [45–50]. Among several Sr/Ba ratios the composition $(Ba_{0.5}Sr_{0.5})(Co_{0.8}Fe_{0.2})O_{3-\delta}$ (BSCF) was favored among many groups [3,51–54]. Compared to SCF, BSCF has a remarkable high oxygen non-stoichiometry [55,56] and tolerance

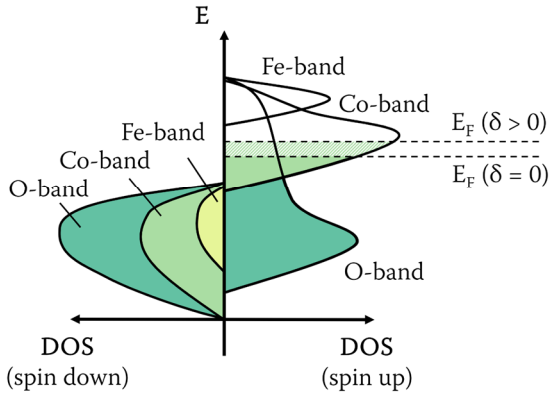

Figure 3. Modified scheme of BSCF band diagram for different oxygen vacancy concentrations δ as proposed by MERKLE ET AL. [71].

towards environments with low oxygen partial pressure (< 10^{-4} atm) [57–60]. As oxygen non-stoichiometries up to δ = 0.8 were measured, more than one anion site within each octahedron can be considered vacant [60]. This emphasizes the tremendous flexibility of the perovskite structure.

Despite enormous potential for high-temperature oxygen conductivity, many groups reported a continuous drop in permeability at long time operation below 840 °C which was explained by the formation of secondary phases [3,61–66]. ŠVARCOVÁ ET AL. [63] demonstrated a sluggish but reversible decomposition of cubic BSCF (c-BSCF) in a two-phase region of cubic and 2H hexagonal (h-BSCF) polytypes. The phase transformation is connected to the local charge disproportion induced by the valence and spin change of Co [67]. This can be connected to the temperature dependent change in oxygen stoichiometry [61], inducing a charge imbalance which is compensated by Co ions. By in-situ TEM analysis of Co- and Fe-$L_{2,3}$ edges, ARNOLD ET AL. [67] determined a valence change from 3+ to 2.8+ (Fe) and 2.6+ to 2.2+ (Co) between room temperature and 950 °C. Moreover, they reported that both, Fe and Co, are in a high spin-state configuration. HARVEY ET AL. [68,69] confirmed a predominant valence state of 3+ for Fe by in-situ and ex-situ X-ray absorption spectroscopy, using transition metal K- and L-edges at a similar temperature range. They reported an initial valence state of 3+ for Co, changing to 2+ above 800 °C. Nevertheless, additional Mössbauer absorption spectroscopy indicated non-negligible amounts of Fe^{4+} and even some Co^{4+} at room temperature [68]. The high spin-state of Fe was confirmed, however, they stated a spin-state change for Co to intermediate spin at 350 °C and high spin at 900 °C.

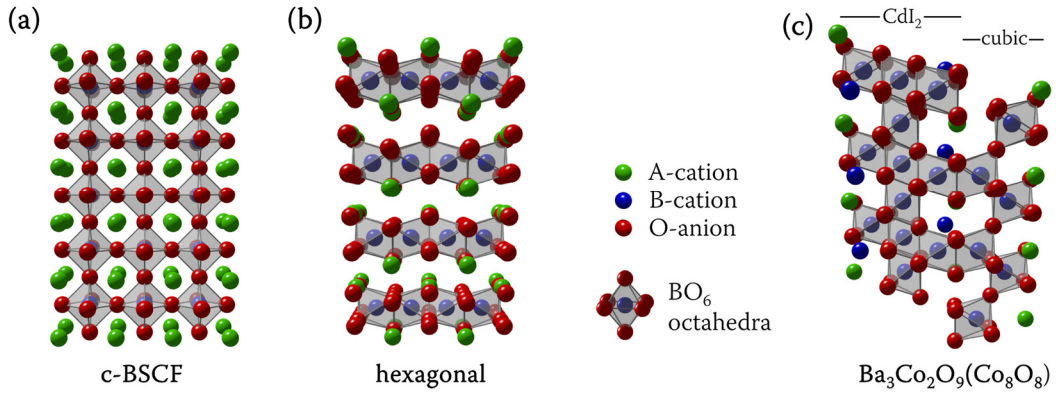

Figure 4. Projected crystal structures of (a) [100] cubic BSCF, (b) [001] hexagonal BSCF and (c) [001] BCO (n = 2) phase. BO_6 octahedrons are highlighted to emphasize the change in configuration between the phases.

MUELLER ET AL. [70] presented a simple electronic band diagram model to motivate why Co is more susceptible to valence changes in the high-temperature regime, compared to Fe. The model was later refined by density functional theory (DFT) calculations by MERKLE ET AL. [71,72]. As depicted in the schematic band structure in Figure 3 the Fermi level E_F is located within a partially filled Co- and O-band. As the removal of oxygen reduces the density of states (DOS) in the O-band, more electrons will occupy Co states. Since the energy level of the Fe-band is ~1 eV higher than the Fermi level no charge will be transferred to Fe [71]. Electrons previously occupying O-band states will now exclusively go into the Co-band and, therefore, lowering the formal oxidation number of Co. Since a higher oxidation state leads to a smaller ionic radius, the cubic phase with its corner sharing BO_6 octahedra is destabilized. This can be rationalized by the elevated tolerance factor (cf. Equation 4) which favors hexagonal phases with much smaller distances between B-site cations [63]. The tolerance factor of BSCF was estimated to be t_{tol} = 0.957 - 1.05 [60,73] which is already close to the stability limit of the cubic phase. In the hexagonal phase the A-site cations and O-anions form close packed layers with the oxygen octahedrons in a face-sharing configuration (cf. Figure 4(b)). Hence, only high temperature and, therefore, a higher oxygen non-stoichiometry, accompanied by the increased ionic radius of the Co cation stabilizes the cubic phase and facilitates oxygen octahedrons connected by sharing corners (cf. Figure 4(a)).

Several studies reported a depletion of Fe in the hexagonal phase with slight variations in the Sr/Ba ratio [74,75]. The compound formula is given by $(Ba_{0.5+x}Sr_{0.5-x})CoO_{3-\delta}$ [62,74,76]. As the hexagonal phase tends to form faster in powder samples compared to

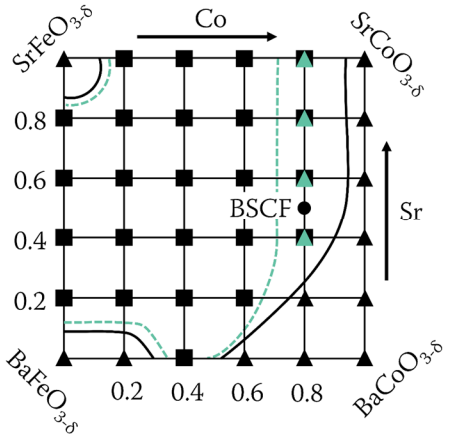

Figure 5. Schematic phase diagram for Ba-Sr-Co-Fe compound system as depicted by YÁNG ET AL. [92] and extended by EFIMOV ET AL. [77]. The cubic perovskite phase is marked by squares; triangles indicate multiphase compounds. Solid lines (black) border the stability range of the cubic phase for 1000 °C, dashed lines (green) for 800 °C.

dense ceramics, it was concluded that secondary phase formation is controlled by a nucleation and growth process where growth rates are limited by kinetics of the involved ions which was confirmed by Johnson-Mehl-Avrami analysis [63,74]. Since the formation of the hexagonal phase reduces the Co content of the cubic phase a 50:50 mixture between the cubic and the hexagonal phase will be reached [74].

In addition to the hexagonal phase, many groups reported an additional secondary phase with lamellar geometry crossing whole grains which did not show up in X-ray diffraction data (XRD) [65,76–78]. Later on, the lamellar phase was identified by our group as barium cobaltite intergrowth structures with stackings composed of CdI_2-type layers and an arbitrary number n of cubic perovskite blocks [79]. The configuration of BO_6 octahedra within the CdI_2-type can be described as edge sharing. The compound is described by the formula $Ba_{n+1}Co_nO_{3n+3}(Co_8O_8)$ (n ≥ 2, BCO) [80]. It is noted that BCO-type intergrowth phases in BSCF contain non-negligible amounts of Fe. However, with respect to former publications the abbreviation BCO will be kept. The formation of BCO layers is reported to have a higher on-set temperature (900 – 1000 °C) compared to the hexagonal phase [79]. A representation of the BCO phase for n = 2 is depicted in Figure 4(c). As BCO and the hexagonal phase are both intergrowth structures in c-BSCF, any arrangement of these three phases are possible [79]. It is believed that BCO phases act as oxygen migration barriers due to the low crystal symmetry and high oxygen stoichiometry [77]. In addition, microstructural investigations by electron microscopy techniques revealed the presence of Co_xO_y phases

at grain boundaries [79,81–84]. Since decomposition is characterized by nucleation and growth, these secondary phases might strongly impact the long-time oxygen conductivity which will be addressed in this thesis.

Another drawback of BSCF pointed out by many researchers, is the high reactivity with CO_2 especially at the permeate side [85–90]. BSCF tends to form (Ba,Sr)CO_3 surface phases at the solid-gas interface, blocking oxygen exchange even at low CO_2 (1 %) concentrations [86,87,90,91]. However, this decomposition is fully reversible by flushing with CO_2 free gas. To counteract CO_2 poisoning coating layers of materials with better CO_2 compatibility were considered.

A first schematic phase diagram for the quasi-quaternary Ba-Sr-Co-Fe compound system was published by YÁNG ET AL. [92] in 2009 and extended by EFIMOV ET AL. [77] in 2010 which is shown in Figure 5. The lines in the plot represent the transition from cubic to multi-phase compounds at 1000 °C (solid) and 800 °C (dashed). Both groups pointed out that end members in this compound system are not pure cubic perovskites. However, by mixing Sr/Ba and Co/Fe many stable cubic compounds can be obtained. Going from high to low temperatures, the stability range for the cubic phase decrease leaving BSCF within the multi-compound area. Therefore, the stability window of BSCF is quite narrow.

2.1.4 Improvement of BSCF

Since BSCF is susceptible to form intergrowth phases with face-sharing or corner-sharing oxygen octahedrons various cation substitutions were considered. Due to the fact that Co is responsible for the decomposition of BSCF, much effort was put into Co-free compounds with a general formula of $Ba_{0.5}Sr_{0.5}B_xFe_{1-x}O_{3-\delta}$ (B = Zn, Mn, Cu, Sb). Even though these materials exhibit a higher phase stability compared to BSCF a considerable sacrifice in oxygen permeability was reported [93–101]. The lower oxygen conductivity can be explained as the thermal induced reduction of valence state is much less pronounced for, e.g., Fe compared to Co. The valence state of Fe in these compounds was determined to be between 3+ and 4+ [94,98,99]. Since highest permeation rates are essential for economic viability, other approaches were considered to stabilize Co containing compounds. Doping was considered promising regarding the stabilization of cubic BSCF. As doping refers to a minor substitution within the compound, specific properties can be targeted without sacrificing the excellent ionic and electronic characteristics of BSCF. Doping strategies to stabilize cubic perovskite

phases can be divided into two approaches. One approach is to introduce elements with a high valence state like Zr, Nb, W to the B-site of the perovskite to increase electrostatic repulsion between BO_6 octahedra and, therefore, promote corner sharing configurations. The second approach is to lower the tolerance factor. Since the tolerance factor of BSCF is, depending on B-site valence state, in the hexagonal regime ($t_{tol} > 1$) lowering of the tolerance factor will contribute to a higher cubic phase stability [102]. Beneficial results were presented for numerous B-site dopants like Zr [103–106], Nb [107–109], B [110], P [110], Zn [111], W [112], Ni [113] and Y [114–116]. Y doping, for example leads to an enormous increase in oxygen permeability of up to 160 % for dopant concentrations as low as 2.5 at% [115]. Even though positive effects were reported for Y- and Zr-doped BSCF, the nanoscale impact of these ions on the microstructure is still not understood. Hence, analytical electron microscopy (cf. Chapter 5.2) including cation lattice-site determination (cf. Chapter 4.3) was carried out on Y-, Sc- and Zr-doped BSCF compounds to generate a deeper understanding on how the microstructure is influenced by these dopants.

As described earlier, the oxygen flux in thin membranes below the critical thickness L_c is limited by surface exchange kinetics. To overcome this limit and to enhance oxygen uptake, several surface coating strategies were investigated. One strategy is to deposit catalytic domains on the membrane surfaces. LEO ET AL. [117–119] reported remarkable improvements in oxygen flux of up to 25 % (Pt particles), 100 % (Ag particles) and 1000 % (Pd particles) by coating BSCF. Even for Y-doped BSCF the oxygen flux could be further enhanced by up to 180 % for Ag coating [120]. Another strategy to boost membrane performance is by increasing membrane surface area by applying porous nanostructured composites. BAUMANN ET AL. [121] reported improved surface exchange rates for BSCF with porous surface activation layers. HONG ET AL. [122] investigated BSCF membranes coated with $La_{0.7}Sr_{0.3}CoO_{3-\delta}$ and found improvement rates in the order of 150 to 200 %. One advantage of $La_{0.6}Sr_{0.4}CoO_{3-\delta}$ (LSC) is the higher tolerance towards CO_2 [123,124]. Therefore, coating with porous CO_2-stable layers will not only increase performance but also protect BSCF against CO_2 exposure. Depending on fabrication parameters mixed phase formations of perovskite LSC and Ruddlesden-Popper $(La,Sr)_2CoO_{4\pm\delta}$ phases have been reported [125]. This hetero-interface system shows an enormous enhancement of oxygen reduction reaction kinetics in the range of 3 to 4 orders of magnitude around 500 °C [125–129]. Despite these benefits, no extended analysis about the compatibility of the compound system LSC and BSCF has been reported, yet. Hence, the thin film LSC-coated BSCF was investigated by means of

high-resolution transmission electron microscopy to outline interdiffusion phenomena within this thesis (cf. Chapter 5.4).

2.2 Electron Microscopy

To overcome the limits of visible light microscopy (VLM), high-energy electron-based microscopes were developed. Due to the correlation between wavelength and the smallest distinguishable feature, the shorter wavelength of fast electrons pushed the resolution limit by several orders of magnitude. In order to control the path of electrons and, therefore, form magnified images electromagnetic lenses, instead of glass lenses as in VLM, are used. These kind of lenses suffer from severe aberrations, mainly spherical aberrations. This is one of the limiting factors for the resolution in electron microscopy. However, modern high-end microscopes are equipped with correction lens systems to correct aberration up to high orders pushing the resolution limit even further. Even though some electron microscopes exist, which operate under pressures up to ~10^3 Pa, most of them require high vacuum within the sample chamber and even ultrahigh vacuum (< 10^{-6} Pa) in the region of the electron emitter to prevent contamination of field emission electron sources which are implemented in modern high-resolution scanning and transmission electron microscopes.

A field emission gun (FEG) consists of a sharp tip (cathode) followed by two anodes. By applying a high voltage between the tip and the first anode, electrons can overcome the potential barrier between the tip and the vacuum by quantum tunneling. The applied voltage is usually called extraction voltage and is in the range of several kV. To accelerate the electron to their final speed, an appropriate voltage is applied to the second anode. Depending on the type of electron microscope the final kinetic energy of electrons ranges between several 100 eV to several hundred keV. Since FEGs do not only provide a high brightness but also a high spatial and temporal coherence, they are essential for many analytical methods based on electron interference phenomena.

In electron microscopy two fundamental types of microscopes can be distinguished; the scanning electron microscope and the transmission electron microscope which are explained in the following sections.

2.2.1 Scanning electron microscopy

In scanning electron microscopy (SEM), the image is generated sequentially by scanning a focused electron beam with a small diameter, called probe, over a rectangular sample area. SEM is a surface technique which allows high-resolution imaging of bulk specimens with macroscopical dimensions. The interaction between the electron probe and the sample is used for image formation. The electron intensity emitted from the

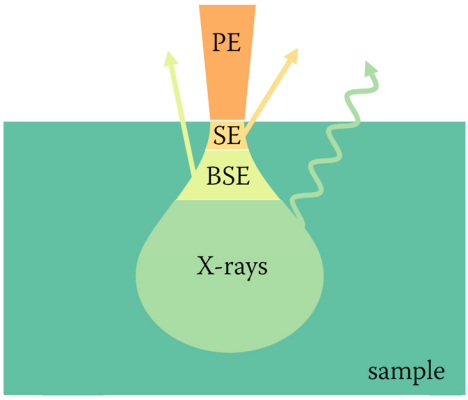

Figure 6. Schematic representation of the interaction volume in SEM.

bulk sample is measured by suitable detectors and converted into a digital gray value. By synchronizing the movement of the probe and the readout of the detector, a digital image of the scanned sample area is generated. Therefore, the magnification is determined by the size of the rastered area. However, the resolution is governed by the interaction between electron beam and sample. The incident electrons will scatter at the sample's atoms close to the surface which leads to emission of either electrons or photons which carry useful sample information. The sample volume characterized by scattering events is known as the interaction volume which is dependent on several parameters like primary beam energy, probe size, and predominant scattering mechanism. The interaction volume of different signals, which will be explained in the following, is illustrated in Figure 6.

The primary electrons interact with the sample material by different processes, e.g. phonon and plasmon excitation, electron–electron scattering or elastic Rutherford scattering. Apart from elastic Rutherford scattering, the incident electron loses energy in these scattering events and will slow down. As a high-energy incident electron can transfer its energy to several electrons in the sample, many excited electrons are generated, each of them with the ability to scatter again. Most excited electrons with a small kinetic energy will not reach the surface because the average distance between scattering events, denoted as mean free path, is small. Hence, only low-energy electrons created near the surface can escape from the sample and are detected by suitable detectors (cf. Figure 6). By convention, electrons with a kinetic energy below 50 eV are denoted as secondary electrons (SE). Due to the small escape depth, a SE detector can be utilized to image the near surface region of the sample. Hence, this type of contrast is often referred to as topography contrast.

Rutherford scattering of incident electrons with nuclei leads only to a negligible energy transfer. Electrons which are backscattered elastically can easily escape from the sample due to their large mean free path, even if scattering takes place some distance away from the surface (cf. Figure 6). These electrons and, by convention, all electrons with a kinetic energy above 50 eV, are referred to as backscattered electrons (BSE). The intensity of BSE resulting from elastic Rutherford scattering is strongly dependent on the atomic number Z and the observable contrast is denoted as Z-contrast. However, the reader should keep in mind that even though it is called Z-contrast , it also includes contributions from topography and dynamical diffraction phenomena.

Since inelastic collisions can remove inner-shell electrons within the sample's atoms, the transition of outer-shell electrons into unoccupied core states can generate high-energy photons (X-rays). The X-ray energy is characteristic for each element, allowing qualitative and even quantitative elemental analysis. This will be described in more detail in Chapter 2.2.2.3. As X-rays have a high mean free path, the interaction volume in bulk specimens is quite large which is indicated in Figure 6.

2.2.2 Transmission electron microscopy

In conventional transmission electron microscopy (TEM) a thin sample is illuminated by a parallel defocused electron beam generated by a condenser-lens system. Scattering of the incident electron beam and the atoms in the sample causes changes in the locally transmitted electron phase and intensity. An imaging-lens system guides the transmitted electrons to an electron-sensitive phosphorous viewing screen or electron camera, e.g., a charge-coupled device (CCD) camera.

In TEM it is suitable to distinguish two different modes of operation, the imaging mode and the diffraction mode with the two different electron optical paths depicted in Figure 7(a,b). For the imaging mode, the lower lens system projects the exit electron wave of the object on the detector plane where the electron intensity is recorded. It is emphasized that the 'real' exit wave of the sample is different compared to the measured electron wave at the detector plane due to considerable lens aberrations in the imaging-lens system. How this affects the transfer of contrast is described in Chapter 2.2.2.1. Apertures in the back focal plane of the objective lens, often referred to as diffraction plane, can be used to adjust image contrast by selecting specific reflections. If the undiffracted beam is selected, areas, where the electrons are more strongly diffracted, appear dark on the electron detector. This is called bright-field (BF) imaging.

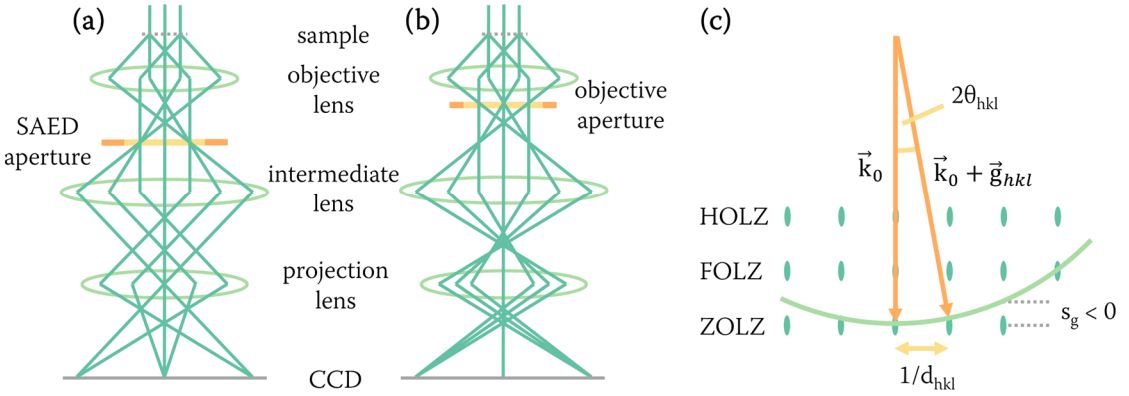

Figure 7. Electron optical path within the microscope in (a) diffraction and (b) imaging mode. (c) Simplified representation of the Ewald sphere in reciprocal space.

The other case, where a specific Bragg reflection is selected, is called dark-field (DF) imaging. The lenses of the imaging system can also be tuned in such a way that the back focal plane of the objective lens, the Fourier plane, is projected on the detector plane. Since the Fourier plane contains diffraction information this mode is called diffraction mode. By inserting an aperture in a virtual image plane within the optical path, the diffraction information can be limited to a certain sample area, therefore, this technique is called selected area electron diffraction (SAED).

Crystalline materials with a high periodicity on an atomic scale are especially interesting for TEM because the electrons propagating through the specimen produce a distinctive interference spot pattern in the far-field region. This is often referred as diffraction since the term reflects the wave nature of electrons, as suggested by the wave-particle duality principle. In electron microscopy, the diffraction pattern can be found in the back focal plane of the objective lens because the focal plane of an imaging-lens corresponds to the far-field region according to Fraunhofer's diffraction equation. The parallel coherent electron illumination in TEM can be expressed by the concept of plane waves with a wave vector of $\vec{k}_0$. The length of $\vec{k}_0$ corresponds to the reciprocal electron wavelength λ^{-1}. The interaction of crystalline materials with coherent electron illumination can be described by Bragg´s law (cf. Equation 5) which predicts constructive electron interference at Bragg angles θ_{hkl}.

$$n\lambda = 2d_{hkl} \sin \theta_{hkl} \tag{5}$$

In Bragg's law n represents the diffraction order and d_{hkl} the plane distance of a crystallographic plane set with hkl Miller indices. As each reflection can be attributed to a set of crystallographic planes, crystal structure and lattice parameter can be

obtained from diffraction patterns. Bragg diffraction can be motivated geometrically by the so-called Ewald construction in reciprocal space. In the reciprocal space the crystal is represented by a set of reciprocal lattice points d_{hkl}^{-1} where each point corresponds to a set of lattice planes in real space. The incident electron beam is described by a wave vector $\vec{k}_0$ which terminates at the origin of the reciprocal lattice. A sphere, the so-called Ewald Sphere, with radius k_0 is constructed around the origin of the wave vector as depicted in Figure 7(c). In this construction Bragg diffraction occurs if the surface of the Ewald Sphere coincides with a reciprocal lattice point which can be seen as diffraction spots in the back focal plane of the objective lens. One satisfied diffraction condition for a scattering vector $\vec{g}_{hkl}$ is depicted in Figure 7(c). The resulting wave vector of the scattered electron wave is given by $\vec{k}_0 + \vec{g}_{hkl}$. It is useful to label the planes perpendicular to the incident beam because they yield information on the 3D crystal structure. The plane containing the origin of the reciprocal lattice is called zero order Laue zone (ZOLZ) followed by first and higher order Laue zones (FOLZ and HOLZ) as shown in Figure 7(c). Considering specimens with finite dimensions, reciprocal lattice points are broadened along the incident beam direction proportional to t^{-1} with the specimen thickness t which is distinctly below 1 µm. Due to the extension of the reciprocal lattice points along the electron-beam direction and due to the small radius of curvature of the Ewald sphere for high-energy electrons, a large number of reflections can be observed in diffraction patterns. Bragg diffraction also occurs if the Ewald sphere passes through the reciprocal lattice rod at a distance s_g from the reciprocal lattice point. The distance s_g is denoted as excitation error and is indicated in Figure 7(c).

SAED patterns are acquired with electrons propagating along a path with high crystal symmetry, so-called low-index zone-axes. These low-index zone-axes are important for high-resolution TEM or for crystal structure analysis. Kikuchi lines in diffraction patterns can be utilized to orient specimens into specific orientations, e.g., two-beam diffraction conditions. The formation of Kikuchi lines requires a convergent electron beam, either generated by changing the condenser system or by diffusely scattered electrons in thick samples. The electrons in the convergent beam are Bragg diffracted on specific crystal planes which lead to the formation of pairs of cones. The intersection between these cones and the Ewald sphere are referred as Kikuchi lines even though they are in principal parabolas. The distance between Kikuchi lines is $2\theta_{hkl}$ of the corresponding set of crystallographic planes.

2.2.2.1 High-resolution transmission electron microscopy

In order to understand the principle of high-resolution TEM (HRTEM) it is necessary to consider the effects of the imaging-lens system on the electron wave exiting the sample. In case of sufficient thin samples, the exit electron wave can be written as $\Psi_e = \Psi_0 \exp(-i\tilde{\sigma}V_z)$ with Ψ_0 being the incident electron wave, V_z the potential projected along the incident direction and $\tilde{\sigma}$ the interaction constant. For the sake of simplicity, the incident electron wave is set to unity ($\Psi_0 \approx 1$). For very thin samples consisting of weak scattering elements, V_z can be considered small ($V_z \ll 1$) allowing to approximate the exit wave by the first two expansion terms as given in Equation 6.

$$\Psi_e \approx 1 - i\tilde{\sigma}V_z \tag{6}$$

This so-called weak-phase object approximation allows generating an easily interpretable representation of the image formation. The influence of the imaging-lens system on the exit wave function is given by the convolution between Ψ_e and the point spread function of the imaging system $H(u)$. The function $H(u)$ characterizes how each spatial frequency component u is transferred into the final wave image Ψ_i which is detected at the detector plane. The convolution can be written as a pointwise product in the frequency domain as shown in Equation 7. The frequency domain (or reciprocal space) is connected with the space domain by the Fourier transformation $\Psi_i(u) = \mathcal{F}\{\Psi_i(x,y)\}$.

$$\Psi_i(u) = \Psi_e(u)H(u) \tag{7}$$

$H(u)$ is often referred to as contrast transfer function. $H(u)$ is composed of three terms as given in Equation 8.

$$H(u) = A(u)E(u)B(u) \tag{8}$$

Here, the aperture function $A(u)$ describes the highest transmitted spatial frequency, the envelope function $E(u)$ reflects the damping of high spatial frequencies due to partial temporal and spatial coherence and $B(u)$ contains the aberration effects of the imaging-lens system. $B(u)$ is a complex function often written as an exponential function as seen in Equation 9 with λ being the electron wavelength, C_s the spherical aberration coefficient and Δf the defocus value.

$$\begin{aligned} B(u) &= \exp\big(i\chi(u)\big) \\ \chi(u) &= \pi\Delta f\lambda u^2 + \frac{1}{2}\pi C_s\lambda^3 u^4 \end{aligned} \tag{9}$$

By neglecting $\tilde{\sigma}^2$ terms, the image intensity I_m of a weak-phase object can be written as

$$I_m = |\Psi_i|^2 \approx 1 + 2\tilde{\sigma}V_z(x,y) \otimes \mathrm{Im}\big(H(x,y)\big) \tag{10}$$

The image contrast is dictated by the imaginary part of $H(x,y)$ which is given by $B(u)$. Hence, the imaginary part of $H(u)$ can be written as $\mathrm{Im}\big(H(u)\big) = A(u)E(u)\sin\big(\chi(u)\big)$. By neglecting $A(u)$ and E(u), the contrast transfer in the final image is given by the shape of $\sin\big(\chi(u)\big)$ which is only dependent on λ, C_s and Δf. Since the sign of $\sin\big(\chi(u)\big)$ can change with spatial frequency, there is no intuitive transfer of contrast into the final image.

For crystalline samples, high-resolution imaging requires low indexed zone axis orientations as there the distance between the atomic columns is big enough to be resolved by the microscope. The high-resolution image is generated by the interference between multiple reflexes. Hence, a large objective aperture has to be chosen. In general, samples cannot be approximated as weak-phase objects due to non-negligible contributions of amplitude contrast in addition to the phase contrast. As the phase contrast component is severely altered by aberrations of the imaging-lens system it is hard to directly identify atomic columns in the final image. Therefore, image simulations are an essential step in interpreting high-resolution TEM images.

2.2.2.2 Scanning transmission electron microscopy

Scanning transmission electron microscopy (STEM) is related to SEM. However, instead of detecting SE or BSE, transmitted electrons are used for image formation. Most modern transmission electron microscopes provide the necessary scanning coils and detectors for STEM operation. Since samples for STEM are thin, the interaction

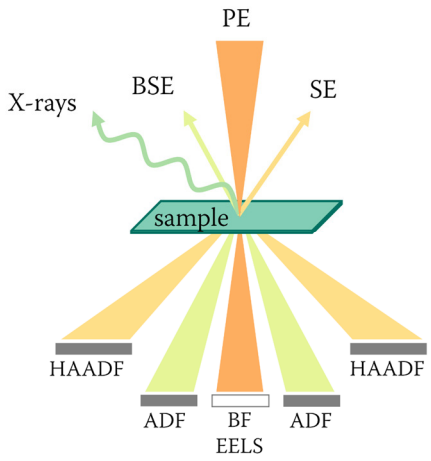

Figure 8. Schematic graph of the STEM mode in a transmission electron microscope. For the sake of simplicity lenses between the sample and detectors were omitted.

volume is drastically reduced compared to SEM. Therefore, the resolution is ultimately limited by the probe size produced by the condenser system. A set of annular detectors is mounted in the diffraction plane below the sample to detect electrons scattered into different angles as depicted in Figure 8. The imaging-lens system located between the sample and the detectors can be used to change the virtual distance that an electron has to travel to reach the detector. This virtual distance between sample and detector is referred to as camera length (CL). The on-axis detector (cf. Figure 8) collects electrons which are not or only slightly scattered by the sample. Therefore, areas with strong Bragg diffraction will appear dark, comparable to TEM BF imaging. The first off-axis annular detector (cf. Figure 8) collects mostly Bragg-diffracted electrons like in the TEM DF mode. Yet, in contrast to TEM DF imaging, not a specific Bragg reflection is selected but an annular region within the diffraction plane. Hence, for this annular dark-field (ADF) detector, the contrast is not necessarily comparable to TEM DF imaging. The outer detector, the high-angle annular detector (HAADF) only collects electrons which are strongly scattered by the sample. Since scattering to higher angles is mostly incoherent, the contrast is mainly dictated by the differential Rutherford cross-section $\frac{\mathrm{d}\sigma}{\mathrm{d}\Omega}$ (cf. Equation 11) with e and ε_0 being constants for the elementary change and the vacuum permittivity, E_0 the energy of the electrons, Z the atomic number, and θ the scattering angle.

$$\frac{\mathrm{d}\sigma}{\mathrm{d}\Omega} = \frac{Z^2 e^4}{256\pi^2 {\varepsilon_0}^2 {E_0}^2} \frac{1}{\sin^4\left(\frac{1}{2}\theta\right)} \tag{11}$$

As the equation shows pronounced scattering for higher Z elements, the contrast obtained by the HAADF detector is often called Z-contrast. Since diffraction is negligible, HAADF-STEM images unlike HRTEM images can be interpreted directly even at atomic resolution.

2.2.2.3 Energy dispersive X-ray spectroscopy

In SEM and (S)TEM inelastic electron-electron interaction between the incident electron beam and the sample can be used for analytical purposes. As inelastic collisions can cause the removal of inner-shell electrons in the sample material, the energy released by the transition of an outer-shell electron into empty states can generate high-energy photons (X-rays) as indicated in Figure 9(a). These X-rays can be detected by energy dispersive X-ray detectors. The energy of the emitted X-rays is dependent on the atom's energy levels and is, therefore, characteristic for the type of element. Since electrons are accelerated by the sample's nuclei, an additional bremsstrahlung spectrum

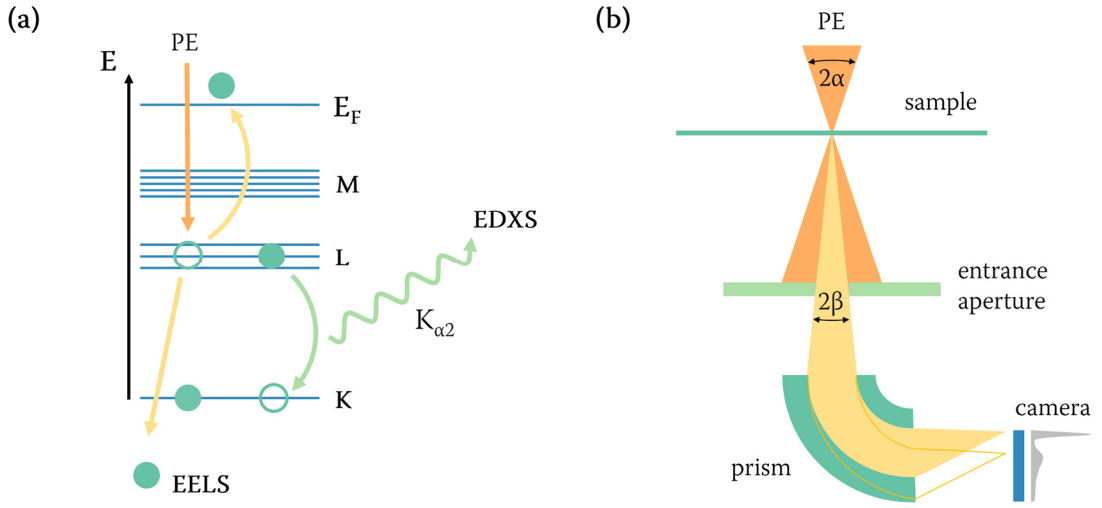

Figure 9. (a) Scheme for inelastic interaction between PE and core-level electron in the specimen. Recombination process can generate high energy photons detectable by EDXS. (b) Simplified model of a spectrometer used for EELS. The combination of convergence half-angle α and collection half-angle β are important parameter for the reproducibility of EELS spectra.

will be superimposed to the sharp characteristic elemental X-ray peaks. To analyze elemental peaks quantitatively one has to consider the complex relationship between the measured X-ray intensity and the element concentration. Therefore, CLIFF AND LORIMER [130] proposed a quantification technique for thin samples based on the negligence of secondary fluorescence and X-ray absorption within the sample. Based on their assumption the relative concentrations $C_{A,B}$ of elements A and B can be connected to the characteristic X-ray line intensities $I_{A,B}$ in the following way.

$$\frac{C_A}{C_B} = k_{A,B}\frac{I_A}{I_B} \quad \text{with} \quad \sum_i C_i = 1 \tag{12}$$

The microscope specific $k_{A,B}$ -factor or Cliff-Lorimer-factor yields a connection between the weight percentage of two elements and their characteristic X-ray intensity. The overall concentration of all elements in normalized to 100 %. In derived $k_{A,B}$-factors for different combinations of elements the relation

$$k_{A,B} = \frac{k_{A,X}}{k_{B,X}} \tag{13}$$

can be utilized. These factors can be obtained from analyzing samples with known composition. In this work the quantitative analysis was performed by using the implemented $k_{A,B}$-factors in the FEI (FEI company, Hillsboro, USA) TEM Imaging and

Analysis (TIA, version 4.7 build 1489) and Bruker (Bruker Corporation, Billerica, USA) ESPRIT (version 1.9.4.3448) software package.

2.2.2.4 Electron energy loss spectroscopy

Interaction between primary electrons (PE) and inner-shell electrons can result in significant energy transfer, allowing the excited inner-shell electron to jump into a vacant energy state. At low temperatures free states can only be found above the Fermi level. Hence, the transferred energy will be the energy difference between the Fermi level and the energy level of the bound electron (cf. Figure 9(a)). By using an energy-dispersive electron detector, characteristic ionization edges which yield elemental information can be observed. This technique is called electron energy loss spectroscopy (EELS). In many microscopes, the spectrometer is mounted at the bottom of the microscope column on the optical axis as depicted in Figure 9(b). An entrance aperture limits the angular distribution of electrons entering the spectrometer. Electrons are deflected by a magnetic sector prism according to their energy. The energy dispersed electron beam is recorded using a slow-scan CCD camera. EELS provides a higher energy resolution (< 1 eV) compared to EDXS (> 100 eV) which is mainly limited by the energy spread and the stability of the PE beam. In contrast to EDXS, where X-ray generation is considered isotropic, inelastic scattering (apart from phonons) is mainly directed in forward direction. Depending on the momentum transfer related to the symmetry of electronic states, spectral features might change if the convergence angle of the beam or the collection angle of the spectrometer is varied. Therefore, it is very important to use fixed convergence and collection angles to provide comparability of spectra. Electron energy loss spectra can be split into two distinctive electron loss regions; the low-loss (0 – 50 eV) and core-loss (above 50 eV) region. Elastically scattered electrons are detected in the zero-loss (ZL) peak whose shape and width is given by the electron gun characteristics and the beam's monochromaticity.

The low-loss region contains information on weakly bound electrons from the conduction or valence band. Electrons scattered inelastically by plasmons form the plasmon peak which is much more pronounced compared to interband transitions. Plasmon scattering increases dramatically with sample thickness and facilitates the determination of the local sample thickness (cf. Appendix 8.3).

High-energy electron losses (core-loss) originate from inner-shell interactions and, therefore, yield information on the elements present and their binding states. The onset energy of these so-called ionization edges corresponds to the transition from the inner-

shell state to the lowest unoccupied state (usually close to the Fermi level). The ionization edge will contain features at energy losses above the onset energy because transitions into higher unoccupied states are also possible. The part close to the ionization edge onset, the so-called energy loss near-edge structure (ELNES), contains information about the density of states close to the Fermi level. This part is very sensitive towards the change in bonding nature or valence state. The region far away from the ionization onset referred to as extended energy loss near-edge fine structure (EXELFS), is generated by core electrons with sufficient kinetic energy to leave the specimen. These free electrons can be scattered by adjacent atoms and therefore carry information about the surroundings.

In addition to spectrum features, there is also an exponential decaying background with loss energy ΔE. The background intensity I_{BG} can be modeled by the so-called power law which is written below.

$$I_{BG} = w[\Delta E\ ]^{-v} \tag{14}$$

Hereby, w and v represent fit parameters which are only valid for a limited energy-loss range of the spectrum. With increasing thickness PE will tend towards multiple scattering within the sample. This will not only affect the low-loss regime but also the ionization edges. Electrons scattering at inner shell electrons can undergo several additional plasmon scattering processes depending on sample thickness. Hence, for multiple scattering ionization edges are convoluted with the low-loss spectrum. In order to get single scattering spectra various deconvolution techniques are available to remove contributions from plasmon scattering. The most common method for ionization edges is the Fourier-ratio method which was also employed within this thesis. Background subtraction and deconvolution of EELS spectra was performed using the DigitalMicrograph (Gatan inc., Pleasanton, USA) software suite (version 1.85.1535). For additional processing of spectra (e.g. filtering) self-written software programs were used. If not stated otherwise, the convergence angle was fixed at 16.7 mrad with a collection angle of 6.7 mrad.

2.2.3 Instrumentation

SEM investigations were performed either with a LEO (now: Carl Zeiss AG, Oberkochen, Germany) 1530 microscope or a FEI (FEI company) Quanta 650 environmental SEM both equipped with a FEG. If not stated otherwise, the Everhart-Thornley detector was used for the acquisition of SE SEM images. Channeling

contrast images for the determination of grain sizes were obtained by the semiconductor BSE detector mounted in the FEI Quanta microscope.

TEM analysis was performed in an aberration-corrected FEI Titan^3 80-300 (FEI company) and a FEI Tecnai Osiris microscope operated at either 80, 200 or 300 kV depending on sample characteristics. The Titan^3 microscope is equipped with an EDAX (Ametek Inc., Berwyn, USA) 30 mm^2 Si(Li) EDXS detector and a Gatan (Gatan Inc., Pleasanton, USA) post-column spectrometer Tridiem 865 HR. The Osiris microscope includes a Super-X EDXS detection system employing four Bruker (Bruker Corporation) windowless Silicon Drift Detectors.

2.2.4 Sample preparation

BSCF TEM samples were prepared by conventional techniques involving cutting, polishing and dimple grinding. Dimple grinding was performed until electron transparency was reached. Additional low energy (2 keV) thinning was carried out by Ar^+-ion polishing using a Precision Ion Polishing System (Gatan inc., model: 691). Prior TEM investigation samples were coated with a thin carbon layer to avoid charging phenomena induced by the electron beam. Thin regions were masked to avoid any artifacts in the recorded images.

SEM samples were polished using diamond lapping film with a grit size of 30 µm down to 0.5 µm. To visualize secondary phases an etching procedure involving a colloidal SiO_2/water suspension (MasterMet2, ITW Test & Measurement GmbH, Düsseldorf, Germany) was further employed. As the etching speed of secondary phases in BSCF differs quite strongly, phase specific topography features can be generated as demonstrated by MÜLLER ET AL. [76].

3 Methodical Developments

This chapter focuses on methodical improvements connected to the investigation of BSCF. The first part will deal with filtering techniques to separate signal from noise in large spectral data sets. Multivariate statistical methods are evaluated regarding their limit in processing EDXS spectra. Furthermore, possible artifact formation will be addressed. In the second part of the chapter a new method for determining the valence state of Co within BSCF is presented. In addition, the measurement of Fe-valence state, using a well-established technique, is motivated at the end of the chapter.

3.1 Filtering by principal component analysis (PCA)

Samples in electron microscopy are often susceptible towards beam damage, especially in STEM mode where the electron beam is condensed on a tiny sample area. This imposes the use of low dwell times accompanied by poor counting statistics, mostly encountered in core-loss EELS or EDXS. Especially weak features or elements with small concentrations are often lost within the noise. With the evolution towards higher stability of microscope parameters, the acquisition of large spectrum images has become possible. Here, the electron probe scans along a rectangular sample area while simultaneously recording a full spectrum at each rastering point, producing data cubes up to 2048 x 2048 pixel, each spectrum containing up to 2048 energy channels. To realize an acceptable acquisition time, the dwell time at each point has to be kept extremely low which is the reason why the individual spectra within the data cube suffer from poor signal-to-noise ratio (SNR). However, as these large data sets contain a high level of redundant information, appropriate filtering techniques based on statistics can be applied to retrieve information hidden in the noisy data. One approach is multivariate analysis, which relies on the reduction of the original variables to a reduced number of transformed variables. This reduction of dimensionality is based on the assumption that the set of original variables is highly correlated which is especially the case for large spectrum collections. The most prominent method is principal component analysis (PCA) [131,132]. Here, the data cube is decomposed into an orthogonal set of uncorrelated variables called principal components (PC) in a way that the first few PCs contain most of the data's variation. High variance components are considered to reflect relevant information, whereas low variance PCs account for noise. By projecting the original data into a subspace with only the first few PCs, the relevant information is solely retained. Basically, the data set is represented by a linear

combination of the chosen fundamental PCs. The main advantage of PCA is that no a-priori information is necessary to compute the PCs. The filtering approach is especially advantageous for beam-sensitive samples, as the dwell time at each sample position can be extremely short. Since most of the information can be recovered even from very noisy data, this might help to extend electron spectroscopic techniques to a broader range of materials.

3.1.1 Calculation

Given a spectrum collection, the raw data set is represented by a $(n \times c)$ matrix X with n being the number of spectra in the data cube and c the number of energy channels. Usually PCA is performed on centered data $\bar{X}$ as this minimizes the approximation error [133]. Centering is carried out by subtracting the spectrum mean from each row according to Equation 15.

$$\bar{X}_{ij} = X_{ij} - \frac{1}{c}\sum_{k=1}^{c} X_{ik} \tag{15}$$

PCs can be understood as eigenvectors or eigenspectra, here denoted as $\vec{p}_i$, from the Eigen-equation of the covariance matrix $C = \bar{X}\bar{X}^*$. The degree of contained variation within each PC is expressed by its corresponding eigenvalue (EV) λ_i. Therefore, the PC with the highest EV, contains the most significant piece of information. PCs with low EVs can be attributed to noise. One should take into account, that PCs should be understood as abstract components, not necessarily reflecting physically observable spectra due to the orthogonality criteria. By arranging the eigenvectors according to their EV in decreasing order, the squared $(c \times c)$ loading matrix $\tilde{L}$ can be constructed (cf. Equation 16).

$$\tilde{L} = (\vec{p}_a\ \vec{p}_b\ \vec{p}_c \ldots) \text{ with } \lambda_a < \lambda_b < \lambda_c \ldots \tag{16}$$

By choosing only a few significant PCs with high EVs (e.g. the first k PCs), the dimension of the score matrix reduces to $(c \times k)$. The initial data set can now be represented in terms of k PCs. If we introduce the score matrix $\tilde{S} = \bar{X}\tilde{L}$, the transformation of the initial data set into the reduced set $\bar{X}_r$ can be written as presented in Equation 17.

$$\bar{X}_r = \tilde{S}\tilde{L}^T \tag{17}$$

The crucial part about PCA is the choice on how many PCs are necessary to describe the initial data set. A high number of PCs might introduce noise in the filtered data set,

whereas a low number might not reflect the initial data correctly and, therefore, introduces serious artifacts, especially for features with low peak-to-background ratio. One criterion often employed to justify the number of PCs is the Scree plot where the explained variance fraction of each PC ($\lambda_i/\sum_n \lambda_n$) (or its logarithm) is plotted in a descending order [134]. The position showing a considerable change in slope where the course of the explained variance fraction levels off, is considered the crossover point between relevant and non-relevant components. However, this criterion can strongly rely on the visual interpretation of the person analyzing the data. Therefore, one should never rely on this criterion alone. In spectrum images it is also suitable to include the score matrix to justify the number of retained PCs. As the score matrix contains the weights for each PC, a spatially resolved image showing the weight of one PC, can aid to judge the contribution to the final image. Also, the corresponding eigenspectra can help to further motivate the relevance of individual PCs.

One drawback of PCA is its inability to handle non-Gaussian noise. This is particularly bad for EELS and EDXS as their signal obeys Poisson counting statistics. KEENAN AND KOTULA [135] presented a method for time-of-flight secondary ion mass spectrometry where they scaled the initial data set appropriately, to account for Poisson counting statistics, before performing PCA. It was later successfully applied to EELS [136,137] and EDXS [138,139]. This form of PCA is often referred to as weighted PCA (wPCA).

Unfortunately, for large data sets, the computation of the covariance matrix is quite costly, as the computation complexity is in the order of $\mathcal{O}(c^2 n)$ [140]. However, as only a very limited number of significant components is necessary, computing time can be reduced drastically by just extracting the first few components iteratively (usually in the range of 2 to 20 components). One of the most prominent iterative algorithms to extract PCs is the non-linear iterative partial least squares (NIPALS) algorithm [141]. However, NIPALS suffers from the loss of orthogonality with increasing PCs due to limited computing accuracy. To account for that, a Gram-Schmidt re-orthogonalization procedure for scores and loadings within each iteration step was introduced [142]. This so-called Gram-Schmidt PCA algorithm was employed in this thesis, as it performs reasonably fast on modern multicore machines. The implementation was realized in C++ using the template library EIGEN [143] for highly optimized low-level matrix functions in combination with the QT FRAMEWORK [144]. This implementation allows filtering spectra of large data sets of more than 512 x 512 pixels (= 262144 spectra)

within minutes on an Intel (Intel Corporation, Santa Clara, USA) Core i7-3770K quad-core machine.

3.1.2 Filtering of EDXS spectra by PCA

To assess the benefits and limits of multivariate filtering for EDXS, data sets with different SNRs were constructed from real measurement data. For that, one spectrum image (SI) with a high pixel resolution of 2048 x 2048 pixel was recorded in the FEI Osiris microscope. The recording time was chosen to be 60 min which resulted in a SI with 238 million X-ray counts in total. The combined counting rate as displayed in the acquisition software was less than 140 kcps. Each pixel of the SI contains 2048 energy channels. The raw data of the SI was downsized to 256 x 256 pixel by integrating (binning) the counts per energy channel and/or discarding some of the spectra according to specific pixel patterns. The pattern to downsize each block of 8 x 8 pixel is depicted in Figure 10. The resulting seven binned SIs are referred to in terms of their effective measurement time which can be calculated by the original recording time (60 min) multiplied by the number of retained pixel divided by the total number of pixel in the original image. The corresponding effective measuring times are added to the binning pattern in Figure 10. Resulting SIs were checked for binning artifacts, however, no indications were found. One advantage of this method is that SIs with different SNR were obtained from the same sample region with identical microscope parameters. Another advantage is that the introduction of artificial noise, which might not fully reflect the experimental noise, can be avoided.

Elemental maps were derived by plotting the integrated intensity around a specific emission line for each spectrum within the SI. The integration windows were chosen to include at least 90 % of the peaks intensity. Elemental maps of Sr-K$\alpha_{1,2}$, Ba-L$\alpha_{1,2}$, Fe-K$\alpha_{1,2}$,

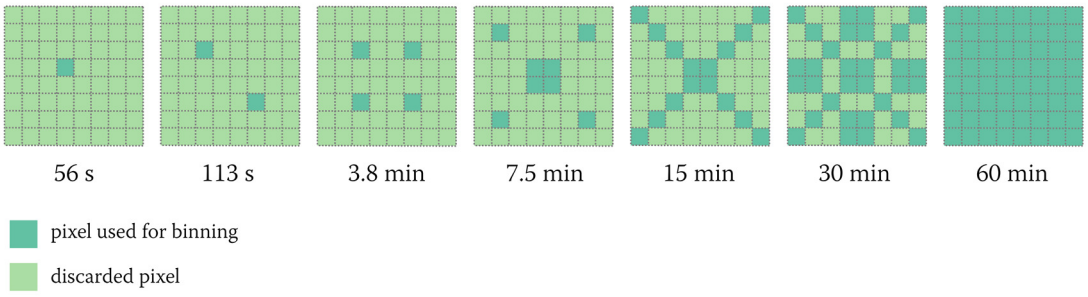

Figure 10. 8 x 8 pixel patterns used for binning the SI from 2048 x 2048 to 256 x 256 pixel. The value under each pattern corresponds to the effective measurement time.

Co-Kα$_{1,2}$ and O-Kα were investigated. Background subtraction was omitted as the background in the individual spectra was not distinguishable from the elemental emission lines due to the poor signal quality. The elemental maps before filtering are depicted in Figure 11. From the images, it is obvious, that there is a steady improvement in image quality with increasing effective measurement time as the noise level decreases. This is especially pronounced for peaks with low intensity, e.g. Sr-Kα$_{1,2}$. Interestingly, many features are already visible in the image with very low effective measurement times.

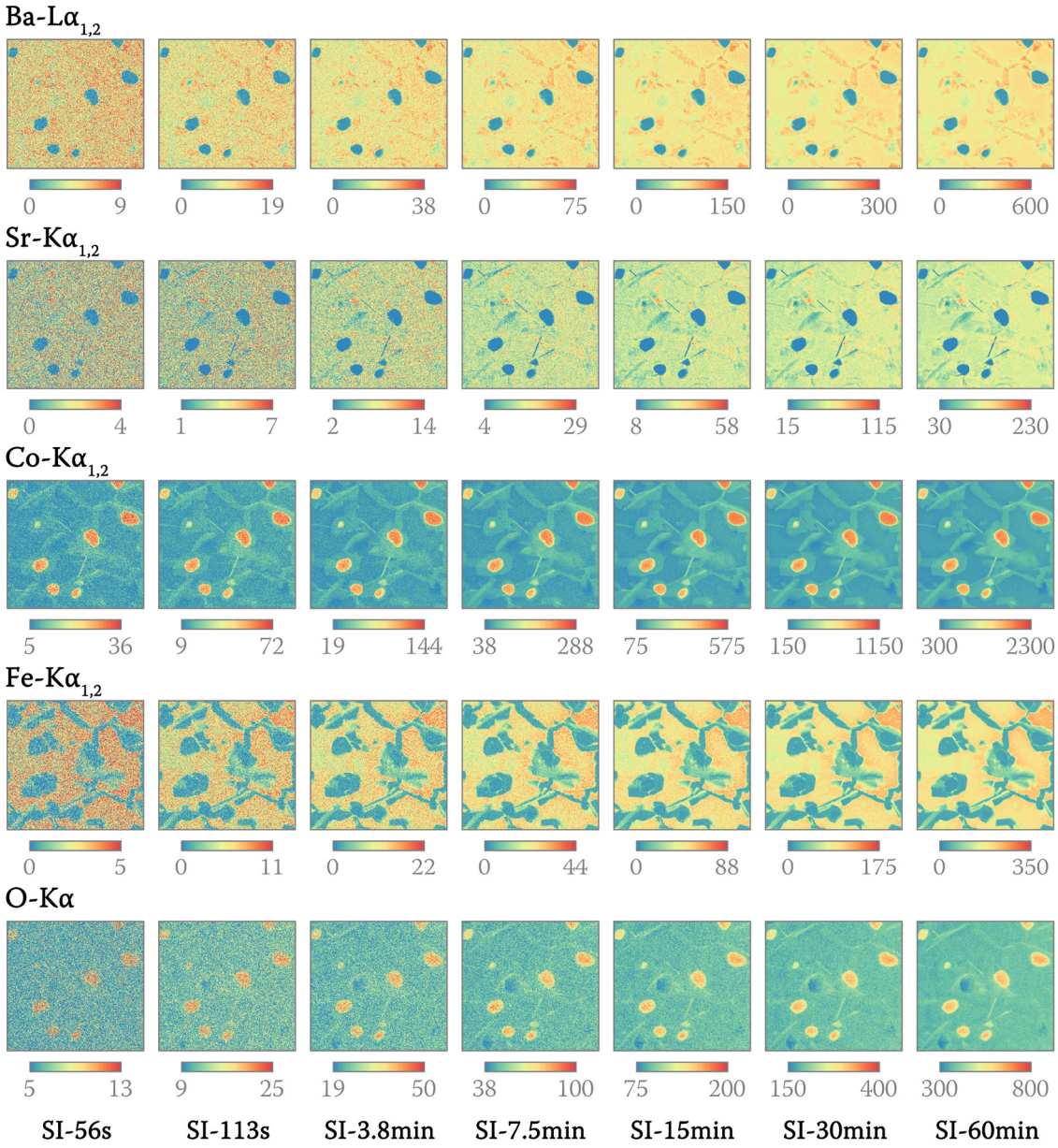

Figure 11. Mappings of the integrated intensity of selected EDXS emission lines and effective measurement times. The color scale denotes the number of X-ray counts of the corresponding emission line.

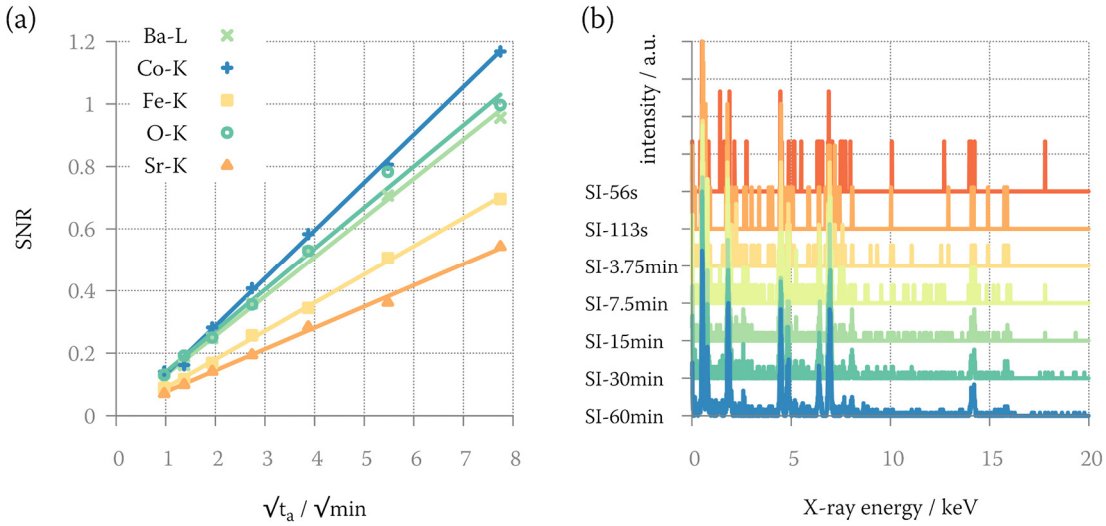

Figure 12. (a) SNR derived from mappings of the integrated X-ray counts of Ba-L$\alpha_{1,2}$, Co-K$\alpha_{1,2}$, Fe-K$\alpha_{1,2}$, O-Kα and Sr-K$\alpha_{1,2}$ emission lines. (b) Unfiltered representative spectrum from SIs with different effective measurement times t_a. All spectra are taken from the same position (later referred to as position A).

To quantify the SNR for the individual SIs, a homogeneous region within the elemental maps was selected. Here, the mean intensity μ and the standard deviation σ was calculated. The SNR ratio is then defined by the ratio of μ and σ according to Equation 18.

$$SNR = \frac{\mu}{\sigma} \tag{18}$$

It can be assumed that the SNR is mainly dictated by counting statistics, often referred to as shot noise. The noise level is hereby $\sqrt{N}$ with N being the number of X-ray counts. As the number of counts scales linearly with the effective acquisition time t_a, the relation between SNR and square root of t_a should be linear. In Figure 12(a) the measured SNR for the selected emission lines is plotted over the square root of t_a. The graph shows, that the relation between t_a and the SNR is satisfied for all emission lines. To get an idea about the noise level within each individual spectrum of the SI, a spectrum from the same sample region in different binned SIs is displayed in Figure 12(b). The spectra were scaled and vertically shifted for better visibility. The average X-ray counts within each spectrum varies from ~57 counts (SI-56s) to ~2658 counts (SI-60min).

The first 21 PCs were calculated for each binned SI with both algorithms, PCA and wPCA. The eigenvalues for each data set are depicted in Figure 13(a,b). Here one can

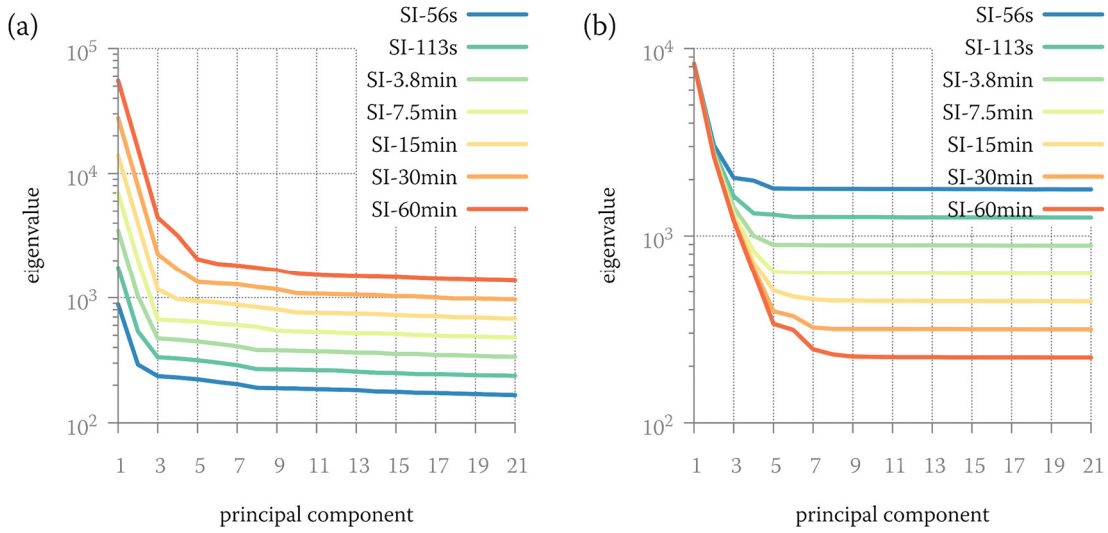

Figure 13. Eigenvalues in decreasing order after applying (a) PCA and (b) wPCA to the binned SI data sets.

see, that the eigenvalues from the PCA algorithm decrease up to the last PC whereas for wPCA the eigenvalues level off after less than 10 PCs. This makes it very hard to determine the number of relevant PCs when using PCA, as there is still significant information contained in the higher PCs. This already indicates one of the major shortcomings of PCA. Within the eigenvalue plot for wPCA, the significant components are identified reliably. As seen from the graph, the number of PCs containing significant information increases with the increase of effective measurement time, which can be interpreted that more and more significant information is captured within the first few components.

Score plots of the data set SI-56s, SI-7.5min and SI-60min derived by wPCA filtering are plotted in Figure 14 with the corresponding eigenspectra for SI-60min. Each pixel of the score plot represents a factor describing the contribution of a specific eigenspectrum to the data set. The values for creating the score plots were taken from the score matrix. Since PCA imposes no other restrictions on the eigenspectra besides being orthogonal, negative values within the eigenspectra are possible. Hence, eigenspectra do not necessarily represent physically measurable spectra. It is obvious that there are three components which are recovered in all data sets. The number of non-noise PCs increases with the effective measurement time. SI-56s contains 4 relevant components, whereas the score plots of SI-7.5min suggests information up to the 6th or 7th PC. For SI-60min, there is even information in the 9th PC, as seen in the eigenspectrum and score

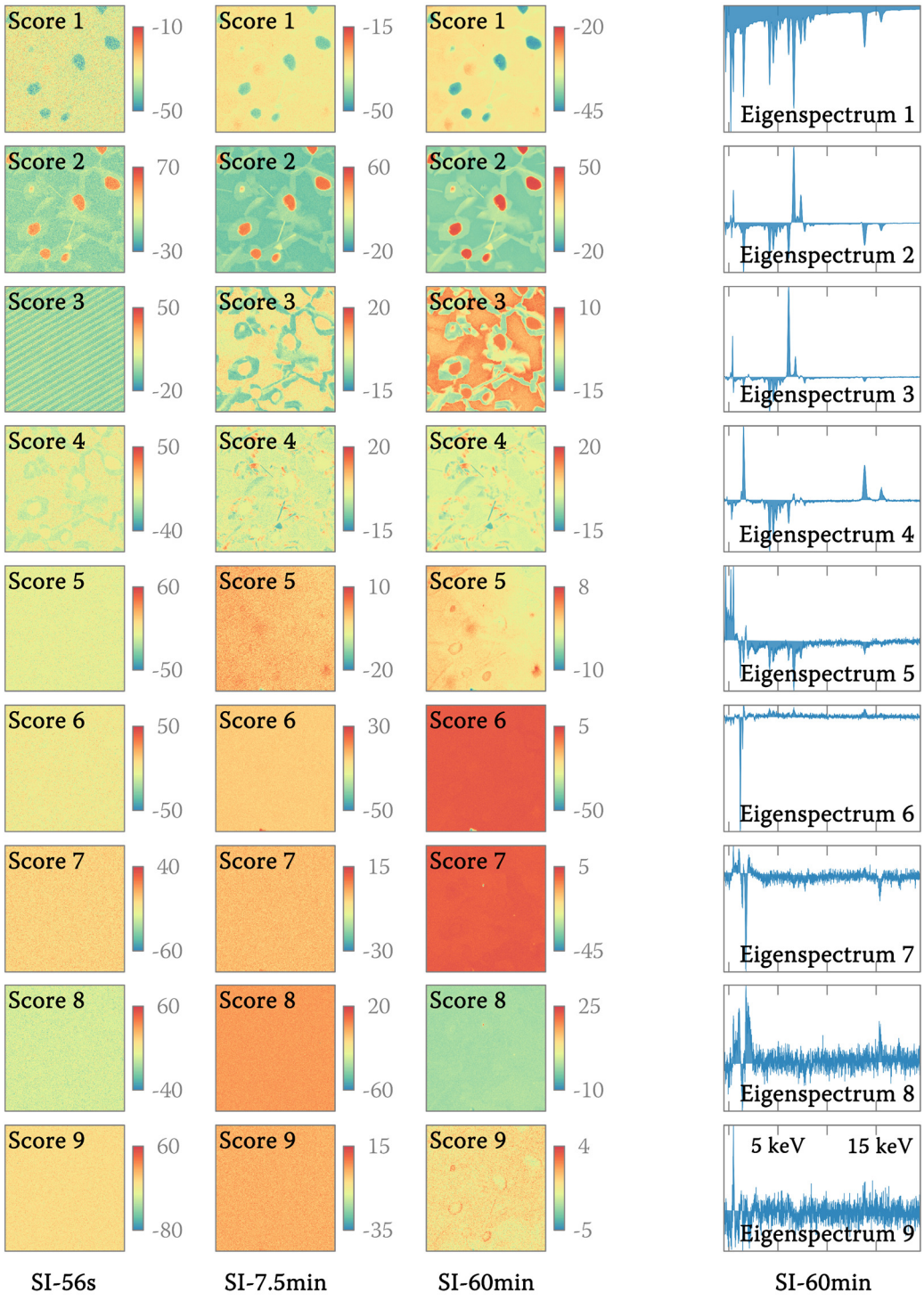

Figure 14. Score plots derived by wPCA filtering SI-56s, SI-7.5min and SI-60min data sets. The corresponding eigenspectra are added for the SI-60min data set. The color scale reflects the scaling factor for the corresponding eigenspectrum and is not directly connected to any physical property.

plot. As some PCs were not recovered within the high noise data, certain information cannot be reconstructed. Interestingly, a periodic scanning noise was identified in the third score of the SI-56s data set. This could be attributed to the noise peak within the

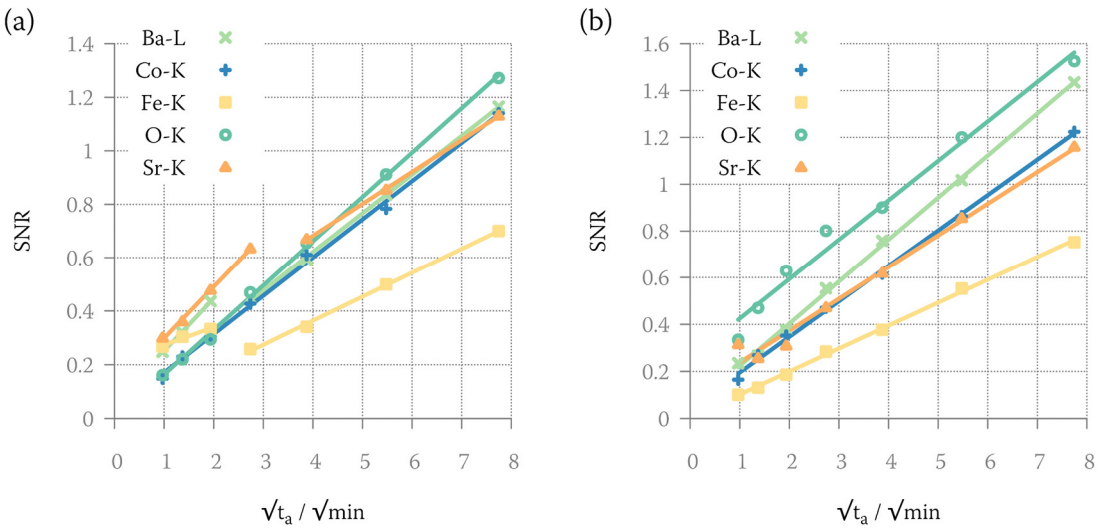

Figure 15. SNR derived from mappings of the integrated X-ray counts of Ba-L$\alpha_{1,2}$, Co-K$\alpha_{1,2}$, Fe-K$\alpha_{1,2}$, O-Kα and Sr-K$\alpha_{1,2}$ X-ray emission lines after (a) PCA and (b) wPCA filtering.

EDXS spectrum, which seems to change periodically during the spectrum acquisition. The noise peak can be avoided by clipping the spectra, which is done automatically depending on acquisition software. However, this does not lead to additional information being recovered.

For wPCA filtering, the number of PCs was chosen in a way that at least all the PCs were included before the eigenvalues level off. Higher score plots and corresponding eigenspectra were checked and included if there was still relevant information

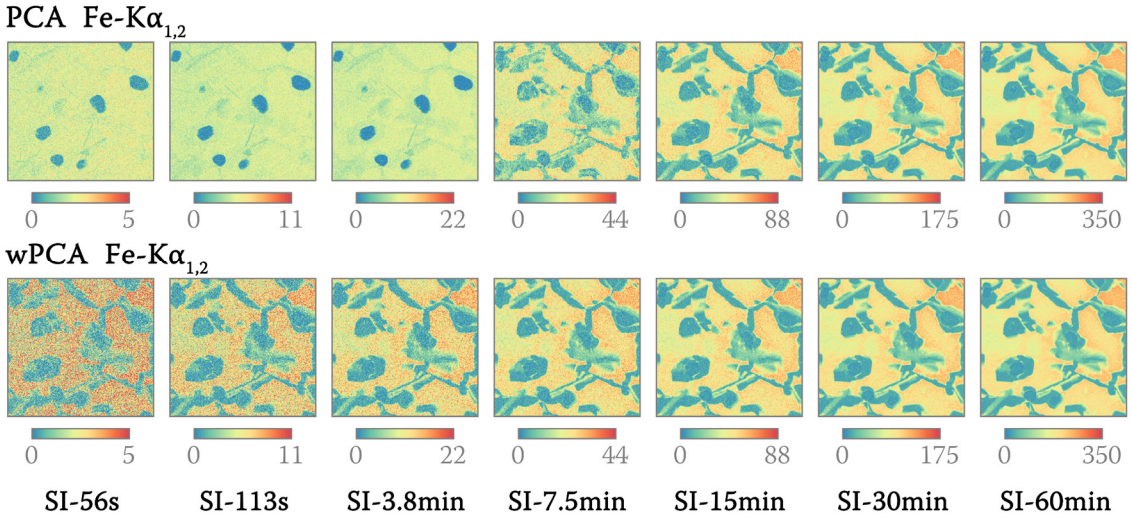

Figure 16. Mappings of the integrated intensity of Fe-K$\alpha_{1,2}$ and corresponding effective measurement times after PCA and wPCA filtering. The color scale denotes the number of X-ray counts of the corresponding emission line in the filtered spectra.

contained. A leading number of 10 PCs was assumed for PCA because it was difficult to identify any break within the eigenvalue plot computed by the PCA algorithm. All filtered images can be found in the appendix chapter 8.1. SNRs for the filtered data are presented in Figure 15(a,b). Linear regression was applied to fit the data in the graph. For PCA, there are some jumps within the SNR plots. To further visualize this, the linear fit was split into two appropriate regions, where necessary. The change in slope is especially obvious for Fe-K$\alpha_{1,2}$ (cf. Figure 15(a)). These two regimes are caused by the inability of PCA to extract the Fe variation within the leading PCs in the high noise SIs (SI-56s, SI-113s, SI-3.8min). This leads to severe artifacts within the reconstructed data, which would promote drawing false conclusions about the elemental distribution. This was also observed for simulated atomic resolved EELS data filtered by PCA [145]. There, the reconstruction of data with a high noise level led to the generation of additional defect-like features within the reconstructed image.

PCA and wPCA filtered Fe-K maps are presented in Figure 16. Here, the elemental distribution after PCA filtering of SI-56s, SI-113s and SI-3.8min does not reflect the actual elemental distribution seen in the unfiltered images (cf. Figure 11). Starting at SI-7.5min, the Fe distribution matches the one seen in the in the unfiltered images (cf. Figure 11). Further increase up to 40 PCs did not change the reconstructed image, which indicates that the information is scattered among many high indexed PCs. Therefore, applying PCA is pretty dangerous if noise levels are high. This problem is significantly reduced by switching to wPCA. The Fe-K$\alpha_{1,2}$ map closely resembles the elemental distribution seen in the original image.

Given the SNR values for wPCA filtered SIs in Figure 15(b), the SNR is improved for all X-ray emission lines by 5 to 150 %. The strongest improvement was observed for Sr-K$\alpha_{1,2}$, Ba-L$\alpha_{1,2}$ and O-Kα especially for the noisiest data sets (SI-56s, SI-113s). By comparing SNR values for wPCA filtered data and SNRs of unfiltered data, the increase

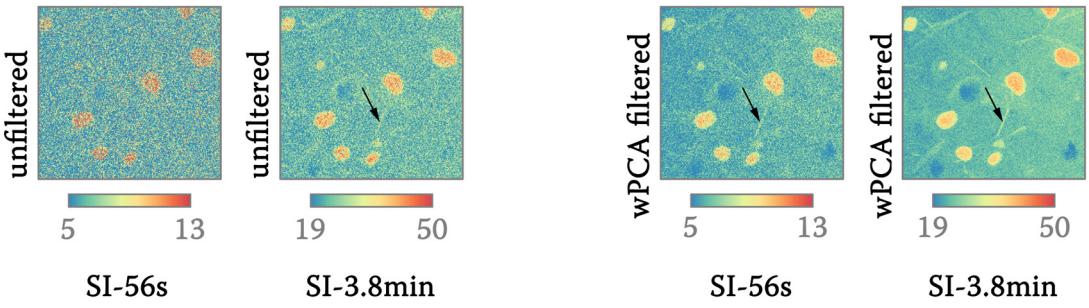

Figure 17. O-K map before and after wPCA filtering. The color scale denotes the number of X-ray counts of the O-Kα emission line.

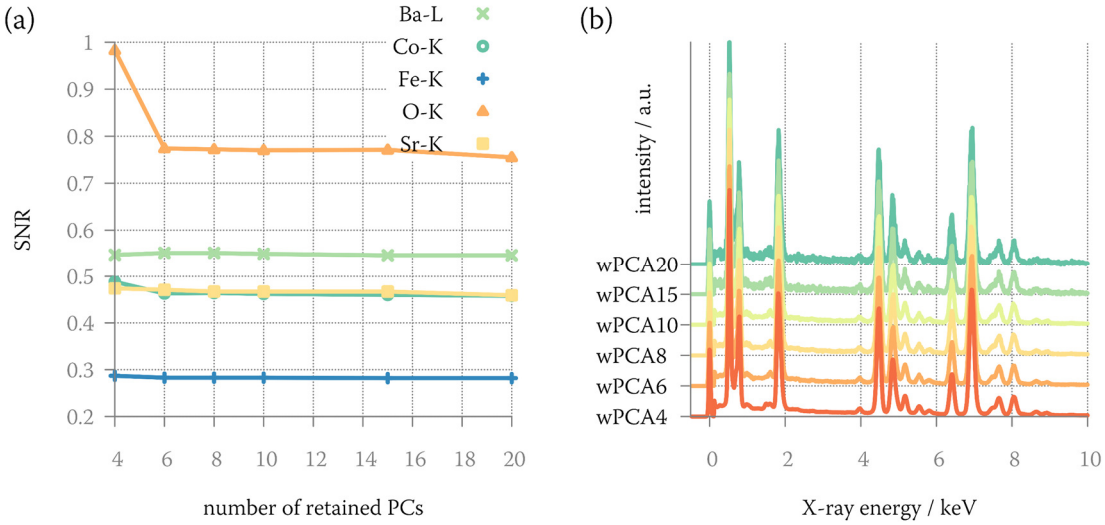

Figure 18. (a) SNRs and (b) one representative spectrum of wPCA filtered SI-7.5min data set for a different number of retained PCs. The spectra in (b) are shifted for improved visibility and are labeled by 'wPCA' followed by the number of retained PCs. All spectra are taken from the same position (later denoted as position A).

by filtering is equivalent to a factor of 1.4 - 4 in acquisition time. This is especially beneficial for samples susceptible towards contamination or beam damage as shorter measurement times can be realized.

The visual improvement is demonstrated for the O-K map which is depicted in Figure 17 before and after wPCA filtering. The high noise in SI-56s makes it hard to identify features within the sample. However, after wPCA filtering with the first 4 PCs, a lamellar feature (black arrow) is visible which first appear in unfiltered spectra with four times higher effective measurement time (SI-3.8min). Even though wPCA is superior to PCA, artifacts could not be suppressed completely. The wPCA filtered Ba-L$\alpha_{1,2}$ map of the SI-56s data set showed some features which disappeared when filtering data sets with higher effective measurement time (≥ SI-118s). This can be attributed to a 'missing' PC that could not be recovered in the high noise data set. In Figure 14 it can be seen that the 4th score in SI-7.5min and SI-60min does not appear in SI-56s. This creates some bias within the reconstructed image. Similar observations were made by PARISH ET AL. [146] when filtering EDXS maps (40 x 40 pixels) with high noise levels. PCA-filtered maps of simulated spectra with a mean of 500 counts per pixel lead to an incorrect chemical distribution. However, with 5000 counts per pixel, PCA provided an accurate description of the chemical distribution. For the data set here, the counts per pixel were ~57 for the SI with the lowest SNR (SI-56s). However, artifact-free images

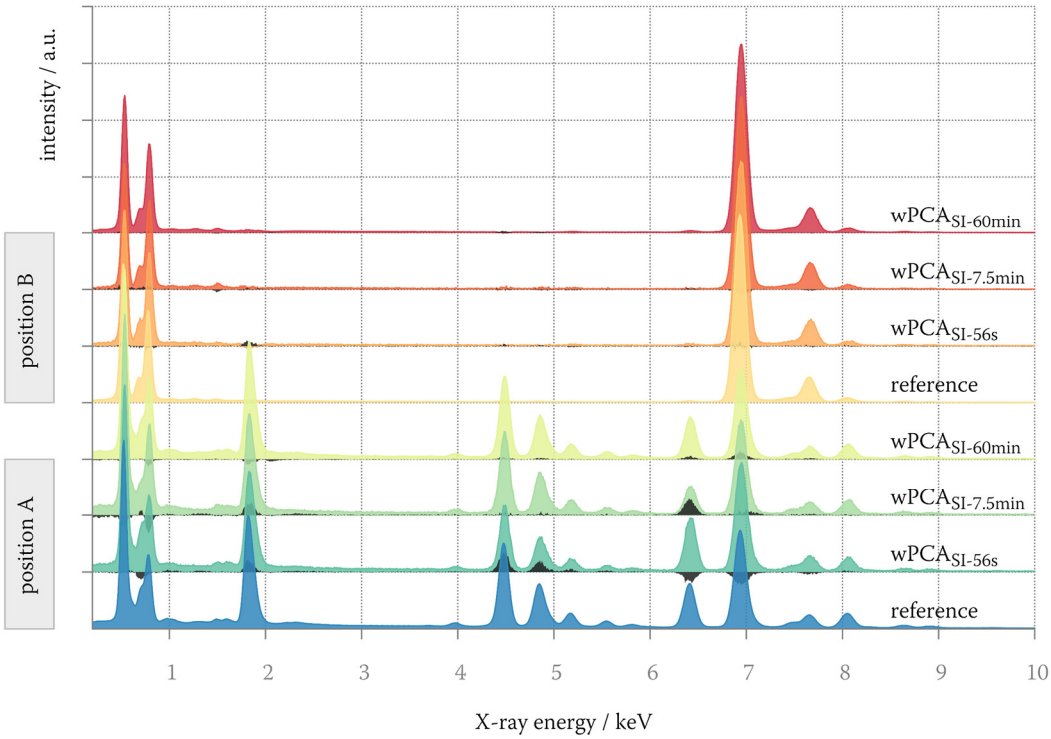

Figure 19. Reconstructed and reference spectra for two positions within the SIs. The difference between reconstructed spectrum and reference spectrum is superimposed on each spectrum (black).

could already be obtained starting from the SI-113s (wPCA) and SI-7.5min (PCA) having average counts per pixel of 114 and 384. This can be attributed to the higher number of pixel (256 x 256 pixels). A way to distinguish chemical features from filtering artifacts involves integrating a number of unfiltered spectra that form a certain feature in the filtered image (masking). If the integrated unfiltered spectrum resembles the suggested composition change, the feature can be considered as a 'true' feature. However, this procedure would take much of the simplicity of (w)PCA as suitable masking areas have to be chosen manually.

To check the impact of exceeding the 'optimal' number of PCs on the reconstructed data, SNRs and spectra were evaluated for a different number of PCs. Exemplarily, this is shown for the SI-7.5min data set in Figure 18(a,b). However, the results are similar for the other data sets. The number of retained PCs was varied between 4 and 20. The eigenvalue plot suggests a number of at least 4 components (cf. Figure 13(b)). However, the score plots suggest that there is still information within higher components (up to 6, cf. Figure 14). Therefore, the reconstruction with six leading PCs can be regarded as the 'optimal' PC number for this specific data set. In principle, by choosing a higher

number, noise from PCs not containing chemically useful signal is introduced. However, Figure 18(a) suggest, that the SNR only reduces slowly, if at all, even by exceeding the 'optimal' number of PCs significantly. Figure 18(b) shows spectra of the same sample region after wPCA filtering with a different number of PCs. Here, the difference is much more obvious in the form of noisier spectra which is noticeable if at least 10 PCs are taken into account. The higher noise level within the spectra makes it increasingly hard to distinguish small features. However, compared to the original data (cf. Figure 12(b)), the improvement is still significant.

In order to rate the accuracy of filtering regarding the individual spectra, some spectra of the maps were re-acquired with extremely long exposure time and, therefore, high SNR. The sample did not show any signs of beam damage which is why these reacquired spectra can be regarded as quasi 'noise-free' reference spectra. In Figure 19 wPCA filtered and reference spectra of two sample region (labeled position A, B) are given. The reference spectra were subtracted from the filtered spectra and superimposed on each spectrum (black). These superimposed black spectra are regarded as reconstruction error. For position B, only minor reconstruction errors were observed even for the SI with the lowest SNR (SI-56s). However, for position A, significant deviations in peak height were observed even for SI with higher SNR. The reconstruction error is quite pronounced for the Fe-K peak at 6.4 keV. This is critical for quantification as the ratio of emission lines is clearly altered. Therefore, if reliable quantification of (w)PCA data is intended, the average X-ray counts per pixel should be far higher than in the SI-60min data set with a mean value of 2658.

In summary, wPCA clearly surpasses PCA when dealing with EDXS SIs because artifacts within the elemental distribution maps can be mostly avoided. However, depending on the investigated sample, SI with extremely low counting statistic should be treated carefully. In the presented case, the limit where wPCA could still recover chemically meaningful distribution maps were around 50 to 100 counts per spectra. The SNR was found to increase slowly when slightly surpassing the number of 'optimal' PCs. However, the individual spectra suffer noticeably when including too many noisy PCs, making the identification of small spectral features impossible. In general, the SNR of composition maps can be significantly increased leading to a noticeable higher image quality. The individual spectra also benefit from filtering if the number of PCs is kept reasonably low, but still high enough to include all the chemically relevant PCs. However, these spectra should be handled with extreme care, as even SIs with moderate

SNR show significant deviations from the 'true' spectrum. This hampers precise quantification of filtered SIs.

3.2 Valence state determination of Fe and Co

Transition metals (TM) exhibit distinctive features in their density of states at the ionization threshold which are related to the electron distribution within d-orbitals. Due to spin-orbit coupling $2p$ core levels are split into a high fourfold degenerated $2p_{3/2}$ and a low twofold degenerate $2p_{1/2}$ state. The excitation of electrons from these energy levels to narrow unoccupied d-band states gives rise to two distinctive peaks in EELS spectra, labeled L_3 ($2p_{3/2} \rightarrow 3d$) and L_2 ($2p_{1/2} \rightarrow 3d$). Due to the sharpness of these peaks they are referred to as white-lines. Considering the degeneracy, one could expect a statistical branching ratio $I_{L_3}/[I_{L_3} + I_{L_2}]$ for the white-line intensities $I_{L_{2,3}}$ of $2/3$. However, most studies reported ratios not satisfying the statistical branching ratio, but instead a correlation to the unoccupied d-state density [147–149]. The white-line intensity ratio I_{L_3}/I_{L_2} was measured to increase from d^0 to d^5 configuration with a maximum value of 6 followed by a decrease to d^{10} [150,151].

The fine structure of ionization edges and, therefore, the nature of $3d$ TM white-lines is dictated by the density of states above the Fermi level. A simple model of the electronic structure in $3d$ TM can be motivated by considering the perturbation of degenerated energy states induced by the crystalline environment. The underlying theory called crystal field theory is suitable for explaining many properties in transition metals. Within this theory the interaction between ligands and orbital electrons is reduced to the electrostatic interaction only. The probability distribution function derived by the Schrödinger equation for the five d-orbitals is depicted in Figure 20(a) (90 % probability). Images were generated by the freeware tool ORBITAL VIEWER [152].

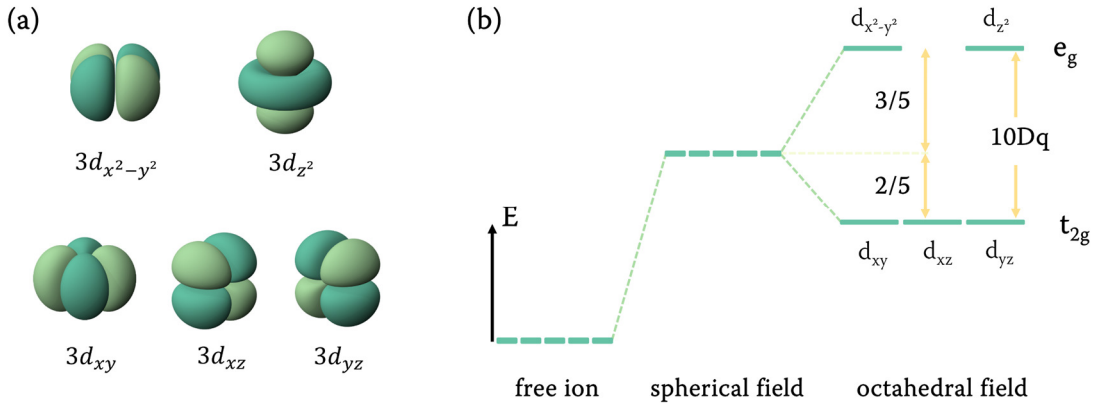

Figure 20. (a) 3d TM electron orbitals (90 % probability) [152]. (b) Ligand induced change of band structure in TMs.

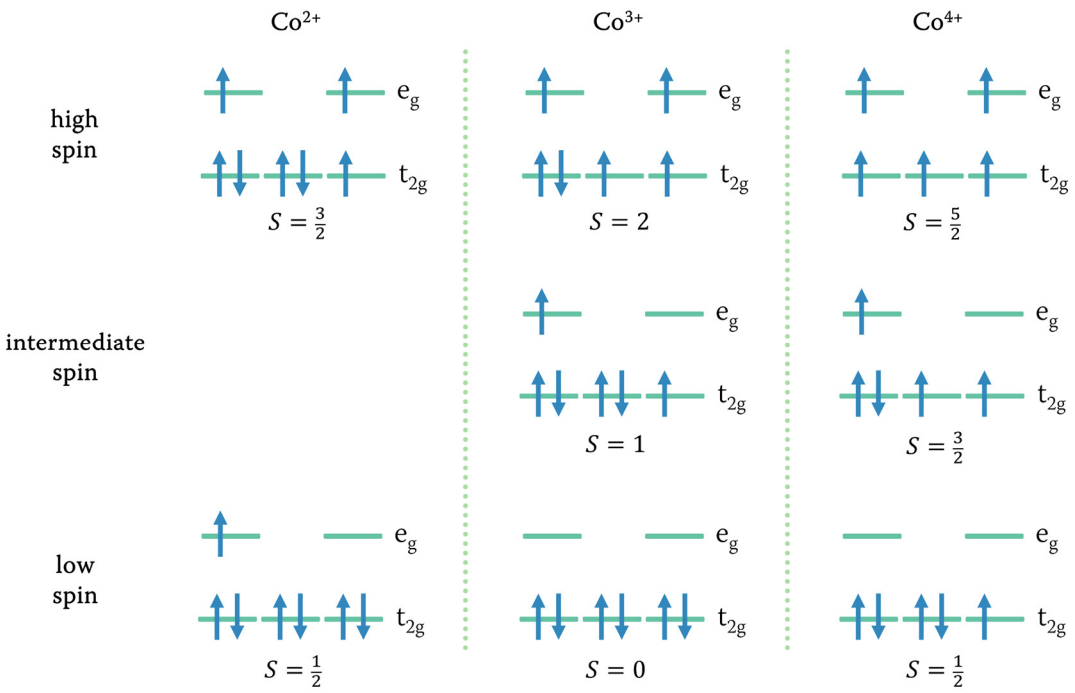

Figure 21. Possible spin state configuration of Co^{2+}, Co^{3+} and Co^{4+} ions.

Given a free TM ion with its charge condensed in one point, the d-orbital energy level is fivefold degenerated as depicted in Figure 20(b). By considering a negative ligand field with spherical symmetry the energy level of the ground states rises due to Coulomb repulsion. However, the fivefold degeneracy remains. The degeneracy can be (partially) lifted within an octahedral environment, where the central ion is surrounded by six equidistant anions, as for the B-site ions Fe and Co in the cubic BSCF phase. The set of d-orbitals split into two groups with different energy levels, depending on the orientation towards the octahedral ligand field. As the electrons within the orbitals $d_{x^2\text{-}y^2}$ and d_{z^2} are closer to the negative charge of the surrounding anions, the energy levels rise as a consequence to the repulsive force. The other orbitals d_{xy}, d_{yz} and d_{xz} do not point towards the surrounding anions, which reduces their energy compared to a homogeneous spherical charge distribution. The higher energy level is denoted e_g with a degeneracy of two, whereas the lower threefold degenerated level is called t_{2g}. The difference between t_{2g} and e_g is referred to as splitting parameter $10Dq$. Splitting does not affect the sum of all five energy levels. Therefore, the energy shift can be described by the splitting parameter with $-4Dq$ for t_{2g} and $6Dq$ for e_g (cf. Figure 20(b)).

The population of e_g and t_{2g} states in an octahedral coordinated TM is subject to variations, especially for Co and Fe. The electron configuration is strongly dependent

on the energy difference $10Dq$ and the exchange energy. If $10Dq$ is small compared to the energy required for pairing single electrons in t_{2g} orbitals, it is energetically favorable for one or more electrons to populate free states on the elevated e_g level, which leads to the generation of unpaired electrons. This changes the overall spin-state configurations, resulting in different magnetic properties. As the spin of paired electrons is canceled out, only the number of unpaired electrons contribute to the resulting spin S. Depending on the relative value of S the configurations are referred to as low spin (LS), intermediate spin (IS) or high spin (HS). It is worth noting that LS, HS and IS do not refer to an explicit S value. Spin state transitions can be induced by, e.g., temperature changes in a number of TM compounds including BSCF. Spin state transitions of Co ions have been reported in BSCF by many researchers with a transition from LS to IS at ~623 K and IS to HS at ~1173 K [67,69,153,154]. In contrast, spin transitions were not found for Fe in BSCF. Possible spin configurations for Co^{2+} (d^7), Co^{3+} (d^6) and Co^{4+} (d^5) are depicted in Figure 21.

There are many reports linking the white-line intensity ratio to the TM oxidation state [8,155–160]. PEARSON ET AL. presented a method to derive normalized white-line ratios which showed a linear dependency on d-state occupancy by background subtraction and edge integration [149]. This technique was successfully applied for various TMs including Co [156,157]. However, for BSCF the white-line intensity method is hampered as there is a considerable overlap between the Ba-$M_{4,5}$ and the Co-$L_{2,3}$ white-lines. An alternative approach involves the exploitation of the correlation between oxidation state and chemical shift. The energy on-set of core-loss TM edges shifts towards higher energies with increasing TM valence state [8]. This can be explained by the reduced screening field around the nucleus as the number of outer electrons decreases [8,161]. However, the chemical shift is not only dependent on the oxidation state but also the nature of final states above the Fermi level which is related to the bonding between TM and ligand atoms [161]. Furthermore, the onset determination is strongly dependent on the precise calibration and stability of the spectrometer. This often limits the measurement accuracy, especially if the expected chemical shift is small. Other methods to derive oxidation states rely on the approach of using fine structure features within the white-lines which are accessible by modern microscopes with high energy resolution (0.3 - 0.4 eV) [162]. It is assumed, that the white-line features can be described by a superposition of reference spectra, either simulated or experimental, with known parameters [163,164]. However, this cannot be applied for BSCF as all of the Co ions are in an intermediate valence state [67]. Not very

much attention was payed to the white-line distance which is also subject to change for different Co-oxidation states. An empiric motivated method to derive the valence state from the Co white-line distance will be presented in the following section.

3.2.1 Co white-line distance technique in BSCF

EELS spectra of standard materials with known Co-valence state were recorded as reference. As the ligands strongly influence spectral features, the focus was set on reference materials where Co ions are octahedrally coordinated by oxygen anions like CoO (Co^{2+}) and $LiCoO_2$ (Co^{3+}). Co_3O_4 was included as a mixed Co^{2+}/Co^{3+} compound, containing both oxidation states, with Co^{2+} being tetrahedral and Co^{3+} octahedral coordinated. Due to the lack of suitable high valence standards, $CoSi_2$ was taken as Co^{4+} reference. Here, Co is 4-fold coordinated by Si ions. Metallic cobalt was included for comparison. Deconvoluted spectra of CoO (99.999 % purity), Co_3O_4 (99 % purity), $LiCoO_2$ (99.5 % purity), $CoSi_2$ (99 % purity) powders and metallic Co are presented in Figure 22(a). Valence states were confirmed by the white-line method to rule out beam damage [165]. The edge onset positions are shifted to higher energy losses with increasing oxidation state of Co among the Co-oxide compounds. This is reasonable due to the reduced screening effect as described earlier. The white-line shape differs strongly for $CoSi_2$ showing more resemblance to a hydrogenic ionization edge. The $CoSi_2$ spectrum is close to that of metallic cobalt which can be attributed to the metallic

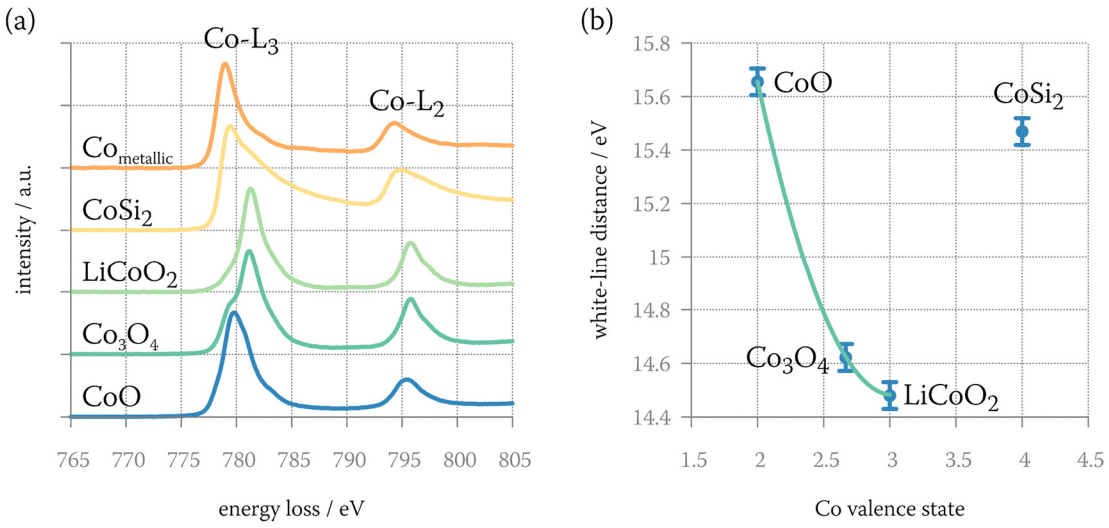

Figure 22. (a) EELS reference spectra of CoO (Co^{2+}), Co_3O_4 ($Co^{2.67+}$), $LiCoO_2$ (Co^{3+}), $CoSi_2$ (Co^{4+}) and metallic Co. An arbitrary intensity offset was introduced to improve visibility. (b) White-line distance as a function of Co-valence state with second-order polynomic fit function.

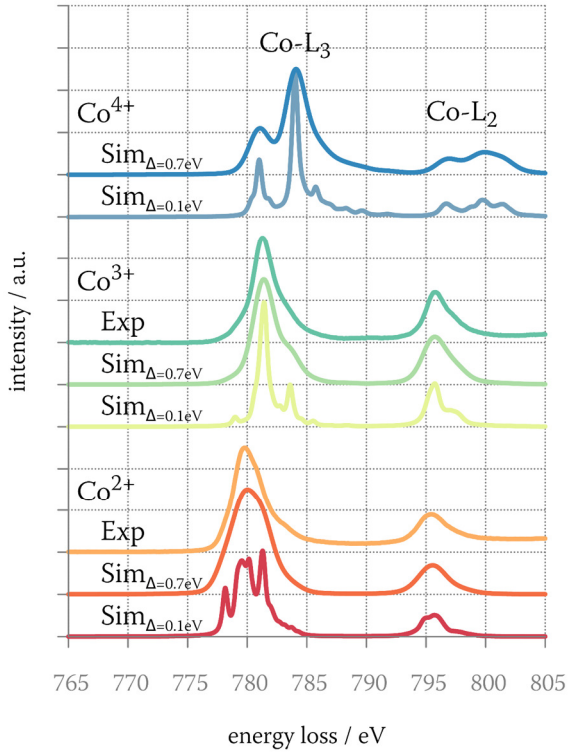

Figure 23. Simulated spectra of Co^{2+}, Co^{3+} and Co^{4+} with gauss broadening of either Δ = 0.1 eV or Δ = 0.7 eV. Experimental spectra of CoO (Co^{2+}) and $LiCoO_2$ (Co^{3+}) were added for comparison. An arbitrary intensity offset was introduced to improve visibility.

bonding character and different ligand configuration. The white-line distances of the reference materials, obtained by Gaussian fits (±0.4 eV around the peak), are given in Figure 22(b). It is obvious that there is a monotonic relation between the white-line distance and valence state in the range of 2+ to 3+ which is used as a base for this technique. There is an overlap in white-line distance for the range 2+ → 3+ and 3+ → 4+ which makes it very hard to distinguish between Co^{2+}/Co^{4+} compounds.

To further motivate the white-line distance technique, simulations for different Co-valence states with well-defined ligand parameters were conducted. The charge transfer multiplet model implemented in the software package CTM4XAS was used [166]. An octahedral symmetry was assumed throughout the simulation. The splitting parameter $10Dq$ should increase with increasing Co-valence state because it is assumed that the Co environment does not change considerably upon oxidation [167]. As reported by SUGANO ET AL. [168] the splitting parameter for trivalent cations is around ~2.5 eV and about half (~1.25 eV) for divalent cations. In ionic Co compounds the combination 2.4 eV (Co^{3+}) and 1.2 eV (Co^{2+}) was demonstrated to be a reliable combination and is, therefore, used within this work [169]. This is also close to the value

estimated from the splitting of the O-K edge in BSCF [69]. For Co^{4+} cations WARDA ET AL. [170] suggested a value of 3 eV, even though their measurement indicated a smaller value which was attributed to elongation and repulsion effects. Since an elongation effect is not expected for BSCF, a splitting parameter of 3 eV for Co^{4+} was used within this thesis. The simulated temperature was set to 300 K. Simulation parameters are summarized in Table 1. To compare simulated and experimental spectra, Lorentzian (Υ_{L3} = 0.2 eV) and Gaussian (Δ = 0.7 eV) broadening was applied to correct for lifetime broadening and energy resolution. Due to Coster-Kronig transitions, Lorentzian broadening was increased to Υ_{L2} = 0.4 eV for the Co-L_2 white-line [171]. An additional offset to the energy position of 0.65 eV (Co^{2+}) and 0.3 eV (Co^{3+}) was introduced to improve the match with the experimental data.

Simulated and measured spectra are depicted in Figure 23. Simulations show good agreement with CoO and $LiCoO_2$ spectra in terms of fine structure and white-line intensity. An experimental spectrum of Co^{4+} was not added to the graph as the ligand configuration is different in $CoSi_2$ compared to the simulation which hampers the comparison of fine structure. The simulated Co^{4+} spectrum deviates strongly from the $CoSi_2$ spectrum due to the different ligands and bounding characteristic. White-line distances obtained by the method presented earlier are included in Table 1. Here, experimental and simulated white-line distances are in reasonable good agreement. It has to be noted, that the white-line distance is strongly dependent on the splitting parameter. However, the error arising from the splitting parameter is considered to be small because the simulated white-line distances agree well with the experimental data

ion	10Dq	white-line distance	
		simulation	experiment
metallic	-	-	15.33 eV
Co^{2+}	1.2 eV	15.51 eV	15.66 eV
Co^{3+}	2.4 eV	14.35 eV	14.48 eV
Co^{4+}	3.0 eV	15.84 eV	15.47 eV

Table 1. Crystal splitting parameters used in the simulations. Simulated and experimental white-line distances for different oxidation states are listed for comparison.

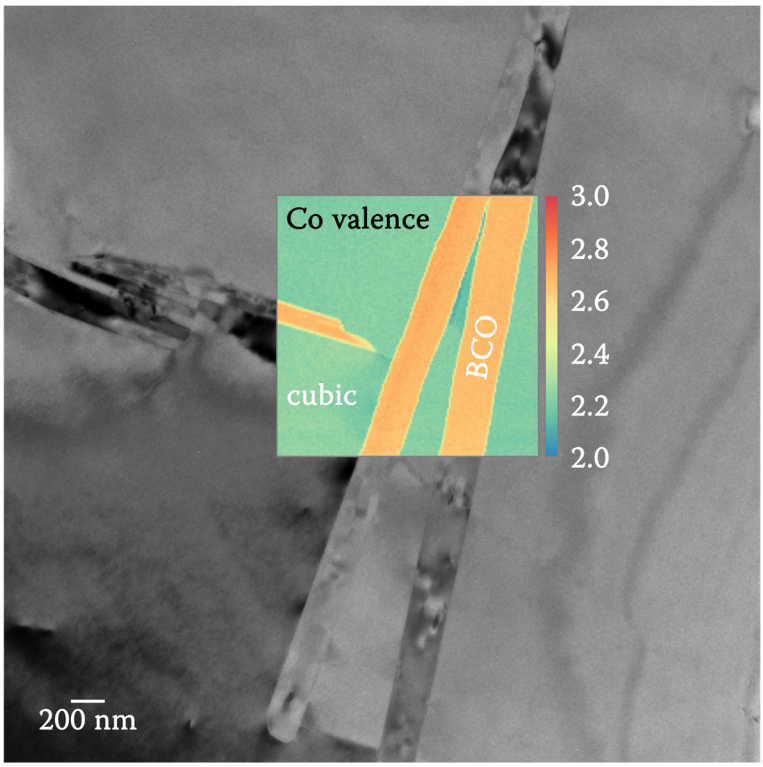

Figure 24. BF TEM image of $(Ba_{0.5}Sr_{0.5})(Co_{0.8}Fe_{0.2})_{0.99}Y_{0.01}O_{3-\delta}$ annealed in air at 880 °C for 10 days. The Co-valence state derived by the white-line distance technique is superimposed on the image.

from the reference materials. The reference materials were specifically chosen due to their ligand configuration which is similar to BSCF. To determine the valence states of unknown materials, a suitable interpolation routine has to be chosen. As Co_3O_4 with a valence state of 2.67+ is not on the direct line connecting Co^{2+} and Co^{3+}, a linear relationship is considered unlikely. A very good fit between Co-valence state η_{Co} and white-line distance τ_{Co} (in eV) is obtained by a second-order polynomial fit (cf. Figure 22(b)) given in Equation 19.

$$\tau_{Co} = 1.124\eta_{Co}^2 - 6.793\eta_{Co} + 24.746 \tag{19}$$

This fit also approximates the white-line distances one gets, if the non-integer valence spectrum is constructed as a superposition of Co^{2+} and Co^{3+} spectra. Therefore, this polynomial fit function was used within this thesis to derive Co-oxidation numbers. Interestingly, though only the data points between 2+ and 3+ were used, the function also describes Co^{4+} correctly (fit: 15.56 eV; measured: 15.47 eV). It should be noted that compounds containing Co^{4+} and Co^{2+} ions cannot be described reliably due to the ambiguity of the function. The systematic error for the Co-valence state is estimated to

±0.2 as the white-line distance is also influenced by ligand and spin configuration which was not further investigated here.

Using the white-line ratio technique, deconvolution is crucial as the white-line ratio increases with the specimen thickness [158]. On the contrary, the white-line distance is very robust towards changes in sample thickness and does not necessarily require single scattering spectra. Another advantage of the white-line distance technique is that superimposed edges in the region between the Co-$L_{2,3}$ white-lines do not require complex deconvolution routines which might induce additional errors. Due to that, this technique can be automated quite easily. To demonstrate the determination of Co-valence state using the white-lines distance technique, an EELS spectrum image of $(Ba_{0.5}Sr_{0.5})(Co_{0.8}Fe_{0.2})_{0.99}Y_{0.01}O_{3-\delta}$ (annealed in air at 880 °C for 10 days) was recorded and automatically evaluated. In order to improve the SNR due to the short measurement time, wPCA was performed as presented in Chapter 3.1. The resulting valence-state map of Co is depicted in Figure 24. The sample consists of a cubic perovskite phase with low Co-valence state and precipitates which were identified as $Ba_{n+1}Co_nO_{3n+3}(Co_8O_8)$ (BCO, $n \geq 2$) phase. The Co-valence map shows high homogeneity within the cubic matrix and the BCO intergrowth phase which was further confirmed by EDXS analysis. The Co-valence state in the cubic BSCF phase is 2.2+ and approximately 2.7+ in the BCO phase. The latter agrees well with the mean Co-valence state of 2.8+ reported by SUN ET AL. [80].

3.2.2 Calibration of Fe white-line ratio technique

As no complex overlap exists for the Fe-$L_{2,3}$ white-lines, the well-established white-line ratio technique can be applied to derive Fe oxidation states which was successfully applied in many studies [159,172,173]. The white-line ratio method strongly depends on microscopic conditions and parameters like edge background modeling or energy integration windows. Hence, reference spectra of well-known standards have to be obtained in order to correctly calibrate the relationship between white-line ratio and Fe valence state for the given microscope settings. Here, $FeTiO_3$ (Fe^{2+}), α-Fe_2O_3 (Fe^{3+}) and $SrFeO_3$ (Fe^{4+}) were picked as reference materials. Within the reference materials, the Fe cation is coordinated by six oxygen anions. Metallic Fe was included to rule out decomposition during the preparation routine. Spectra for $SrFeO_3$ and metallic Fe were taken from the publication by FELDHOFF ET AL. [98] accessed via the EELS DB website [174]. EELS spectra of $FeTiO_3$, α-Fe_2O_3, $SrFeO_3$ and metallic Fe are depicted in

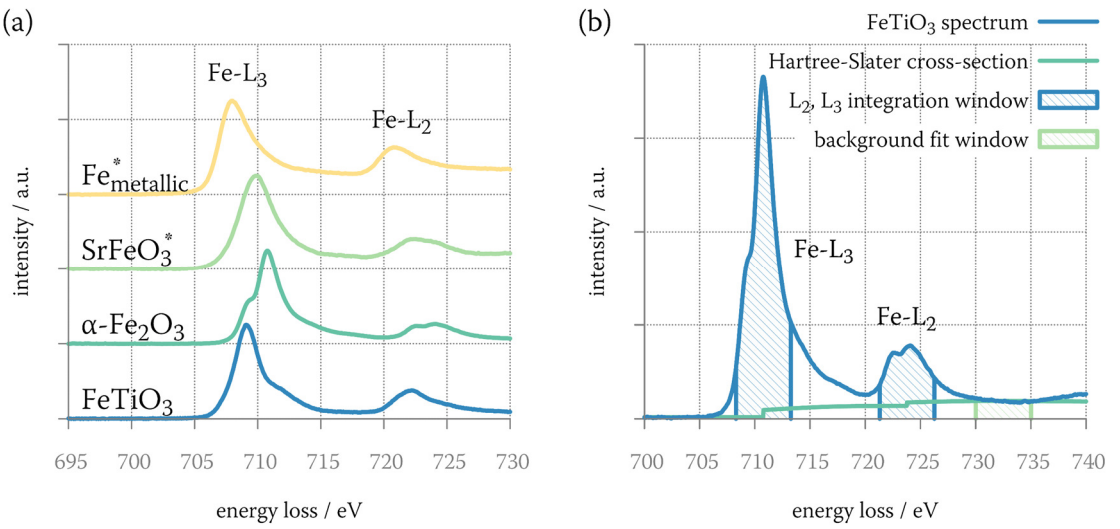

Figure 25. (a) Reference spectra of $FeTiO_3$ (Fe^{2+}), α-Fe_2O_3 (Fe^{3+}), $SrFeO_3$ (Fe^{4+}) and metallic Fe. Reference spectra with asterisk were taken from [98,174]. An arbitrary intensity offset was introduced to improve visibility. (b) Exemplary image showing how the white-line ratio was determined in an α-Fe_2O_3 EELS spectrum.

Figure 25(a). As no low-loss spectra were available for $SrFeO_3$ and metallic Fe, deconvolution was carried out for $FeTiO_3$ and α-Fe_2O_3 only. The edge onset does not increase monotonously which emphasizes that the shift in onset energy is not dictated by the valence state alone. The exponential decaying EELS background was removed by a power-law fit. The remaining background within the white-lines was modeled using the Hartree-Slater cross-section since one electron Hartree-Slater calculations were successful in describing experimental white-line ratios [149]. The Hartree-Slater cross-section was taken from the software package Gatan DigitalMicrograph. The onset of the cross-section was aligned with the peak of the Fe-L_3 edge. The cross-section was scaled by using a background fit window of 5 eV from 730 to 735 eV (cf. Figure 25(b)).

sample	ion	white-line ratio
metallic	-	2.91 ± 0.35
$FeTiO_3$	Fe^{2+}	3.39 ± 0.08
α-Fe_2O_3	Fe^{3+}	4.10 ± 0.08
$SrFeO_3$	Fe^{4+}	4.78 ± 0.35

Table 2. Fe $L_{2,3}$ white-line ratio for reference compounds with different Fe oxidation state.

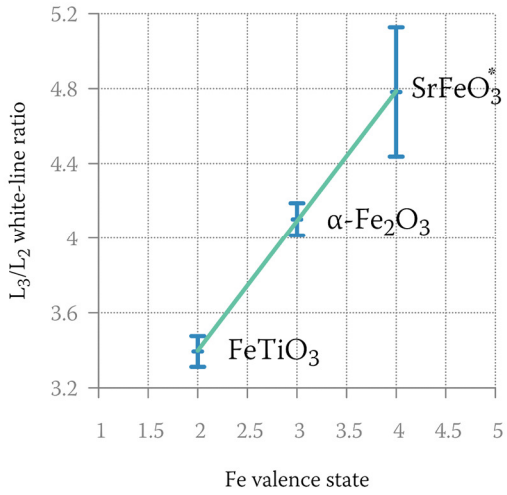

Figure 26. Fe L_3/L_2 white-line ratio as a function of valence state.

After subtracting the background, the intensity of the individual white-line was integrated with an integration window of 5 eV. Each window was centered on one of the two steps within the cross-section (cf. Figure 25(b)). The ratio of the integrated L_3/L_2 intensity is summarized in Table 2. As the white-line ratio technique is dependent on sample thickness, the error bar for metallic Fe and $SrFeO_3$ is significantly higher as the spectra were not deconvoluted to account for multiple scattering [158]. The measured white-line ratios suggest a linear relation between white-line ratio and Fe valence state (cf. Figure 26). A linear fit, obtained by regression analysis is used within this work to derived Fe valence states. The linear fit connecting the Fe white-line ratio χ with the Fe valence state η_{Fe} is summarized in Equation 20.

$$\chi = 0.694\eta_{Fe} + 2.010 \tag{20}$$

When applying this relation to determine the valence state, an accuracy of about ±0.3 is expected.

4 Cation site determination by ALCHEMI

Atom location by channeling enhanced microanalysis (ALCHEMI) is a powerful technique enabling the precise determination of dopant lattice sites within a host crystal. The theoretical foundation of dynamical electron diffraction will be established in the first two parts of this chapter. In the third part, experimental results are described from applying the revised ALCHEMI technique to determine the dopant lattice position in doped BSCF.

Sc and Y were chosen as B-site dopants in BSCF as they possess a fixed valence state and, therefore, a stable ionic radius. Hence, if incorporated into the B-site they are believed to compensate the reduced ionic radius of Co below the critical temperature of BSCF (840 °C). The dopant concentrations of the investigated samples are 3 at% for Sc-doped BSCF (BSCF3Sc) and 1, 3, 10 at% for Y-doped BSCF (BSCF1Y, BSCF3Y, BSCF10Y). All samples were prepared with intended B-site doping. Since the ionic radius of Y (90 pm) is considerable larger than other B-site elements (54.5 – 74.5 pm) this raised the question if Y is actually located on the intended lattice site. For example, in the related perovskites $SrCoO_{3-\delta}$ and $BaZrO_{3-\delta}$ there are reports demonstrating that Y can be located on both lattice sites [175–177]. Interestingly, mixed occupancy was reported to have beneficial effects on phase stability for $SrCoO_{3-\delta}$. Hence, to fully understand the impact of individual dopants on the phase stability of BSCF it is essential to precisely know where the dopants are located.

4.1 Theoretical background

For most analytical techniques where obtaining reliable quantitative results is of major interest, channeling conditions should be avoided. However, dynamical diffraction phenomena can be utilized to determine lattice positions of specific elements. The basic idea of this technique is to tune the X-ray emission on certain lattice sites by changing their illumination intensity due to channeling phenomena. First experiments with X-rays starting in 1969 turned out to be quite successful in locating impurities [178–180]. However, X-ray diffraction techniques require relatively large single crystals limiting the application spectrum considerably. The concept was adapted to TEM by Taftø and Spence [4] in 1982 under the acronym ALCHEMI. ALCHEMI relies on characteristic X-ray emission caused by electron exposure at dynamical diffraction orientations. ALCHEMI in TEM not only provides an improved spatial resolution of

several 100 Å, but also an increased sensitivity up to 0.1 at% for a wide range of impurity elements [181].

In order to understand the underlying principle of this method, it is helpful to discuss dynamical diffraction theory which describes the propagation of electrons within a crystal. In a crystal structure the high symmetry is reflected by a periodic potential $V(\vec{r})$ which can be decomposed into a Fourier series by reciprocal lattice vectors $\vec{g}$ and the Fourier coefficients $V_{\vec{g}}$ (cf. Equation 21). For the sake of convenience $V_{\vec{g}}$ was substituted by $2\pi^2\hbar^2 U_{\vec{g}}/me$ in the following equations.

$$V(\vec{r}) = \sum_{\vec{g}} V_{\vec{g}} \exp(2\pi i \vec{g}\vec{r}) = -\frac{2\pi^2\hbar^2}{me} \sum_{\vec{g}} U_{\vec{g}} \exp(2\pi i \vec{g}\vec{r}) \qquad (21)$$

To find the electron wave function ψ, the Schrödinger Equation has to be solved for the periodic potential $V(\vec{r})$. Since the electrons in an electron microscope behave like relativistic particles corrections in the non-relativistic equation are needed. As the spin is not important in this specific case relativistic corrections for the mass and wavelength are sufficient [182]. The stationary Schrödinger Equation is given by Equation 22 with $\psi(\vec{r})$ being the electron wave function, e the elementary charge, eE the kinetic electron energy, m the relativistic mass and ħ the reduced Planck constant.

$$\left(-\frac{\hbar^2}{2m}\nabla^2 + eE + eV(\vec{r})\right)\psi(\vec{r}) = 0 \qquad (22)$$

The most general solution for a periodic potential are so-called Bloch waves $b^{(j)}(\vec{k},\vec{r})$ as shown in Equation 23.

$$b^{(j)}(\vec{k},\vec{r}) = \sum_{\vec{g}} C_{\vec{g}}^{(j)} \exp\left(2\pi i\left(\vec{g} + \vec{k}^{(j)}\right)\vec{r}\right) \qquad (23)$$

Hereby, $\vec{g}$ denotes a reciprocal lattice vector and $C_g^{(j)}$, the Bloch wave coefficients and $\vec{k}^{(j)}$ the wave vector of the Bloch wave j. By the superposition principle, the total electron wave function $\psi(\vec{r}) = \sum_j \alpha_j b^{(j)}(\vec{r})$ is therefore characterized by a linear combination of Bloch waves with the excitation amplitude α_j. The excitation amplitude in the case of normal electron incident direction is given by the boundary condition. Before the electron beam enters the sample all electrons are solely in the undiffracted beam. The boundary condition is satisfied for $\alpha_j = C_0^{(j)*}$. By introducing $K^2 = me(E + V_0)(2\hbar^2\pi^2)^{-1}$ and inserting Equation 21 into the Schrödinger

Equation 22 the dispersion relation is obtained (Equation 24) which is considered one of the most fundamental set of equations from dynamical diffraction theory.

$$\left[K^2 - \left(\vec{k}^{(j)} + \vec{g}\right)^2\right] C_g^{(j)} + \sum_{\vec{h} \neq \vec{g}} U_{\vec{g}-\vec{h}} C_{\vec{h}}^{(j)} = 0 \qquad (24)$$

Here K can be regarded as the electron wave vector inside the crystal and $\vec{k}^{(j)} + \vec{g}$ as wave vectors of the individual Bloch waves. Each equation can be attributed to one Bloch wave which is characterized by a specific wave vector $\vec{k}^{(j)}$. Depending on experimental setup the number of reciprocal lattice vectors can be small (e.g. two beam case) which can simplify the determination of $\vec{k}^{(j)}$ and $C_g^{(j)}$ significantly.

With the approximation $K \gg g$ and introducing $\gamma^{(j)} = k_z^{(j)} - K$ with $k_z^{(j)}$ being the z-component of $k^{(j)}$ the bracket in Equation 24 can be written as $2K\left(s_g - \gamma^{(j)}\right)$ where s_g denotes the excitation error corresponding to the scattering vector g. Equation 24 can now be written in matrix form as given in Equation 25 with the matrix elements given by $A_{11} = 0$, $A_{gg} = s_g$ and $A_{hg}^* = A_{gh} = U_{g-h}/2K$.

$$\begin{pmatrix} A_{11} & \cdots & A_{1n} \\ \vdots & \ddots & \vdots \\ A_{1n} & \cdots & A_{nn} \end{pmatrix} \begin{pmatrix} C_1^{(j)} \\ \vdots \\ C_n^{(j)} \end{pmatrix} = \gamma^{(j)} \begin{pmatrix} C_1^{(j)} \\ \vdots \\ C_n^{(j)} \end{pmatrix} \qquad (25)$$

This Eigenvalue equation for different Eigenvalues $\gamma^{(j)}$ can now be solved to get the relation between the Fourier coefficients $C_i^{(j)}$.

We now discuss one of the simplest approximations where only two reflections, the zero-order beam and one Bragg reflection, are excited. Equation 25 now reduces to a homogeneous system of equations as written in Equation 26.

$$\begin{pmatrix} -\gamma^{(j)} & \frac{U_g}{2K} \\ \frac{U_g}{2K} & \gamma^{(j)} + s_g \end{pmatrix} \begin{pmatrix} C_0^{(j)} \\ C_g^{(j)} \end{pmatrix} = 0, \qquad (j = 1,2) \qquad (26)$$

This approximation is often referred as two-beam theory. It is noted that two-beam conditions are never exactly fulfilled for high-energy electrons due to the small curvature of the Ewald sphere which typically leads to intersection of several reciprocal lattice rods.

A system of linear equations only has a non-zero solution if its determinant is zero resulting in the following quadratic Equation 27.

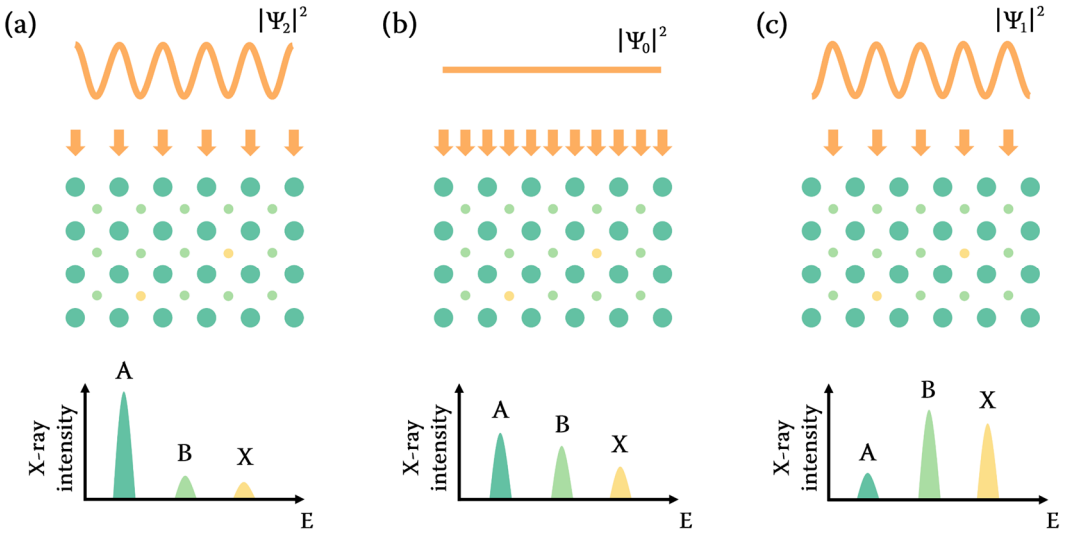

Figure 27. Schematic principle of ALCHEMI technique. Electron wave propagation in a crystal with corresponding EDXS spectra for (a) $s_g < 0$, (b) $s_g = 0$ and (c) $s_g > 0$.

$$\begin{vmatrix} -\gamma^{(j)} & \frac{U_g}{2K} \\ \frac{U_g}{2K} & \gamma^{(j)} + s \end{vmatrix} = \left(\gamma^{(j)}\right)^2 - s_g\gamma^{(j)} - \frac{U_g^2}{4K} = 0 \tag{27}$$

Eigenvalues and eigenvectors can be derived by solving this quadratic equation. This allows getting the relation between both Fourier coefficients. By introducing the substitution $\beta = \operatorname{arccot}(s_g\xi_g)$ with $\xi_g = \frac{U_g}{K}$, as employed in most textbooks, the total wave function can be written in a simplified manner (cf. Equation 28)

$$\psi(\vec{r}) = \cos\frac{\beta}{2}b^{(1)}(\vec{r}) + \sin\frac{\beta}{2}b^{(2)}(\vec{r}) \tag{28}$$

with the two Bloch waves $b^{(1)}(\vec{r})$ and $b^{(2)}(\vec{r})$ (cf. Equation 29).

$$\begin{aligned} b^{(1)}(\vec{r}) &= \cos\frac{\beta}{2}e^{2\pi i\vec{k}^{(1)}\vec{r}} - \sin\frac{\beta}{2}e^{2\pi i(\vec{k}^{(1)}+\vec{g})\vec{r}} \\ b^{(2)}(\vec{r}) &= \sin\frac{\beta}{2}e^{2\pi i\vec{k}^{(2)}\vec{r}} + \cos\frac{\beta}{2}e^{2\pi i(\vec{k}^{(2)}+\vec{g})\vec{r}} \end{aligned} \tag{29}$$

Considering the exact Bragg case ($s_g = 0$) the excitation amplitude for both Bloch waves is $1/\sqrt{2}$. Here, the electron probability for each Bloch wave can be expressed by Equation 30.

$$\begin{aligned} |\Psi_1|^2 &= \left|b^{(1)}(\vec{r})\right|^2 = 2\cos^2(\pi\vec{g}\vec{r}) \\ |\Psi_2|^2 &= \left|b^{(2)}(\vec{r})\right|^2 = 2\sin^2(\pi\vec{g}\vec{r}) \end{aligned} \tag{30}$$

Given that the scattering vector $\vec{g}$ contains the periodicity of the lattice, $|\Psi_{1,2}|^2$ reflects this periodicity. By assuming a cubic lattice with lattice parameter a and two sites within the unit cell, e.g., heavy A-site and light B-site elements, the term within the sin/cos function can be written as $\vec{g}\vec{r} = \frac{1}{a}x$. Therefore, one propagating waves $|\Psi_1|^2$ has its maximum on A-sites whereas $|\Psi_2|^2$ resides at B-sites. By adjusting the excitation error, and therefore $\beta = \operatorname{arccot}(s_g \xi_g)$, the contribution of each wave to the total electron wave function $\psi(\vec{r})$ can be tuned (cf. Equation 28). A negative excitation error as depicted in Figure 27(a) leads to a higher electron dose on heavy A-site atoms (Ba and Sr in BSCF) whereas a positive excitation error constrains electrons to move along B-site columns (cf. Figure 27(c)). The phenomenon of electrons travelling along certain lattice planes is often referred to as channeling. For $s_g = 0$ both amplitude terms are identical, leading to an even electron density on both lattice positions. An even electron intensity for both sides can also be achieved by choosing a 'random' orientation where many Bragg reflexes are excited. In the following part this will be referred to as non-channeling case.

Assuming, that the inelastic interaction for X-ray generation is strongly localized at the atom positions, the electron density on each lattice site is correlated to the X-ray emission intensity of the elements located there. For impurity atoms at, e.g., the B-site positions, the characteristic emission line of the impurities would show the same changes in intensity compared to other B-site atoms while changing the excitation error. This is indicated in Figure 27(a-c) where the impurities are denoted by X. This allows to deduce the position of impurity atoms.

TAFTØ AND SPENCE [4,181] introduced an equation based on the characteristic X-ray intensity ratio changes of impurity atoms and reference elements for different excitation errors to determine lattice-site occupancies. Since this formula relies on ratios, unknown experimental parameters can be avoided. Therefore, it could be successfully applied to a number of materials over the years [4,183,184]. However, many studies pointed out that the assumption of a strong localization of characteristic X-ray emission is not justified for many materials especially for weakly bound electrons which can lead to quite large errors and even unphysical results [185–187]. Especially for electrons channeling along atomic columns (axial channeling), delocalization is highly pronounced compared to electrons channeling along lattice planes (planar channeling) [188–190]. Additionally, high electron energies further increase delocalization [186,190]. In order to minimize errors induced by delocalization phenomena various

correction factors were introduced [186,191,192]. However, the use of these factors was not straightforward and could not be applied to every compound. Recently, with increasing computing power, quantum mechanical simulation of the X-ray emission under certain channeling orientations has become popular. It is now possible to accurately model characteristic X-ray emission using first-principle calculations [193–197]. Since delocalization effects are already considered in the calculation no correction factors have to be obtained, providing a high applicability for many compounds.

4.2 Simulation of inelastic ionization cross-sections and their verification by experimental data for undoped BSCF

Electron channeling within BSCF can be simulated using the Bloch wave approach. Crystal structure data were taken from [198]. Initial simulations of the standing electron wave in BSCF was performed to find suitable orientations where A/B-site channeling is highly pronounced. In the simulation, a two-beam case with a {111}-type reflection was used. A 3° tilt from the [112] zone axis orientation with a systematic row case where only $n\vec{g}_{111}$ [n ∈ ℤ] reflections are excited was assumed. Microscope high tension (HT) was set to 200 kV. Equation 25 was solved for 15 reflections because many reflections are excited for large HT values. The projected atomic positions for the exact [112] orientation is displayed in Figure 28. The planes where channeling is highly pronounced according to two-beam theory are marked by dashed lines. The calculation was performed using the software package JEMS [199]. Simulations were performed for a number of scattering parameters with the scattering parameter k_x defined as zero for the symmetrical case. We like to emphasize that the scattering parameter corresponds to the tilt along the systematic row. It is denoted in units of the absolute scattering vector for {111}-planes g_{111}. Hence, $k_x = \pm 0.5$ represents a two-beam case with $s_g = 0$. Due to the tilt angle away from the zone axis, electrons will propagate along crystallographic planes rather than atomic columns. Hence, the electron dose was integrated along the $[\bar{1}10]$ direction (cf. Figure 28). The simulated intensity of the standing electron wave as a function of scattering parameter in BSCF at 100 nm thickness is depicted in Figure 29. The position of A- and B-site planes is indicated in the plot. The picture clearly displays high symmetry for positive and negative scattering parameters. Hence, only one branch $k_x \geq 0$ will be discussed. Pronounced channeling on the A-site is observed for scattering parameters close to $k_x \approx 0.0$. As suggested by two-beam theory, the electron intensity is similar on both lattice sites for $k_x = 0.5$ which corresponds to an excitation error of $s_g = 0$. The evolution of the intensity on

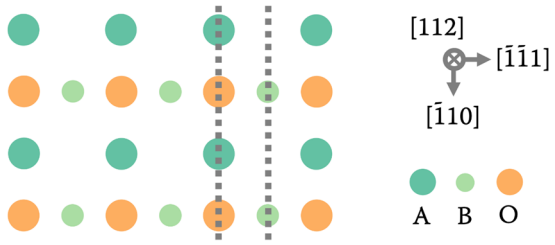

Figure 28. Projected atom positions in [112] zone-axis orientation.

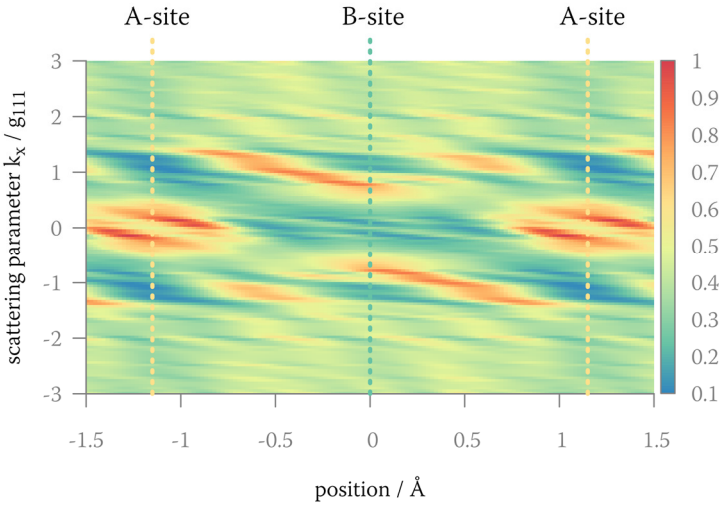

Figure 29. Simulation of the intensity of the standing electron wave within BSCF as a function of scattering parameter (100 nm specimen thickness). The intensity is denoted in relative units. A- and B-site element positions are marked in the picture by dotted vertical lines.

both lattice sites by changing the excitation error is comparable to what is expected from two-beam theory. A negative excitation error ($k_x = 0.5 - \delta$) will predominantly illuminate heavy A-site atoms whereas a positive excitation ($k_x = 0.5 + \delta$) leads to enhanced B-site illumination. Strong B-site illumination is given by a scattering parameter close to $k_x \approx 1$. In general, the difference in intensity between both lattice sites will decrease with increasing scatting vector. Almost no difference between A- and B-site atoms can be observed for $k_x > 1.25$. If the beam is far away from the symmetry point the electron wave converges to a non-channeling case. There, all lattice sites are illuminated evenly.

The electron dose on specific lattice sites can be associated with either the specific energy loss (EELS ALCHEMI) or the characteristic X-ray emission (EDXS ALCHEMI) of an element located at a certain lattice site. In both cases, the cross-section for inelastic scattering has to be known as a function of electron incident direction. To calculate the inelastic ionization cross-section σ, the Bloch wave model has to be extended by atomic scattering factors. A general expression for the inelastic cross-section based on Bloch wave theory has been derived by ALLEN & JOSEFSSON [200–202] and was used within this work by using the software package ICSC as described in their paper [197]. Mean square thermal displacement parameters $\langle u^2 \rangle$ were obtained from Rietveld fit parameters of BSCF synchrotron data published by TOMKIEWICZ ET AL. [56]. Since data for doped BSCF does not exist, parameters of Sc and Y were assumed to be equal to Fe

and Co. All parameters are listed in Table 3. To present a general idea on the localization of the inelastic electron-electron interaction in BSCF, the impact parameters for ionization b_{rms}, as published by OXLEY & ALLEN [203], are added in Table 3. It is obvious that channeling in BSCF is fairly localized especially at low HT. Only for O a high contribution due to delocalization effects can be expected. A convergence angle of 1.42 mrad was taken into account in the simulation which was also used during data acquisition at the microscope. Inelastic ionization cross-sections for Sr-K were simulated for different sample thicknesses and microscope HTs. The inelastic scattering cross-section as a function of scattering parameter for various sample thicknesses is depicted in Figure 30(a). The HT was set to 80 kV in the simulation. One can see that the scattering cross-section decreases with increasing sample thickness. For an infinite thick sample ($t \to \infty$) channeling disappears and the inelastic cross-section converges to the non-channeling result as pointed out by ALLEN & JOSEFSSON [201]. Only minor changes in features for different sample thicknesses are observed. Hence, sample thickness will mainly affect the channeling intensity.

To illustrate the interdependence of inelastic cross-section and HT, calculations were carried out for a constant sample thickness of 100 nm. In general, the inelastic cross-section per atom decreases with increasing HT values. The non-channeling inelastic

Element X-ray line	X-ray energy [keV]	b_{rms} [Å]			$\langle u^2 \rangle$ [Å²]
		80 keV	200 keV	300 keV	
O-Kα	0.52	0.552	0.726	0.803	0.0322
Sc-$K\alpha_{1,2}$	4.09; 4.08	0.081; 0.082	0.105; 0.105	0.115; 0.115	0.0240
Ba-$L\alpha_{1,2}$	4.47; 4.45	0.075; 0.075	0.096; 0.097	0.106; 0.106	0.0215
Fe-$K\alpha_1$	6.40	0.054	0.069	0.075	0.0240
Co-$K\beta_1$	7.65	0.052	0.058	0.064	0.0240
Sr-$K\alpha_1$	14.17	0.027	0.034	0.036	0.0215
Y-$K\alpha_1$	14.96	0.026	0.032	0.034	0.0240

Table 3. Impact parameters b_{rms} for X-ray emission events derived from the parametrized form published by OXLEY & ALLEN [203]. Mean square thermal displacement factors $\langle u^2 \rangle$ used in the calculation of the inelastic scattering cross-section were taken from [56]. Values for Sc and Y were assumed to be equal to Fe and Co.

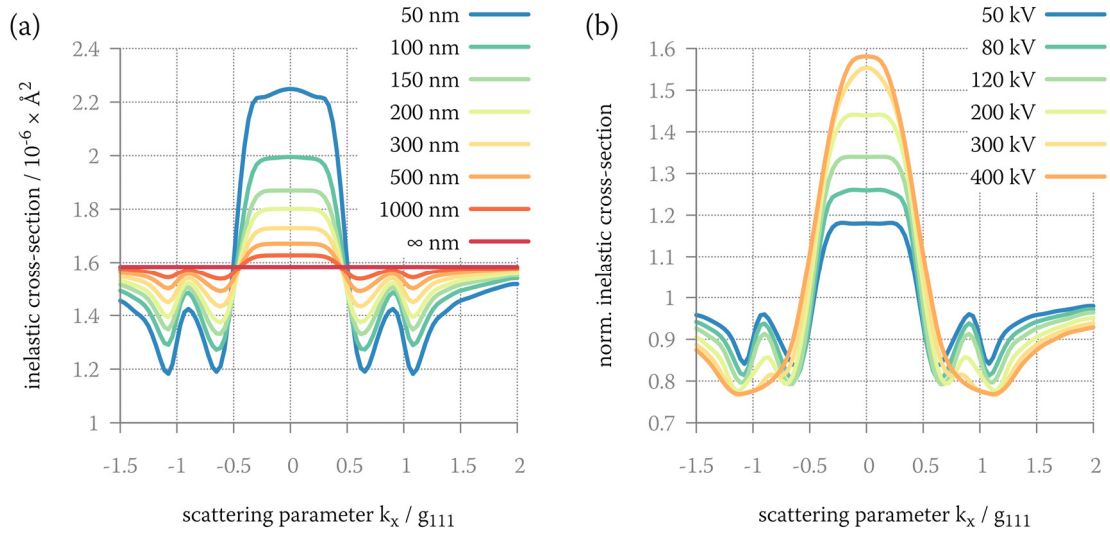

Figure 30. (a) Simulation of the inelastic cross-section per atom for Sr-K X-ray emission as a function of scattering parameter for various sample thicknesses at 80 kV. The upper limit case (t → ∞ nm) was added for comparison. The simulated HT was fixed at 80 kV. (b) Simulation of the normalized inelastic cross-section per atom for Sr-K X-ray emission as a function of scattering parameter for various HT values. The simulated sample thickness was 100 nm.

cross-section per atom drops in a good approximation linearly from 1.6×10^{-6} Å² at 50 kV to 1.0×10^{-6} Å² at 400 kV. However, the channeling intensity increases with higher HT. To visualize the channeling intensity, the inelastic cross-section $\sigma(k_x)$ for different scattering parameters was normalized with the non-channeling inelastic cross-section σ_{nc} (cf. Equation 31).

$$\sigma_n(k_x) = \frac{\sigma(k_x)}{\sigma_{nc}} \tag{31}$$

The normalized inelastic cross-section for several HT values is depicted in Figure 30(b). Here it is obvious that the change in cross-section is much more pronounced for elevated HTs. However, going to larger HT values distinctive features begin to soften and finally disappear which can be seen for the peak at $k_x \approx \pm 0.9$.

Experimental spectra for undoped BSCF were recorded with a convergence angle of 1.42 mrad to verify the simulated data. To reduce sample contamination a large area (100 – 200 nm) was illuminated. The exposure time for each spectrum was 100 – 500 s, depending on sample thickness. In order to accurately set the scattering parameter, the dark field coils were utilized. Here, a C++ program using the microscope's scripting interface was written to successively tilt the beam by a defined angle for each spectrum.

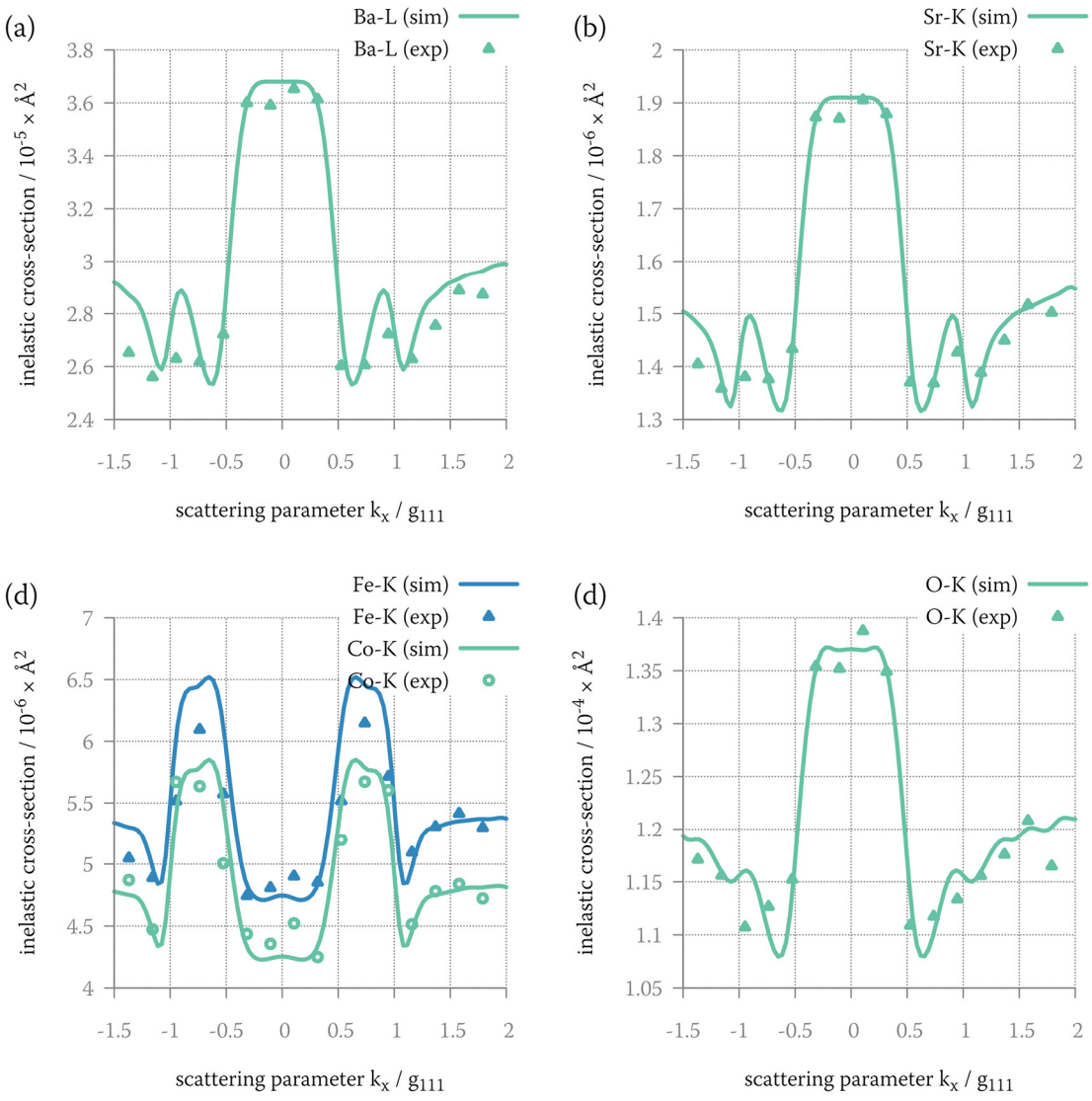

Figure 31. Simulated and experimental data for (a) Ba-L, (b) Sr-K, (c) Co-K, (d) Fe-K and (e) O-K X-ray emission. Experimental data were fitted by a scaling parameter. HT and sample thickness was the same for simulation and experiment.

Background subtraction was performed by a linear model. Peak intensities were obtained by integration over the elemental emission peak. Kα emission lines were used for Sr, Fe and Y and Sc. Due to the overlap between Co-Kα and Fe-Kβ, the Kβ emission line was used for Co. Since the energy for the Ba-K emission lines is fairly high (> 30 keV) the Lα lines were used instead. All the employed emission lines and their energies can be found in Table 3. As the sample thickness is a parameter within the simulation, local thicknesses were determined. This was done by either using convergent beam electron diffraction CBED [204] or EELS. Additional information about the thickness determination in BSCF using EELS can be found in Appendix 8.3.

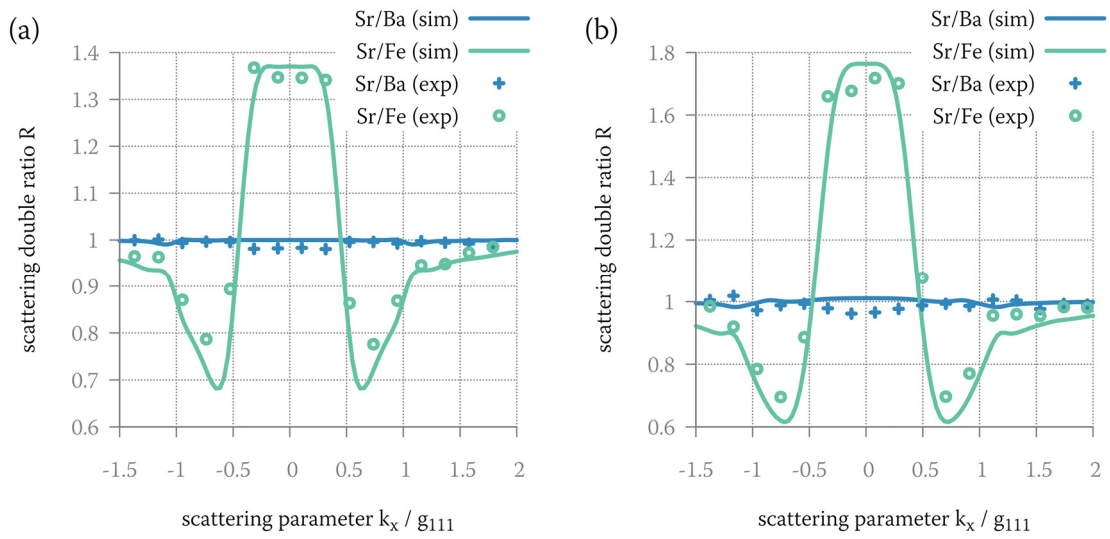

Figure 32. Simulated and experimental scattering double ratios as a function of scattering parameter for (a) 80 kV and (b) 200 kV.

Experimental spectra and simulated inelastic cross-sections for BSCF at 80 kV can be found in Figure 31. Peak intensities were fitted to simulated data by using a scaling parameter. The local sample thickness was measured to be (130 ± 10) nm. The same sample thickness was used for the simulation. There is a reasonable good agreement between experiment and simulation. Small discrepancies can be seen for Fe especially at $k_x \approx 0.75$. Due to the good counting statistics (20 k – 80 k counts per peak), the statistical error with less than 1 % is negligible. Reasons for the deviation in the intensity changes for the inelastic cross-section have to be found elsewhere and will be discussed in Chapter 4.3.

Since the concentration of dopants in BSCF is much smaller than the host elements, errors are much more pronounced there. It was observed that the robustness of this method could be increased significantly by not just considering the absolute intensity of one peak but the ratio between two elements within the same spectrum. Hereby, changes in the illumination, as well as absorption-related phenomena, can be removed. In order to relate the experimental ratios with the simulated cross-section ratios, spectra were normalized using the intensity ratio acquired under non-channeling conditions. This double ratio approach allows a direct correlation between simulated and experimental data without any fitting parameters. The inelastic cross-section σ_i of element i is connected to the measured integrated elemental peak intensity I_i. The double ratio between element A and B is defined in the following way.

$$R_{A/B} = \left[\frac{I_A}{I_B}\right]\left[\frac{I_A^{nc}}{I_B^{nc}}\right]^{-1} = \left[\frac{\sigma_A}{\sigma_B}\right]\left[\frac{\sigma_A^{nc}}{\sigma_B^{nc}}\right]^{-1} \quad (32)$$

Hereby, the I_i^{nc} and σ_i^{nc} denote the integrated peak intensity and the inelastic cross-section for element i in non-channeling case, respectively. Another advantage of the scattering double ratio method is that results are much easier to understand because the ratio should be one and independent of the scattering parameter for elements located on the same lattice site (in case of similar impact parameters).

Experimental results for BSCF acquired at 80 kV and 200 kV and corresponding simulations are depicted in Figure 32(a,b). For the sake of clarity, only a reduced set of double ratios is shown. It can be seen that the scattering double ratios agree well with the simulation. A pronounced change in the double ratio between Ba and Sr is not observed because both elements are located on the same lattice site. This also applies for Fe and Co (not shown in the graph). Remaining double ratios of different cationic pairs were close to the simulated curves. Therefore, it can be concluded that BSCF does not contain a high concentration of antisite defects, which is reasonable due to the large size mismatch between A- and B-site cations.

4.3 Dopant lattice site in BSCFY and BSCFSc

Is was shown in the previous subchapter that channeling can be precisely modeled. Its application for site determinations of dopant cations in BSCF will be described in the following. To visualize the impact of doping on electron channeling, simulations were performed for a number of A- and B-site occupancies in 10 at% Y-doped BSCF. In Figure 33 the scattering double ratios for (a) 100 %, (b) 80 %, (c) 60 % and (d) 40 % Y B/A-site fractions are plotted. Here the simulated sample thickness and HT was set to 150 nm and 300 kV, respectively. It is obvious that full B-site occupation of Y removes any dependence between the scattering double ratio Fe/Y and the scattering parameter. Scattering double ratio changes are identical for Sr/Fe and Sr/Y. For lower Y B-site

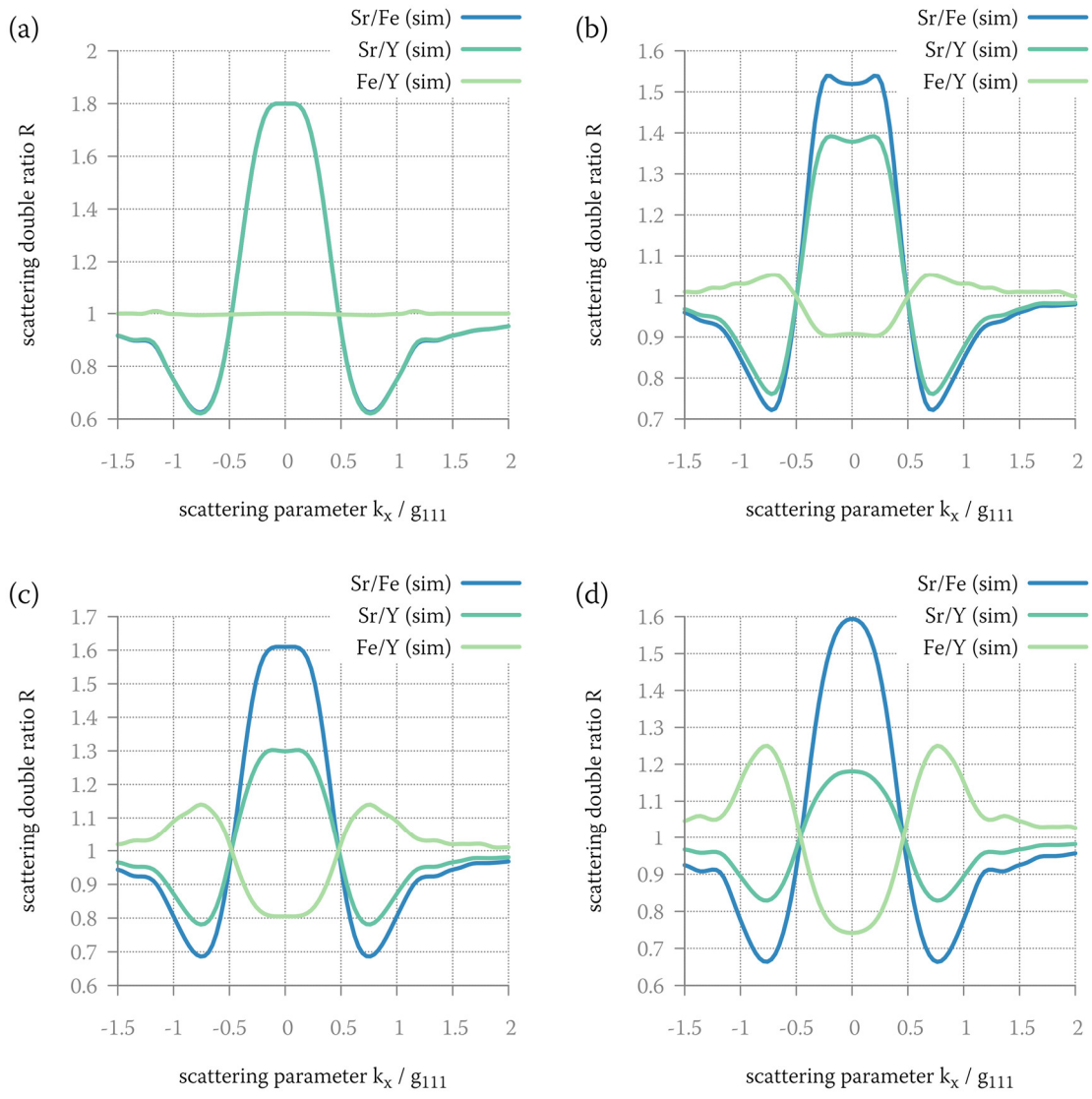

Figure 33. Simulated scattering double ratios as a function of scattering parameter for BSCF10Y with Y B/A-site ratios of (a) 100 %, (b) 80 %, (c) 60 % and (d) 40 %. The simulated thickness was 150 nm with the HT set to 300 kV.

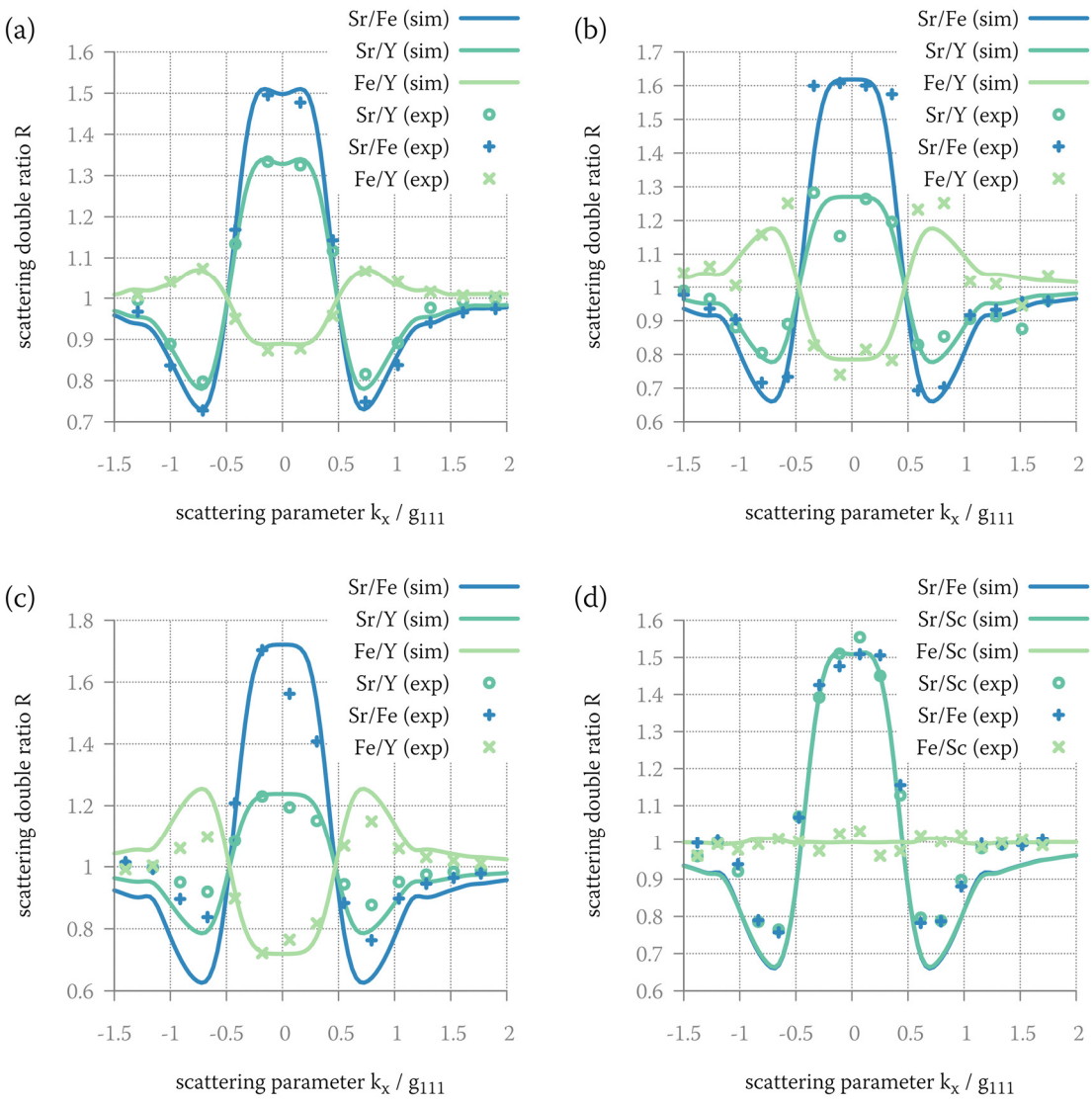

Figure 34. Simulated scattering double ratios and experimental data for (a) BSCF10Y, (b) BSCF3Y, (c) BSCF1Y and (d) BSCF3Sc.

occupancy and, therefore, higher Y A-site fraction, features emerge in the scattering double ratio of Fe and Y. The intensity increases with the increase of Y A-site occupancy. As the feature for Fe/Y increases, the intensity of the scattering double ratio Sr/Y decreases relative to Sr/Fe. The shape of the peak for Sr/Fe changes as a function of Y B-site occupancy with some double-peak features for 80 % Y B-site occupancy. The distance between Sr/Fe and Sr/Y can be seen as a good indicator for the Y B-site occupancy. However, one has to be careful because this relation is not linear. Hence, fitting between simulations and measurements is required to improve accuracy.

Samples were annealed at 1000 °C where the cubic phase is believed to be stable and afterward quenched in water to prevent secondary phase formation during cooling. For

sample	HT	thickness [nm]	Y- or Sc-occupancy on B-sites
BSCF10Y	300 keV	170 ± 10	75 %
BSCF3Y	200 keV	130 ± 10	55 %
BSCF1Y	200 keV	125 ± 10	45 %
BSCF3Sc	200 keV	190 ± 10	100 %

Table 4. Simulation parameters for best fit with experimental results and Y- or Sc-occupancy on B-sites.

a detailed analysis of high-temperature secondary phases, the reader is referred to Chapter 5.1 and 5.2. Since the Sc-K X-Ray emission line is superimposed by Ba-L_l, deconvolution is necessary. For this purpose, a reference spectrum of undoped BSCF was fitted using least regression routines. Deconvoluted peak heights for Sc-K were derived by subtracting the fitted reference spectrum. Experimental results including simulated scattering double ratios are depicted in Figure 34(a-d). Samples thicknesses were (a) (168 ± 10) nm (BSCF10Y), (b) (128 ± 10) nm (BSCF3Y), (c) (124 ± 10) nm (BSCF1Y) and (d) (189 ± 10) nm (BSCF3Sc). HT was 200 kV for BSCF3Y, BSCF1Y and BSCF3Sc and 300 kV for BSCF10Y in both experiment and simulation. Given the assumed thicknesses of 170 nm (BSCF10Y), 130 nm (BSCF3Y), 125 nm (BSCF1Y) and 190 nm (BSCF3Sc) the best match between experiment and simulation can be achieved for the dopant B-site occupancies given in Table 4. For all samples, reasonable fits were obtained. The relative A-site occupancy for Y decreases with increasing Y-doping concentration (BSCF1Y: 55 %, BSCF3Y: 45 %, BSCF10Y: 25 %). However, focusing on the total Y A-site concentration, the concentration increases with increasing Y-doping concentration from 0.55 at% (BSCF1Y) and 1.35 at% (BSCF3Y) to 2.5 at% (BSCF10Y). In contrast, no A-site occupation of Sc ions was measured for BSCF3Sc.

Minor discrepancies between simulations and experimental data can be observed for BSCF3Y, BSCF1Y and BSCF3Sc. Some might be induced by the low dopant concentrations (~0.2 % per elementary cell for BSCF1Y) and artifacts due to the deconvolution procedure in BSCF3Sc. However, the reason for the less pronounced channeling in the range $0.75 < |k_x| < 1$ (cf. Figure 34(c,d)) cannot be explained by that alone, since Fe and Sr are not affected by the low dopant concentration or deconvolution. This overestimation in the simulated data was also present in undoped

BSCF as seen in Figure 32. As already mentioned before, errors caused by low counting statistics can be neglected especially for elements with high concentrations and strong X-ray emission peaks like Ba, Sr, Co and Fe. In the simulation, the channeling intensity is strongly dependent on the given thermal displacement value. Hence, some contribution to the deviation between experiment and simulation can be attributed to the limited accuracy for the mean thermal displacement $\langle u^2 \rangle$ values. Additionally, prolonged illumination increases the sample temperature, causing the thermal displacement values to change considerable which was not considered here. While tilting the sample along the systematic row, excitations of non-systematic row reflections are unavoidable. Depending on the type of additional excited reflections, this might be one of the biggest error contributions. Furthermore, sample contamination has to be taken into account because long exposure times were used. Especially in thin sample regions considerable amorphization due to sample preparation was observed. Hence, it is reasonable to assume that thin amorphous surface layers are present even in thick sample regions which might affect the channeling intensity. Other microscope related parameters like sample drift might also contribute to observed discrepancies.

5 SECONDARY PHASE FORMATION IN DOPED BSCF

In the following chapter, the microstructure of different BSCF materials is presented and discussed. In the first part of the chapter the secondary phase formation in undoped BSCF is elucidated, with focus on the decomposition route in the intermediate temperature range (700 – 900 °C). The second part of the chapter deals with Sc-, Zr- and Y- doped BSCF. The effect of dopants is evaluated depending on secondary phase formation after extended heat treatments with focus on Y-doped BSCF. Oxygen permeation experiments will be correlated with the observation of secondary phase formation to characterize the impact of Y on the ionic transport properties. Part three focuses on the impact of certain material parameters like A/B-cation ratio and grain size variations to identify favorable fabrication parameters for doped and undoped BSCF. The final part of the chapter concentrates on coating BSCF and Y-doped BSCF with LSC to further promote surface exchange and protection against CO_2 poisoning. Interdiffusion between LSC layer and BSCF substrate after thermal annealing will be discussed to evaluate the material compatibility.

Sample fabrication

The investigated samples were provided by our cooperation partners, the Institute for Applied Materials - Materials for Electrical and Electronic Engineering (IAM-WET, Karlsruhe Institute of Technology) and the Faculty of Science & Technology - Inorganic Membranes Group (University of Twente). BSCF, Sc-doped BSCF (BSCFSc), Zr-doped BSCF (BSCFZr) and Y-doped BSCF (BSCFY) from IAM-WET was prepared by either using commercially available powder (Fraunhofer Institute for Ceramic Technologies and Systems, IKTS) or by in-house produced powder (IAM-WET, KIT). In-house IAM-WET powders were synthesized by the solid-state reaction route, where ingredients ($BaCO_3$, $SrCO_3$, Co_3O_4, Fe_2O_3, Y_2O_3, Sc_2O_3, ZrO_2 MERCK, Darmstadt, Germany) were ground together in the desired stoichiometric ratio. For B-site doping, the nominal stoichiometry is given as $(Ba_{0.5}Sr_{0.5})(Co_{0.8}Fe_{0.2})_{1-x}X_xO_{3-\delta}$ (X = Sc, Zr, Y; x = 0.01, 0.03, 0.1). The samples are denoted as 'BSCF', followed by the nominal dopant concentration (in at%) and the dopant element (e.g. BSCF3Sc). Beside doped BSCF, samples with different A/B-cation ratio were produced using the same fabrication procedure. The nominal stoichiometry for these samples is given by $(Ba_{0.5}Sr_{0.5})_x(Co_{0.8}Fe_{0.2})O_{3-\delta}$ (x = 0.95, 1.05), referred to as $(BS)_{0.95}CF$ and $(BS)_{1.05}CF$. The calcination temperature was in the range of 900 °C to 1130 °C (depending on composition) with a dwell time of 2 - 12 h. The calcinated material was ground using a

powder	producer	preparation route	D_{50} [µm]	annealing temperature
BSCF	IAM-WET	solid-state	1.9	640 – 1110 °C
BSCF1Y	IAM-WET	solid-state	2.1	640 – 1110 °C
BSCF3Y	IAM-WET	solid-state	2.0	640 – 1110 °C
BSCF10Y	IAM-WET	solid-state	2.0	640 – 1110 °C
BSCF3Sc	IKTS	solid-state	6.3	700 – 1000 °C
BSCF3Y	IKTS	solid-state	7.1	700 – 1000 °C
BSCF3Zr	IKTS	solid-state	5.8	700 – 1000 °C
BSCF	IKTS	solid-state	2.4	700 – 900 °C
BSCF1Zr	IAM-WET	solid-state	0.3	700 °C
BSCF3Zr	IAM-WET	solid-state	0.2	700 °C
BSCF1Y	IAM-WET	solid-state	0.2	700 °C
BSCF10Y	IAM-WET	solid-state	0.2	700 °C
$(BS)_{0.95}CF$	IAM-WET	solid-state	2.2	750 °C
$(BS)_{1.05}CF$	IAM-WET	solid-state	2.4	750 °C
BSCF	Twente	spray pyrolysis	n.a.	700 °C
BSCF3Zr	Twente	spray pyrolysis	n.a.	700 °C

Table 5. Sample nomenclature with associated fabrication parameters and resulting particle sizes.

zirconia ball mill to a D_{50}-value in the range of a few micrometers. X-ray diffraction (XRD) confirmed the phase purity of powders. Densification was achieved by either isostatic pressing at 250 MPa or uniaxial pressing at 10 kN/cm². Pressed samples were kept at 500 °C for 1 h (heating rate: 1 K/min) before sintering at high temperatures (> 1000 °C). Unless stated otherwise, sintering was performed at 1050 °C for 2 h (BSCF), 1100 °C for 12 h (BSCFSc, BSCFZr), 1100 °C for 2 h (BSCF1Y, BSCF3Y) or 1150 °C for 2 h (BSCF10Y) with heating and cooling rates of 5 K/min.

BSCF and BSCF3Zr powders from the University of Twente were fabricated using the spray pyrolysis technique. The resulting powders were ball milled and calcined at 850 °C for 5 h. XRD analysis of the final powders confirmed phase purity. Dry-milled and sieved (125 µm mesh) powders were pressed in a two-step process with 50 MPa uniaxial followed by 400 MPa isostatic pressing. Sintering temperatures were chosen in the range between 950 °C and 1150 °C depending on desired microstructure with a sintering time of 3 h (950 – 1050 °C) or 24 h (1150 °C). The preparation methods and the investigated annealing temperature range within the scope of this thesis are summarized in Table 5.

5.1 Secondary phase formation in BSCF

To shed some light on the decomposition route of BSCF, long-time annealing experiments in the temperature range between 640 and 1110 °C were performed. SEM analysis was conducted using the fast phase mapping technique by secondary electron (SE) SEM imaging as described in [76]. For this technique, samples were polished and etched with a colloidal SiO_2 suspension. Due to the different etching speed for different secondary phases, topography contrast is generated, which is easily observable by a SE detector in SEM. It has been demonstrated that distinctive SE contrasts can be attributed to the hexagonal phase (dark), the cubic phase (intermediate gray), a lamellar phase with plate-like morphology (bright, rectangular) and cobalt-oxide precipitates (bright, round). In general, the plate-like phase is composed of an arbitrary stacking sequence of cubic, hexagonal and $Ba_{n+1}Co_nO_{3n+3}(Co_8O_8)$ (BCO, n ≥ 2) planes.

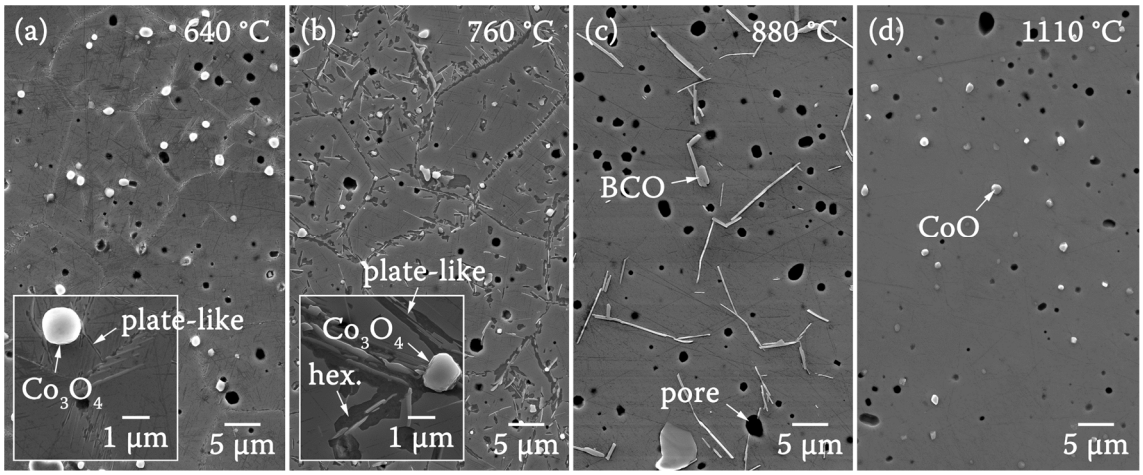

Figure 35. SE SEM images of BSCF annealed at (a) 640 °C, (b) 760 °C, (c) 880 °C for 10 days and (d) 1110 °C for 24 h in ambient air. To improve visibility an image taken at a higher magnification is inserted in image (a) and (b).

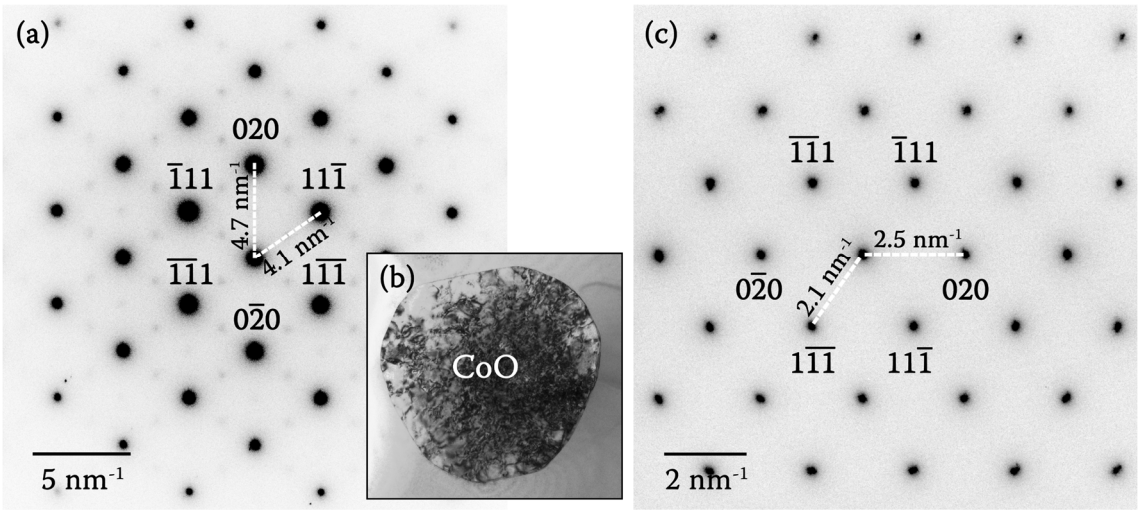

Figure 36. (a) SAED image of a CoO precipitate in BSCF with (b) corresponding BF TEM image. (c) SAED image of Co_3O_4 in BSCF.

SE SEM image of BSCF annealed at 640, 760, 880 for 10 days and 1110 °C for 24 h are presented in Figure 35. Some of the secondary phases are labeled to guide the reader. Note that lamellar phases are labeled BCO above 840 °C and plate-like phases below 840 °C. The labels already reflect the results obtained from additional TEM analysis, especially the identification of CoO, BCO, and Co_3O_4 as presented later on in this chapter. In the high-temperature regime (> 840 °C, cf. Figure 35(c,d)) no hexagonal phase is present which is in accordance with previous publications [63,64,76]. According to the SE images, decomposition of BSCF into the hexagonal phase is highly pronounced at 760 °C (cf. Figure 35(b)) with the hexagonal phase forming at grain boundaries, plate-like phases, and Co_3O_4 precipitates. As plate-like precipitates have a length of several micrometers, they can cross a significant fraction of the grain. The formation of the hexagonal phase around these plate-like precipitates leads to a non-negligible spread of the hexagonal phase into the grain interior, which was also confirmed by TEM analysis of BSCF [205]. Significantly less hexagonal phase is visible in BSCF annealed at a lower temperature (640 °C), which can be attributed to reduced kinetics. Co_xO_y precipitates can be observed in all images except at 880 °C (Figure 35(c)), where only BCO phases are present. This will be subject to later discussions.

EDXS suggested a higher Co/O concentration ratio within cobalt-oxide precipitates in samples annealed at lower temperatures. TEM-SAED was utilized for the identification of the cobalt oxide phase. SAED confirmed, that samples annealed at high temperatures (> 950 °C) show reflections which can be attributed to CoO (rock salt structure, $Fm\bar{3}m$) whereas samples annealed below 800 °C show reflections of Co_3O_4 (spinel structure,

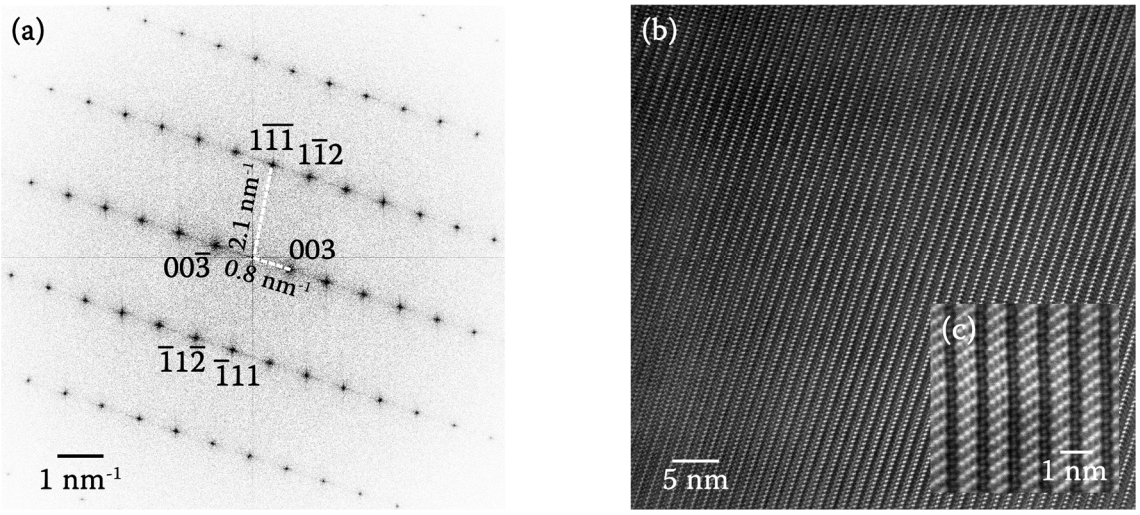

Figure 37. (a) Diffractogram of BCO phase in [110] orientation. (b) HRTEM and (c) HAADF-STEM image of BCO-type intergrowth platelets in [110] orientation.

$Fd\bar{3}m$) (cf. Figure 36(c)). The measured lattice parameters of (0.43 ± 0.02) nm and (0.81 ± 0.02) nm match well with the lattice parameters reported in literature for CoO ((0.4178 ± 0.0001) nm [206]) and Co_3O_4 ((0.80850 ± 0.00009) nm [207]). Some additional weak reflections can be seen in Figure 36(a), indicating a super structure within the CoO matrix. This might be attributed to defects as CoO is known to accommodate cation vacancies [208]. Also, the BF image in Figure 36(b) shows many dislocations within the CoO grain.

Surprisingly, neither CoO nor Co_3O_4 was detected within samples in the temperature range between ~800 and ~950 °C. The only secondary phase present was the BCO phase. A diffractogram of the BCO phase observed in a sample annealed at 880 °C is depicted in Figure 37(a). The derived a and c lattice parameter (trigonal, $R\bar{3}m$) was (0.56 ± 0.02) nm and (3.57 ± 0.02) nm which is fairly close to the parameter published by SUN ET AL. [80] of (0.56901 ± 0.00004) nm and (3.5937 ± 0.0005) nm. A high-resolution TEM image is presented in Figure 37(b) including a HAADF-STEM image (cf. Figure 37(c)) along the same projection. The image suggests a well-defined stacking order with alternating layers of one CdI_2-type and two cubic perovskite layers. This corresponds to n=2 in the general formula of the barium cobaltite intergrowth series $Ba_{n+1}Co_nO_{3n+3}(Co_8O_8)$ [46,79].

EELS spectra for all observed primary/secondary BSCF phases in the temperature range between 640 °C and 1110 °C are presented in Figure 38. The spectra include the O-K, Fe-$L_{2,3}$, Ba-$M_{4,5}$ and Co-$L_{2,3}$ ionization edges, acquired under identical microscope conditions (cf. Chapter 2.2.2.4). The Co-valence state derived from these spectra with

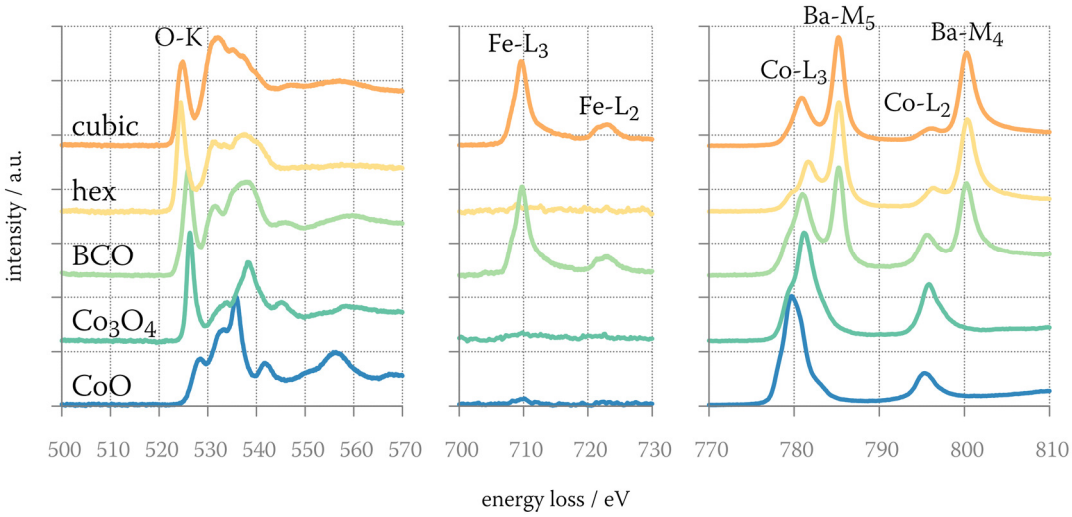

Figure 38. EELS spectra of secondary phases within the BSCF compound system in the temperature range between 640 °C and 1110 °C.

the white-line distance technique described in Chapter 3.2.1 are 2.05+ (CoO), 2.19+ (cubic), 2.67+ (BCO), 2.58+ (hexagonal) and 2.64+ (Co_3O_4). The valence state of the hexagonal phase was subject to change regarding thermal history and position on the sample, varying in the range of 2.5+ to 2.8+. The valence state of Fe was determined using the white-line ratio technique with the calibration curve derived in Chapter 3.2.2. The Fe valence state of the cubic BSCF and BCO phase was fairly similar with a white-line intensity ratio of 4.07 (BSCF) and 3.88 (BCO), and a corresponding valence state of 2.97+ (BSCF) and 2.69+ (BCO) respectively. It should be noted, that the error is estimated to be ±0.3. The measured value matches with the fine structure seen in the Fe-$L_{2,3}$ edge. Both, the shoulder at the Fe-L_3 white-line and the double peak of the Fe-L_2 line are present in the reference spectrum for Fe^{3+} (cf. Figure 25(b)), which further confirms an Fe oxidation state close to 3+. This agrees well with data from other groups [67–69].

Regarding the O-K ionization edge, there is a considerable change in fine structure when comparing the EELS spectra of different phases. The most noticeable feature is the O-K pre-peak at ~525 eV. The pre-peak arises due to transitions of electrons from $1s$ to $2p$ states, hybridized by the transition metals [209,210]. The intensity of this pre-peak is linearly correlated to the population of $3d$ states and, therefore, the valence state. It is clearly visible that the pre-peak is highly pronounced for Co_3O_4 compared to CoO. To compare pre-peak intensities, the ratio between main peak and pre-peak was calculated. For that, the spectrum was divided at the minimum between pre-peak and

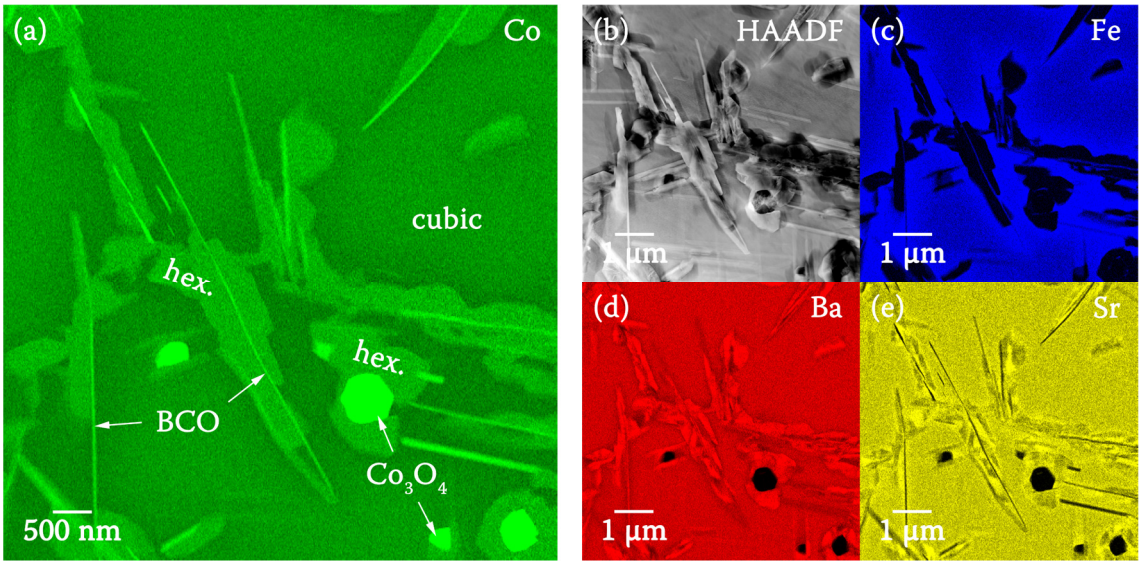

Figure 39. Quantified STEM EDXS elemental composition maps of (a) Co, (c) Fe, (d) Ba and (e) Sr with the corresponding (b) HAADF-STEM image.

main peak of the O-K edge. The integrated intensity of the low energy side accounts for the pre-peak and the high energy side up to +30 eV was used as main peak signal. This results in a peak ratio of 9.9 ± 0.7 (CoO), 8.8 ± 0.7 (cubic), 6.3 ± 0.7 (BCO), 6.0 ± 0.7 (hexagonal) and 4.7 ± 0.7 (Co_3O_4). The order closely resembles the one expected by the measured Fe and Co oxidation states, derived from their white-lines. This can be interpreted as confirmation for the valence state determination technique.

The chemical composition of all secondary phases was evaluated by EDXS. As oxygen cannot be quantified reliably, only the cation concentrations were determined. Quantification results are summarized in Table 6. Note, that the systematic errors are estimated to be ±3 at%. Each phase has a characteristic chemical composition which

phase	Ba [at%]	Sr [at%]	Co [at%]	Fe [at%]
cubic	27.5	24.0	38.0	10.5
hexagonal	28.6	23.5	46.2	1.7
BCO	21.1	3.1	66.8	9.0
Co_3O_4	0.3	0.2	97.8	1.7
CoO	0.2	0.1	97.9	1.8

Table 6. EDXS quantification results for different phases in BSCF. The systematic error is estimated to be ±3 at%.

makes it easy to identify individual phases with high lateral precision in STEM EDXS mappings. In Figure 39, quantified cation composition maps of BSCF annealed at 760 °C for 10 days, are presented. Co_3O_4 can be identified by its high Co signal and almost full depletion of all the other cations. BCO-type lamellars can be reliably identified by their lack of Sr, as seen in the Sr map (cf. Figure 39(e)). The hexagonal phase shows up in the Fe mapping due to its depletion in iron (cf. Figure 39(c)). The distribution of secondary phases suggest that the dominant secondary phase with the highest volume fraction is the hexagonal phase. This is consistent with other reports [63,64,76]. Given the cation distribution maps, the Sr/Ba cation ratio varies strongly within the hexagonal phase. This agrees well with other studies where the stoichiometry of the hexagonal phase is usually described as $(Ba_{0.5+x}Sr_{0.5-x})CoO_{3-\delta}$ [74,205]. The variation in stoichiometry is considered to be responsible for the strong fluctuation in measured Co-valence state which was reported earlier.

5.1.1 Correlation with degradation

Since the first report of BSCF, the inherent phase instability of the cubic BSCF phase in the intermediate temperature range is known. In the first publication, SHAO ET AL. [3] connected the drop in oxygen conductivity at a temperature below 825 °C to the reversible formation of secondary phases. The secondary phase was later identified as a hexagonal phase with low oxygen vacancy concentration and, therefore, negligible oxygen conductivity [63]. The decomposition of the cubic phase into a mixture of a new Fe-rich cubic phase and a Co-rich hexagonal phase was reported and discussed by many researchers [62,64,74,77,78,84,104,106]. The main reason for the decomposition can be attributed to the multivalent TM valence change due to temperature-dependent changes in the oxygen stoichiometry. Since the valence band of Co is much lower than the valence band [71] of Fe, charge compensation occurs by changes of the Co-valence state. Hence, lowering the temperature results in an increase of Co-valence state and, therefore, a decrease in its ionic radius. This decrease promotes the formation of secondary phases because the corner-sharing configuration of oxygen octahedrons in the cubic perovskite phase cannot be maintained. Therefore, the Co-valence state in secondary phases formed in the intermediate temperature range (600 – 900 °C) is considerably increased compared to the one in the cubic phase (cf. Figure 38). In terms of Goldschmidt tolerance factor, a lower B-site ionic radius favors a hexagonal phase which is indeed the most pronounced secondary phase in BSCF below the critical temperature (T < 840 °C).

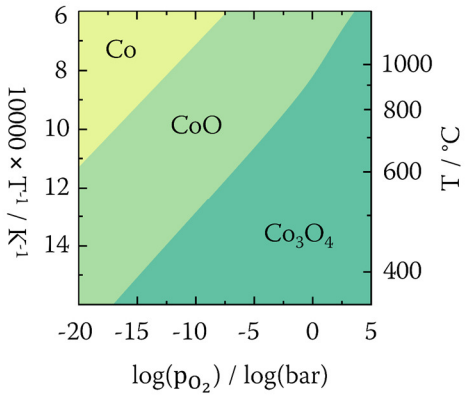

Figure 40. Co-O phase diagram as a function of $\log(p_{O_2})$ and temperature [265].

The kinetic decomposition into the hexagonal phase in dense ceramics can be described by the Johnson–Mehl–Avrami model. Here the volume fraction of the cubic and hexagonal BSCF phase was derived from integral XRD data. Depending on the publication, BSCF tends towards an equilibrium state with a volume fraction of the hexagonal phase of 21 % [64], 31 % [84] or 50 % [74]. However, all publications report an Avrami coefficient close to one, indicating a two-dimensional nucleation and growth process. Nucleation occurs at grain boundaries which are believed to be quickly saturated, followed by a sluggish growth as secondary phases require a significant rearrangement of cations. The sluggish growth is mainly dictated by the exchange of Fe in favor of Co. This is connected to the reduced spacing (face sharing octahedrons) within the hexagonal lattice and the smaller ionic radius of Co compared to Fe. Since the equilibrium concentration of the hexagonal phase is not reached, the cation redistribution can be seen in the surrounding area of the hexagonal phase. In that area, the Fe concentration is slightly elevated and the Co concentration slightly reduced (cf. Figure 39(a,c)). The nucleation of the hexagonal phase is connected to certain lattice sites because the hexagonal phase shares an orientation relationship towards the cubic host lattice [77,79,205]. As it is now repeatedly shown that BSCF has non-negligible amounts of secondary phases other than the hexagonal phase (e.g. plate-like, Co_xO_y phases), these phases have to be also included into the decomposition model. This can be done by treating them as additional nucleation sites for the hexagonal phase which is justified by the microstructure investigations. In addition to grain boundaries, most of the plate-like and Co_xO_y phases are decorated by the hexagonal phase (cf. Figure 39). Hence, the suppression of Co_xO_y and plate-like precipitates is of great importance

regarding the decomposition rate of the cubic BSCF phase as they might significantly accelerate the formation of the hexagonal phase.

There are a lot of studies published dealing with the formation of the hexagonal phase, however, only a few of them point out the presence of other secondary phases. This can be attributed to the low volume fraction which renders these phases invisible when using common integral analysis techniques. Phases with plate-like morphology and fast formation kinetics were subjects of TEM investigations as they have a higher onset temperature (~900 °C) [76,77,79]. The plate-like phase can be described as a modular intergrowth structure of an arbitrary number of cubic, hexagonal and recently discovered $Ba_{n+1}Co_nO_{3n+3}(Co_8O_8)$ (BCO, $n \geq 2$) lamellae [79,80,100,211]. As the hexagonal phase does not form above 840 °C, the phase with plate-like morphology is entirely composed of BCO as shown in this thesis. Beside the plate-like phase, there are also reports about CoO and Co_3O_4 precipitates over the entire temperature range [79,81–84,212,213]. During sintering, Co is expelled from the cubic lattice and crystallizes in form of CoO precipitates. The presence of Co_3O_4 in some studies can be explained by the Co-O phase diagram which is depicted in Figure 40. As seen in the graph, there is a phase transition between CoO and Co_3O_4 at ~900 °C and atmospheric pressure ($p_{O_2} \approx 0.21\ bar$). Therefore, depending on thermal history, either CoO or Co_3O_4 is present within the sample. Surprisingly, CoO and Co_3O_4 was not present after annealing the sample at 880 °C for 10 days. This indicates that there is an additional phase transition in the intermediate temperature range. The appearance of the BCO phase in the same temperature range implies a reaction of the CoO phase with the Ba from the cubic phase, resulting in the formation of BCO platelets. This can be further supported by the results published by SUN ET AL. [80], who investigated the barium cobaltite intergrowth series in great detail. It is reported, that the BCO-type phase forms at a narrow temperature window between (800 – 950 °C) by the reaction of cobalt-oxide (Co_2O_3) with barium carbonates ($BaCO_3$). This agrees well with the publication by MÜLLER ET AL. [76] who found out that the volume fraction of the plate-like phase is only significant in samples annealed at temperatures between 800 and 900 °C. It also explains why the volume fraction of the BCO phase does not depend on the duration of the annealing treatment. As the formation kinetics of the plate-like phase was considered to be quite fast, CoO consumed in the reaction process of the BCO phase is quickly depleted. Hence, no additional reaction is possible. The minor amount of BCO phases at lower temperatures (< 800 °C) can be explained by the thermal history. While samples are cooled down after the sintering process (950 – 1200 °C), they pass through

the reaction temperature range. Therefore, the BCO phases observed after annealing at lower temperatures might be remnants from reactions occurring between 800 and 950 °C during cooldown from the sintering temperature. However, additional BCO type phases in the low temperature regime (< 800 °C) cannot be ruled out because the impact of other cations like Sr and Fe on the formation of the BCO phase is not known. Furthermore, the BCO phase in BSCF contains Fe which is also not considered in previous studies of barium cobaltites.

5.2 Secondary phase formation in doped BSCF

In order to counteract the decomposition of the oxygen-conducting cubic perovskite phase, BSCF was doped with the TM ions Yttrium (Y), Scandium (Sc) and Zirconium (Zr). These dopants were chosen because of their fixed valence state and larger ionic radius compared to trivalent Co ions. The incorporation of such ions on the B-site of a perovskite lattice decreases the Goldschmidt tolerance factor and is, therefore, believed to enlarge the stability regime of the cubic phase. The focus was set on Y-doped BSCF because the most pronounced suppression of secondary phases was observed there as shown in the following.

Cobalt oxide precipitation

SE SEM images of quenched ceramic samples after homogenization at 1000 °C for 24 h are presented in Figure 41(a-e). Images were taken from the bulk interior far away from the surface. At this temperature BSCF, BSCF3Sc and BSCF1Y samples show round precipitates embedded in the cubic perovskite matrix, which could be unambiguously attributed to CoO. Some of the CoO precipitates are highlighted by white arrows. The black contrast in the images can be attributed to pores within the ceramic material. The size of the CoO precipitates is strongly increased for BSCF3Sc which is assumed to be caused by the elevated powder particle size and different sintering profile. Comparing BSCF and BSCF1Y, the number density of CoO precipitates is significantly lower for the BSCF1Y sample, already indicating minor improvements in cubic phase stability. No secondary phases are present in BSCF3Y and BSCF10Y which was further confirmed by

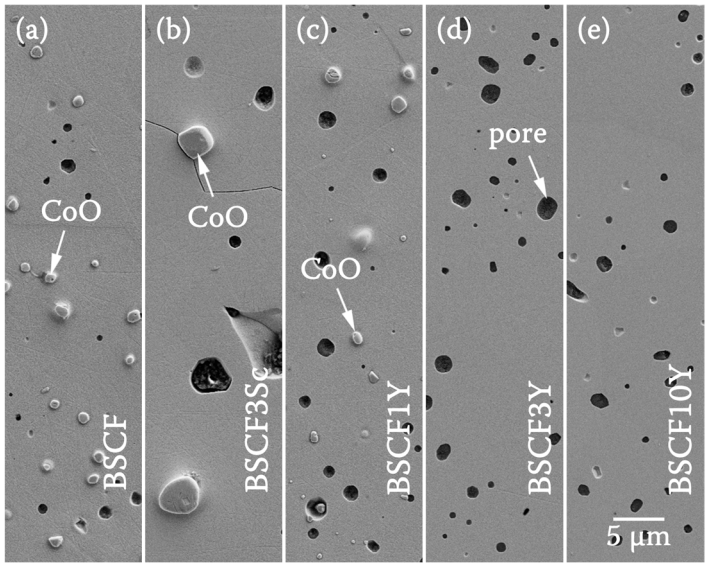

Figure 41. SE SEM images of (a) BSCF, (b) BSCF3Sc, (c) BSCF1Y, (d) BSCF3Y and (e) BSCF10Y annealed at 1000 °C for 24 h in ambient air.

TEM analysis. This clearly demonstrates the enhanced cubic phase stability for Y-doped BSCF because the formation of CoO precipitates can be suppressed completely.

In a study concerning the effect of sintering conditions on BSCF, BAUMANN ET AL. [81] attributed the CoO precipitation to the lowered melting point of CoO in the presence of BaO. At 1130 °C incongruent melting of the BSCF phase occurs, leading to the recrystallization of CoO or Co_3O_4, depending on thermal history. However, BUYSSE ET AL. [82] also reported Co_3O_4 at a sintering temperature of 1100 °C and later on in Chapter 5.3 it will be shown that Co_3O_4 even forms at sintering temperatures as low as 1050 °C. This indicates that the onset temperature for Co_xO_y precipitation is much lower than previously reported. The outdiffusion of Co might also be connected to the fact that the Co concentration in BSCF is already close to the solubility limit [214]. Hence, BSCF might intrinsically tend towards a lower Co concentration. The tendency of the cubic perovskite phase towards a lower cobalt content is also observable below the critical temperature (840 °C). Here, cubic BSCF decomposes into a Co-enriched hexagonal phase, simultaneously forming a cubic phase with reduced Co content [74]. However, at high temperature the formation of the hexagonal phase is thermodynamically unfavorable and, therefore, CoO precipitation occurs to lower the Co content of the cubic phase. As CoO is the only secondary phase observed in the sinter process, it is safe to assume that the intended BSCF stoichiometry is modified. The removal of Co by CoO precipitation is expected to result in an A/B-cation ratio larger than one. This unintended deviation can in principle be compensated by the formation of A-site rich phases (e.g. BaO, SrO) or by an increased concentration of B-cation vacancies. The latter alternative is more plausible because SrO or BaO could not be observed in any sample by TEM analysis. Since Y ions in Y-doped BSCF are located on the A- and B-lattice site, the A/B-cation ratio is already altered (cf. Chapter 4.3). Given, that in BSCF3Y and BSCF10Y the A/B-cation ratio exceeds one, Co outdiffusion might be suppressed as the sample is already in a thermodynamic equilibrium state. This explains why BSCF3Y and BSCF10Y do not tend towards CoO precipitation during the sintering process. Mixed A/B-site occupancy is also observed for BSCF1Y. However, the low Y concentration does not significantly alter the A/B-site ratio. Therefore, CoO precipitation is only reduced and not completely suppressed. As Sc is entirely located on the B-site, no significant reduction of CoO precipitation is observed there.

Microstructure in the intermediate temperature range

A comparative study in the temperature range between 700 and 1000 °C for 3 at% Y-, Sc- and Zr-doped BSCF was performed to assess secondary phase formation for each of the dopants. Representative SE SEM images of BSCF3Zr, BSCF3Sc and BSCF3Y annealed at 700 °C for 100 h are depicted in Figure 42(a-c). Some secondary phases are marked in the images. The types of secondary phases occurring in BSCF3Sc and BSCF3Zr are identical to the ones observed in undoped BSCF. TEM confirmed the presence of the hexagonal phase, the plate-like phase and several BCO/Co_xO_y precipitates depending on thermal history. However, for BSCF3Y only the hexagonal phase was observed at temperatures ≤ 800 °C, whereas no secondary phases were present above 800 °C. The suppression of BCO can be explained by the absence of CoO in the high-temperature range since all of these phases (CoO, BCO, Co_3O_4) are closely related (cf. Chapter 5.1.1). The improvement in phase stability is also reflected by measurements of the electrical conductivity conducted by CHRISTIAN NIEDRIG [91] (IAM-WET, KIT). There, the electrical conductivity decreases considerably for BSCF3Sc, BSCF3Zr and BSCF but not for BSCF3Y. A more detailed description can be found in the PhD thesis of PHILIPP MÜLLER [215]. Hence, Y was regarded as the most promising candidate and, therefore, investigated in more detail.

To characterize the thermal stability of Y-doped BSCF in relation to undoped BSCF, samples with different Y concentrations were annealed for 10 days. Resulting SE SEM images from the bulk interior of BSCF, BSCF1Y, BSCF3Y and BSCF10Y annealed at 640, 760 and 880 °C are depicted in Figure 43(a-l). To further visualize the secondary phases, simplified schemes are inserted in each SE image. Some of the secondary phases were labeled with white arrows. At 880 °C annealing temperature, BCO phases are present

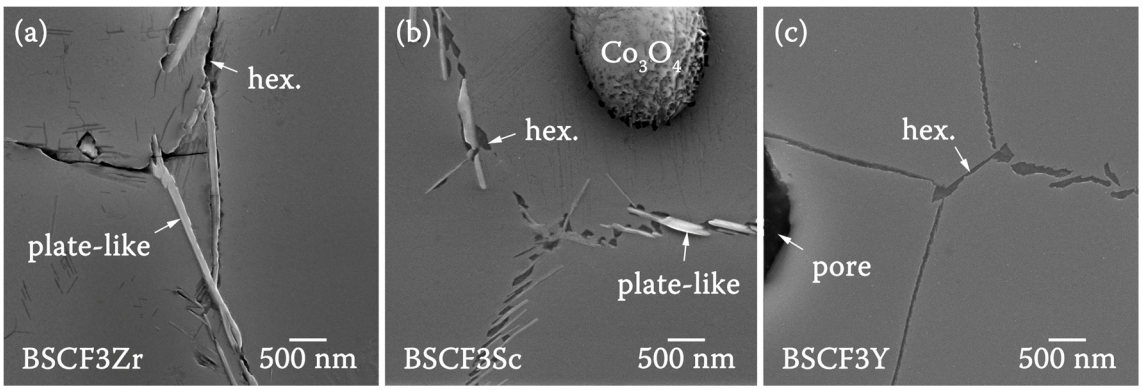

Figure 42. SE SEM images of (a) BSCF3Zr, (b) BSCF3Sc and (c) BSCF3Y after heat treatment at 700 °C for 100 h.

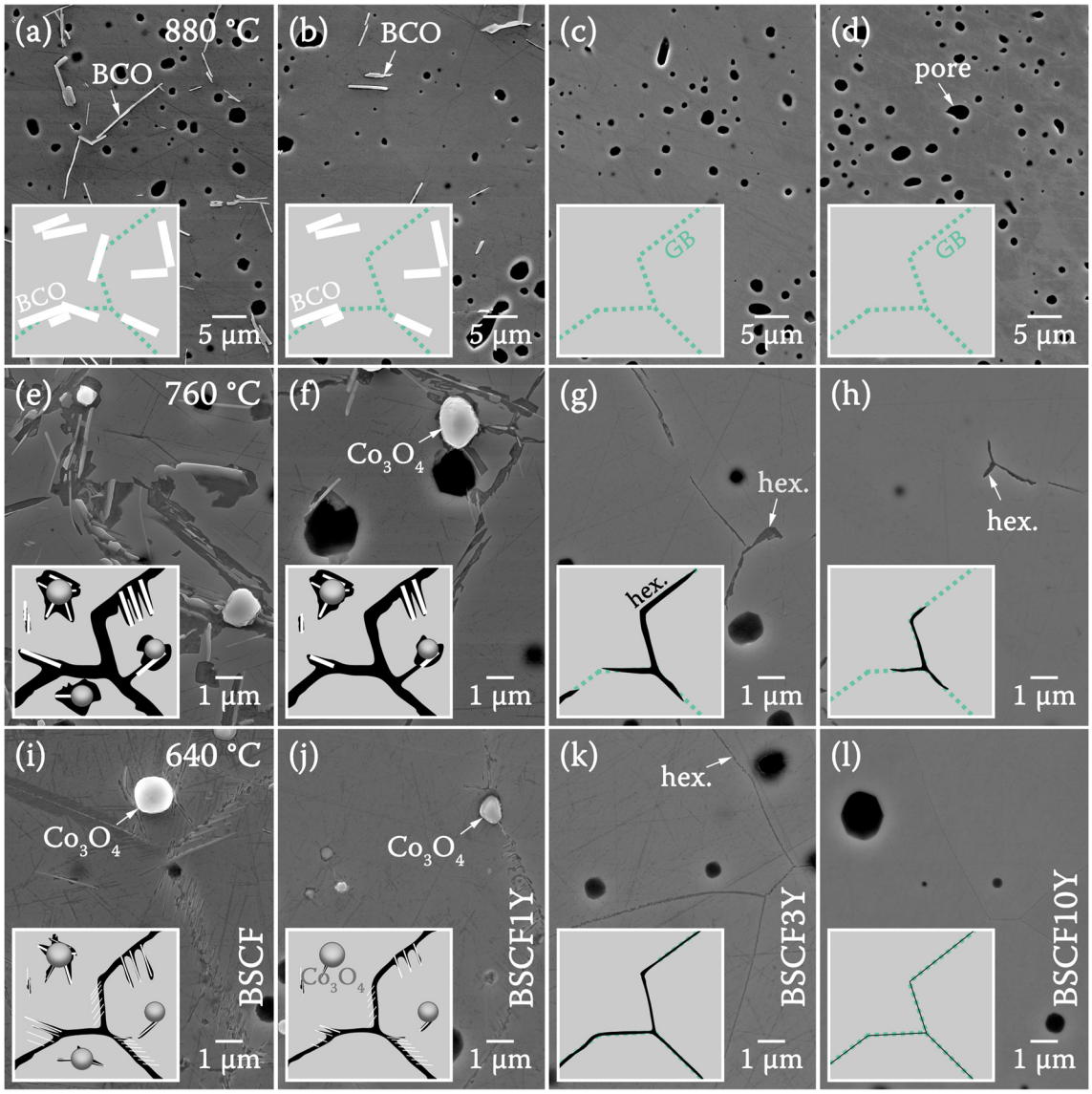

Figure 43. SE SEM images of (a,e,i) BSCF, (b,f,j) BSCF1Y, (c,g,k) BSCF3Y and (d,h,l) BSCF10Y annealed at (a-d) 880 °C, (e-h) 760 °C and (i-l) 640 °C for 240 h. Simplified schemes of the secondary phase distribution is superimposed on each image. Different phases in the schemes are indicated by black regions (hexagonal phase), bright rectangular regions (BCO above 760 °C and plate-like phase at 760 °C and below), round precipitates (Co_3O_4).

within BSCF and BSCF1Y. This is reasonable because BSCF and BSCF1Y contain CoO precipitates at 1000 °C (cf. Figure 41). Since the samples were homogenized at 1000 °C before being cooled down to 880 °C, the high-temperature CoO phase decomposes almost completely into BCO-type lamellae, as discussed for BSCF in Chapter 5.1.1. Consequently, the BCO phase is absent in BSCF3Y and BSCF10Y because Co outdiffsuion does not occur at high temperatures. EDXS analysis of the BCO phase in BSCF1Y agrees well with the composition derived from the BCO phase in undoped

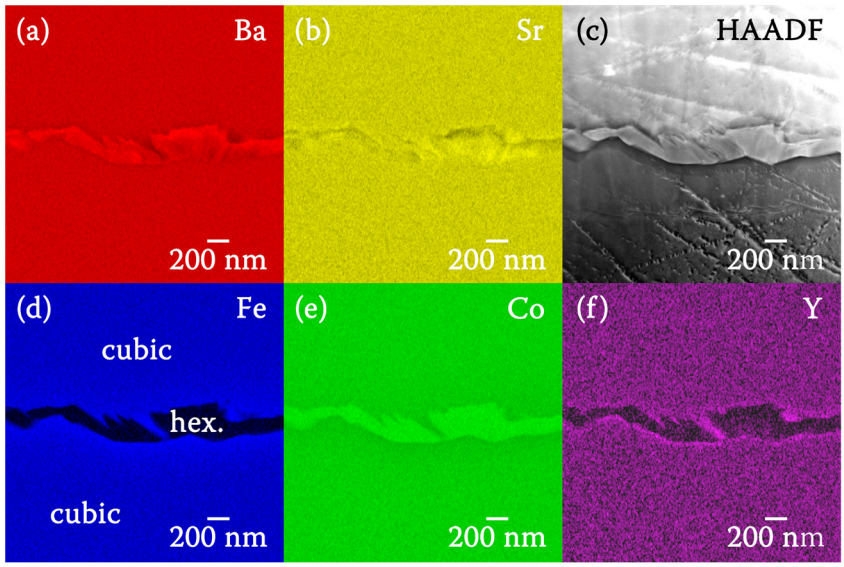

Figure 44. EDXS elemental distribution map for (a) Ba, (b) Sr, (d) Fe, (e) Co and (f) Y with the corresponding (c) HAADF-STEM image.

BSCF. Within the detection limit of EDXS, Y is not present in the BCO phase. At 760 °C, the formation of secondary phases (hexagonal and plate-like phase) is highly pronounced in undoped BSCF and slightly less pronounced in BSCF1Y. For BSCF3Y and BSCF10Y the content of secondary phases is almost negligible. Only the hexagonal phase partially decorates grain boundaries, especially grain-boundary triple points. The lowest annealing temperature (640 °C) essentially resembles the observed at 760 °C. However, the content, especially of the hexagonal phase, is strongly reduced which can be attributed to the reduced cation movement at lower temperatures.

To quantitatively investigate the content of secondary phases, SE SEM images were analyzed by image analysis techniques. Secondary phases can be easily distinguished by their individual gray value which is the basis of this approach. Artifacts, e.g. scratches

sample	volume fraction [vol%]		
	Co_3O_4	hexagonal	plate-like
BSCF	1.3 ± 0.5	19.7 ± 2.8	4.7 ± 1.0
BSCF1Y	1.0 ± 0.5	5.9 ± 1.1	1.5 ± 0.8
BSCF3Y	0.0 + 0.1	1.3 ± 0.4	0.0 + 0.1
BSCF10Y	0.0 + 0.1	0.6 ± 0.3	0.0 + 0.1

Table 7. Volume fraction of secondary phases after heat treatment at 760 °C for 10 days.

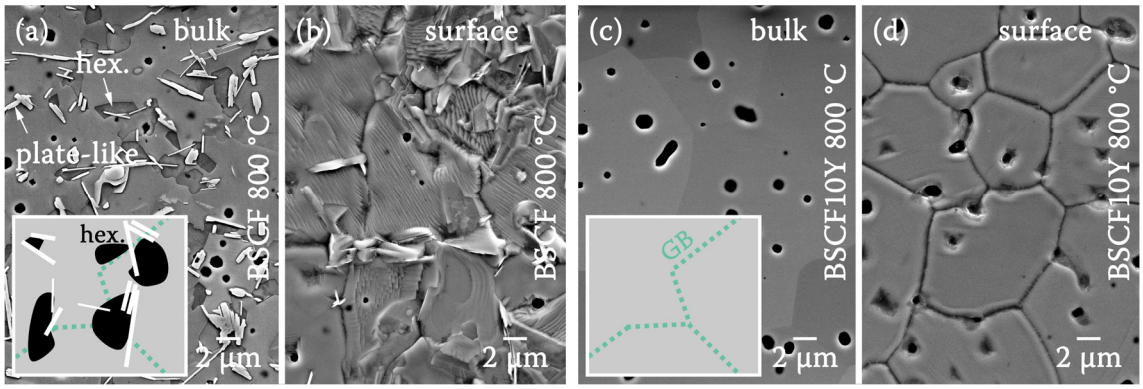

Figure 45. SE SEM images of (a,b) BSCF and (c,d) BSCF10Y showing (a,c) the bulk interior and (c,d) the surface after annealing at 800 °C for 43 days. A simplified scheme of the secondary phase distribution is inserted in the images showing the bulk interior.

on the sample surface, were removed manually. As the whole sample was exposed to ambient air, the oxygen pressure and, therefore, the chemical potential within the sample, is assumed to be homogeneous. Hence, no anisotropic behavior in secondary phase formation is expected which justifies the determination of secondary phase volume fractions from 2D SEM images. The result is summarized in Table 7 for the 760 °C sample. It is obvious that the volume fraction is drastically reduced with increasing Y-dopant concentration. If BSCF is compared with BSCF10Y, the reduction in volume fraction of secondary phases is more than one order of magnitude.

Further analysis of the hexagonal phase in BSCFY was performed by EDXS STEM. The elemental distribution close to a grain boundary for BSCF3Y annealed at 760 °C for 10 days is depicted in Figure 44(a-f). The hexagonal phase at the grain boundary is well visible in all images. The distribution maps suggest a similar stoichiometry as the hexagonal phase in undoped BSCF, including the strong variation in the Ba/Sr-ratio. In addition to the depletion of Fe, the hexagonal phase is also depleted in Y. The Y concentration in the hexagonal phase was slightly less than 50 % (BSCF3Y: < 1.5 at%) of the Y concentration in the cubic phase. SAED analysis resulted in a lattice parameter of a = (0.56 ± 0.01) nm and c = (0.44 ± 0.01) nm, which is identical to the lattice parameter reported for the hexagonal phase in undoped BSCF [64]. Hence, the hexagonal phase in BSCF and BSCFY can be considered identical despite the small Y content.

Since the decomposition of BSCF is controlled by sluggish cation kinetics, a long-time annealing (43 days at 800 °C in ambient air) experiment was performed to assess the phase composition near equilibrium. NIEDRIG ET AL. [64] reported, that after

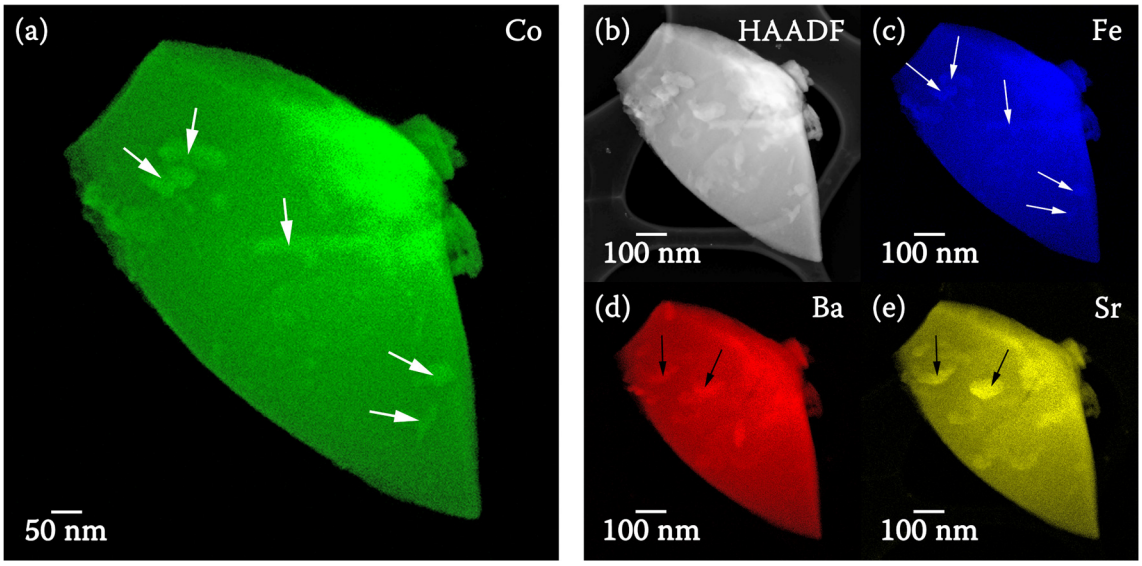

Figure 46. EDXS maps of BSCF powder particle showing the measured characteristic X-ray intensity for (a) Co, (c) Fe, (d) Ba and (e) Sr with the corresponding (b) HAADF-STEM image.

approximately 40 days of annealing at 800 °C, the phase transition from cubic BSCF to a combination of cubic and hexagonal phases is completed by 90 %. Hence, an annealing time of 43 days can be considered close to equilibrium conditions. To reduce systematic errors, the samples (BSCF and BSCF10Y) were simultaneously annealed in the same oven. The samples were polished prior annealing to obtain additional information about the formation of surface phases. SE SEM images after annealing showing the bulk interior or the surface are presented in Figure 45(a-d). The specimens showing the bulk interior were treated as previously described whereas the surface structure was imaged without any sample preparation. As expected, the secondary phase formation is very pronounced in BSCF with a high hexagonal phase content and many plate-like precipitates. Secondary phases are not only present within the bulk but also on the surface. Bulk SE SEM images suggest a volume fraction of secondary phases of 23.0 vol% consisting of (16.4 ± 2.7) vol% hexagonal phases and (6.6 ± 1.7) vol% plate-like phases. This is consistent with the 20 % reduction of the Bragg peaks of the cubic phase in XRD observed by NIEDRIG ET AL. [64]. For BCSCF10Y secondary phases are completely absent in the bulk and on the surface (cf. Figure 45(c,d)). It is worth mentioning, that the weak contrast observed in the bulk image can be attributed to dynamical electron diffraction (electron channeling) due to different grain orientations. The contrast at grain boundaries on the sample surface is the result of thermal etching due to the long annealing time. The complete absence of secondary phases was confirmed by TEM analysis. Hence, the cubic phase of BSCF10Y can be considered stable at 800 °C.

Since powders are believed to equilibrate much faster than dense ceramics additional annealing experiments were conducted with as-calcinated BSCF and BSCF10Y powders. Surprisingly, BSCF10Y powders annealed at 800 °C for 10 days clearly showed the hexagonal phase. Nevertheless, the hexagonal phase was less pronounced in BSCF10Y powders compared to BSCF powders. However, STEM analysis of as-calcinated powders before the annealing process revealed small inhomogeneities in the chemical composition. An EDXS elemental distribution map of a single BSCF particle is shown in Figure 46(a-e). Only non-quantified images are presented here, as quantification leads to artifacts due to the underlying structure of the carbon grid. The contrast was slightly adjusted to improve visibility. The images clearly suggest that there are some regions with enhanced Co and Fe signal (white arrow) and other areas with increased Ba and Sr signal. Since STEM images only show the projected sample, it is impossible to judge if these inhomogeneities are on the surface or within the grain. However, it can be concluded that the cations are not uniformly distributed within the initial powder. This results in regions with lower cubic phase stability, which facilitates the formation of the hexagonal phase even within BSCF10Y. In addition, the small grain size and large surface area lead to a much faster decomposition as demonstrated by MUELLER ET AL. [74].

Discussion about the effect of Y-ions on the decomposition of the cubic BSCF phase

As already outlined in Chapter 5.1.1, the secondary phase formation and decomposition rate of the cubic BSCF phase are strongly dependent on the available nucleation sites. The occurrence of BCO or Co_xO_y phases, however, is completely suppressed in BSCF3Y and BSCF10Y which is attributed to the mixed A/B-site occupancy of the Y ions. The absence of these secondary phases significantly reduces possible nucleation sites which explain why the formation of the hexagonal phase is less pronounced (cf. Figure 43). As the plate-like and Co_xO_y phases tend to extend into the grain interior, the absence of these phases limits the formation of the hexagonal phase to grain boundary regions only. It will be shown in Chapter 5.3.1 that grain boundary areas and, therefore, the available nucleation sites can also be minimized by fabrication parameters, which leads to a further reduction of the hexagonal phase. It is noted that the simple model dealing with available nucleation sites cannot explain the fact, that the volume fraction of the hexagonal phase decreases in BSCF10Y compared to BSCF3Y annealed at the same temperature, as they should contain the same concentration of nucleation sites (in the case of similar grain sizes). The different volume fraction of the hexagonal phase in these

samples are, therefore, attributed to the formation kinetics which might slow down with increasing Y concentration. This can be motivated by the EDXS results.

EDXS shows a strong depletion of Y ions in the hexagonal phase which can be attributed to the reduced B-site spacing in the hexagonal phase compared to the cubic phase. Since the radius of Y^{3+} (90 pm) ions is even larger than the radius of Fe^{3+} ions (55 – 64.5 pm) [216], the incorporation on the B-site of the hexagonal phase is highly unlikely by considering the fact that the much smaller Fe cation cannot be tolerated there. The residual Y signal in the hexagonal phase can be attributed to Y ions located on the A-site of the perovskite, as some Y ions are detected on the A-site of the cubic BSCF phase. The concentration of Y within the hexagonal phase is consistent with the measured Y A-site occupancy of 45 % in BSCF3Y (cf. Chapter 4.3) by taking the error margins for EDXS into account. Remaining B-site Y cations are forced to move out before the cubic phase collapses into the hexagonal phase. Hence, the formation of the hexagonal phase is not only limited by the kinetics of Co and Fe cations but also the kinetics of Y ions on the B-site. The large ionic radius of Y ions suggests slow diffusion properties which might be the reason for the decrease of the hexagonal-phase content in Y-doped BSCF. As the B-site content of Y increases with increasing Y dopant concentration (cf. Chapter 4.3), this would explain why the highest Y concentration has the strongest effect in suppressing the hexagonal phase.

EELS investigations of the cubic BSCF phase

EELS spectra were recorded on samples annealed at 1110 °C for 24 h. It is worth noting, that the thin sample region, which is required for EELS, is affected by electron-beam damage leading to modifications of the O-K and Co-$L_{2,3}$ edges. This effect is quite pronounced in cubic BSCF when the focused electron beam is kept at the same sample position for several seconds. The pre-peak of the O-K edge moves closer to the main peak and decreases in its height, combined with an increase in Co-$L_{2,3}$ white-line distance. Both phenomena indicate a decrease in average TM valence state, which is most likely caused by oxygen loss of the cubic lattice due to knock-on damage. This results in a new equilibrium state with a higher oxygen vacancy concentration associated with a lower Co-valence state. The observations suggest, that the sample equilibrates until Co reaches a valence state of 2+. To reduce beam induced damage, spectra with short acquisition times were taken on different sample positions and afterward added. Resulting spectra containing the Fe-$L_{2,3}$, Co-$L_{2,3}$, Ba-$M_{4,5}$, Sr-$L_{2,3}$ and Y-L_3 edges, acquired in the cubic phase of BSCF, BSCF1Y, BSCF3Y and BSCF10Y are

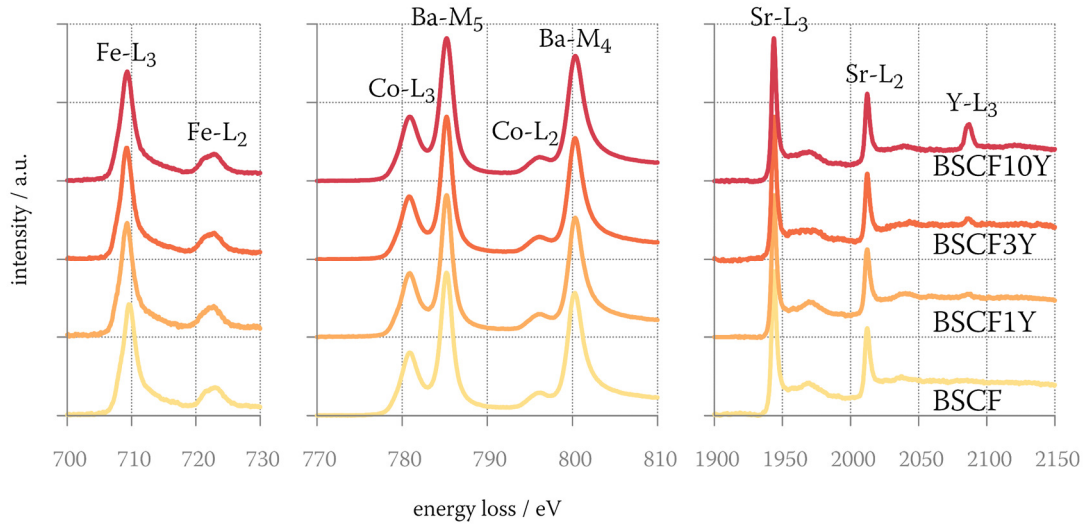

Figure 47. EELS spectra containing the Fe-$L_{2,3}$, Co-$L_{2,3}$, Ba-$M_{4,5}$, Sr-$L_{2,3}$ and Y-L_3 ionization edges in the cubic phase of BSCF, BSCF1Y, BSCF3Y and BSCF10Y. The spectra are vertically shifted and scaled for better visibility.

depicted in Figure 47. All spectra were deconvoluted with corresponding low-loss spectra acquired at the same sample position. The Y-L_3 edge increases with increasing Y-dopant concentration which confirms the successful Y incorporation in the cubic perovskite matrix. Average valence states were derived from Fe-$L_{2,3}$ and Co-$L_{2,3}$ white-lines either with the white-line ratio or white-line distance technique as elaborated in Chapter 3.2. Interestingly, the valence state of Co was nearly identical, with 2.19+ (BSCF) and 2.18+ (BSCF1Y, BSCF3Y and BSCF10Y). The statistical error in determining the white-line distance is estimated to be ±0.05 eV which translates into an error of about ±0.03 in Co-valence state. Therefore, the measured values are identical within the statistical error window. Note, that the systematic error of the Co-valence state is much higher (±0.2).

The resulting Fe-valence states were 2.97+ (BSCF), 2.84+ (BSCF1Y), 3.29+ (BSCF3Y) and 2.83+ (BSCF10Y). The determined Fe-valence states show considerable deviations, even for multiple measurements performed on the same sample. This might be associated to the sequential acquisition procedure of the low-loss and high-loss spectra. Hence, the deconvoluted spectra might not be an accurate description of single scattering which is considered essential for applying the white-line ratio technique [158]. The highest deviation observed for spectra acquired in the same sample corresponded to a valence state change of 0.3+. As the Fe-valence state is reported to be much more stable towards changes due to its considerable higher valence band [71],

it is assumed that the measured variation is an indication of the measurement error. This can be further motivated by the fact, that the position of the Fe-$L_{2,3}$ peak does not change within the measurement error margin.

As the measured average valence state of the TM cations in BSCF is much lower than 3+, the introduction of Y^{3+} ions has to result in either the reduction of oxygen vacancies, the decrease in TM valence state, or any combination of both effects. Assuming a fixed oxygen vacancy concentration of $\delta = 0.8$ at 1110 °C (which is plausible since BSCF was reported to have a vacancy concentration of $\delta = 0.74$ at 1100 K [56]) and a fixed Fe-valence state of 3+, the introduction of 10 at% Y would cause a reduction of the Co-valence state by about 0.1 which is little above the statistical error. This change can be further reduced by considering cation vacancies which are most likely present in Y-doped BSCF due to the observed mixed occupancy of Y ions (cf. Chapter 4.3). Consequently, although no change in Co-valence state was measured, a change of the oxygen vacancy concentration cannot be ruled out.

Correlation of secondary phase formation with electrical conductivity and oxygen permeation measurements

Oxygen permeation measurements were performed by STEFAN BAUMANN [121] (Materials Synthesis and Processing (IEK-1), Forschungszentrum Jülich) on samples provided by the IAM-WET in a common project. Oxygen permeation rates were measured on disc-type membranes (effective diameter of 13 mm) with a thickness of 0.5 mm (BSCF), 0.75 mm (BSCF1Y), 0.8 mm (BSCF3Y) and 0.55 mm (BSCF10Y) in a temperature range between 650 to 1000 °C. Additional long time investigations were performed at 700, 800 and 900 °C. Disc-shaped membranes were embedded in quartz glass tubes and sealed with gold rings. One side was fed with air (feed side, 250 Nml/min) and the other swept with argon (permeate side, 50 Nml/min). A more detailed description of the experimental setup can be found in [81]. For the long time permeation experiments, the feed gas was changed to synthetic air. Since the oxygen flux is connected to the membrane thickness, the oxygen flux was normalized to a thickness of 0.65 mm by using the Wagner equation. As the oxygen flux is not only controlled by bulk diffusion but also by surface exchange kinetics, the characteristic thickness has to be taken into account which was reported to be ~0.4 mm (BSCFY) and ~1 mm for BSCF [120,122]. Therefore, the modified Wagner equation for (partly) surface-controlled diffusion was used for normalizing the fluxes (cf. Equation 3). Normalized fluxes for a reference thickness of 0.65 mm are plotted in Figure 48. A

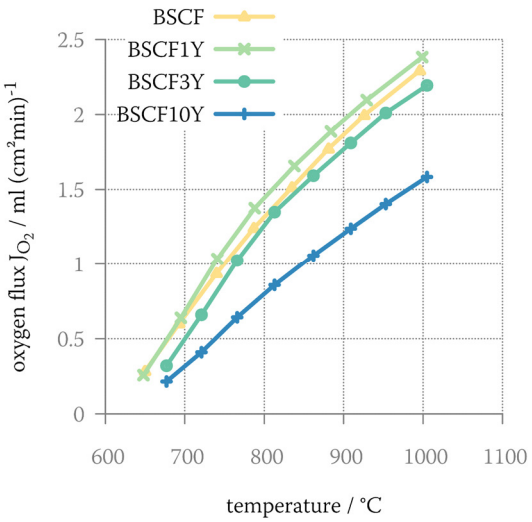

Figure 48. Oxygen flux as a function of temperature for different samples normalized to a reference thickness of 0.65 mm. The measurement was performed by STEFAN BAUMANN [81].

minor flux improvement of 4 -11 % compared to BSCF can be observed for BSCF1Y, whereas higher dopant concentrations are disadvantageous for oxygen transport with a reduction of 6 - 26 % (BSCF3Y) and 36 - 52 % (BSCF10Y). Hence, strong doping lowers oxygen diffusivity, especially in the low-temperature regime. This result is in contrast to the data published by HAWORTH ET AL. [115] who reported significant enhancements of up to 160 % for 2.5 at% Y-doped BSCF and even moderate gains (~70 %) for 10 at% Y-doping. However, they only substituted the Fe site, whereas in this study both B-site elements (Fe, Co) were targeted. They attributed the increase in permeability for Y-doped BSCF to the measured higher oxygen vacancy concentration in low doped samples and to the increase in lattice parameter [115]. The higher oxygen vacancy concentration can be rationalized by the measured mixed occupancy for Y cations (cf. Chapter 4.3) because this might lead to a significant cation vacancy concentration. The decrease in permeability for high dopant concentrations is most likely a result of a higher Y-O binding energy. Density functional theory calculations for the related mixed ionic electronic conductor $BaCo_{0.7}Fe_{0.3-x}O_{3-d}$ (x = 0.08 - 0.2) have shown a considerable higher average binding energy for Y-O compared to Fe-O and Co-O [102]. Hence, with increasing dopant concentration, the movement of oxygen anions might be impeded as some of them are trapped by Y cations. The reduction in oxygen permeability could be compensated by using functional surface layers that increase the oxygen surface exchange kinetics which will be discussed in Chapter 5.4.

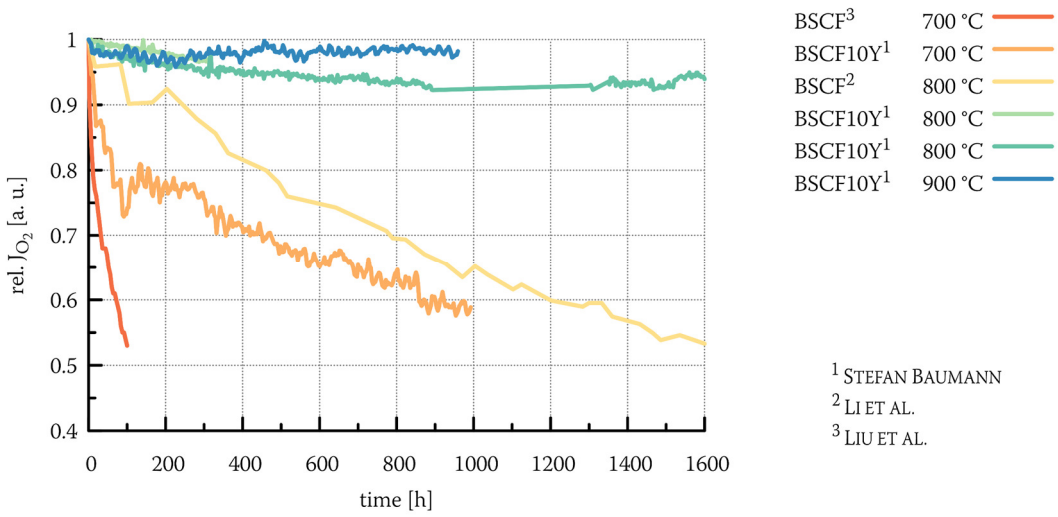

Figure 49. Oxygen flux normalized with the initial oxygen flux as a function of measurement time. The data were acquired by STEFAN BAUMANN [81]. Permeation data of BSCF from the paper of LI ET AL. [84] and LIU ET AL. [223] are added for comparison.

The activation energy (E_A) according to Arrhenius' law was calculated for the high temperature regime (T > 850 °C) where E_A is nearly constant with (35 ± 3) kJ/mol (BSCF), (27 ± 4) kJ/mol (BSCF1Y), (24 ± 5) kJ/mol (BSCF3Y) and (34 ± 4) kJ/mol (BSCF10Y). The activation energies are similar within the error limit for all samples with a slightly higher E_A value for BSCF and BSCF10Y. The activation energy for BSCF agrees reasonably well with values published by other groups which are 41.9 kJ/mol [3], 46.3 kJ/mol [66], 43.5 - 41.2 kJ/mol [217], 32.0 – 36.4 kJ/mol [121], 25 kJ/mol [82] and 41.5 - 44.4 kJ/mol [84]. For temperatures below 850 °C, the data points do not obey Arrhenius' law which might be connected to the appearance of secondary phases (either in the bulk or on the surface). The data suggest a strong increase in E_A which occurs in all the samples.

The samples showed distinctive microstructure differences after oxygen permeation experiments and long term annealing in ambient air (no oxygen partial pressure gradient). The long time permeability of BSCF10Y was investigated at 900 °C over a course of ~40 days. No significant reduction in permeability was observed during the entire measurement (cf. Figure 49) which is expected from the complete absence of secondary phases in the bulk as demonstrated by SEM and TEM analysis (cf. Figure 43). However, significant formation of secondary phases was observed on the surface of both membrane sides. The moderate surface decoration with secondary phases did not affect the measured oxygen flux in the experiment because oxygen permeation was bulk-

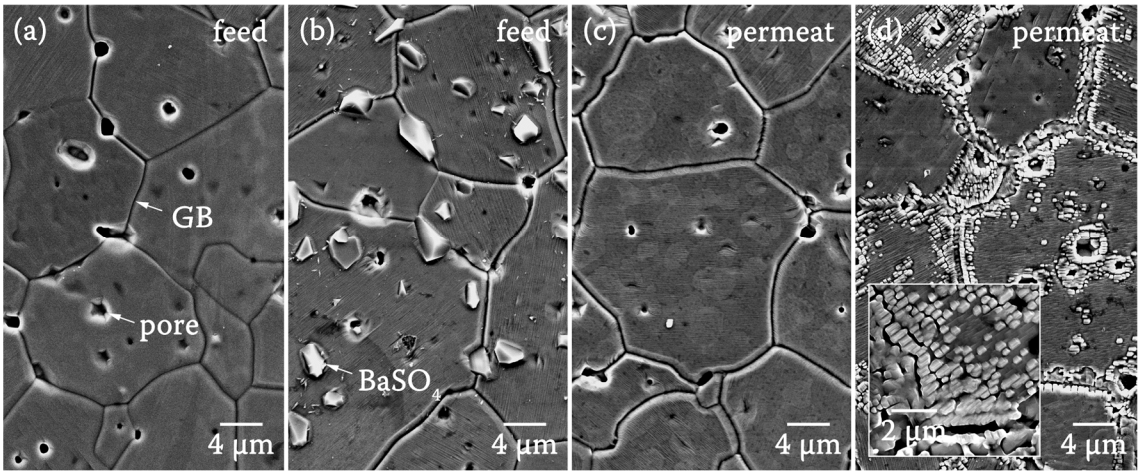

Figure 50. SE SEM images of permeation pellet surface after ~40 days at 900 °C. The images were taken (a,c) far away and (b,c) close to the gas inlet on either the (a,b) feed or (c,d) permeate side. A magnified region was superimposed in (d).

diffusion limited (thickness: 1.28 mm). However, as thin membranes are beneficial in terms of oxygen permeability and production costs, the occurrence of secondary surface phases has to be addressed. SE SEM images of the membrane surface after oxygen conductivity measurement at 900 °C for ~40 days are depicted in Figure 50. The concentration of secondary surface phases is more pronounced in the center of each membrane side which can be attributed to the pressure gradient in the feed (synthetic air) and flush gas (argon). This is a consequence of the experimental setup because the gas inlet was mounted in the center on each membrane side. Grooves at grain boundaries are observed in all the images due to thermal etching. Far away from the gas inlet, secondary phases do not form on the surface (cf. Figure 50(a,c)). However, close to the gas inlet, several secondary phases are present. The secondary phases on the feed side could be identified by EDXS as $BaSO_4$ phase. According to COLVILLE AND STAUDHAMMER [218], $BaSO_4$ crystallizes in an orthorhombic lattice (*Pnma* space group) with lattice parameters a = 0.888 nm, b = 0.545 nm, and c = 0.715 nm. Sulphur is assumed to originate from small impurities within the feed gas. This assumption is supported by the observation that permeation measurements performed in ambient air show a much higher $BaSO_4$ content compared experiments in well-controlled synthetic air. However, $BaSO_4$ precipitates can also arise if Sulfur-containing materials are involved in the fabrication process. YAREMCHENKO ET AL. [219] demonstrated the formation of $BaSO_4$ when using Sulphur-containing binders. They reported that $BaSO_4$ precipitates on the surface drastically decrease the oxygen exchange kinetics and are, therefore, considered unfavorable.

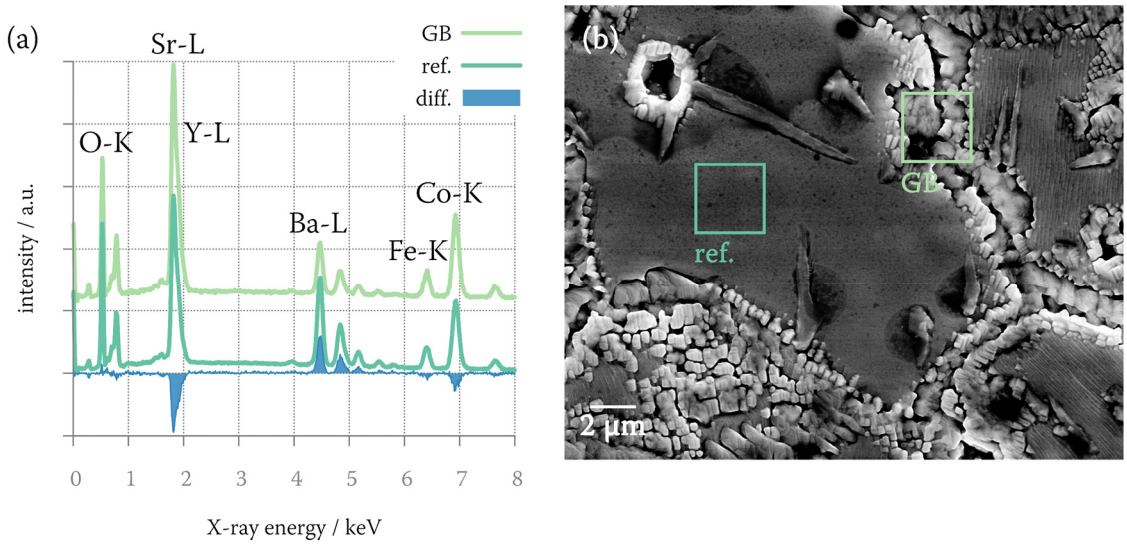

Figure 51. (a) Comparative SEM EDXS spectra of reference and GB region of permeate side of a permeation pellet operated at 900 °C for ~40 days. The difference spectra is added superimposed in the graph. Spectra are vertically shifted for clarity. A SE SEM image is presented in (b) with the reference and GB regions marked by squares.

The permeate side of the permeation pellet showed the presence of many rectangular precipitates close to grain boundaries (GB) and pores (cf. Figure 50(d)). SEM EDXS spectra with high SNR, taken at a reference position without the secondary phases, and at a GB region where many of these precipitates accumulate, are shown in Figure 51(a). The regions, where these spectra were recorded, are marked in the SE SEM image in Figure 51(b). Note that the spectra were obtained from a bulk sample with the microscope operated at 20 keV. Therefore, the EDXS spectra also contain a significant fraction of the underlying cubic phase. The most prominent peaks in the spectra are marked. After subtracting the GB spectrum from the reference spectrum a Ba reduction and Sr increase with only minor changes for Fe and Co is observed. Since the high energy side of the Sr-L peak also contains the Y-L peak, some part might be attributed to Y. However, the peak position of the signal difference suggests that most of the change can be attributed to Sr. Similar observations have been made by VENTE ET AL. [53] who reported a considerable surface roughening especially for membrane areas close to the inlet of the sweep gas as the oxygen partial pressure is lowest there. This was traced back to the difference in self-diffusion coefficients of the constituents in the applied chemical potential gradient, leading to cation demixing. Sr segregation and the formation of Sr-rich particles was also reported for the related compound $La_{0.8}Sr_{0.2}CoO_{3-\delta}$, which was connected to a significant decrease in electrochemical

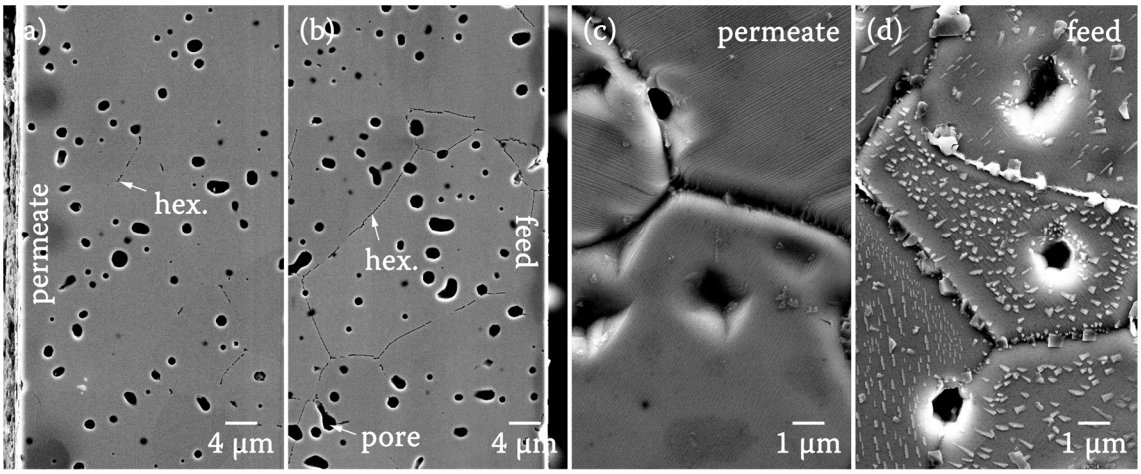

Figure 52. SE SEM images of cross-sections showing the bulk interior perpendicular to the (a) feed and (b) permeate side of a permeation pellet operated at 800 °C for 200 h in synthetic air with images of the (c) permeate surface and (d) feed surface.

performance [220–222]. Interestingly, this effect was overcome by modifying the surface with less reducible cations.

There is a minor, but noticeable reduction in oxygen permeability for BSCF10Y operated at 800 °C (cf. Figure 49), mainly within the first few hundred hours. This reduction is even more pronounced at 700 °C and continues over the whole measurement. Additional permeation data for BSCF are added in the graph from the publication by LI ET AL. [84] and LIU ET AL. [223]. With these data it can be seen, that the degradation for BSCF10Y is much slower compared to undoped BSCF which can be attributed to the reduced content of secondary phases as already suggested by the microstructure analysis. In contrast to samples not employed in a permeation setup (cf. Figure 45), some of the BSCF10Y membranes operated at 800 °C contain minor amounts of the hexagonal phase. This suggests that the overall phase stability of the cubic perovskite phase is affected by the oxygen partial pressure gradient. How the oxygen partial pressure and, therefore, the chemical potential affects the secondary phase formation characteristics can be seen if the microstructure close to the surface of the permeate side is compared with the feed side. This is shown in the SE SEM images in Figure 52. Many grain boundaries close to the feed side are decorated with the hexagonal phase (cf. Figure 52(b)), whereas close to the permeate side (cf. Figure 52(a)) only some grain boundaries contain the hexagonal phase. This behavior is also reflected by the surface, with the feed side showing numerous secondary phase precipitates and almost no secondary phases on the permeate side (cf. Figure 52(c,d)). The strong difference of secondary phase formation between feed and permeate side was also

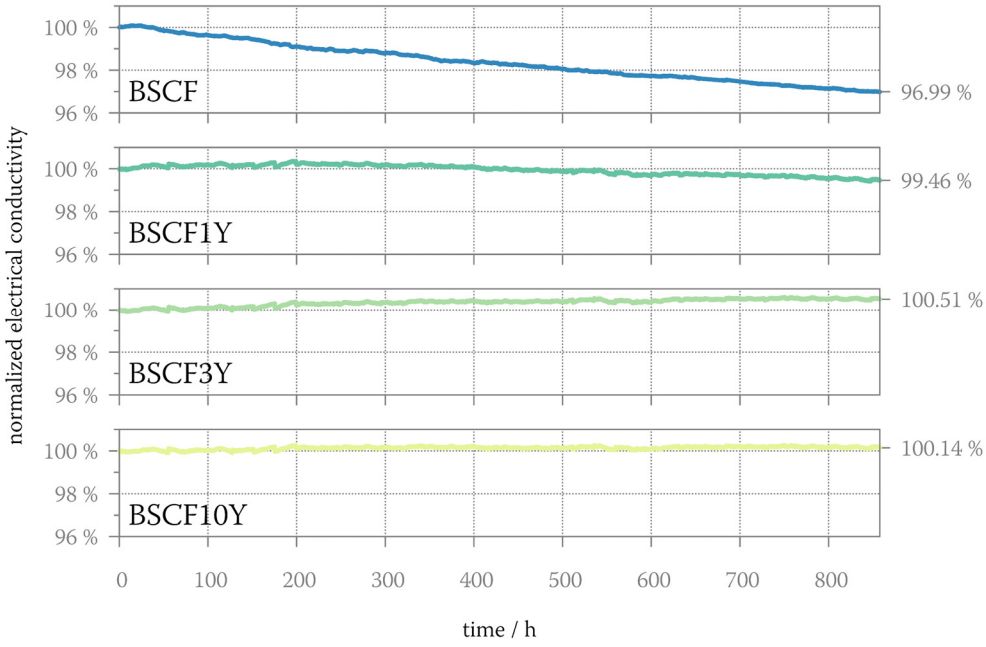

Figure 53. Electrical conductivity as a function of time for BSCF, BSCF1Y, BSCF3Y and BSCF10Y conducted at 800 °C. The measurement on Y-doped BSCF was performed by LANA UNGER. Reference data for BSCF were taken from an earlier publication by NIEDRIG ET AL. [64].

observed for undoped BSCF [78]. Hence, the stability of the cubic phase can be considered higher in low oxygen partial pressure environments. This is understandable because a low oxygen partial pressure leads to a higher concentration of oxygen vacancies and, therefore, to a lower Co-oxidation state which stabilizes the cubic phase. However, since the oxygen partial pressure during annealing experiments is closer to the condition on the feed side than on the permeate side, there might be other parameters influencing the secondary phase formation behavior in BSCF10Y, e.g. cation demixing phenomena due to the chemical potential gradient.

Electrical conductivity measurements on Y-doped BSCF samples were performed by LANA UNGER (IAM-WET, KIT) over a period of ~850 h at 800 °C using the four probe method. Additional information about the experimental setup can be found in a previous publication by NIEDRIG ET AL. [64] dealing with undoped BSCF. It is noted that this method determines the total electrical conductivity consisting of an electronic and ionic component. The measured total conductivity decreases with increasing Y concentration. This agrees with the results described in the PhD thesis of PATRICK HAWORTH [114]. He argued that the reduction of the total electrical conductivity in

BSCF10Y compared to BSCF is mainly due to the reduction of the electronic component.

The total electrical conductivity is presented in Figure 53. For better comparability, the individual curves were normalized to one at the beginning of the experiment. In electrical conductivity experiments, the formation of secondary phases can be well monitored because the presence of secondary phases affects the electron movement. However, only a qualitative assessment can be made because the relation between electrical conductivity and the newly formed phase is usually quite complex. For BSCF there is a strong decrease of the electrical conductivity which is attributed to the formation of the numerous secondary phases as described earlier. A much smaller decrease is observed for BSCF1Y which is consistent with the reduced content of secondary phases. For BSCF3Y the total conductivity slowly increases with time. According to the microstructural investigations, BSCF3Y only contains the hexagonal phase suggesting that the hexagonal phase is responsible for the higher electrical conductivity. It was shown that the electrical conductivity of $Ba_{0.5}Sr_{0.5}Co_xFe_{1-x}O_{3-\delta}$ increases with increasing Co content between 700 and 1000 °C [224,225]. Hence, it is reasonable to assume that the hexagonal phase with its extraordinary high Co content possesses a higher electrical conductivity than the cubic BSCF phase. Compared to BSCF3Y, BSCF and BSCF1Y also contain plate-like and Co_xO_y phases. Since the plate-like phase is characterized by a stacking sequence of various secondary phases, the large number of interfaces could induce an additional resistivity leading to a decrease in electrical conductivity. The electrical conductivity in BSCF10Y is very stable compared to all other samples. After more than 850 h the total electrical conductivity is close to the initial conductivity with a negligible increase of 0.14 %. This confirms the microstructural investigations which showed no (T = 800 °C) or only a negligible amount of the hexagonal phase (T < 800 °C). This clearly underlines the effects of the improved stability of the cubic BSCF phase for Y-doped BSCF.

5.3 Impact of fabrication parameters on secondary phase formation in BSCF

Material properties and performance of MIEC membranes are not only dictated by their intended chemical composition but also by fabrication parameters. Considerable attention has been paid to the relation between grain-size and oxygen permeability. Many researchers reported that large grain sizes in BSCF are highly beneficial to the achievable oxygen conductivity [226–229] whereas others stated that there is no correlation [81,230] or only mild improvements to a certain threshold value [231]. A common denominator in these studies is the focus on short-term impact. The following subchapter focuses on the long-time impact of the grain size in the intermediate-temperature regime (760 °C) where various secondary phases are expected. The formation of secondary phases is related to the change of oxygen diffusivity by combining microstructure analysis and electrical conductivity relaxation experiments.

Another aspect of fabrication is the unintended deviation of material stoichiometry. Intended deviations of A/B-cation ratios, investigated by GE ET AL. [232,233] and ZHOU ET AL. [234], showed enhanced oxygen permeability for small A-site deficiencies up to 6 at% whereas B-site deficiency mainly lowers oxygen permeation. However, A-site deficiency did reduce the long-time stability at 850 °C [232]. All studies were conducted above the critical temperature where secondary phase formation is not expected. To extend the understanding of deviations in the A/B-cation ratio, samples with 5 at% A-cation deficiency/excess were fabricated and heat treated at 750 °C. The results of this study are presented in the second part of this subchapter.

5.3.1 Grain size dependence of secondary phase formation

The effect of grain size was investigated to characterize the influence of certain fabrication parameters on the degradation behavior of the cubic perovskite phase. BSCF and BSCF10Y samples were investigated by LUKAS GRÜNEWALD [235] within the framework of his Bachelor thesis. In order to correlate the relation between grain size and secondary phases, the grain size of the as-sintered samples was determined by utilizing electron channeling in SEM. Hereby, backscattered electron (BSE) images of polished sample cross-sections were analyzed to derive grain-size information using image analysis technique. The annular BSE semiconductor detector mounted below the objective pole piece of the FEI ESEM microscope was used for electron detection. Best results were obtained for electron energies between 10 and 12 keV which were

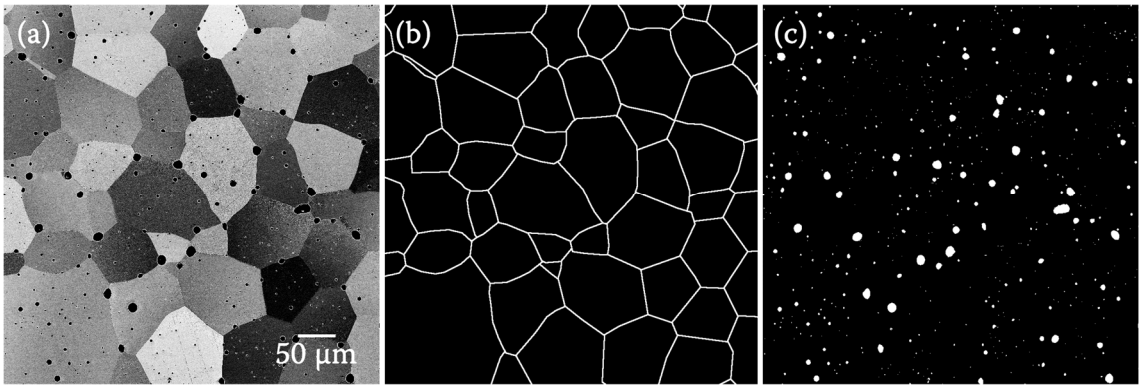

Figure 54. (a) Representative 12 keV BSE SEM image acquired using the backscattered electron detector. Intensity variations are caused by dynamical electron scattering due to different grain orientations. Processed image of (b) grain boundaries (white) and (c) pores (white) which was used as input for grain-size determination.

employed throughout the experiment. To increase the accuracy, grain boundaries were redrawn manually where necessary. It is noted that these 2D methods underestimate the grain size, as some grain intersections will not reflect the real grain size especially if grains are cut close to their tip. However, a comparative study on cubic zirconia with grain sizes derived from 2D and 3D data did only show minor discrepancies that can also be attributed to experimental uncertainties [237]. Hence, in most studies, grain sizes from 2D data can be considered sufficiently accurate – taking into account the high complexity and costs for 3D methods. To estimate sample porosity, the image histogram was adjusted to separate pores from the rest of the image. A representative BSE SEM image with the processed grain boundary map and corresponding porosity image is depicted in Figure 54. The grain surface area A of individual grains and porosity were analyzed using ImageJ [236]. To get good statistics, at least 300 grains were evaluated. Log-normal grain size distributions were assumed and fitted to equivalent diameter ($d = 2\sqrt{A/\pi}$) distributions using least square fitting routines. The probability density function of the log-normal distribution is given in Equation 33.

$$f(d) = \frac{1}{\sqrt{2\pi}\sigma d}\exp\left(-\frac{[ln(d) - \mu]^2}{2\sigma^2}\right) \tag{33}$$

Hereby μ denotes the mean value and σ the standard deviation, which are considered fitting parameters for the grain size distribution histograms. As the mode $d_0 = \exp(\mu - \sigma^2)$ (highest point in the distribution) gives the most probable grain size, this value will be regarded as the sample grain size in the following.

To obtain samples with different grain sizes, the sintering temperature and sintering time were varied, and the specimens were characterized by the method described above. The resulting grain sizes are depicted in Figure 55(a,b). The fitting parameters are summarized in Appendix 8.2. Note, that samples fabricated at the KIT (IAM-WET) and University of Twente are treated separately due to the difference in fabrication procedure and annealing parameters. For more information on sample fabrication, the reader is referred to the sample preparation paragraph at the beginning of Chapter 5. To avoid confusion within this chapter, the samples from the University of Twente are labeled with an asterisk. An overview of the investigated samples and their fabrication parameters including the origin of raw powders, sintering temperature T_s, sintering time t_s and grain size d_0 is given in Table 8. BSCF was not sintered beyond 1170 °C since there was some evidence for melting at higher temperatures. This agrees with

sample	powder	sintering condition		grain size
		T_s [°C]	t_s [h]	d_0 [µm]
BSCF-1050	IAM-WET	1050	2	6.1 ± 0.3
BSCF-1070	IAM-WET	1070	2	9.2 ± 0.3
BSCF-1120	IAM-WET	1120	2	13.9 ± 0.3
BSCF-1170	IAM-WET	1170	2	60.9 ± 2.1
BSCF10Y-1070	IAM-WET	1070	2	3.1 ± 0.3
BSCF10Y-1120	IAM-WET	1120	2	5.1 ± 0.3
BSCF10Y-1170	IAM-WET	1170	2	10.8 ± 0.8
BSCF10Y-1220	IAM-WET	1220	2	26.1 ± 1.0
BSCF*-950	Twente	950	3	3.3 ± 0.2
BSCF*-1050	Twente	1050	3	11.4 ± 0.4
BSCF*-1150	Twente	1150	24	82.3 ± 1.6
BSCF3Zr*-950	Twente	950	3	2.4 ± 0.1
BSCF3Zr*-1050	Twente	1050	3	9.0 ± 0.3
BSCF3Zr*-1150	Twente	1150	24	59.6 ± 1.3

Table 8. Sample denotation, fabrication parameters and resulting grain sizes.

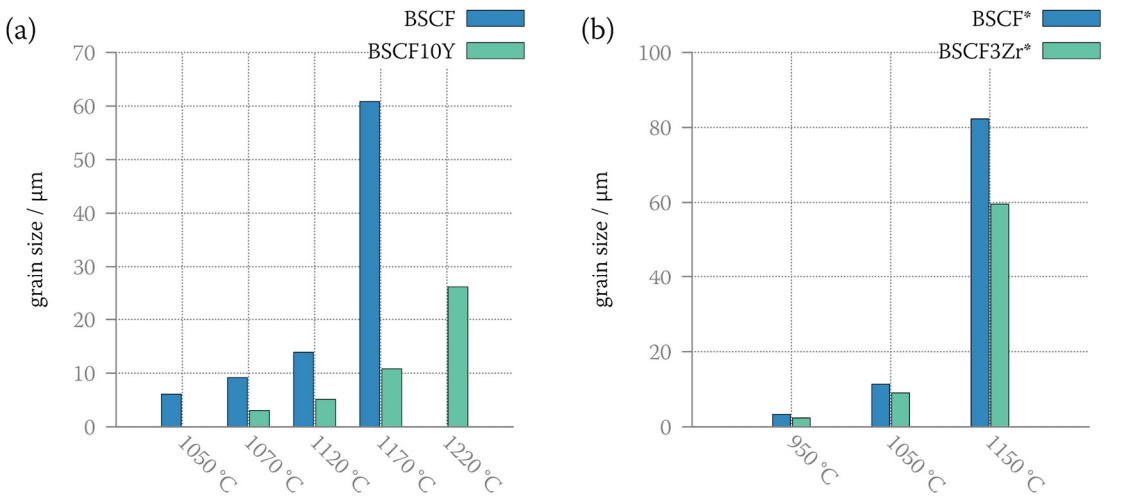

Figure 55. Grain sizes as a function of sintering temperature for samples fabricated at the (a) KIT (IAM-WET) or (b) the University of Twente. Additional sintering parameters are summarized in Table 8.

results obtained by BAUMANN ET AL. [81] who reported incongruent melting for BSCF at 1150 °C. As BSCF10Y did not show any signs of melting it is safe to assume that BSCF10Y has a higher melting point compared to BSCF.

As expected, a higher sintering temperature yields a larger grain size with an almost exponential dependence on temperature. Comparing BSCF with BSCF10Y and BSCF*

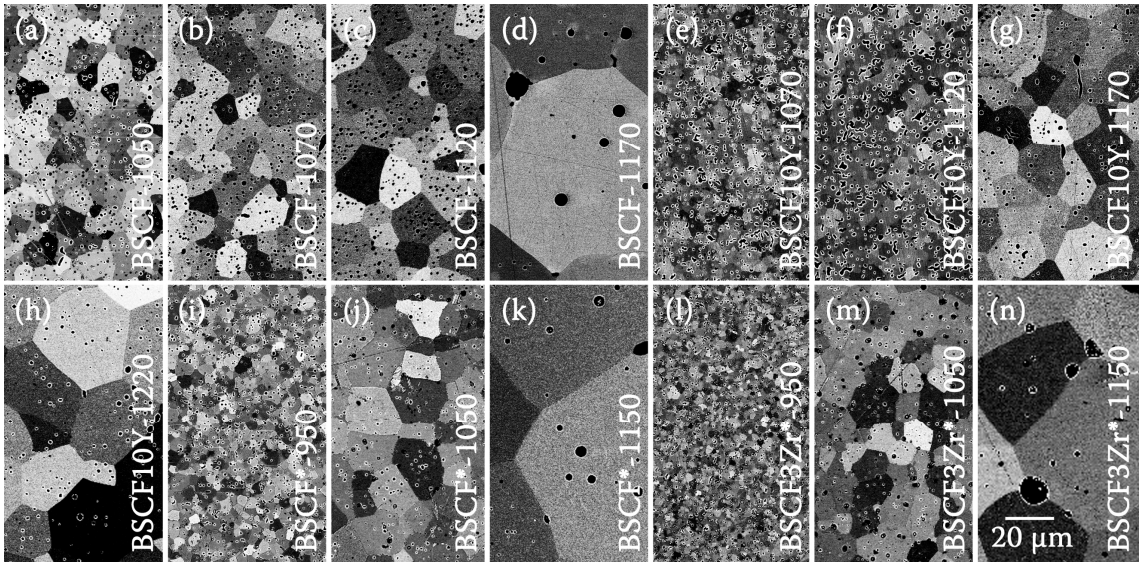

Figure 56. 12 keV BSE SEM images of as-sintered (a) BSCF-1050, (b) BSCF-1070, (c) BSCF-1120, (d) BSCF1170, (e) BSCF10Y-1070, (f) BSCF10Y-1120, (g) BSCF10Y-1170, (h) BSCF10Y-1220, (i) BSCF*-950, (j) BSCF*-1050, (k) BSCF*-1150, (l) BSCF3Zr*-950, (m) BSCF3Zr*-1050 and (n) BSCF3Zr*-1150. Note that the three- or four-digit numbers in the sample name refer to the sintering temperature.

with BSCF3Zr*, the sinter activity seems to be reduced by both dopants Zr and Y. 10 at% Y doping leads to an average grain size reduction of ~70 % whereas 3 at% Zr doping results in a grain size decrease of ~25 % compared to BSCF and BSCF*, respectively. The porosity of all samples was in the range between 2 and 5 %. BSE SEM images of the as-sintered samples are shown in Figure 56. Abnormal grain growth was not observed in any of the samples within this series. However, SUSANNE WACHS [238] presented in her Bachelor thesis evidence for abnormal grain growth in Zr-doped BSCF for samples sintered for 120 h at 1100 °C. Since the sintering time employed here is considerably shorter, abnormal grain growth might not be pronounced and, therefore, not observable. Ideal kinetic grain growth can be described by Equation 34 with d_m^n, $d_{m,0}^n$ being the final and initial grain size, K_0 some constant, R the gas constant, Q the activation energy for grain growth, n the kinetic grain growth exponent and t_s, T_s the sintering time and temperature.

$$d_m^n - d_{m,0}^n = K_0 \exp\left(-\frac{Q}{RT_s}\right) t_s \tag{34}$$

The kinetic grain growth exponent for BSCF was reported to be close to 3 [231,239]. The initial grain size is believed to be in the range of the powder particle size. It was assumed that the initial grain size was approximately 2 µm, which corresponds to the D_{50}-value of the powder. Using linear regression, the grain-growth activation energy yields (857 ± 52) kJ/mol (BSCF), (750 ± 45) kJ/mol (BSCF10Y), (480 ± 27) kJ/mol (BSCF*) and (615 ± 44) kJ/mol (BSCF3Zr*). However, by closely observing the fit for BSCF, the highest sintering temperature point (1170 °C) seems to be much higher than expected by the extrapolation of the lower-temperature data points. This is related to the huge jump in grain size between 1120 and 1170 °C. According to BAUMANN ET AL. [81] liquid phases start to appear in BSCF at a temperature of about 1150 °C. Hence, sintering at 1170 °C might already be in the liquid sintering regime where the activation energy for grain growth might differ considerably. By neglecting the highest sintering temperature point, the activation energy for grain growth drops down to (512 ± 41) kJ/mol (BSCF) which is quite close to the value obtained for BSCF*. Additionally, the determined values are close to the values reported elsewhere which are between 372 and 740 kJ/mol [81,228,230,239]. The huge spread among different publications already suggests that there are other factors (e.g. impurities, deviation in stoichiometry) which influence the grain-growth characteristics in BSCF. Considering the dopants Zr and Y, the activation energy for grain growth increases in both cases with a much stronger increase for Y.

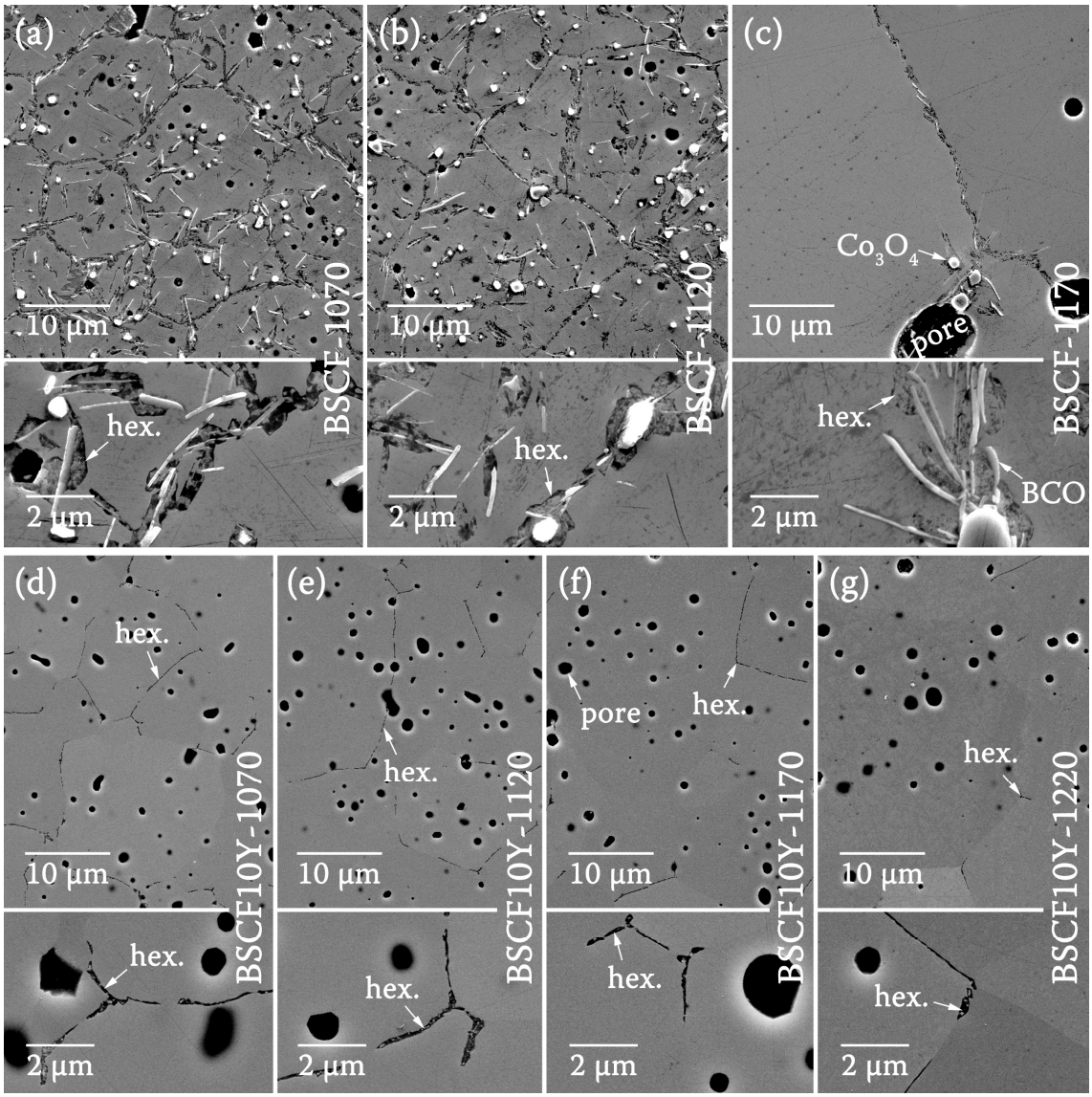

Figure 57. 15 keV SE SEM images showing secondary phase formation after long time annealing (21 days at 750 °C) for (a) BSCF-1070, (b) BSCF-1120, (c) BSCF-1170, (d) BSCF10Y-1070, (e) BSCF10Y-1120, (f) BSCF10Y-1170 and (g) BSCF10Y-1220.

Dopants like Y and Zr are known for their inhibiting effect on grain growth [106,240–244]. RAVKINA ET AL. [106] reported Zr-rich crystallites close to grain boundaries in Zr-doped BSCF which might slow down grain growth due to the solute drag effect. Solute drag effects were also reported for the related compound $BaZrO_3$ where SHIRPOUR ET AL. [242] reported Y enrichments at grain boundaries for 6 at% Y-doping. However, dopant segregation at grain boundaries was not detected using EDXS in the investigated samples. Nevertheless, an increased dopant concentration at grain boundaries may still exist considering the detection limit of EDXS. It is also possible that solute atoms already separate from the grain boundary in the early stages

of sintering. Another effect to consider is the Zener pinning of grain boundaries on CoO or BCO precipitates in BSCF, BSCF* and BSCF3Zr*. As BCO and CoO phases are suppressed in BSCF10Y, pinning effects are not expected there. Depending on when CoO precipitates form during the sintering process, this might affect the grain growth characteristics and also the activation energy for grain growth.

Long-time annealing of BSCF and BSCF10Y

BSCF-1070, BSCF-1120, BSCF-1170, BSCF10Y-1070, BSCF10Y-1120, BSCF10Y-1170 and BSCF10Y-1220 were annealed at 750 °C for 21 days in ambient air to simulate the effect of aging. To minimize systematic errors all samples were annealed in the same oven. Annealed samples were polished and etched using the procedure described in Chapter 5.1 which yields characteristic topographies for secondary phases in BSCF. SE SEM images showing the secondary bulk phases of annealed samples are depicted in Figure 57. A high concentration of secondary phases can be seen in undoped BSCF (cf. Figure 57(a-c)) which consist of the hexagonal phase, the plate-like phase, and Co_3O_4 precipitates. In contrast, no secondary phases besides the hexagonal phase are present in any of the BSCF10Y (cf. Figure 57(d-g)) samples. Similar to the results reported earlier, the hexagonal phase decorates grain boundaries, plate-like and Co_3O_4 precipitates in undoped BSCF. Since many plate-like precipitates do not grow parallel to grain boundaries, the decoration of plate-like phases by the hexagonal phase is accompanied by a considerable spread of the hexagonal phase into the grain interior especially in samples with small grain sizes. According to the SE SEM image (cf. Figure 57(a,b)), the Co_3O_4 precipitates are randomly distributed in the BSCF-1070 and BSCF-1120 sample. However, as the image only represent a 2D section of the sample it cannot be ruled out that Co_3O_4 precipitates are close to grain boundaries above or below the investigated slice. For BSCF-1170 (cf. Figure 57(c)), precipitates predominantly reside close to grain boundaries. Judging by the images, the size of Co_3O_4 precipitates seems to considerably increase accompanied by a decrease in number density which reduces the effective area for secondary phase nucleation for higher sintering temperatures. Considering the different grain sizes, the samples with the largest grain size shows the lowest content of secondary phases in both BSCF and BSCF10Y. This is most obvious between (b) BSCF-1120 and (c) BSCF-1170 where the grain size increased by a factor of nearly 4 from 13.9 to 60.9 µm. For BSCF10Y (cf. Figure 57(d-g)), secondary phases are restricted solely to grain boundaries which are decorated by the hexagonal phase because Co_3O_4 and plate-like precipitates are absent.

To characterize secondary phase formation quantitatively, the image contrast of numerous SEM images was evaluated by image analysis techniques as described in Chapter 5.1. Quantification of a statistically relevant area yields a secondary phase volume fraction of (28.0 ± 3.2) vol% for BSCF-1070, (18.7 ± 2.8) vol% for BSCF-1120 and (3.8 ± 1.1) vol% for BSCF-1170. The biggest share in secondary phase volume fraction can be attributed to the hexagonal phase with only minor amounts of plate-like and Co_3O_4 phases. Even though the volume fraction of secondary phases in BSCF10Y is close to zero a similar trend was observed with (0.77 ± 0.08) vol% for BSCF10Y-1070, (0.54 ± 0.05) vol% for BSCF10Y-1120, (0.25 ± 0.04) vol% for BSCF10Y-1170 and (0.13 ± 0.02) vol% for BSCF10Y-1220. Both trends are fairly linear with sintering temperature even though the relative changes are much stronger for BSCF with a slope of -0.242 $\frac{\text{vol\%}}{°C}$ compared to -0.004 $\frac{\text{vol\%}}{°C}$ for BSCF10Y. Hence, it can be assumed that samples with a higher tendency towards secondary phase formation like BSCF benefit most by increasing the sintering temperature.

Long-time annealing of BSCF and BSCF3Zr**

In order to characterize the interdependence between grain size, oxygen diffusivity and secondary phase formation a combined investigation involving in-situ conductivity relaxation and ex-situ electron microscopy investigations were conducted. In-situ conductivity relaxation experiments were performed to characterize the evolution of oxygen diffusion parameters in BSCF* and BSCF3Zr*. In these experiments, the partial oxygen pressure is abruptly changed from 0.33 to 1 atm (oxidation) and from 1 atm to 0.33 atm (reduction). The samples respond by incorporating or removing oxygen from the perovskite lattice which can be monitored by measuring the evolution of the electrical conductivity. The obtained electrical relaxation curves contain information about the chemical diffusion coefficient D_{chem} and/or the surface exchange coefficient k_{chem} depending on which transport mechanism is the limiting factor for oxygen diffusion [13]. The electrical conductivity was measured by the four probe DC method. Experiments were performed by SAIM SAHER [245]. D_{chem} and k_{chem} values were successively measured over a period of 312 h at a temperature of 700 °C where pronounced secondary phase formation is expected.

The measured logarithmic D_{chem} and k_{chem} values as a function of annealing time are presented in Figure 58 for (a,c) BSCF* and (b,d) BSCF3Zr*. The values obtained from oxidation steps are usually higher compared to D_{chem} or k_{chem} values from reduction steps which is widely reported among literature [104,246–249]. This phenomenon was

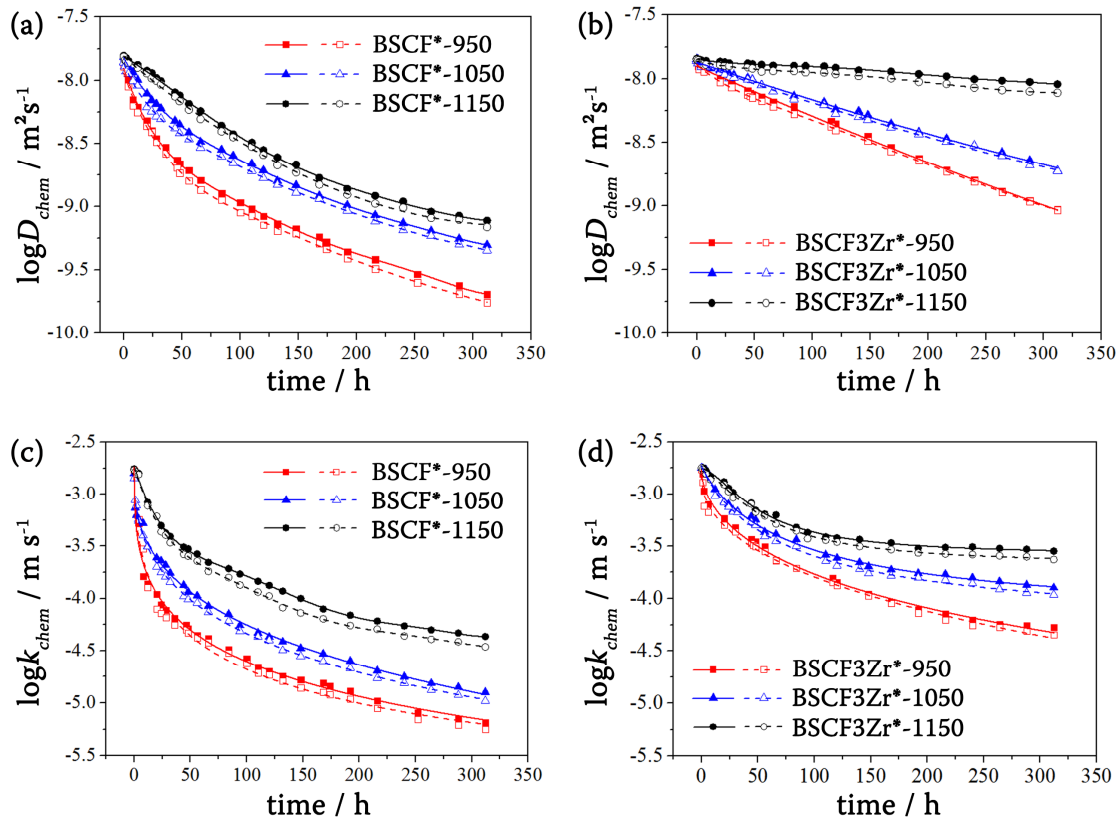

Figure 58. Results from in-situ long time conductivity relaxation experiments for (a,c) BSCF* and (b,d) BSCF3Zr* with (a,b) $\log D_{chem}$ and (c,d) $\log k_{chem}$ as a function of annealing time. Oxidation steps (0.33 to 1.0 atm p_{O_2}) are represented by closed symbols whereas open symbols correspond to reduction steps (1.0 to 0.33 atm p_{O_2}). Experiments were performed by SAIM SAHER [245] within a collaborative framework.

attributed to nonlinearities regarding the oxygen transport characteristics [249]. As seen in Figure 58(a-d) k_{chem} and D_{chem} values decrease over time in all samples. For BSCF3Zr*, the decrease is significantly lower compared to undoped BSCF* samples sintered at the same temperature. Hence, Zr-doping can be considered to have a beneficial effect regarding the decomposition of the cubic BSCF phase. Interestingly, $\log D_{chem}$ of BSCF3Zr* decreases linearly whereas essentially all other plots show a stronger decline of $\log D_{chem}$ or $\log k_{chem}$ within the first 100 hours. Comparing samples with the same stoichiometry, a higher sintering temperature and, therefore, larger grain size reduces the degradation of k_{chem} and D_{chem} significantly. Another interesting point is that BSCF3Zr*-1150 does not show any further reduction for k_{chem} after ~150 hours which indicates that an equilibrium state is reached. The slower degradation for Zr-doped BSCF was also found by RAVKINA ET AL. [106] in an oxygen

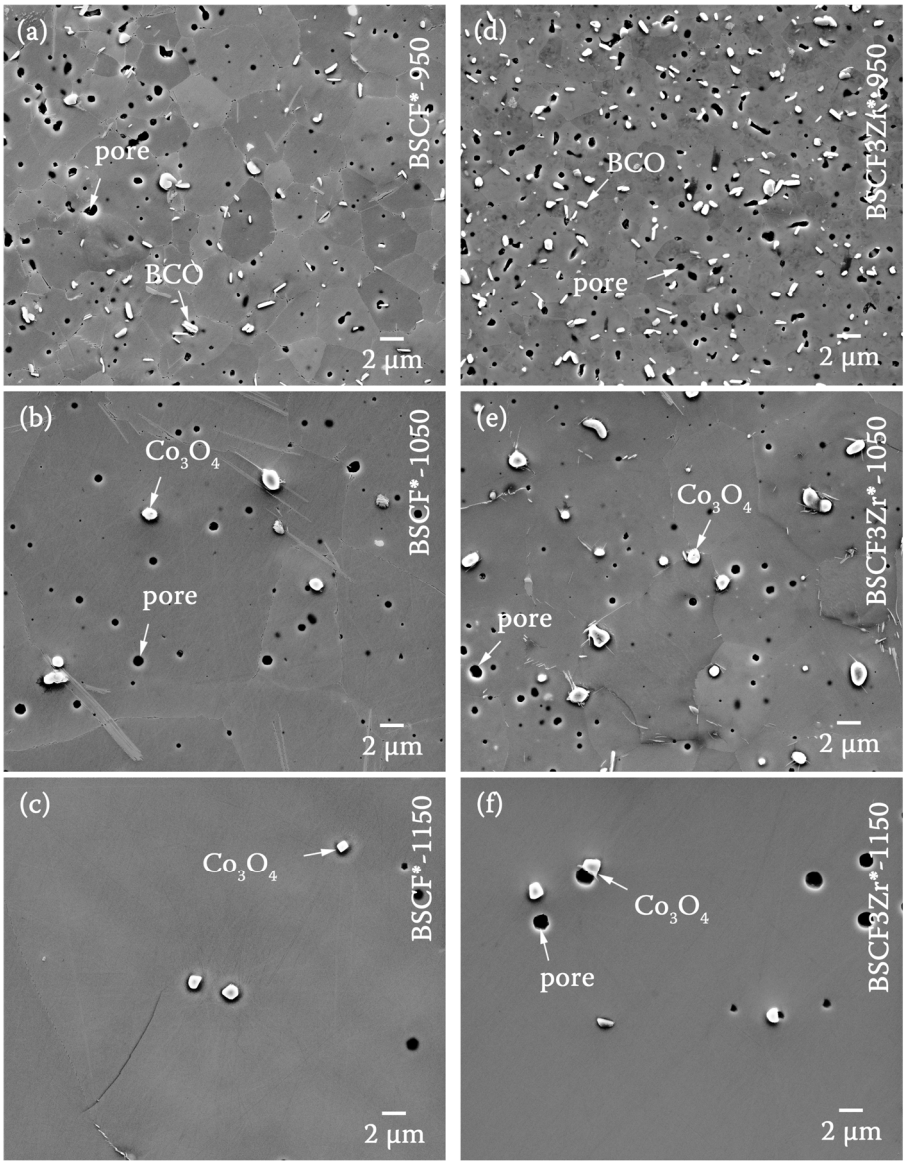

Figure 59. 12 keV SE SEM images of as-sintered (a-c) BSCF* and (d-f) BSCF3Zr* sintered at (a,d) 950 °C, (b,e) 1050 °C and (c,f) 1150 °C.

permeation experiment setup at 750 °C. Beneficial effects are even more pronounced for higher Zr concentrations. However, the very small solubility limit of Zr ions in BSCF leads to the formation of $SrZrO_3$ or $BaZrO_3$ phases if dopant concentration is increased up to 5 at% [104,106]. Contrary to Y doping, multisite occupation of Zr is not expected as the ionic radius of Zr (72 pm [216]) is slightly smaller compared to that of Sc (74.5 pm) where measurements showed exclusive B-site occupation (cf. Chapter 4.3).

To characterize the secondary phase formation, samples were investigated before and after the conductivity relaxation measurement. SE SEM images of the bulk interior of as-sintered samples are presented in Figure 59. Some precipitates are labeled to guide the reader. Since the samples were slowly cooled down to room temperature, a small

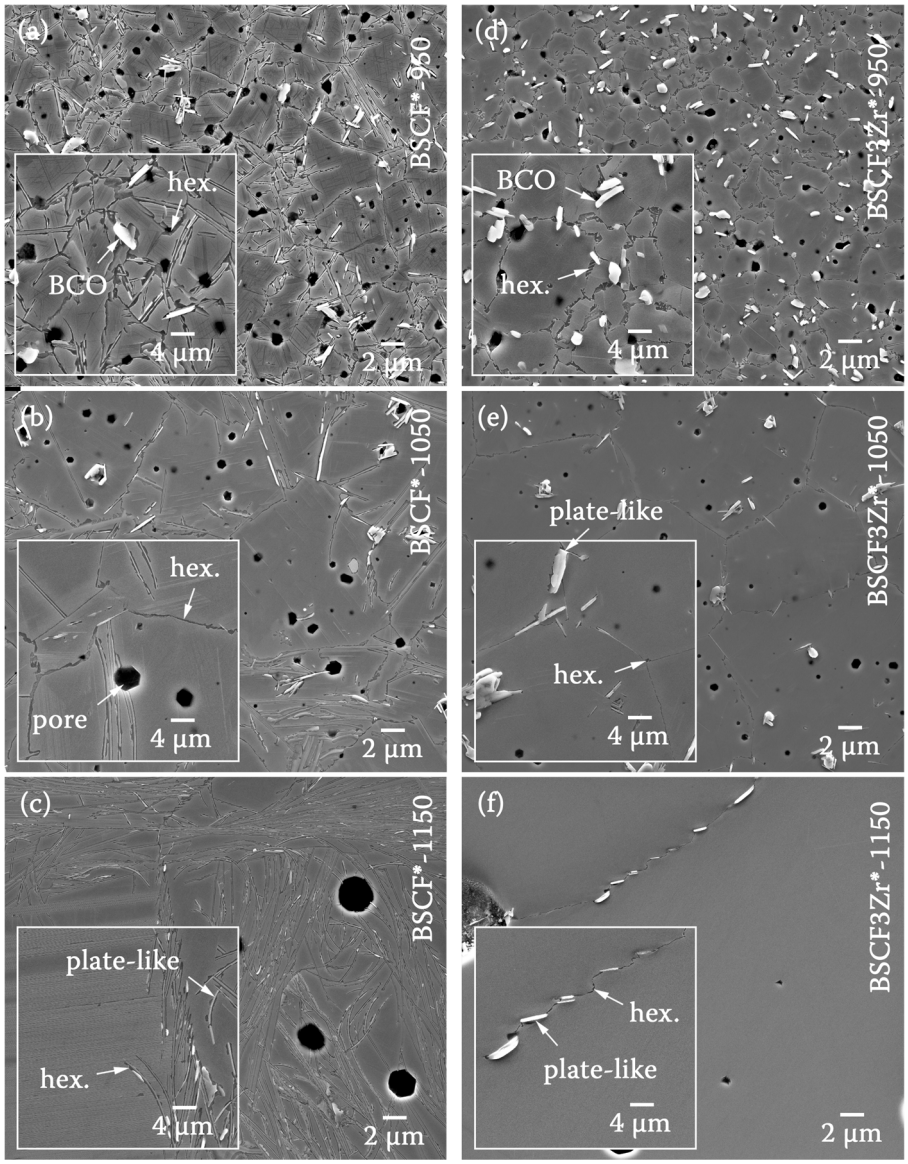

Figure 60. 12 keV SE SEM images of (a-c) BSCF* and (d-f) BSCF3Zr* after conductivity relaxation measurements (312 h) performed at 700 °C. Samples were sintered at (a,d) 950 °C, (b,e) 1050 °C and (c,f) 1150 °C.

content of the hexagonal and plate-like phase is present in all the images. Samples sintered at 1050 and 1150 °C show the precipitation of Co_3O_4 phases. As elaborated previously, this phase can be considered as a byproduct of the sintering process because BSCF tends towards a lower Co content (cf. Chapter 5.1, 5.2). Interestingly, the images suggest a reduction of Co_3O_4 precipitates at the highest sintering temperature (1150 °C). Samples sintered at 950 °C contained the BCO phase instead of Co_3O_4 precipitates. This is in agreement with the assumption about the reaction between Co and Ba in the temperature range between 800 and 950 °C (cf. Chapter 5.1.1). Given that the samples were sintered for only 3 hours, the formation kinetics of the BCO phase must be fast

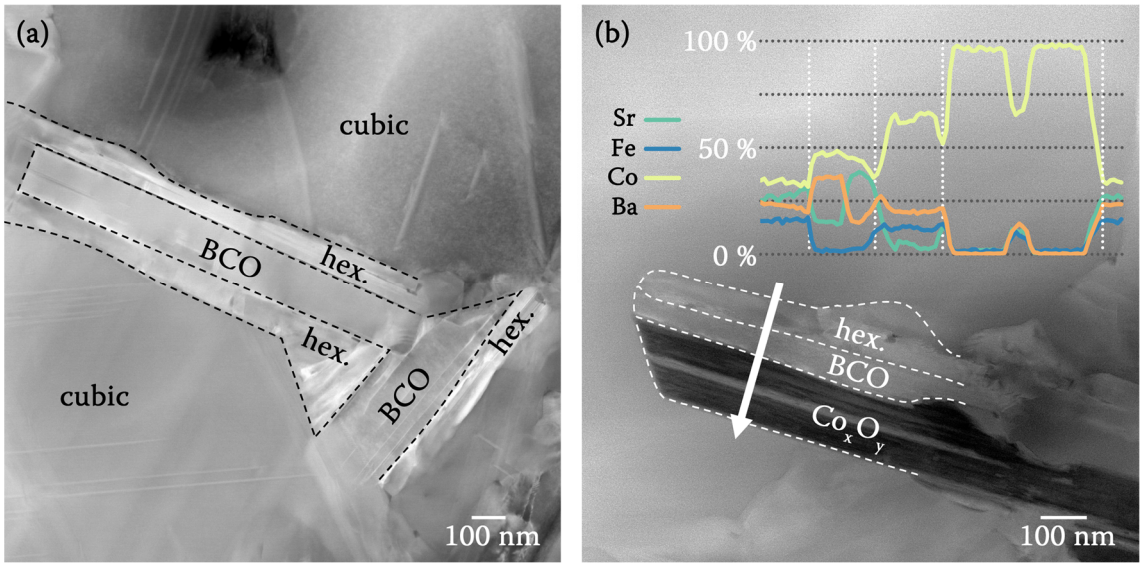

Figure 61. HAADF-STEM images showing secondary phase formation in BSCF3Zr*-950 with (a) BCO precipitates at grain boundaries and (b) a yet unreported lamellar Co_xO_y phase. A cation composition profile along the white arrow is inserted in the image. Some boundaries between different phases are marked with dashed lines.

which was also reported by MÜLLER ET AL. [76]. Interestingly, the content of either Co_3O_4 or BCO precipitates seems to be lower for BSCF* compared to BSCF3Zr* when sintered at 950 and 1050 °C. Many BCO and Co_3O_4 precipitates are found close to grain boundaries or pores which suggest that Co can be solely expelled from the cubic lattice there. Higher sintering temperatures would lead to fast grain growth and quick densification preventing Co outdiffusion. This could explain why the Co_xO_y formation is less pronounced in samples sintered at higher temperatures. However, it is also possible that the composition range where the cubic phase can be considered stable increases.

Representative SE SEM image of the samples after conductivity relaxation experiments are presented in Figure 60. Considering the volume fraction of secondary phases, a significant decrease is obvious by the comparison of BSCF*-950 and BSCF*-1050 as well as BSCF3Zr*-950 and BSCF3Zr*-1150. The significant reduction of secondary phases is most likely responsible for the slower decrease of D_{chem} and k_{chem} which is especially apparent for samples sintered at higher temperatures. Grain boundaries are decorated with the hexagonal phase in all samples which contributes to the reduction of D_{chem}. As the grain size and, therefore, grain boundary area decreases with increasing sintering temperature, the content of the hexagonal phase at the grain boundary also decreases which can be considered as one reason for the improvement of the sample properties

after high-temperature sintering. Hardly any secondary phases have formed in BSCF3Zr*-1150 (cf. Figure 60(f)). Only a thin hexagonal-phase film at grain boundaries and occasional formation of plate-like precipitates are observed. TEM reveals that the grain interior consists exclusively of the cubic BSCF phase in BSCF3Zr*. However, BSCF*-1150 (cf. Figure 60(c)) contains a high concentration of lamellar plate-like precipitates which is unexpected because this sample shows the lowest drop in D_{chem} and k_{chem} among all BSCF* samples (cf. Figure 58). Hence, there might be some other still unknown parameters that can positively affect $\log D_{chem}$ and $\log k_{chem}$.

By comparing BSCF* and BSCF3Zr* (cf. Figure 60) a noticeable reduction of the secondary phase content is obvious for BSCF3Zr* especially at the highest sintering temperature (1150 °C). This can be attributed to the fact that large plate-like precipitates crossing whole grains are less pronounced in BSCF3Zr* compared to BSCF*. A detailed TEM investigation revealed that plate-like precipitates in BSCF3Zr*-950 are mostly composed of the BCO phase surrounded by the hexagonal phase. A representative HAADF-STEM is depicted in Figure 61(a). Lamellae consisting of different phases are marked by dashed lines. The BCO phase can be considered as a remnant from the sintering process because it is already present in the as-prepared specimen. It is believed to originate from the reaction of Co with Ba between 800 and 950 °C as mentioned earlier. Therefore, the BCO phase solely contributes in the form of additional nucleation sites for the hexagonal phase. Since as-sintered BSCF3Zr*-1050 and BSCF3Zr*-1150 contain less BCO/Co_3O_4 type phases, fewer nucleation sites for the hexagonal phase are present which explains the reduced content of the hexagonal phase and, therefore, the reduced degradation in the conductivity relaxation measurement. Additionally, the larger grain size also lowers nucleation sites due to the reduced grain boundary area.

A new rare Co-rich phase was discovered in BSCF3Zr* (cf. Figure 61(b)) which does not match with any previously mentioned secondary phase. The superimposed EDXS cation concentration profile along the arrow shows the sole presence of Co in this new phase. As EDXS spectra also contained a significant O-K peak which was higher compared to Co_3O_4 and CoO, a less stable cobalt oxide compound is assumed. It turned out that this phase is particularly sensitive to the electron beam and could not be characterized in more detail. Hence, a metastable Co_xO_y compound with high Co-oxidation state (Co^{3+}, Co^{4+}) can be assumed.

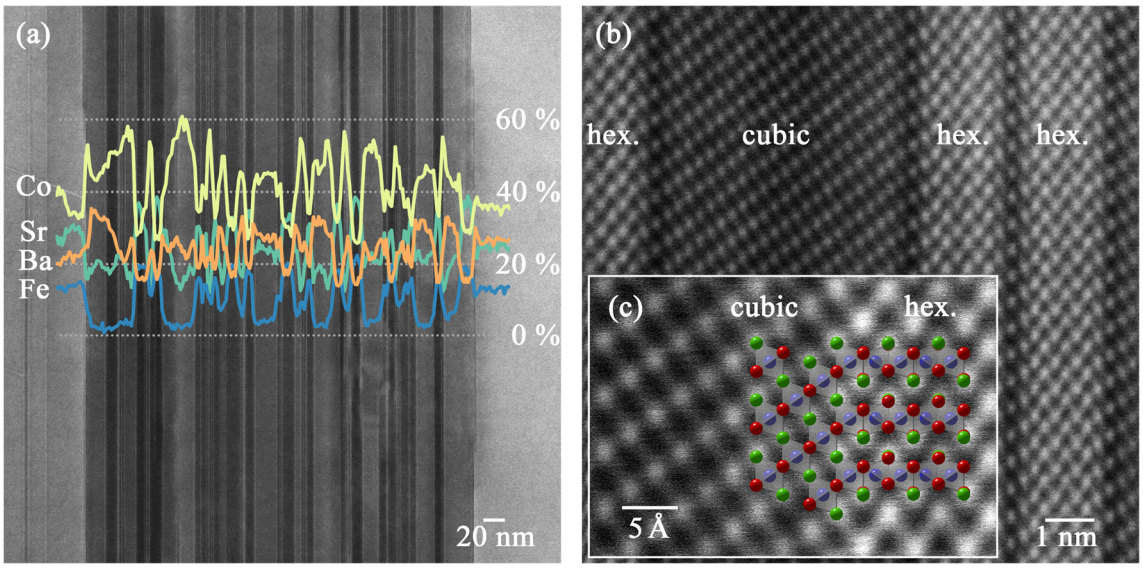

Figure 62. (a) HAADF-STEM image of a lamellar plate-like precipitate in BSCF*-1150. The concentration of cations (in at%) perpendicular to the lamella is superimposed in the image. (b) High-resolution HAADF-STEM image of the lamella showing multiple stackings of cubic and hexagonal layers. The image was recorded in $[110]_{cubic}$ and $[100]_{hex}$ orientation, respectively. In the magnified HAADF-STEM image (c) A-site ions (green), B-site ions (blue) and oxygen ions (red) are marked to illustrate the change in configuration of the oxygen octahedrons (grey).

BSCF* also contains another type of plate-like precipitate crossing whole grains (cf. Figure 60(a-c)). A representative HAADF-STEM image of such a phase in BSCF*-1150 is shown in Figure 62(a). The EDXS cation composition profile derived perpendicular to the lamellae is superimposed in the image. Within the image a stacking-type substructure is visible. The chemical composition clearly shows strong deviations from the expected chemical composition of the cubic phase. Regions, where the Fe content is close to zero, can be attributed to lamellae of the hexagonal phase. High-resolution HAADF-STEM images clearly confirm alternating regions of cubic and hexagonal phases as depicted in Figure 62(b). It should be mentioned that only A-site cations can be seen in the image because they scatter electrons more strongly. In the magnified HAADF-STEM image in Figure 62(c) A-site positions are accentuated by green circles. Based on the A-site cations, B-site and oxygen positions were added as blue and red circles. The projected oxygen octahedrons are highlighted in grey. The oxygen octahedron configuration changes from corner sharing (cubic) to face sharing (hexagonal) which was already reported in earlier studies [62,63,75,77,79]. Hence, the hexagonal phase nucleates on certain lattice sites leading to a specific orientation relationship towards the cubic host matrix [79]. This plate-like phase with exclusive

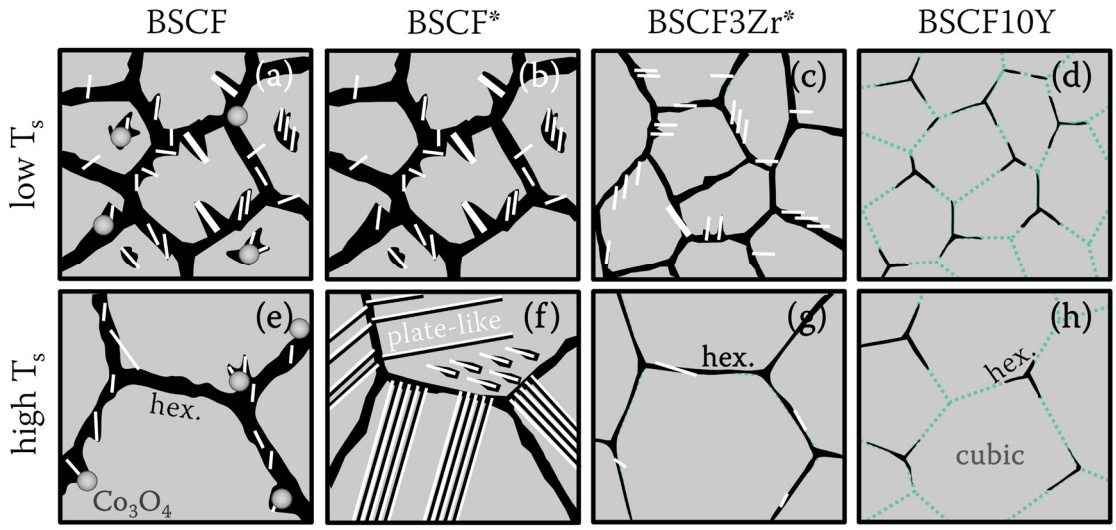

Figure 63. Simplified schemes of the investigated samples sintered at low temperature (low T_s) or high temperature (high T_s).

cubic and hexagonal stacking order (without BCO) is very pronounced in all BSCF* samples. This is considered to be one of the reason for the stronger reduction of $\log D_{chem}$ and $\log k_{chem}$ in BSCF* compared to BSCF3Zr*.

The results concerning secondary phase formation as a function of sintering temperature are summarized in Figure 63. The content of secondary phase is reduced in BSCF, BSCF3Zr* and BSCF10Y if the sintering temperature is increased. This can be attributed to the reduced concentration of nucleation sites for the hexagonal phase due to a combined reduction of grain boundary area and Co_xO_y/BCO precipitates in the as-sintered samples. It is not known, why BSCF* prepared by the spray pyrolysis technique, contains an extraordinary high number of plate-like phases with exclusive cubic and hexagonal stackings (without BCO) in contrast to BSCF fabricated by the solid-state reaction route. One possibility for the difference between BSCF and BSCF* might be connected to the fact that BSCF* was subjected to an electric current and numerous changes in oxygen partial pressure due to the experimental setup. This might affect the growth of certain secondary phases.

5.3.2 The impact of A/B cation ratio on cubic phase stability

Samples for studying the impact of A/B-cation ratio on the stability of the cubic BSCF phase were fabricated with an intended 5 % mismatch of A/B-cation ratio namely 1.05 ($(BS)_{1.05}CF$) and 0.95 ($(BS)_{0.95}CF$). To characterize the impact on secondary phase formation reference samples of BSCF and BSCF10Y were investigated, too. The same sinter parameters were used for BSCF, $(BS)_{1.05}CF$ and $(BS)_{0.95}CF$ with a sintering end temperature of 1050 °C. BSCF10Y was sintered at 1170 °C. X-ray diffractograms (XRD) of the as-calcinated powders acquired by LANA UNGER (IAM-WET, KIT) confirmed cubic symmetry for all samples. XRD data for powders are plotted in Figure 64. Small Bragg peaks for Co_xO_y and minor unidentified Bragg peaks could be observed in some of the samples. The unidentified peaks were attributed to the incomplete reaction of the precursor powder due to the low calcination temperature (900 – 970 °C). However, the Bragg peaks were not present in the compacts after the sintering process. Derived room temperature lattice parameters are 3.976 Å (BSCF), 3.999 Å (BSCF10Y), 3.984 Å ($(BS)_{0.95}CF$) and 3.991 Å ($(BS)_{1.05}CF$). All lattice parameters are similar with variations of less than 0.6 %. Grain sizes of as-sintered samples were determined with the method described previously in Chapter 5.3.1. The resulting grain size in decreasing order are (10.8 ± 0.8) µm (BSCF10Y, cf. Table 4), (6.6 ± 0.3) µm ($(BS)_{1.05}CF$), (6.1 ± 0.3) µm (BSCF) and (5.0 ± 0.4) µm ($(BS)_{0.95}CF$). Hence, the grain size increases for A-cation excess and

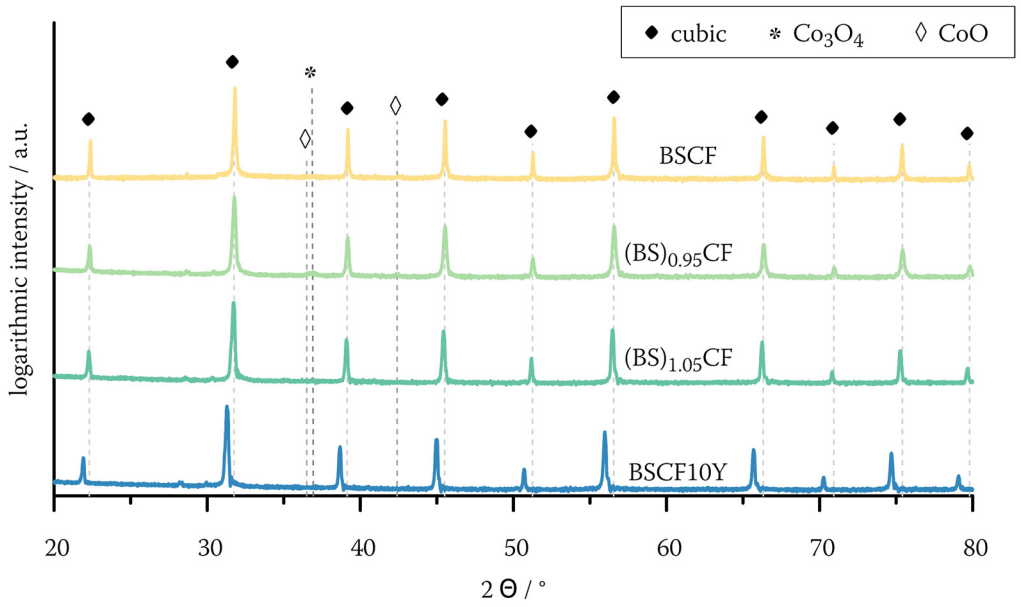

Figure 64. XRD data of as-sintered BSCF, $(BS)_{0.95}CF$, $(BS)_{1.05}CF$ and BSCF10Y. Bragg peaks for the cubic, CoO and Co_3O_4 phase are added in the graph. The data set was acquired by LANA UNGER (IAM-WET, KIT).

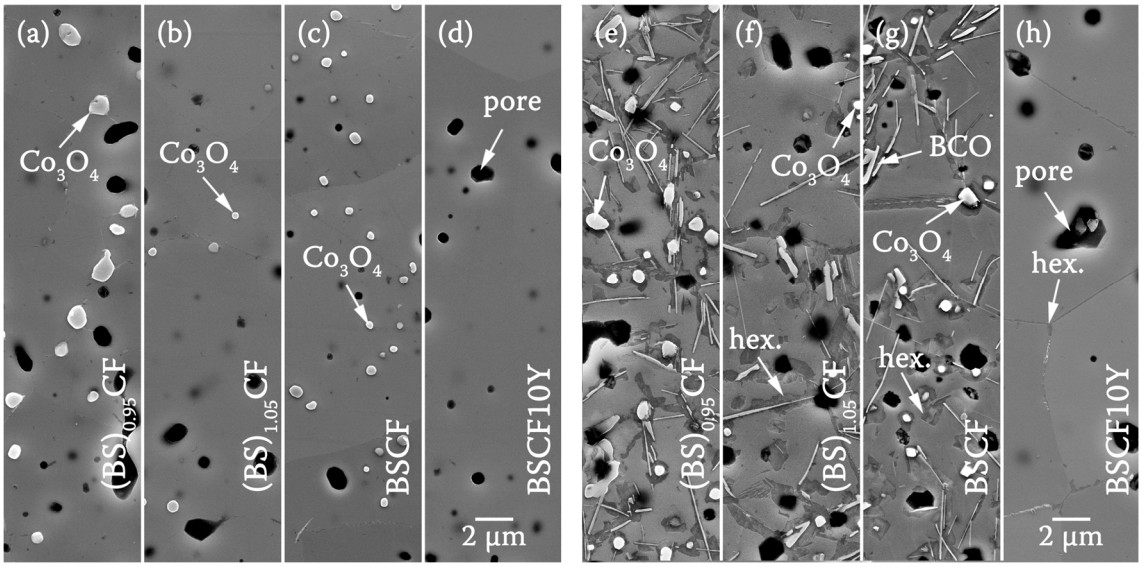

Figure 65. 20 keV SE SEM images of etches samples (a-d) before (as-sintered) and (e-h) after long-time annealing at 750 °C for 21 days. Some of the secondary phases are labeled in (a,e) $(BS)_{0.95}CF$, (b,f) $(BS)_{1.05}CF$, (c,g) BSCF and (d,h) BSCF10Y.

decreases for A-cation deficiency which, at first glance, contradicts the improved/deteriorated sinterability of A/B-site deficient BSCF reported by GE ET AL. [232,233]. However, their conclusions were derived from the shrinkage behavior of the samples which is not necessarily correlated to the final grain size. In one of their papers the crystallite size for various A-site deficient powders calcined at 1000 °C for 5 hours is mentioned [232]. Here, the crystallite size compared to BSCF first decreases for A-site deficiencies between 3 – 9 % with a considerable increase for higher deficiencies which is consistent with the samples presented in this thesis.

SEM EDXS was performed to measure the average cation stoichiometry over a large sample region to minimize contamination. As the accuracy of EDXS regarding absolute concentration with standard less methods is limited (~10 % [250]) only A/B-site ratios are given here. For BSCF10Y the mixed Y occupancy was considered in the calculation. The A/B-site ratio in descending order is 1.084 (BSCF10Y), 1.068 ($(BS)_{1.05}CF$), 1.038 (BSCF) and 0.971 ($(BS)_{0.95}CF$). These values are close to the expected values. The A/B-site ratios of BSCF10Y and $(BS)_{1.05}CF$ are similar which can be explained by the A-site occupation of Y in BSCF10Y. As outlined in Chapter 4.3, 25 % of the Y atoms are located on the A-site of the perovskite even though B-site doping was intended. If an A/B-site ratio of 1.0 is assumed for undoped BSCF, 2.5 at% more / less Y on the A-site / B-site in BSCF10Y leads to an A/B-site ratio of $\frac{100+2.5}{100-2.5} \approx 1.05$. This ratio is identical to the nominal A/B-site ratio of $(BS)_{1.05}CF$.

Etched as-sintered samples show numerous round precipitates in BSCF, $(BS)_{1.05}CF$, $(BS)_{0.95}CF$ as depicted in Figure 65(a-c). Precipitation of secondary phases is highly pronounced for A-cation deficient BSCF ($(BS)_{0.95}CF$) in both density and precipitate size. Significant lower amounts of precipitates are visible in BSCF and $(BS)_{1.05}CF$. On the contrary, as-sintered BSCF10Y does not show any signs of secondary phases (cf. Figure 65(d)). The precipitates can be attributed to Co_3O_4 due to the slow cool down to room temperature after sintering. TEM analysis confirmed spinel Co_3O_4 (space group: $Fd\bar{3}m$) as reported earlier in this thesis. Co_3O_4 precipitate formation was also reported by GE ET AL. [232], however, only for samples with high A-site deficiencies (≥ 20 at%). This can be attributed to the inability of XRD to detect minor amounts of secondary phases especially if the SNR is low. This also explains why there are only few reports in literature about secondary phases with low volume fraction as most groups solely rely of XRD to check phase purity.

As the Co_3O_4 precipitate formation is assumed to be isotropic the volume fraction can be derived from SEM images by quantifying secondary electron contrast. A suitable part of the image intensity histogram was selected to separate the bright Co_3O_4 precipitates from the cubic matrix. The Co_3O_4 volume fraction was then calculated by dividing the number of bright pixels by the number of dark pixels (excluding pores). The volume fraction in descending order is (3.08 ± 0.23) % ($(BS)_{0.95}CF$), (1.24 ± 0.19) % (BSCF) and (0.61 ± 0.07) % ($(BS)_{1.05}CF$). The number density of Co_3O_4 precipitates was (0.064 ± 0.004) μm^{-2} ($(BS)_{0.95}CF$), (0.059 ± 0.004) μm^{-2} (BSCF) and (0.036 ± 0.003) μm^{-2} ($(BS)_{1.05}CF$) with an average particle size (in the same order) of (0.469 ± 0.023) μm^2, (0.193 ± 0.009) μm^2 and (0.161 ± 0.009) μm^2. This highlights that the volume fraction,

sample	compound formula	
	nominal	calculated
BSCF10Y	$(Ba_{0.5}Sr_{0.5})(Co_{0.8}Fe_{0.2})_{0.9}Y_{0.1}O_{3-\delta}$	$(Ba_{0.488}Sr_{0.487}Y_{0.025})(Co_{0.702}Fe_{0.176}Y_{0.075})O_{3-\delta}$
BSCF	$(Ba_{0.5}Sr_{0.5})(Co_{0.8}Fe_{0.2})O_{3-\delta}$	$(Ba_{0.5}Sr_{0.5})(Co_{0.765}Fe_{0.2})O_{3-\delta}$
$(BS)_{0.95}CF$	$(Ba_{0.5}Sr_{0.5})_{0.95}(Co_{0.8}Fe_{0.2})O_{3-\delta}$	$(Ba_{0.5}Sr_{0.5})(Co_{0.749}Fe_{0.211})O_{3-\delta}$
$(BS)_{1.05}CF$	$(Ba_{0.5}Sr_{0.5})_{1.05}(Co_{0.8}Fe_{0.2})O_{3-\delta}$	$(Ba_{0.5}Sr_{0.5})(Co_{0.745}Fe_{0.19})O_{3-\delta}$

Table 9. Samples stoichiometries according to precursor materials (nominal) and calculations based on occupancy (BSCF10Y) and Co_3O_4 content (BSCF, $(BS)_{0.95}CF$, $(BS)_{1.05}CF$).

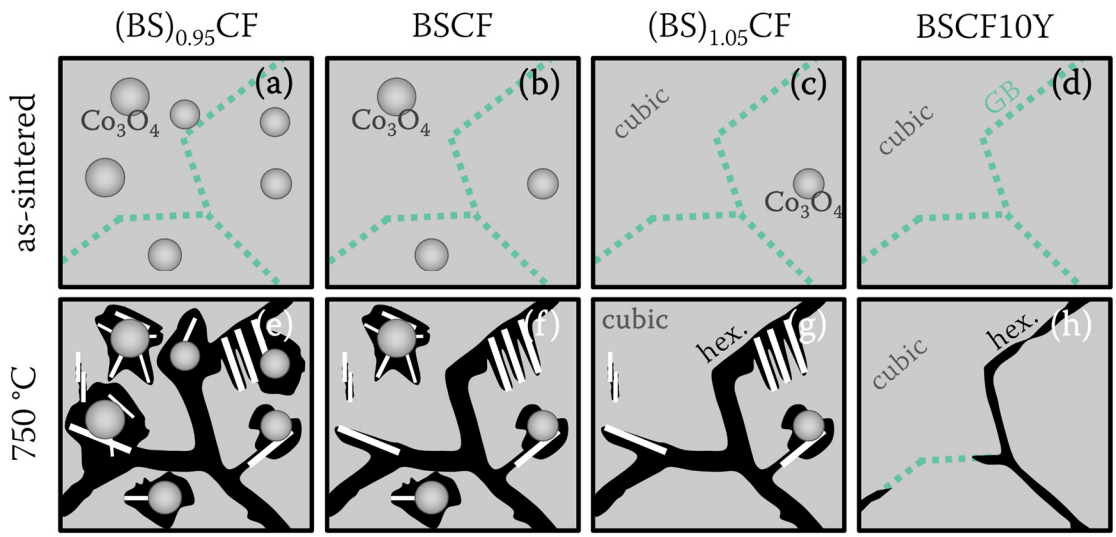

Figure 66. Schematic representation of secondary phase distribution for (a,e) $(BS)_{0.95}CF$, (b,f) BSCF, (c,g) $(BS)_{1.05}CF$ and (d,h) BSCF10Y (a-d) before and (e-h) after long-time heat treatment at 750 °C for 21 days.

the number density and the average particle size of Co_3O_4 are increased for the sample with A-cation deficiency in contrast to the sample with A-cation excess. BSCF resides in the middle with the number density close to $(BS)_{0.95}CF$ but an average particle size close to $(BS)_{1.05}CF$. Within the investigated range the volume fraction is roughly reduced by a factor of two if the A/B-cation ratio is lowered by 5 %. The different volume fractions of Co_3O_4 might also be responsible for the variation of grain size in BSCF, $(BS)_{0.95}CF$ and $(BS)_{1.05}CF$ as these precipitates can act as pinning centers during grain boundary motion. Hence, grain boundary movement and, therefore, grain growth are lowest for $(BS)_{0.95}CF$ because it has the highest Co_3O_4 concentration.

By assuming the correct stoichiometry for the precursor materials, the final stoichiometry of the cubic BSCF phase can be calculated by considering the Co_3O_4 volume fraction. The Co_3O_4 material density was calculated with the crystal data published in [207] by assuming a stoichiometric compound. The resulting stoichiometries are given in Table 9. Since all calculated compound formulas yield an A/B-ratio smaller than one, the values were normalized by scaling the occupancy in a way that the value for the A-site is one. Given the calculated compound formulas, the stoichiometry of the cubic phase is similar in all samples although the initial precursor ratio was varied in the fabrication process. The A/B-cation ratios from the calculated compound formulas are 1.052 (BSCF10Y), 1.036 (BSCF), 1.042 ($(BS)_{0.95}CF$) and 1.070 ($(BS)_{1.05}CF$). All samples exhibit B-cation deficiency after considering Co-loss in the

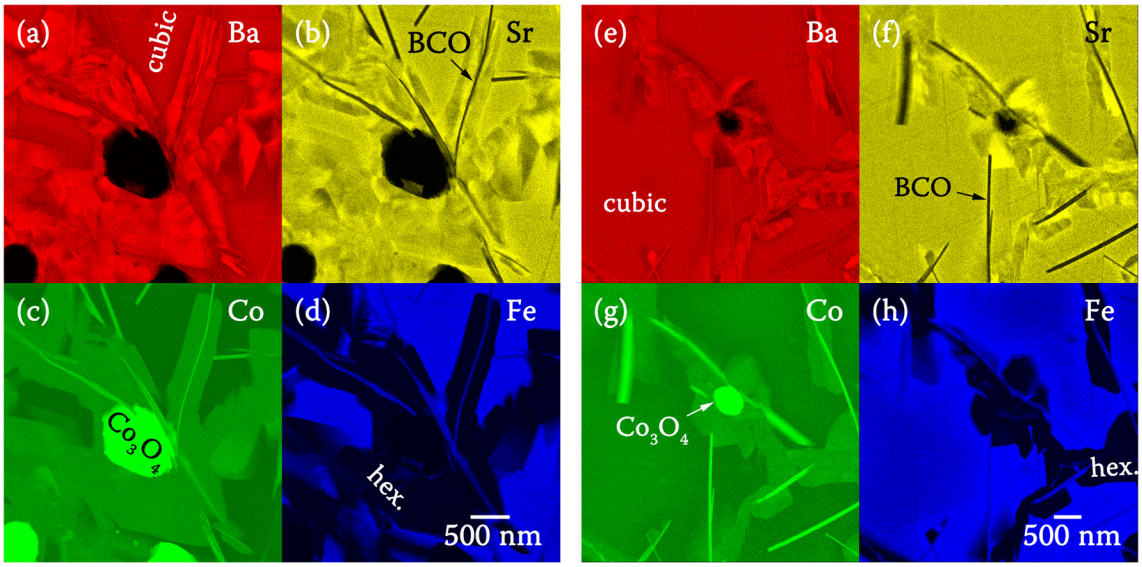

Figure 67. Quantified EDXS elemental map showing secondary phase formation in the vicinity of Co_3O_4 precipitates for (a-d) $(BS)_{0.95}CF$ and (e-h) $(BS)_{1.05}CF$. Maps are color-coded with (a,e) red for Ba, (b,f) yellow for Sr, (c,g) green for Co and (d,h) blue for Fe.

cubic BSCF phase due to Co_3O_4 precipitate formation. This is further supported by EDXS analysis of areas containing only the cubic perovskite phase where deviations were not observed within the margin of error.

SE SEM images of the bulk interior after long-time annealing at 750 °C for 21 days are presented in Figure 65(e-h). Secondary phases are clearly visible in all samples, however, with different volume content. To visualize the presence of secondary phases, a simplified representation of the samples before (as-sintered) and after heat treatment at 750 °C is presented in Figure 66. Secondary phase formation is slightly less pronounced for BSCF and $(BS)_{1.05}CF$ compared to $(BS)_{0.95}CF$. Hexagonal and plate-like phases are well visible in the images. A substantial amount of the hexagonal phase is present in all samples because it decorates grain boundaries as well as plate-like and Co_3O_4 precipitates. For BSCF10Y only negligible amounts of the hexagonal phase compared to BSCF, $(BS)_{0.95}CF$ and $(BS)_{1.05}CF$ is observed. This is in accordance with previous results in Chapter 5.2. A quantification of image contrast yields a secondary phase volume faction of (45 ± 3) % ($(BS)_{0.95}CF$), (36 ± 2) % (BSCF), (21 ± 2) % ($(BS)_{1.05}CF$) and (3 ± 1) % (BSCF10Y). Hence, there is roughly a factor of two regarding long-time secondary phase formation when comparing $(BS)_{0.95}CF$ and $(BS)_{1.05}CF$. However, there is still a big gap between BSCF10Y and the other samples. The reduction of secondary phases in BSCF10Y was discussed in Chapter 5.2 and mainly attributed to the suppression of

Co_xO_y/BCO precipitates due to the tendency of Y to be located on A- and B-sites and the slow Y-diffusion characteristics.

STEM investigations confirmed a significantly higher content of secondary phases in $(BS)_{0.95}CF$ compared to $(BS)_{1.05}CF$. Co_3O_4 precipitates in $(BS)_{0.95}CF$ are much more frequent and (in average) larger compared to precipitates in other samples. EDXS elemental composition maps of $(BS)_{0.95}CF$ and $(BS)_{1.05}CF$ are depicted in Figure 67. Here the distribution maps of individual cations allow a precise phase assignment as each secondary phase shows a characteristic chemical composition (cf. Chapter 5.1). It is quite evident that the hexagonal phase strongly decorates Co_3O_4 grains which contributes significantly to the total amount of hexagonal phase in the sample. This is especially pronounced for $(BS)_{0.95}CF$ where the concentration of Co_3O_4 is highest. Co_3O_4 precipitates are considered nucleation sites for the hexagonal phase and are, therefore, responsible for the faster degradation of $(BS)_{0.95}CF$ compared to $(BS)_{1.05}CF$. Hence, the fabrication of BSCF with 5 at% A-site excess can be considered beneficial in terms of slowing down the decomposition rate of BSCF.

5.4 Functional coating for enhanced surface exchange kinetics

To overcome the surface exchange limit of thin BSCF membranes, coating with high porous $La_{0.6}Sr_{0.4}CoO_{3-\delta}$ (LSC) was investigated. Samples were produced by our cooperation partner IAM-WET. BSCF and BSCF10Y substrates were fabricated with the parameters presented earlier. LSC sol was prepared by dissolving the right amount of La, Sr, Co precursor material within propionic acid to a concentration of 10 wt%. The sol was applied to polished BSCF and BSCF10Y substrates by either dip or spin coating. Coating involved a drying procedure of 5 min followed by a thermal annealing process at 170 °C and calcination at 700 °C (no holding time, heating rate 3 K min^{-1}, cooling rate 10 K min^{-1}). The estimated porosity of the LSC layer was about 30 %. Additional heat treatments were conducted at different temperatures and annealing times. The fabrication parameters of investigated samples are summarized in Table 10. Notice that for one sample (labeled BSCF10Y-5xLSC) the LSC sol was applied five times. The applied sol was dried at 170 °C.

A SE SEM cross-section image showing the as-prepared LSC layer deposited on BSCF10Y is depicted in Figure 68(a). Depending on the sample, the layer thickness was in the range from 80 to 160 nm. For spin coated samples, the layer thickness was quite constant, whereas the dip coating technique produced a significant thicker layer close to the edge of the BSCF/BSCF10Y substrate of up to 500 nm. As depicted in Figure 68(a), the layer did attach well to the substrate without major deviations in thickness. Delamination was not observed among all samples which indicate good adhesion. The image suggests some small surface phases with dark contrast which

sample	coating method	annealing	
		temperature	time
BSCF-LSC	dip	600, 700 °C	100 h
BSCF10Y-LSC	dip	600, 700 °C	100 h
BSCF-LSC	spin	700 °C	250 h
BSCF10Y-LSC	spin	700 °C	250 h
BSCF10Y-5xLSC	spin	750 °C	500 h

Table 10. Fabrication parameters of investigated samples.

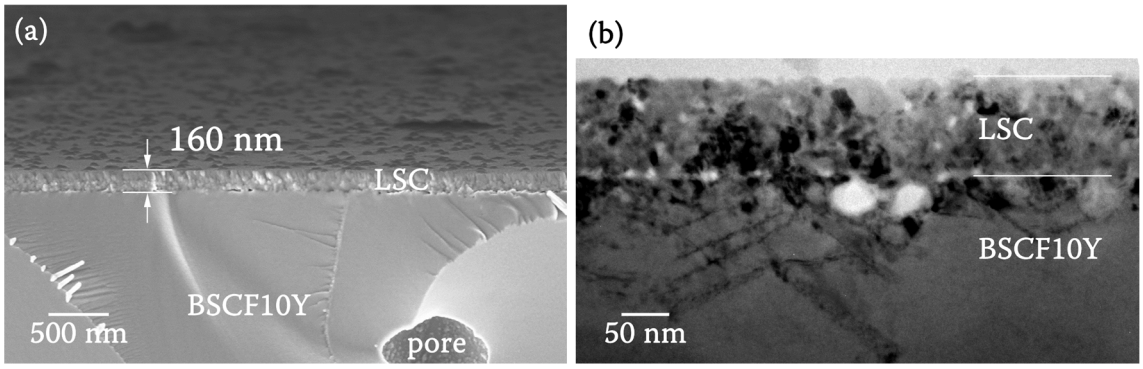

Figure 68. (a) Side view SE SEM image of breaking edge. The LSC layer can be easily distinguished from the BSCF10Y substrate. (b) BF TEM image of as-prepared LSC thin film on BSCF10Y substrate.

might be attributed to cobalt-oxide as this is a common phase in LSC. Many high-temperature XRD studies have already shown the precipitation of Co_3O_4 precipitates during the sol-gel synthesis of LSC up to a temperature of 900 °C [251–253]. Co_3O_4 can be considered as an intermediate phase during the pyrolysis process. As LEVIN DIETERLE [254] demonstrated in his PhD thesis, precipitation of Co_3O_4 occurs close to the sample surface which is consistent with the results presented here. As the precipitation of Co_3O_4 phases reduces the Co content within the LSC phase, this might promote the formation of Ruddlesden-Popper phases with a stoichiometry of $(La,Sr)_{2-x}Co_{1+x}O_{4\pm\delta}$ (LSC_{RP}). TEM BF analysis showed a number of lattice defects at the interface region as depicted in Figure 68(b). The crystallite size suggested by BF TEM images was in the order of a few 10 nanometers. To demonstrate the high porosity of the LSC layer exemplary images of as-prepared samples are shown in Figure 69. The contrast was tuned in order to improve image quality. It is worth mentioning that the gap between LSC and BSCF10Y in the HAADF-STEM image (cf. Figure 69(b)) is due to preferential etching during sample preparation.

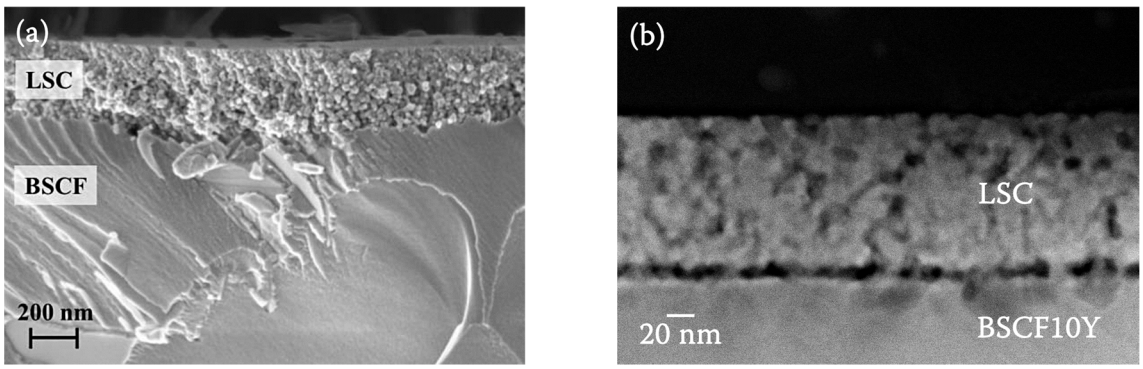

Figure 69. (a) SE SEM image of LSC coated BSCF taken from a joint publication [259]. (b) HAADF-STEM image of as-prepared LSC coated BSCF10Y.

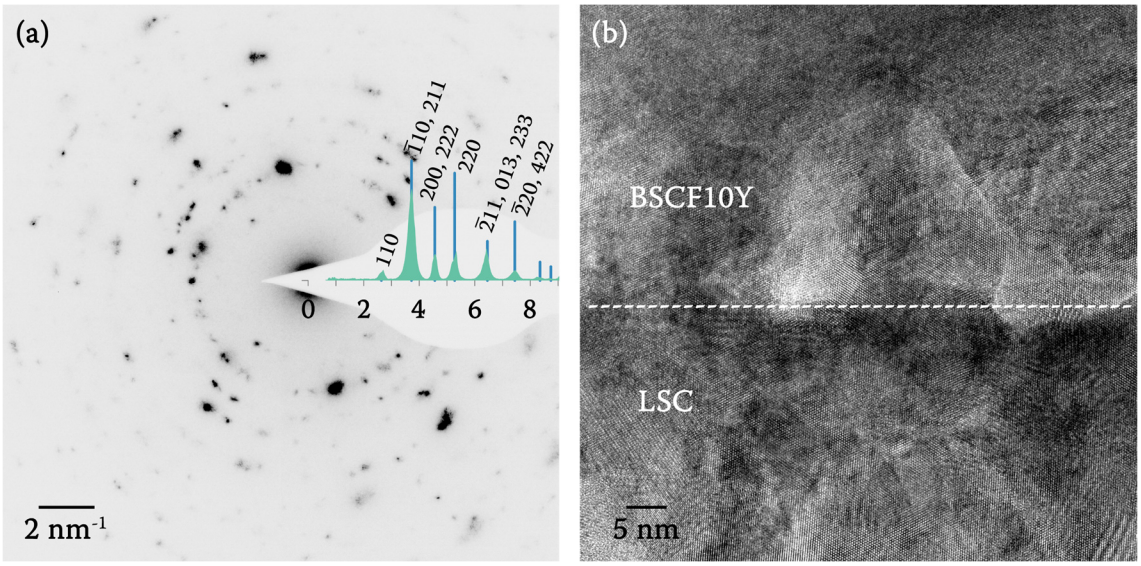

Figure 70. (a) SAED image of LSC layer with superimposed radial scan and reciprocal lattice distances for cubic LSC. (b) HRTEM image of interface region in as prepared LSC coated BSCF10Y.

The crystal structure of the deposited LSC film was investigated by Debye-Scherrer electron diffraction as depicted in Figure 70(a). The radially integrated intensity (after background subtraction) is superimposed on the image including the expected Bragg lines for the perovskite LSC phase with crystal structure data taken from [255] (a = 5.35 Å, R$\bar{3}$c). Due to limitations connected to the microscope's aperture, layer thickness, and grain size, only a low number of grain orientations are captured within each diffraction image. Therefore, the dynamics of the simulated intensity (blue lines) does not match the data derived from the radial scan (green curve). As the Ruddlesden-Popper phase of LSC has a high lattice parameter (a = 3.80 Å, c = 12.52 Å, I4/mmm)

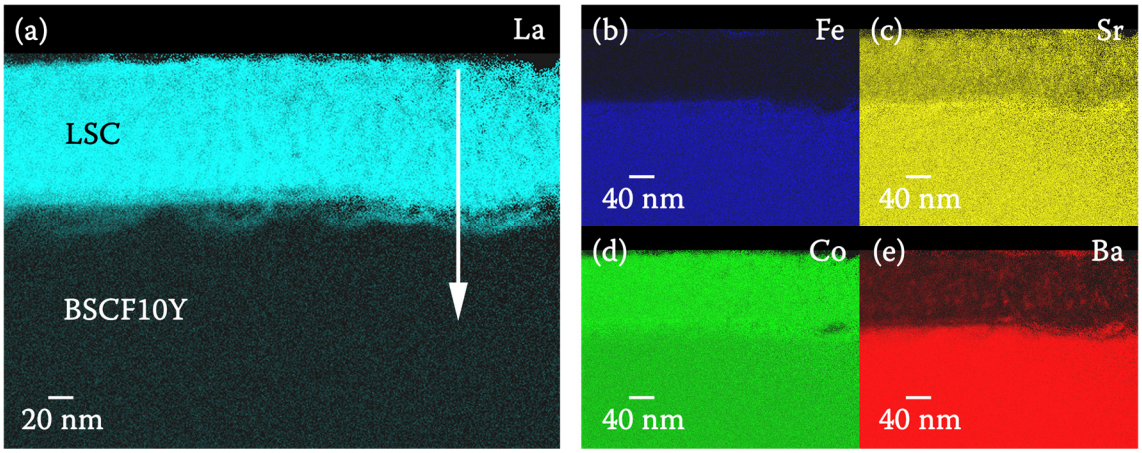

Figure 71. EDXS elemental composition map of as-prepared LSC coated BSCF10Y showing the cation distribution of (a) La, (b) Fe, (c) Sr, (d) Co and (e) Ba.

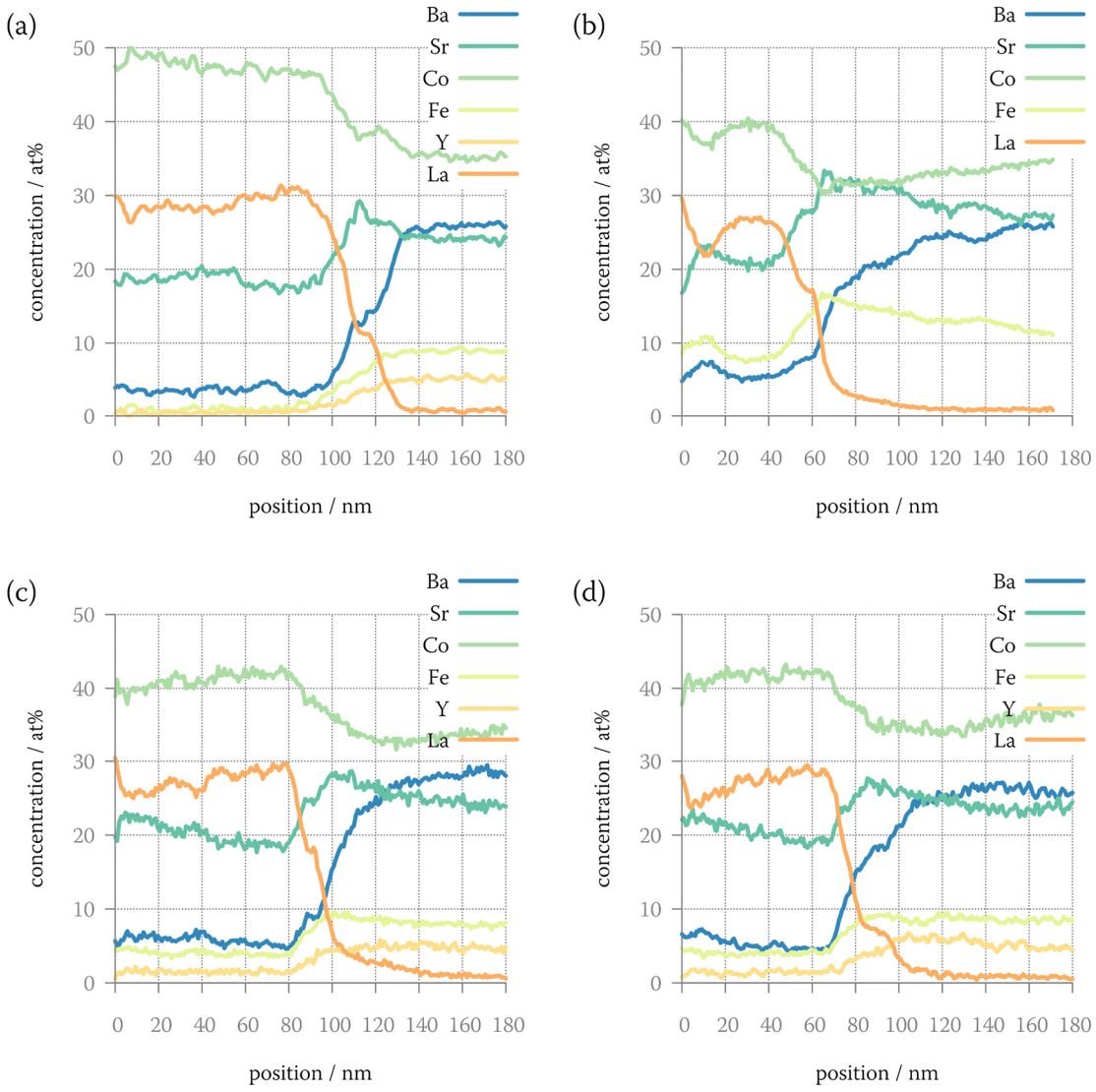

Figure 72. Cation concentration profile of (a) as-prepared BSCF10Y-LSC, (b) BSCF-LSC annealed at 700 °C for 10 days, (c) BSCF10Y-LSC annealed at 700 °C for 10 days and (d) BSCF10Y-LSC annealed at 750 °C for 21 days.

[256] one isolated weak reflection at 1.6 nm^{-1} should appear if the LSC_{RP} phase is present. However, all reflections could be attributed to the LSC perovskite phase with no indication for additional peaks in all of the investigated samples. Concerning some HRTEM diffractograms, additional reflections with low reciprocal lattice vector were observed, though they could be attributed to moiré patterns due to multiple superimposed grains.

HRTEM analysis of as-prepared samples (cf. Figure 70(b)) showed a significant roughness of the BSCF10Y/LSC interface region which is either due to the initial surface roughness of the BSCF10Y substrate or cation interdiffusion during the calcination

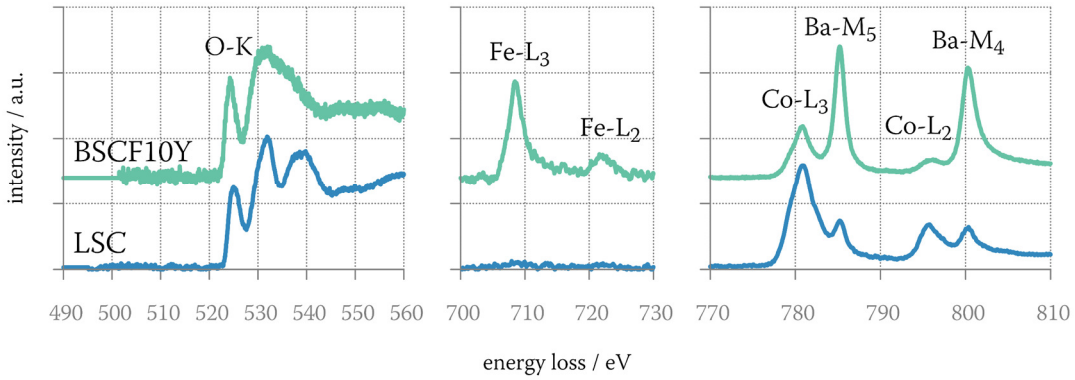

Figure 73. EELS spectra of the LSC layer and the BSCF10Y substrate of as prepared BSCF10Y-LSC sample.

process. To check cation positions, EDXS elemental distribution maps were recorded before and after long time annealing. Chemical composition maps of as-prepared BSCF10Y-LSC are presented in Figure 71(a-e). Here, a transition region between BSCF10Y and LSC is visible. The thickness of this transition region is in the range of 5 – 30 nm, depending on sample position. The cation concentration profile along the white arrow in Figure 71(a) is shown in Figure 72(a). To get data with statistical relevance, the spectra were integrated perpendicular to the layer by at least 50 scanning points. The chemical composition of the LSC layer is fairly homogeneous with minor deviations close to the interface region. Surprisingly, there was a minor amount of Ba (< 5 at%) within the LSC layer which already indicates diffusion occurring during the calcination process of the LSC layer.

EELS investigations were performed to determine the Co oxidation state in both, LSC layer and BSCF10Y substrate for the as-prepared sample. To avoid any contributions from the interface, EELS spectra were taken in the middle of the LSC layer and far away in the BSCF10Y substrate. Deconvoluted spectra containing the O-K, Fe-$L_{2,3}$, Ba-$M_{4,5}$ and Co-$L_{2,3}$ ionization edge are depicted in Figure 73. The Co white-line distance within the LSC layer is (14.81 ± 0.05) eV, which would correspond to a nominal Co oxidation state of 2.48+. However, many groups reported a higher valence state of close or higher than 3+ [220,257,258]. As the white-line distance of Co^{4+} is in a similar range as Co^{2+}, the valence state derived by the white-line distance technique might be severely underestimated. If we assume that the white-line distance fit is also valid for Co oxidation states between 3+ and 4+, the Co oxidation state within LSC would be 3.58+ which is closer to the value of 3.4+ suggested by KONYSHEVA ET AL. [258]. Nevertheless,

the valence state of Co in LSC is considerably higher compared to the BSCF10Y substrate where the Co white-line distance and oxidation state is (15.29 ± 0.05) eV and 2.18+. Furthermore, Ba-$M_{4,5}$ white-lines are visible within the LSC film which makes it hard to compare it to literature values of pure LSC. This presence of the Ba-$M_{4,5}$ edge confirms the EDXS results. The Fe-$L_{2,3}$ white-lines were not visible for LSC which also matches well with the EDXS measurement. Compared to BSCF10Y/BSCF the O-K edge of LSC has a considerable smaller pre-peak with a double-peak structure within the main edge. Interestingly, the pre-peak which is associated with the d-band occupancy is lower in LSC compared to BSCF10Y which would not be expected as a higher TM oxidation state was measured in LSC. This might be attributed to the absence of Fe. EELS line profiles perpendicular to the LSC thin film showed minor variations within the spectrum, mainly for the ratio of the Co-$L_{2,3}$ and Ba-$M_{4,5}$ white-lines.

To further characterize cation interdiffusion, EDXS line profiles were recorded after 10 days of annealing in ambient air at 700 °C (cf. Figure 72(b) for BSCF substrate and (c) for BSCF10Y substrate) and 21 days at 750 °C (cf. Figure 72(d); BSCF10Y substrate only). Comparing the two samples annealed at 700 °C, the one with BSCF10Y as a substrate shows a reasonable homogeneous elemental distribution within the LSC layer whereas there are considerable changes within the LSC layer when deposition was performed on BSCF. The Ba concentration within the LSC layer increases slightly compared to the as-prepared sample to around 5 at% within both samples. Also, a non-negligible amount of Fe is present in both LSC layers, yet, more pronounced for LSC on the BSCF substrate with 7 – 11 at%. Minor traces of Y (~2 at%) are also found within the LSC layer deposited on the BSCF10Y substrate. The interface region is fairly similar compared to the as-prepared samples with a depletion or excess of Sr on either side of the interface and a small plateau in the concentration profile of Ba and La close to the interface. Compared to the as-prepared sample (cf. Figure 72(a)), the thickness of this plateau region did not change significantly. Hence, it is assumed that this region originates from the initial surface roughness (cf. Figure 70(b)) and not from the formation of an interdiffusion layer. Focusing on the La concentration, the profile suggests La diffusion into both substrates (BSCF and BSCF10Y) as the concentration with respect to the interface decrease much slower compared to the as-prepared samples. Interestingly, the composition of the LSC layer did not change significantly comparing the sample annealed for 10 days (cf. Figure 72(c)) and the sample annealed for 21 days (cf. Figure 72(d)).

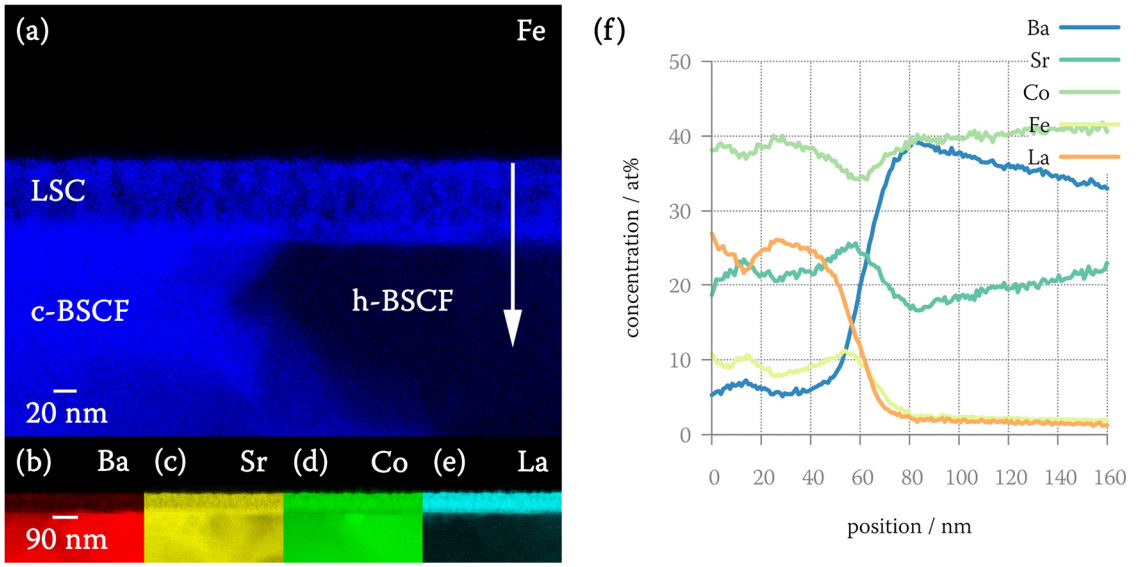

Figure 74. Elemental composition map for (a) Fe, (b), Ba, (c) Sr, (d) Co, (e) La of LSC coated BSCF after annealing at 700 °C for 10 days. Scale bar is identical in (b-e). (f) Concentration profile along the white arrow in (a).

As already mentioned, a considerable amount of Fe is present within the LSC layer, especially for LSC coated BSCF. Furthermore, the cubic perovskite phase of BSCF also shows elevated values of Fe after annealing at 700 °C for 10 days. This can be attributed to the formation of the hexagonal phase which is very pronounced for BSCF at this temperature. As the hexagonal phase is rich in Co and depleted in Fe, the Fe:Co cation ratio changes in the remaining cubic phase. According to MUELLER ET AL. [74] the cubic phase of BSCF tends towards a Fe:Co ratio of 60:40. Hence, the expelled iron from the formation of the hexagonal phase might also be incorporated into the LSC layer explaining the strong increase of Fe in LSC on the BSCF substrate. The formation of the hexagonal phase in BSCF is depicted by EDXS cation composition maps in Figure 74(a-e). The hexagonal region can be easily identified by the absence of Fe. The interface between the hexagonal BSCF phase and LSC is much sharper compared to cubic BSCF and LSC (cf. Figure 72(b)) which is especially obvious in the concentration profile of Ba and La as presented in Figure 74(f).

To demonstrate the enhanced oxygen diffusion characteristics, ECR measurements were performed by LANA UNGER [259]. The thickness of the BSCF substrate was approximately 400 µm. The electrical response of BSCF and LSC coated BSCF was measured at 600 and 700 °C while abruptly changing p_{O_2} from 0.3 to 0.1 bar and from 0.01 bar to 0.003 bar. The derived effective k_{chem} values are presented in Figure 75 with

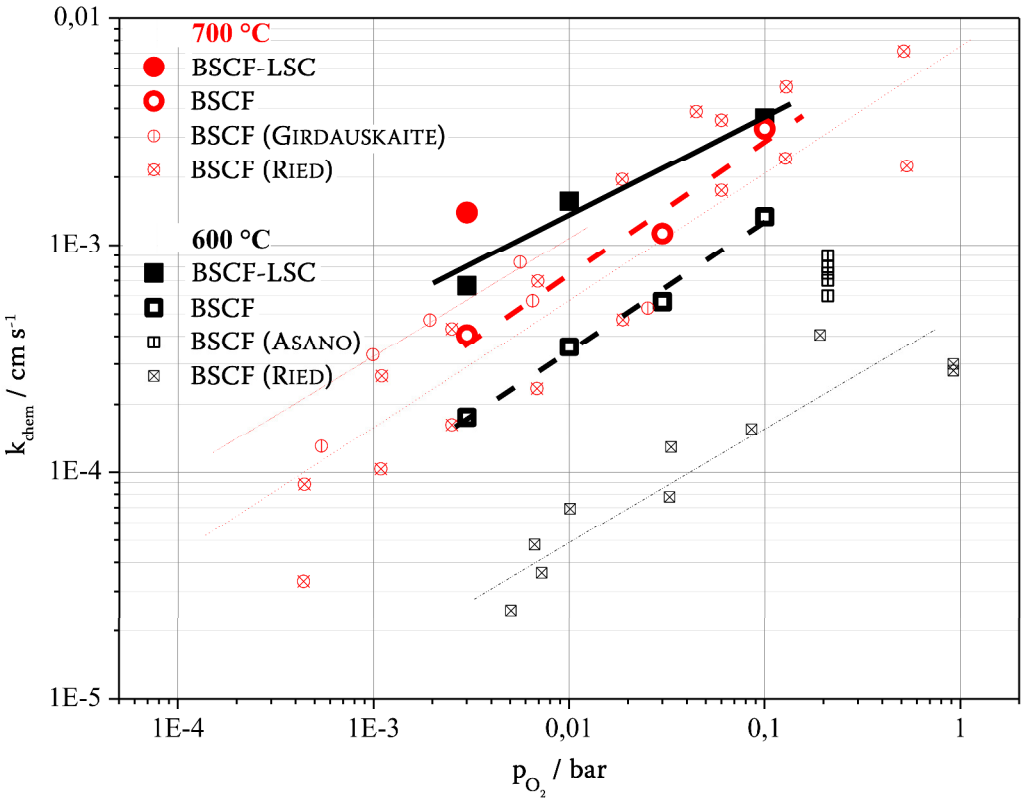

Figure 75. Effective k_{chem} values for BSCF and LSC coated BSCF. Literature data from RIED ET AL. [260], GIRDAUSKAITE ET AL. [261] and ASANO ET AL. [262] are inserted into the plot for comparison. ECR measurements were performed by LANA UNGER within the framework of a joint publication [259].

literature data from RIED ET AL. [260], GIRDAUSKAITE ET AL. [261] and ASANO ET AL. [262]. k_{chem} values acquired at 700 °C agree quite well with literature data whereas values obtained at 600 °C are up to one magnitude higher than values from other researchers. By comparing k_{chem} for uncoated and LSC coated BSCF one can see a considerable gain for LSC coated BSCF. The measurement suggests an increase of about half orders of magnitude for LSC coated BSCF compared to raw BSCF at both 600 and 700 °C.

LSC-LSC_{RP} heterointerfaces are reported to significantly enhance oxygen exchange kinetics by several orders of magnitudes [125,126,129]. However, the presence of LSC-LSC_{RP} heterointerfaces could not be shown by diffraction analysis here. Hence, the gain might be attributed to the surface area increase by the nanoporous LSC film. However, as the LSC film is far from homogeneous (especially on a BSCF substrate) LSC_{RP} phases cannot be ruled out.

6 SUMMARY

The ABO_3 perovskite $(Ba_{0.5}Sr_{0.5})(Co_{0.8}Fe_{0.2})O_{3-\delta}$ (BSCF) in its cubic phase is one of the most sophisticated membrane materials with extraordinary high oxygen permeation over a wide temperature range between 600 – 900 °C. However, the low stability of the cubic phase poses a major obstacle regarding the wide application of BSCF. BSCF tends to form various secondary phases which leads to the degradation of its excellent oxygen permeation properties. This problem was addressed in this thesis by doping BSCF with fixed-valent transition metal ions yttrium (Y), scandium (Sc) and zirconium (Zr). Furthermore, a coating strategy to further improve oxygen exchange and surface stability was investigated.

The BSCF materials were characterized by electron microscopic and spectroscopic techniques. In the course of this thesis, several improvements of characterization techniques evolved that turned out to be an essential prerequisite for understanding the properties of the material system. A new spectroscopic technique to evaluate the cobalt (Co)-valence state in electron energy loss spectroscopy was developed since the well-established method dealing with Co-$L_{2,3}$ white-line intensities cannot be applied in BSCF due to the significant overlap between Ba-$M_{4,5}$ and Co-$L_{2,3}$ ionization edges. In this work, it was demonstrated that not only the white-line intensity but also the white-line distance is correlated with changes of the Co-valence state. Since the distance between the L_2 and L_3 peak positions can be measured with high precision and a high degree of automatization, the evaluation of Co-valence states in large sample areas via spectrum imaging was rendered possible. The Co-valence state can be measured by the white-line distance technique with an accuracy of ±0.2 in secondary phases related to BSCF.

Another methodical concept investigated in this thesis is the noise reduction using multivariate statistics. The impact of principal component filtering on energy dispersive X-ray (EDX) spectrum datasets was carefully studied on experimentally acquired spectra with well-known noise levels. A considerable improvement of the signal-to-noise ratio could be achieved for spectrum images with low counting statistic allowing to recover features which are invisible in the original data set. It was demonstrated that useful information can be extracted even for high noise levels if the initial data set is weighted appropriately. The application of multivariant statistics will in general aid spectroscopic investigations of beam-sensitive materials in electron microscopy.

To gain a deeper understanding of the effect of specific dopants on the BSCF material properties, their lattice position is of great importance. Therefore, the lattice site of Sc- and Y-dopants in BSCF was determined experimentally using transmission electron microscopy (TEM) in combination with EDX spectroscopy. In the ALCHEMI (atom location by channeling enhanced microanalysis) technique, the localization of Bloch waves in a periodic crystal potential was utilized. For specific microscope conditions and sample orientations, the Bloch wave localization can be tuned in a way that the electron intensity is increased on specific lattice sites. This gives rise to enhanced X-ray emission of elements located on the selected lattice site allowing to derive lattice-site occupancies. For BSCF, the expected X-ray intensity was simulated for numerous site occupancies and compared to experimental data. Lattice-site occupancies with an accuracy of about ±5 % were achieved for Y- and Sc-doped BSCF. It was demonstrated that Sc exclusively occupies the intended B-site. Interestingly, a considerable fraction of Y ions are located on both lattice positions with an A-site occupancy of 55 %, 45 %, 25 % for 1 at%, 3 at% and 10 at% Y doping although exclusive B-site doping was intended. A-site occupation of Y can be explained by the fact that the ionic radius of Y is between the typical ionic radii of A and B-site elements.

Microstructural characterizations were carried out on as-fabricated samples and after controlled annealing treatments (aging) to assess secondary phase formation. Microstructure investigations of as-fabricated samples revealed a considerable amount of cobalt-oxide phases embedded in the cubic perovskite matrix of BSCF and Sc-doped BSCF, however, not for Y-doped BSCF with a dopant concentration of at least 3 at%. This could be traced back to Y-ions being located on both lattice sites. Since B-site doping was intended, the non-negligible amount of A-site Y ions leads to the decrease of the A/B-cation ratio to values below one. Additional analysis on intended variations of the A/B-cation ratio demonstrated that BSCF intrinsically tends towards B-cation deficiency which is already present in Y-doped samples.

The formation of $Ba_{n+1}Co_nO_{3n+3}(Co_8O_8)$ (BCO, $n \geq 2$) was successfully linked to the presence of cobalt-oxide precipitates which are formed during sintering. The BCO phase emerges from the reaction between cobalt-oxide precipitates and Ba ions from the cubic phase in a temperature window between 800 and 950 °C. BCO was also demonstrated to exist in a lamellar phase with plate-like morphology [79]. This plate-like phase consists of an arbitrary arrangement of BCO, cubic and hexagonal phase layers.

Below the critical temperature (840 °C) the hexagonal BSCF phase forms which is correlated with a substantial degradation of oxygen permeation. The hexagonal phase nucleates at grain boundaries, cobalt-oxide precipitates, BCO or plate-like lamellae. An increased Co-valence state was measured for BCO/cobalt-oxide (2.7+) and for the hexagonal phase (2.6+) compared to the Co-valence state of the cubic phase (2.2+). The higher valence state and, therefore, reduced ionic radius of Co leads to the destabilization of the cubic BSCF phase and formation of secondary phases with reduced lattice spacing within their crystal lattices.

In contrast to the initial assumptions, doping with Zr and Sc does not substantially suppress secondary phase formation in BSCF. However, the introduction of Y leads to a strong decrease in secondary phase content, especially for high Y concentrations. Starting at 3 at% Y doping, the BCO-type lamellae disappear which can be understood by the disappearance of cobalt-oxide phases and ultimately to the mixed-site occupancy of the Y ion. For 3 at% doping, a thin layer of hexagonal phase was observed exclusively at grain boundaries as other secondary phases are completely suppressed. For 10 at% Y-doped BSCF, secondary phases are completely suppressed at temperatures above 760 °C. This indicates that Y doping increases the thermodynamic stability range of cubic BSCF or, at least, strongly slows down the decomposition kinetics.

The Co-valence state in the cubic phase was measured to be identical for Y-doped and undoped BSCF with a value of 2.2+ indicating that the increase in cubic phase stability is not caused by a reduction of Co-valence state. Chemical analysis of the hexagonal phase in Y-doped BSCF clearly shows the depletion of Fe and Y. The large ionic radius of Y is considered to mainly impede this diffusion process since the ionic radius of Y by far surpasses the ionic radius of iron and cobalt, especially for high dopant concentrations where up to 75 % of Y-ions are located on the B-site.

Another concept investigated in this thesis was the impact of fabrication parameters on secondary phase formation. It turned out that the sintering temperature and, therefore, the final grain size of the ceramic material have a strong effect on the content of secondary phases. Large grain sizes are highly beneficial for BSCF because they provide fewer nucleation sites for the hexagonal phase below the critical temperature. The total content of secondary phases could be reduced significantly by choosing high sintering temperatures which yield large grain sizes. This was especially obvious for Zr-doped BSCF where the secondary phase content was reduced drastically. The evolution of

k_{chem} and D_{chem} confirmed the strongly reduced degradation for samples with increasing grain size [245].

To analyze the impact of stoichiometry changes on the decomposition of the cubic BSCF phase, A/B-cation ratios were varied intentionally by 5 % during sample fabrication. Interestingly, variations of about 5 % did not have an impact on the final stoichiometry of the cubic phase. Different A/B-cation ratios only affect the cobalt-oxide precipitation. The cobalt-oxide volume fraction increases in 5 % A-cation deficient samples and decreases in 5 % B-cation deficient samples with an overall minimum content of cobalt-oxide phases. Samples with high cobalt-oxide content are much stronger affected by the formation of the hexagonal phase compared to samples with low cobalt-oxide content because cobalt-oxide and related BCO- and plate-like phases increase possible nucleation sites. Hence, B-cation deficiency was identified as a favorable fabrication strategy to reduce the content of secondary phases.

In order to increase the chemical stability of the surface and promote oxygen surface exchange kinetics, porous $La_{0.6}Sr_{0.4}CoO_{3-\delta}$ thins films were applied on BSCF and Y-doped BSCF. The chemical compatibility between substrate and thin film was considerably improved by Y-doping due to the improved stability of the cubic BSCF phase. Initial measurements of the oxygen exchange kinetics for BSCF showed an improvement by a factor of five for coated BSCF. This was attributed to the nanoporous LSC layer with an estimated porosity of 30 % and, therefore, strong increase of surface area.

The results of this thesis have considerably improved the understanding of BSCF materials and have revealed options to prevent the decomposition of the cubic BSCF phase. Y doping, B-cation deficiency, and large grain sizes were identified as beneficial material parameters to minimize material degradation. Future concepts of improving long-time permeability might involve the evaluation of other dopants with similar characteristics compared to Y. Furthermore, enhancing the oxygen exchange kinetics by using sophisticated coating layers should be further pursued. Especially the usage of functional layers with $La_{0.6}Sr_{0.4}CoO_{3-\delta}/(La,Sr)_2CoO_{4\pm\delta}$ heterointerfaces has the potential of increasing surface kinetics significantly. Heterointerfaces were reported to enhance oxygen surface exchange reactions by several orders of magnitude [125,126,129]. This yields the potential of further increasing economic viability.

7 REFERENCES

[1] T. Ohji, M. Singh, Engineered ceramics: Current status and future prospects, Wiley, New York (USA), 2016.

[2] B. Jody, E. Daniels, A. Wolsky, Energy Convers. Manage. 38 (1997) S135-S140.

[3] Z. Shao, W. Yang, Y. Cong, H. Dong, J. Tong, G. Xiong, J. Membr. Sci. 172 (2000) 177–188.

[4] J. Taftø, J. Spence, Science 218 (1982) 49–51.

[5] D.B. Williams, C.B. Carter, Transmission electron microscopy: A textbook for materials science, 2nd ed., Springer, New York (USA), 2009.

[6] L. Reimer, Scanning electron microscopy: Physics of image formation and microanalysis, Springer, Berlin, New York (USA), 1998.

[7] L. Reimer, H. Kohl, Transmission electron microscopy: Physics of image formation, 5th ed., Springer, New York (USA), 2008.

[8] R.F. Egerton, Electron energy-loss spectroscopy in the electron microscope, 3rd ed., Springer, New York (USA), 2011.

[9] V.D. Scott, G. Love, S.J.B. Reed, Quantitative electron-probe microanalysis, 2nd ed., Ellis Horwood, Hemel Hempstead (UK), 1995.

[10] S.J. Skinner, J.A. Kilner, Mater. Today 6 (2003) 30–37.

[11] J. Sunarso, S. Baumann, J.M. Serra, W.A. Meulenberg, S. Liu, Y.S. Lin, J.C. Diniz da Costa, J. Membr. Sci. 320 (2008) 13–41.

[12] P. Granger, V.I. Pârvulescu, S. Kaliaguine, W. Prellier, Perovskites and related mixed oxides: Concepts and applications, Wiley-VCH, Weinheim, 2016.

[13] P.J. Gellings, H.J.M. Bouwmeester, The CRC handbook of solid state electrochemistry, CRC Press, Boca Raton (USA), 1997.

[14] Y. Teraoka, T. Nobunaga, N. Yamazoe, Chem. Lett. 17 (1988) 503–506.

[15] H. Bouwmeester, H. Kruidhof, A.J. Burggraaf, Solid State Ionics 72, Part 2 (1994) 185–194.

[16] K. Wiik, S. Aasland, H. Hansen, I. Tangen, R. Ødegård, Solid State Ionics 152–153 (2002) 675–680.

[17] P.-M. Geffroy, J. Fouletier, N. Richet, T. Chartier, Chem. Eng. Sci. 87 (2013) 408–433.

[18] V.M. Goldschmidt, Naturwissenschaften 21 (1926) 477–485.

[19] R.S. Roth, J. Res. Natl. Bur. Stand. (U. S.) 58 (1957) 75–88.

[20] A.M. Glazer, Acta Crystallogr., Sect. B: Struct. Crystallogr. Cryst. Chem. 28 (1972) 3384–3392.

[21] A. Glazer, Acta Crystallogr., Sect. A: Cryst. Phys., Diffr., Theor. Gen. Crystallogr. 31 (1975) 756–762.

[22] N.L. Allan, M.J. Dayer, D.T. Kulp, W.C. Mackrodt, J. Mater. Chem. 1 (1991) 1035–1039.

[23] H. Hayashi, Solid State Ionics 122 (1999) 1–15.

[24] J.-C. Boivin, Int. J. Inorg. Mater. 3 (2001) 1261–1266.

[25] H. Kruidhof, H.J.M. Bouwmeester, R.H. v. Doorn, A.J. Burggraaf, Solid State Ionics 63-65 (1993) 816–822.

[26] W. Harrison, T.H. Lee, Y.L. Yang, D.P. Scarfe, L.M. Liu, A.J. Jacobson, Mater. Res. Bull. 30 (1995) 621–630.

[27] L. Qiu, Solid State Ionics 76 (1995) 321–329.

[28] L.M. Liu, T.H. Lee, L. Qiu, Y.L. Yang, A.J. Jacobson, Mater. Res. Bull. 31 (1996) 29–35.

[29] N. Grunbaum, L. Mogni, F. Prado, A. Caneiro, J. Solid State Chem. 177 (2004) 2350–2357.

[30] S. McIntosh, J.F. Vente, W.G. Haije, D. Blank, H.J.M. Bouwmeester, Solid State Ionics 177 (2006) 833–842.

[31] T. Nagai, W. Ito, T. Sakon, Solid State Ionics 177 (2007) 3433–3444.

[32] C. Zener, Phys. Rev. 81 (1951) 440–444.

[33] R.L. Cook, A.F. Sammells, Solid State Ionics 45 (1991) 311–321.

[34] X. Dong, W. Jin, N. Xu, Chem. Mater. 22 (2010) 3610–3618.

[35] A.F. Sammells, R.L. Cook, J.H. White, J.J. Osborne, R.C. MacDuff, Solid State Ionics 52 (1992) 111–123.

[36] N. Xu, H. Zhao, X. Zhou, W. Wei, X. Lu, W. Ding, F. Li, Int. J. Hydrogen Energy 35 (2010) 7295–7301.

[37] M. Cherry, M.S. Islam, C.R.A. Catlow, J. Solid State Chem. 118 (1995) 125–132.

[38] M.S. Khan, M.S. Islam, D.R. Bates, J. Phys. Chem. B 102 (1998) 3099–3104.

[39] M.S. Islam, Solid State Ionics 154–155 (2002) 75–85.

[40] Y. Teraoka, H.-M. Zhang, S. Furukawa, N. Yamazoe, Chem. Lett. 14 (1985) 1743–1746.

[41] Y. Teraoka, T. Nobunaga, K. Okamoto, N. Miura, N. Yamazoe, Solid State Ionics 48 (1991) 207–212.

[42] S. Pei, M.S. Kleefisch, T.P. Kobylinski, J. Faber, C.A. Udovich, V. Zhang-McCoy, B. Dabrowski, U. Balachandran, R.L. Mieville, R.B. Poeppel, Catal. Lett. 30 (1995) 201–212.

[43] Z. Shao, G. Xiong, J. Tong, H. Dong, W. Yang, Sep. Purif. Technol. 25 (2001) 419–429.

[44] H. Shiiba, C.L. Bishop, Rushton, Michael J. D., M. Nakayama, M. Nogami, J.A. Kilner, R.W. Grimes, J. Mater. Chem. A 1 (2013) 10345.

[45] Z. Shao, S.M. Haile, Nature 431 (2004) 170–173.

[46] X. Sun, S. Li, J. Sun, X. Liu, B. Zhu, Int. J. Electrochem. Sci. 2 (2007) 462–468.

[47] R. Su, Z. Lü, S.P. Jiang, Y. Shen, W. Su, K. Chen, Int. J. Hydrogen Energy 38 (2013) 2413–2420.

[48] A. Botea-Petcu, S. Tanasescu, V. Varazashvili, N. Lejava, T. Machaladze, M. Khundadze, F. Maxim, F. Teodorescu, J. Martynczuk, Z. Yáng, L.J. Gauckler, Mater. Res. Bull. 57 (2014) 184–189.

[49] K. Chen, J. Hyodo, K.M. O'Donnell, W.Rickard, T. Ishihara, S.P. Jianga, J. Electrochem. Soc. 161 (2014) F1163-F1170.

[50] M. Mosiałek, M. Dudek, A. Michna, M. Tatko, A. Kędra, M. Zimowska, J. Solid State Electrochem. 18 (2014) 3011–3021.

[51] S. Tanasescu, Z. Yáng, J. Martynczuk, V. Varazashvili, F. Maxim, F. Teodorescu, A. Botea, N. Totir, L.J. Gauckler, J. Solid State Chem. 200 (2013) 354–362.

[52] A.C. van Veen, M. Rebeilleau, D. Farrusseng, C. Mirodatos, Chem. Commun. (Cambridge, U. K.) (2003) 32–33.

[53] J.F. Vente, S. McIntosh, W.G. Haije, H.J.M. Bouwmeester, J. Solid State Electrochem. 10 (2006) 581–588.

[54] E.G. Babakhani, J. Towfighi, L. Shirazi, A.N. Pour, J. Membr. Sci. 376 (2011) 78–82.

[55] D.N. Mueller, R.A. De Souza, H.-I. Yoo, M. Martin, Chem. Mater. 24 (2012) 269–274.

[56] A.C. Tomkiewicz, M.A. Tamimi, A. Huq, S. McIntosh, Solid State Ionics 253 (2013) 27–31.

[57] J. Ovenstone, J.-I. Jung, J.S. White, D.D. Edwards, S.T. Misture, J. Solid State Chem. 181 (2008) 576–586.

[58] C. Niedrig, W. Menesklou, S.F. Wagner, E. Ivers-Tiffee, J. Electrochem. Soc. 160 (2012) F135-F140.

[59] H. Wang, C. Tablet, W. Yang, J. Caro, Mater. Lett. 59 (2005) 3750–3755.

[60] S. McIntosh, J.F. Vente, W.G. Haije, D.H.A. Blank, H.J.M. Bouwmeester, Solid State Ionics 177 (2006) 1737–1742.

[61] P. Zeng, Z. Chen, W. Zhou, H. Gu, Z. Shao, S. Liu, J. Membr. Sci. 291 (2007) 148–156.

[62] M. Arnold, T.M. Gesing, J. Martynczuk, A. Feldhoff, Chem. Mater. 20 (2008) 5851–5858.

[63] S. Švarcová, K. Wiik, J. Tolchard, H.J.M. Bouwmeester, T. Grande, Solid State Ionics 178 (2008) 1787–1791.

[64] C. Niedrig, S. Taufall, M. Burriel, W. Menesklou, S.F. Wagner, S. Baumann, E. Ivers-Tiffée, Solid State Ionics 197 (2011) 25–31.

[65] P. Müller, L. Dieterle, E. Müller, H. Störmer, D. Gerthsen, C. Niedrig, S. Taufall, S.F. Wagner, E. Ivers-Tiffée, ECS Trans. 28 (2010) 309–314.

[66] M. Rebeilleau-Dassonneville, S. Rosini, A.C. van Veen, D. Farrusseng, C. Mirodatos, Catal. Today 104 (2005) 131–137.

[67] M. Arnold, Q. Xu, F.D. Tichelaar, A. Feldhoff, Chem. Mater. 21 (2009) 635–640.

[68] A.S. Harvey, F.J. Litterst, Z. Yang, J.L.M. Rupp, A. Infortuna, L.J. Gaucklera, Phys. Chem. Chem. Phys. 11 (2009) 3010.

[69] A.S. Harvey, Z. Yang, A. Infortuna, D. Beckel, J.A. Purton, L.J. Gauckler, J. Phys.: Condens. Matter 21 (2009) 15801.

[70] D.N. Mueller, R.A. de Souza, J. Brendt, D. Samuelis, M. Martin, J. Mater. Chem. 19 (2009) 1960–1963.

[71] R. Merkle, Y.A. Mastrikov, E.A. Kotomin, M.M. Kuklja, J. Maier, J. Electrochem. Soc. 159 (2012) B219.

[72] E.A. Kotomin, Y.A. Mastrikov, M.M. Kuklja, R. Merkle, A. Roytburd, J. Maier, Solid State Ionics 188 (2011) 1–5.

[73] B. Liu, Y. Zhang, L. Tang, Int. J. Hydrogen Energy 34 (2009) 435–439.

[74] D.N. Mueller, R.A. De Souza, T.E. Weirich, D. Roehrens, J. Mayer, M. Martin, Phys. Chem. Chem. Phys. 12 (2010) 10320–10328.

[75] M. Arnold, H. Wang, J. Martynczuk, A. Feldhoff, J. Am. Ceram. Soc. 90 (2007) 3651–3655.

[76] P. Müller, H. Störmer, L. Dieterle, C. Niedrig, E. Ivers-Tiffée, D. Gerthsen, Solid State Ionics 206 (2012) 57–66.

[77] K. Efimov, Q. Xu, A. Feldhoff, Chem. Mater. 22 (2010) 5866–5875.

[78] F. Liang, H. Jiang, H. Luo, J. Caro, A. Feldhoff, Chem. Mater. 23 (2011) 4765–4772.

[79] P. Müller, H. Störmer, M. Meffert, L. Dieterle, C. Niedrig, S.F. Wagner, E. Ivers-Tiffée, D. Gerthsen, Chem. Mater. 25 (2013) 564–573.

[80] J. Sun, M. Yang, G. Li, T. Yang, F. Liao, Y. Wang, M. Xiong, J. Lin, Inorg. Chem. Commun. 45 (2006) 9151–9153.

[81] S. Baumann, F. Schulze-Küppers, S. Roitsch, M. Betz, M. Zwick, E.M. Pfaff, W.A. Meulenberg, J. Mayer, D. Stöver, J. Membr. Sci. 359 (2010) 102–109.

[82] C. Buysse, A. Kovalevsky, F. Snijkers, A. Buekenhoudt, S. Mullens, J. Luyten, J. Kretzschmar, S. Lenaerts, J. Membr. Sci. 372 (2011) 239–248.

[83] B. Rutkowski, Mechanical Properties and Microstructure of Dense Ceramic Membranes for Oxygen Separation in Zero-Emission Power Plants, PhD Thesis, RWTH Aachen (2012).

[84] X. Li, T. Kerstiens, T. Markus, J. Membr. Sci. 438 (2013) 83–89.

[85] A. Yan, M. Cheng, Y. Dong, W. Yang, V. Maragou, S. Song, P. Tsiakaras, Appl. Catal., B 66 (2006) 64–71.

[86] M. Arnold, H. Wang, A. Feldhoff, J. Membr. Sci. 293 (2007) 44–52.

[87] A. Yan, V. Maragou, A. Arico, M. Cheng, P. Tsiakaras, Appl. Catal., B 76 (2007) 320–327.

[88] E. Bucher, A. Egger, G.B. Caraman, W. Sitte, J. Electrochem. Soc. 155 (2008) B1218.

[89] A. Waindich, A. Möbius, M. Müller, J. Membr. Sci. 337 (2009) 182–187.

[90] J. Yi, M. Schroeder, J. Membr. Sci. 378 (2011) 163–170.

[91] C. Niedrig, Electrochemical Performance and Stability of $Ba_{0.5}Sr_{0.5}Co_{0.8}Fe_{0.2}O_{3-\delta}$ for Oxygen Transport Membranes, PhD Thesis, KIT (2015).

[92] Z. Yáng, A.S. Harvey, A. Infortuna, L.J. Gauckler, J. Appl. Crystallogr. 42 (2009) 153–160.

[93] H. Wang, C. Tablet, A. Feldhoff, J. Caro, Adv. Mater. 17 (2005) 1785–1788.

[94] Y. Teraoka, H. Shimokawa, C. Kang, H. Kusaba, K. Sasaki, Solid State Ionics 177 (2006) 2245–2248.

[95] A. Feldhoff, J. Martynczuk, H. Wang, Prog. Solid State Chem. 35 (2007) 339–353.

[96] J. Martynczuk, M. Arnold, A. Feldhoff, J. Membr. Sci. 322 (2008) 375–382.

[97] B. Wei, Z. Lü, X. Huang, M. Liu, N. Li, W. Su, J. Power Sources 176 (2008) 1–8.

[98] A. Feldhoff, J. Martynczuk, M. Arnold, M. Myndyk, I. Bergmann, V. Šepelák, W. Gruner, U. Vogt, A. Hähnel, J. Woltersdorf, J. Solid State Chem. 182 (2009) 2961–2971.

[99] J. Martynczuk, F. Liang, M. Arnold, V. Šepelák, A. Feldhoff, Chem. Mater. 21 (2009) 1586–1594.

[100] K. Efimov, T. Halfer, A. Kuhn, P. Heitjans, J. Caro, A. Feldhoff, Chem. Mater. 22 (2010) 1540–1544.

[101] L. Zhao, B. He, X. Zhang, R. Peng, G. Meng, X. Liu, J. Power Sources 195 (2010) 1859–1861.

[102] H. Zhao, N. Xu, Y. Cheng, W. Wei, N. Chen, W. Ding, X. Lu, F. Li, J. Phys. Chem. C 114 (2010) 17975–17981.

[103] X. Meng, B. Meng, X. Tan, N. Yang, Z.-F. Ma, Mater. Res. Bull. 44 (2009) 1293–1297.

[104] S. Yakovlev, C.-Y. Yoo, S. Fang, H.J.M. Bouwmeester, Appl. Phys. Lett. 96 (2010) 254101.

[105] X. Meng, N. Yang, B. Meng, X. Tan, Z.-F. Ma, S. Liu, Ceram. Int. 37 (2011) 2701–2709.

[106] O. Ravkina, T. Klande, A. Feldhoff, J. Solid State Chem. 201 (2013) 101–106.

[107] S. Fang, C.-Y. Yoo, H. Bouwmeester, Solid State Ionics 195 (2011) 1–6.

[108] F. Wang, T. Nakamura, K. Yashiro, J. Mizusaki, K. Amezawa, Solid State Ionics (2014).

[109] Y.V. Egorova, T. Scherb, G. Schumacher, H. Bouwmeester, E.O. Filatova, J. Alloys Compd. 650 (2015) 848–852.

[110] J.M. Porras-Vazquez, P.R. Slater, J. Power Sources 209 (2012) 180–183.

[111] C. Kwak, D.W. Jung, D.-H. Yeon, J.S. Kim, H.J. Park, S.-J. Ahn, S. Seo, S.M. Lee, RSC Adv. 3 (2013) 10669.

[112] M.P. Popov, I.A. Starkov, S.F. Bychkov, A.P. Nemudry, J. Membr. Sci. 469 (2014) 88–94.

[113] E.G. Babakhani, J. Towfighi, L. Shirazi, A. Nakhaeipour, A. Zamaniyan, Z. Shafiei, J. Mater. Sci. Technol. (Shenyang, China) 28 (2012) 177–183.

[114] P. Haworth, The Effect of Yttrium Substitution and Surface Modification on BSCF Perovskites, PhD Thesis, The University of Queensland (2012).

[115] P. Haworth, S. Smart, J. Glasscock, J.C. Diniz da Costa, Sep. Purif. Technol. 81 (2011) 88–93.

[116] P. Haworth, S. Smart, J. Glasscock, J.C. Diniz da Costa, Sep. Purif. Technol. 94 (2012) 16–22.

[117] A. Leo, S. Liu, J.C. Diniz da Costa, Z. Shao, Sci. Technol. Adv. Mater. 7 (2006) 819.

[118] A. Leo, S. Liu, J.C. Diniz da Costa, J. Membr. Sci. 340 (2009) 148–153.

[119] A. Leo, S. Smart, S. Liu, J.C. Diniz da Costa, J. Membr. Sci. 368 (2011) 64–68.

[120] P.F. Haworth, S. Smart, J.M. Serra, J.C. Diniz da Costa, Phys. Chem. Chem. Phys. 14 (2012) 9104–9111.

[121] S. Baumann, J.M. Serra, M.P. Lobera, S. Escolástico, F. Schulze-Küppers, W.A. Meulenberg, J. Membr. Sci. 377 (2011) 198–205.

[122] W.K. Hong, G.M. Choi, J. Membr. Sci. 346 (2010) 353–360.

[123] R. Mukundan, E.L. Brosha, F.H. Garzon, Electrochemical Society Proceedings Series (2002) 142–147.

[124] A. Heel, P. Holtappels, T. Graule, J. Power Sources 195 (2010) 6709–6718.

[125] M. Sase, K. Yashiro, K. Sato, J. Mizusaki, T. Kawada, N. Sakai, K. Yamaji, T. Horita, H. Yokokawa, Solid State Ionics 178 (2008) 1843–1852.

[126] J.W. Han, B. Yildiz, Energy Environ. Sci. 5 (2012) 8598.

[127] Y. Chen, Z. Cai, Y. Kuru, W. Ma, H.L. Tuller, B. Yildiz, Adv. Energy Mater. 3 (2013) 1221–1229.

[128] J. Hayd, H. Yokokawa, E. Ivers-Tiffee, J. Electrochem. Soc. 160 (2013) F351-F359.

[129] E.J. Crumlin, E. Mutoro, S.-J. Ahn, G.J. La O', D.N. Leonard, A. Borisevich, M.D. Biegalski, H.M. Christen, Y. Shao-Horn, J. Phys. Chem. Lett. 1 (2010) 3149–3155.

[130] G. Cliff, G.W. Lorimer, J. Microsc. 103 (1975) 203–207.

[131] K. Pearson, Philos. Mag. 2 (1901) 559–572.

[132] I.T. Jolliffe, Principal Component Analysis, Springer, New York (USA), 2002.

[133] A.A. Miranda, Y.-A. Borgne, G. Bontempi, Neural Process. Lett. 27 (2008) 197–207.

[134] R.B. Cattell, Multivar. Behav. Res. 1 (1966) 245–276.

[135] M.R. Keenan, P.G. Kotula, Surf. Interface Anal. 36 (2004) 203–212.

[136] M. Bosman, M. Watanabe, D.T.L. Alexander, V.J. Keast, Ultramicroscopy 106 (2006) 1024–1032.

[137] S. Lichtert, J. Verbeeck, Ultramicroscopy 125 (2013) 35–42.

[138] M.G. Burke, M. Watanabe, D.B. Williams, J.M. Hyde, J. Mater. Sci. 41 (2006) 4512–4522.

[139] C.M. Parish, L.N. Brewer, Ultramicroscopy 110 (2010) 134–143.

[140] B.M. Wilamowski, J.D. Irwin, The industrial electronics handbook, 2nd ed., CRC Press, Boca Raton (USA), 2011.

[141] H. Wold, Research Papers in Statistics (1966) 411–444.

[142] M. Andrecut, J. Comput. Biol. 16 (2009) 1593–1599.

[143] G. Guennebaud, B. Jacob, others, Eigen (C++ library), 2016.

[144] The Qt Company, Qt (C++ library), http://www.qt.io (2016).

[145] S. Lichtert, J. Verbeeck, Ultramicroscopy 125 (2013) 35–42.

[146] C. Parish, P. Edmondson, M. Miller, Microsc Microanal 17 (2011) 594–595.

[147] J. Fink, Th. Muller-Heinzerling, B. Scheerer, W. Speier, F.U. Hillebrecht, J.C. Fuggle, J. Zaanen, and G.A. Sawatzky, Phys. Rev. B 32 (1985) 4899–4904.

[148] B.T. Thole, G. van der Laan, Phys. Rev. B 38 (1988) 3158–3171.

[149] D.H. Pearson, C.C. Ahn, and B. Fultz, Phys. Rev. B 47 (1993) 8471–8478.

[150] T.G. Sparrow, B.G. Williams, C. Rao, J.M. Thomas, Chem. Phys. Lett. 108 (1984) 547–550.

[151] J. Graetz, C.C. Ahn, H. Ouyang, P. Rez, B. Fultz, Phys. Rev. B 69 (2004).

[152] D. Manthey, Orbital Viewer, http://www.orbitals.com/orb/ov.htm (2004).

[153] B.X. Huang, J. Malzbender, R.W. Steinbrech, P. Grychtol, C.M. Schneider, L. Singheiser, Appl. Phys. Lett. 95 (2009) 51901.

[154] B.X. Huang, J. Malzbender, R. Steinbrech, L. Singheiser, J. Membr. Sci. 359 (2010) 80–85.

[155] R.D. Leapman, L.A. Grunes, Phys. Rev. Lett. 45 (1980) 397–401.

[156] Z.L. Wang, J.S. Yin, Y.D. Jiang, Micron 31 (2000) 571–580.

[157] Z. Wang, J. Bentley, N. Evans, Micron 31 (2000) 355–362.

[158] H. Tan, J. Verbeeck, A. Abakumov, G. van Tendeloo, Ultramicroscopy 116 (2012) 24–33.

[159] P.A. van Aken, B. Liebscher, Phys. Chem. Miner. 29 (2002) 188–200.

[160] T. Riedl, T. Gemming, K. Wetzig, Ultramicroscopy 106 (2006) 284–291.

[161] C.C. Ahn, Transmission electron energy loss spectrometry in materials science and the EELS atlas, 2nd ed., Wiley, New York (USA), 2004.

[162] O.L. Krivanek, J.H. Paterson, Ultramicroscopy 32 (1990) 313–318.

[163] M. Merz, P. Nagel, C. Pinta, A. Samartsev, H. v. Löhneysen, M. Wissinger, S. Uebe, A. Assmann, D. Fuchs, S. Schuppler, Phys. Rev. B 82 (2010).

[164] L.A.J. Garvie, P.R. Buseck, Nature 396 (1998) 667–670.

[165] P. Müller, M. Meffert, H. Störmer, D. Gerthsen, Microsc. Microanal. 19 (2013) 1595–1605.

[166] E. Stavitski, F.M.F. de Groot, Micron 41 (2010) 687–694.

[167] D.W. Oxtoby, H.P. Gillis, A. Campion, Principles of modern chemistry, 7th ed., Brooks/Cole Cengage Learning, Belmont (USA), 2012.

[168] S. Sugano, Y. Tanabe, H. Kamimura, Multiplets of Transition-Metal Ions in Crystals, Academic Press, San Diego (USA), 1970.

[169] V.V. Mesilov, V.R. Galakhov, B.A. Gizhevskii, A.S. Semenova, D.G. Kellerman, M. Raekers, M. Neumann, Phys. Solid State 55 (2013) 943–948.

[170] S.A. Warda, W. Massa, D. Reinen, Z. Hu, G. Kaindl, F.M.F. de Groot, J. Solid State Chem. 146 (1999) 79–87.

[171] R.F. Egerton, Ultramicroscopy 107 (2007) 575–586.

[172] L. Cave, T. Al, D. Loomer, S. Cogswell, L. Weaver, Micron 37 (2006) 301–309.

[173] P.A. van Aken, B. Liebscher, V.J. Styrsa, Phys. Chem. Miner. 25 (1998) 323–327.

[174] P. Ewels, T. Sikora, V. Serin, C.P. Ewels, L. Lajaunie, Microsc. Microanal. 22 (2016) 717–724.

[175] K. Zhang, R. Ran, L. Ge, Z. Shao, W. Jin, N. Xu, J. Alloys Compd. 474 (2009) 477–483.

[176] D. Han, K. Kishida, K. Shinoda, H. Inui, T. Uda, J. Mater. Chem. A 1 (2013) 3027.

[177] D. Han, K. Shinoda, T. Uda, G. Brennecka, J. Am. Ceram. Soc. 97 (2014) 643–650.

[178] B.W. Batterman, Phys. Rev. Lett. 22 (1969) 703–705.

[179] L.S. Edelheit, J.C. North, J.G. Ring, J.S. Koehler, F.W. Young, Phys. Rev. B 2 (1970) 2913–2923.

[180] J.A. Golovchenko, B.W. Batterman, W.L. Brown, Phys. Rev. B 10 (1974) 4239–4243.

[181] J.C.H. Spence, J. Taftø, Journal Microsc. 130 (1983) 147–154.

[182] E.R. Pike, P.C. Sabatier, Scattering, Two-Volume Set: Scattering and inverse scattering in Pure and Applied Science, Academic Press, London (UK), 2001.

[183] T.C. McCormick, J.R. Smyth, G.E. Lofgren, Phys. Chem. Miner. 14 (1987) 368–372.

[184] M.K. Miller, J. Bentley, J. Phys. Colloq. 47 (1986) 463–468.

[185] J. Spence, M. Kuwabara, Y. Kim, Ultramicroscopy 26 (1988) 103–112.

[186] S.J. Pennycook, Ultramicroscopy 26 (1988) 239–248.

[187] C.J. Rossouw, P.S. Turner, T.J. White, Philos. Mag. B 57 (1988) 227–241.

[188] K.M. Krishnan, Ultramicroscopy 24 (1988) 125–141.

[189] J. Spence, M. Kuwabara, Y. Kim, Ultramicroscopy 26 (1988) 103–112.

[190] P.R. Munroe, I. Baker, J. Mater. Res. 7 (1992) 2119–2125.

[191] Z. Horita, H. Kuninaka, T. Sano, M. Nemoto, J.C.H. Spence, Philos. Mag. A 67 (1993) 425–432.

[192] Z. Horita, Ultramicroscopy 66 (1996) 1–4.

[193] W. Nüchter, W. Sigle, Philos. Mag. A 71 (1995) 165–186.

[194] T. Soeda, S. Matsumura, C. Kinoshita, N.J. Zaluzec, J. Nucl. Mater. 283-287 (2000) 952–956.

[195] T. Morimura, M. Hasaka, Mater. Charact. 52 (2004) 35–41.

[196] T. Morimura, M. Hasaka, Ultramicroscopy 106 (2006) 553–560.

[197] M.P. Oxley, L.J. Allen, J. Appl. Crystallogr. 36 (2003) 940–943.

[198] H. Koster, F.H.B. Mertins, Powder Diffr. 18 (2003) 56.

[199] P. Stadelmann, Microsc. Microanal. 9 (2003) 60–61.

[200] L.J. Allen, C.J. Rossouw, Phys. Rev. B 47 (1993) 2446–2452.

[201] L.J. Allen, T.W. Josefsson, Phys. Rev. B 52 (1995) 3184–3198.

[202] L.J. Allen, T.W. Josefsson, Phys. Rev. B 53 (1996) 11285–11287.

[203] M.P. Oxley, L.J. Allen, Ultramicroscopy 80 (1999) 125–131.

[204] P.M. Kelly, A. Jostsons, R.G. Blake, J.G. Napier, Phys. Status Solidi A 31 (1975) 771–780.

[205] O. Ravkina, A. Yaremchenko, A. Feldhoff, J. Membr. Sci. 520 (2016) 76–88.

[206] S. Sasaki, K. Fujino, Y. Takéuchi, Proc. Jpn. Acad., Ser. B 55 (1979) 43–48.

[207] G. Will, N. Masciocchi, W. Parrish, M. Hart, J. Appl. Crystallogr. 20 (1987) 394–401.

[208] K. Persels Constant, T.O. Mason, S.J. Rothman, J.L. Routbort, J. Phys. Chem. Solids 53 (1992) 405–411.

[209] C. Colliex, T. Manoubi, and C. Ortiz, Phys. Rev. B 44 (1991) 11402–11411.

[210] F.M.F. de Groot, M. Grioni, J. C. Fuggle, J. Ghijsen, G.A. Sawatzky, and H. Petersen, Phys. Rev. B 40 (1989).

[211] R. David, A. Pautrat, H. Kabbour, M. Sturza, S. Curelea, G. André, D. Pelloquin, O. Mentré, Chem. Mater. 23 (2011) 5191–5199.

[212] H. Gasparyan, J.B. Claridge, M.J. Rosseinsky, J. Mater. Chem. A 3 (2015) 18265–18272.

[213] Y. Chen, B. Qian, S. Li, Y. Jiao, M.O. Tade, Z. Shao, J. Membr. Sci. 449 (2014) 86–96.

[214] S. Asagi, S. Suzuki, M. Miyayama, Key Eng. Mater. 388 (2009) 49–52.

[215] P. Müller, Electron Microscopical Investigations of Doped and Undoped $Ba_{0.5}Sr_{0.5}Co_{0.8}Fe_{0.2}O_{3-d}$ for Oxygen Separation Membranes, PhD Thesis, KIT (2013).

[216] R.D. Shannon, Acta Cryst. (1976) 751–767.

[217] Z. Chen, R. Ran, Z. Shao, H. Yu, J.C. Diniz da Costa, S. Liu, Ceram. Int. 35 (2009) 2455–2461.

[218] A.A. Colville, K. Staudhammer, Am. Mineral. 52 (1967) 1877–1880.

[219] A.A. Yaremchenko, C. Buysse, V. Middelkoop, F. Snijkers, A. Buekenhoudt, J.R. Frade, A.V. Kovalevsky, J. Membr. Sci. 428 (2013) 123–130.

[220] Z. Cai, M. Kubicek, J. Fleig, B. Yildiz, Chem. Mater. 24 (2012) 1116–1127.

[221] N. Tsvetkov, Q. Lu, L. Sun, E.J. Crumlin, B. Yildiz, Nat. Mater. (2016).

[222] N. Tsvetkov, Q. Lu, B. Yildiz, Faraday discussions 182 (2015) 257–269.

[223] Y. Liu, X. Zhu, W. Yang, AIChE J. 61 (2015) 3879–3888.

[224] Z. Yáng, A.S. Harvey, A. Infortuna, J. Schoonman, L.J. Gauckler, J. Solid State Electrochem. 15 (2011) 277–284.

[225] J.-I. Jung, S.T. Misture, D.D. Edwards, Solid State Ionics 206 (2012) 50–56.

[226] H. Wang, C. Tablet, A. Feldhoff, J. Caro, J. Membr. Sci. 262 (2005) 20–26.

[227] M. Arnold, J. Martynczuk, K. Efimov, H. Wang, A. Feldhoff, J. Membr. Sci. 316 (2008) 137–144.

[228] J.S. Yoon, M.Y. Yoon, E.J. Lee, J.-W. Moon, H.J. Hwang, Solid State Ionics 181 (2010) 1387–1393.

[229] D. Gao, J. Zhao, W. Zhou, R. Ran, Z. Shao, J. Membr. Sci. 366 (2011) 203–211.

[230] M. Salehi, F. Clemens, E.M. Pfaff, S. Diethelm, C. Leach, T. Graule, B. Grobéty, J. Membr. Sci. 382 (2011) 186–193.

[231] T. Klande, O. Ravkina, A. Feldhoff, J. Eur. Ceram. Soc. 33 (2013) 1129–1136.

[232] L. Ge, W. Zhou, R. Ran, S. Liu, Z. Shao, W. Jin, N. Xu, J. Membr. Sci. 306 (2007) 318–328.

[233] L. Ge, R. Ran, K. Zhang, S. Liu, Z. Shao, J. Membr. Sci. 318 (2008) 182–190.

[234] W. Zhou, R. Ran, Z. Shao, W. Zhuang, J. Jia, H. Gu, W. Jin, N. Xu, Acta Mater. 56 (2008) 2687–2698.

[235] L. Grünewald, Elektronenmikroskopische Charakterisierung von Yttrium-dotierten BSCF-Keramiken (german), Bachelor Thesis, KIT (2015).

[236] J. Schindelin, C.T. Rueden, M.C. Hiner, K.W. Eliceiri, Mol. Reprod. Dev. 82 (2015) 518–529.

[237] P. Bobrowski, Z. Pędzich, M. Faryna, Micron 78 (2015) 73–78.

[238] S. Wachs, Elektronenmikroskopische Untersuchungenvon Y- und Zr-dotierten BSCF-Keramiken (german), Bachelor Thesis, KIT (2013).

[239] L. Wang, R. Dou, M. Bai, Y. Li, D. Hall, Y. Chen, J. Eur. Ceram. Soc. 36 (2016) 1659–1667.

[240] P.-L. Chen, I.-W. Chen, J. Am. Ceram. Soc. 79 (1996) 1793–1800.

[241] E.W. Leib, R.M. Pasquarelli, J.J. do Rosário, P.N. Dyachenko, S. Döring, A. Puchert, A.Y. Petrov, M. Eich, G.A. Schneider, R. Janssen, H. Weller, T. Vossmeyer, J. Mater. Chem. C 4 (2016) 62–74.

[242] M. Shirpour, B. Rahmati, W. Sigle, P.A. van Aken, R. Merkle, J. Maier, J. Phys. Chem. C 116 (2012) 2453–2461.

[243] J. Boonlakhorn, P. Kidkhunthod, B. Putasaeng, T. Yamwong, P. Thongbai, S. Maensiri, J. Mater. Sci.: Mater. Electron. 26 (2015) 2329–2337.

[244] K. Bodišová, D. Galusek, P. Švančárek, V. Pouchlý, K. Maca, Ceram. Int. 41 (2015) 11975–11983.

[245] S. Saher, M. Meffert, H. Störmer, D. Gerthsen, H.J.M. Bouwmeester, J. Mater. Chem. A 5 (2017) 4982–4990.

[246] E. Bucher, A. Egger, P. Ried, W. Sitte, P. Holtappels, Solid State Ionics 179 (2008) 1032–1035.

[247] D. Chen, Z. Shao, Int. J. Hydrogen Energy 36 (2011) 6948–6956.

[248] X Chen, S Wang, Y.L Yang, L Smith, N.J Wu, B.-I Kim, S.S Perry, A.J Jacobson, A Ignatiev, Solid State Ionics 146 (2002) 405–413.

[249] J. Lane, J. Kilner, Solid State Ionics 136-137 (2000) 997–1001.

[250] J. Trincavelli, S. Limandri, R. Bonetto, Spectrochim. Acta, Part B 101 (2014) 76–85.

[251] S. Cizauskaite, A. Kareiva, Open Chemistry 6 (2008).

[252] C. Peters, Grain-size effects in nanoscaled electrolyte and cathode thin films for solid oxide fuel cells (SOFC), PhD Thesis, KIT (2009).

[253] N.P. Bansal, B. Wise, Ceram. Int. 38 (2012) 5535–5541.

[254] L. Dieterle, Electron microscopy study of pure and Sr-substituted $LaCoO_3$, PhD Thesis, KIT (2012).

[255] V.G. Sathe, A.V. Pimpale, V. Siruguri, S.K. Paranjpe, J. Phys.: Condens. Matter 8 (1996) 3889.

[256] M. Sánchez-Andújar, M.A. Señarís-Rodríguez, Solid State Sciences 6 (2004) 21–27.

[257] Y.A. Mastrikov, R. Merkle, E.A. Kotomin, M.M. Kuklja, J. Maier, Phys. Chem. Chem. Phys. 15 (2013) 911–918.

[258] E. Konysheva, S.M. Francis, J.T.S. Irvine, J. Electrochem. Soc. 157 (2010) B159.

[259] L.-S. Unger, M. Meffert, V. Wilde, H. Stormer, C. Niedrig, W. Menesklou, S.F. Wagner, D. Gerthsen, E. Ivers-Tiffee, ECS Trans. 72 (2016) 37–45.

[260] P. Ried, E. Bucher, W. Preis, W. Sitte, P. Holtappels, 10th International Symposium on Solid Oxide Fuel Cells (SOFC-X), June 3 - 8, 2007, pp. 1217–1224.

[261] E. Girdauskaite, H. Ullmann, V. Vashook, U. Guth, G. Carman, E. Bucher, W. Sitte, Solid State Ionics 179 (2008) 385–392.

[262] K. Asano, C. Niedrig, W. Menesklou, S.F. Wagner, E. Ivers-Tiffée, J. Electrochem. Soc. 163 (2016) F302-F307.

[263] T. Malis, S.C. Cheng, R.F. Egerton, J. Electron Microsc. Tech. 8 (1988) 193–200.

[264] E. Müller, T. Volkenandt, D.Z. Hu, D.M. Schaadt, D. Gerthsen, Microsc. Microanal. 16 (2010) 612–613.

[265] M. Chen, B. Hallstedt, L.J. Gauckler, J. Phase Equilib. 24 (2003) 212-227.

List of Tables

LIST OF FIGURES

OWN PUBLICATIONS AND CONFERENCE CONTRIBUTIONS

REVIEWED PUBLICATIONS

P. MÜLLER, H. STÖRMER, M. MEFFERT, L. DIETERLE, C. NIEDRIG, S.F. WAGNER, E. IVERS-TIFFÉE, AND D. GERTHSEN. Secondary phase formation in $Ba_{0.5}Sr_{0.5}Co_{0.8}Fe_{0.2}O_{3-\delta}$ (BSCF) studied by electron microscopy. Chemistry of Materials, **25**, 564-573 (2013). doi: 10.1021/cm303670m

P. MÜLLER, M. MEFFERT, H. STÖRMER, AND D. GERTHSEN. Fast mapping of the cobalt valence state in $Ba_{0.5}Sr_{0.5}Co_{0.8}Fe_{0.2}O_{3-d}$ by Electron Energy Loss Spectroscopy. Microscopy & Microanalysis, **19**, 1595-1605 (2013). doi: 10.1017/S1431927613013536

M. MEFFERT, H. STÖRMER, D. GERTHSEN. Capabilities of Analytical Transmission Electron Microscopy for the Analysis of Structural, Chemical and Electronic Properties Exemplified by the Study of Y-Doped (Ba,Sr)(Co,Fe)$O_{3-\delta}$. ECS Transactions, **66**, 143-146 (2015). doi: 10.1149/06602.0143ecst

D. FUCHS, A. SLEEM, R. SCHÄFER, A. G. ZAITSEV, M. MEFFERT, D. GERTHSEN, R. SCHNEIDER, H. V. LÖHNEYSEN. Incipient localization of charge carriers in the two-dimensional electron system in $LaAlO_3/SrTiO_3$ under hydrostatic pressure. Physical Review B, **92**, 155313-155320 (2015). doi: 10.1103/PhysRevB.92.155313

M. MEFFERT, H. STÖRMER, AND D. GERTHSEN. Dopant-Site Determination in Y- and Sc-Doped $(Ba_{0.5}Sr_{0.5})(Co_{0.8}Fe_{0.2})O_{3-\delta}$ by Atom Location by Channeling Enhanced Microanalysis and the Role of Dopant Site on Secondary Phase Formation. Microscopy & Microanalysis, **22**, 113-121 (2016). doi: 10.1017/S1431927615015536

L.-S. UNGER, M. MEFFERT, V. WILDE, H. STÖRMER, C. NIEDRIG, W. MENESKLOU, S. F. WAGNER, D. GERTHSEN, AND E. IVERS-TIFFÉE. Influence of a $La_{0.6}Sr_{0.4}CoO_{3-\delta}$ Functional Layer on $(Ba_{0.5}Sr_{0.5})(Co_{0.8}Fe_{0.2})O_{3-\delta}$ Oxygen Transport Membranes (OTMs). ECS Transactions, **22**, 113-121 (2016). doi: 10.1017/S1431927615015536

D. KRIEGNER, M. SYTNYK, H. GROISS, M. YAREMA, W. GRAFENEDER, P. WALTER, A-C. DIPPEL, M. MEFFERT, D. GERTHSEN, J. Stangl, and W. Heiss. Galvanic Exchange in Colloidal Metal/Metal-Oxide Core/Shell Nanocrystals. J. Phys. Chem. C, **120**, 19848-19855 (2016). doi: 10.1021/acs.jpcc.6b06405

M. MEFFERT, L.-S. UNGER, L. GRÜNEWALD, H. STÖRMER, S. F. WAGNER, E. IVERS-TIFFÉE, AND D. GERTHSEN. The impact of grain size, A/B-cation ratio and Y-doping on secondary phase formation in $(Ba_{0.5}Sr_{0.5})(Co_{0.8}Fe_{0.2})O_{3-\delta}$. J. Mater. Sci., **52**, 2705-2719 (2017). doi: 10.1007/s10853-016-0562-8

S. SAHER, M. MEFFERT, H. STÖRMER, D. GERTHSEN, AND H. J. M. BOUWMEESTER. Grain-size dependence of the deterioration of oxygen transport for pure and 3 mol% Zr-doped $Ba_{0.5}Sr_{0.5}Co_{0.8}Fe_{0.2}O_{3-\delta}$ induced by thermal annealing. J. Mater. Chem. A, **5**, 4982-4990 (2017). doi: 10.1039/C6TA10454A

CONTRIBUTIONS TO CONFERENCES

P. MÜLLER, M. MEFFERT, H. STÖRMER, C. NIEDRIG, S.F. WAGNER, E. IVERS-TIFFÉE, AND D. GERTHSEN. Electron Microscopy investigations of zirconium-, yttrium- and scandium-doped BSCF3X (Talk). **Electroceramics XIII**. Enschede, Netherlands, June 24th - 27th (2012).

P. MÜLLER, M. MEFFERT, H. STÖRMER, C. NIEDRIG, S. F. WAGNER, E. IVERS-TIFFÉE, AND D. GERTHSEN. Analysis of co-doped BSCF3X by Electron Microscopy (Poster). **12th International Conference on Inorganic Membranes**, Enschede, Netherlands, July 9th - 13th (2012).

M. MEFFERT, P. MÜLLER, H. STÖRMER, C. NIEDRIG, S. F. WAGNER, E. IVERS-TIFFÉE, AND D. GERTHSEN. Electron microscopy study of BSCF3X (Poster). **The 15th European Microscopy Congress**, Manchester, United Kingdom, September 16th – 21st (2012).

M. MEFFERT, P. MÜLLER, H. STÖRMER, C. NIEDRIG, S. F. WAGNER, E. IVERS-TIFFÉE, AND D. GERTHSEN. Electron microscopy study of BSCF3X (Poster). **CFN Summerschool 2012 on Nano-Energy**, Bad Herrenalb, Germany, September 14th - 17th (2012).

M. MEFFERT, P. MÜLLER, H. STÖRMER, C. NIEDRIG, S. F. WAGNER, E. IVERS-TIFFÉE, AND D. GERTHSEN. Electron microscopy study of Y-doped BSCF (Talk). **DPG Spring Meeting SKM**, Regensburg, Germany, March 10th - 15th (2013).

M. MEFFERT, P. MÜLLER, H. STÖRMER, C. NIEDRIG, S. F. WAGNER, E. IVERS-TIFFÉE, AND D. GERTHSEN. Electron Microscopy Study of Yttrium-doped BSCF3Y (Talk). **2nd International Conference on Materials for Energy**, Karlsruhe, Germany, May 12nd - 16th (2013).

M. MEFFERT, P. MÜLLER, H. STÖRMER, C. NIEDRIG, S. F. WAGNER, E. IVERS-TIFFÉE, AND D. GERTHSEN. Electron Microscopy Study of Yttrium-doped BSCF3Y (Talk). **19th International Conference on Solid State Ionics**, Kyoto, Japan, June 2nd - 7th (2013).

M. MEFFERT, P. MÜLLER, H. STÖRMER, C. NIEDRIG, S. F. WAGNER, E. IVERS-TIFFÉE, AND D. GERTHSEN. Electron microscopy study of Yttrium-doped $Ba_{0.5}Sr_{0.5}Co_{0.8}Fe_{0.2}O_{3-\delta}$ (Poster). **Microscopy Conference (MC),** Regensburg, Germany, August 25th - 30th (2013).

M. MEFFERT, P. MÜLLER, H. STÖRMER, C. NIEDRIG, S. F. WAGNER, E. IVERS-TIFFÉE, AND D. GERTHSEN. Influence of yttrium doping on the stability of the cubic $Ba_{0.5}Sr_{0.5}Co_{0.8}Fe_{0.2}O_{3-\delta}$ phase studied by electron microscopy (Poster). **Summer School: Inorganic Membranes for Green Chemical Production and Clean Power Generation**, Valencia, Spain, September 4th - 6th (2013).

L.-S. UNGER, M. MEFFERT, L.-S. UNGER, C. NIEDRIG, H. STÖRMER, S. F. WAGNER, D. GERTHSEN, AND E. IVERS-TIFFÉE. Enhanced Oxygen Surface Reaction in $(Ba_{0.5}Sr_{0.5})(Co_{0.8}Fe_{0.2})O_{3-d}$ by Nanoscaled $(La_{0.6}Sr_{0.4})CoO_{3-d}$ Functional Layer (Talk). **E-MRS Spring Meeting 2014**, Lille, France, Mai 26th - 30th (2014).

M. MEFFERT, P. MÜLLER, H. STÖRMER, L.-S. UNGER, C. NIEDRIG, S. F. WAGNER, E. IVERS-TIFFÉE, AND D. GERTHSEN. Effect of Yttrium doping on the cubic phase of $Ba_{0.5}Sr_{0.5}Co_{0.8}Fe_{0.2}O_{3-\delta}$ studied by electron microscopy (Talk). **Electroceramics XIV**, Bucharest, Romania, June 16th - 20th (2014).

L.-S. UNGER, M. MEFFERT, L.-S. UNGER, C. NIEDRIG, H. STÖRMER, S. F. WAGNER, D. GERTHSEN, AND E. IVERS-TIFFÉE. Surface activation of $(Ba_{0.5}Sr_{0.5})(Co_{0.8}Fe_{0.2})O_{3-d}$ by means of a $(La_{0.6}Sr_{0.4})CoO_{3-d}$ functional layer (Talk). **Electroceramics XIV**, Bucharest, Romania, June 16th – 20th (2014).

M. MEFFERT, P. MÜLLER, H. STÖRMER, L.-S. UNGER, C. NIEDRIG, S. F. WAGNER, E. IVERS-TIFFÉE, AND D. GERTHSEN. Electron microscopy study of yttrium doped $Ba_{0.5}Sr_{0.5}Co_{0.8}Fe_{0.2}O_{3-d}$ (Poster). **3. Jahrestagung KIT-Zentrum Energie**, Karlsruhe, Germany, June 26th (2014).

M. MEFFERT, P. MÜLLER, H. STÖRMER, L.-S. UNGER, C. NIEDRIG, S. F. WAGNER, E. IVERS-TIFFÉE, AND D. GERTHSEN. Effect of Yttrium (Y) doping on the thermodynamical stability of the cubic $Ba_{0.5}Sr_{0.5}Co_{0.8}Fe_{0.2}O_{3-d}$ phase (Poster). **13th International Conference on Inorganic Membranes**, Brisbane, Australia, July 6th – 9th (2014).

M. MEFFERT, P. MÜLLER, H. STÖRMER, L.-S. UNGER, C. NIEDRIG, S. F. WAGNER, S. SAHER, H. BOUWMEESTER, E. IVERS-TIFFÉE, AND D. GERTHSEN. Effect of yttrium (Y) and zirconium (Zr) doping on the thermodynamical stability of the cubic $Ba_{0.5}Sr_{0.5}Co_{0.8}Fe_{0.2}O_{3-d}$ phase (Poster). **Microscopy & Microanalysis 2014 Meeting**, Hartford, USA, August 3rd – 7th (2014).

M. MEFFERT, P. MÜLLER, H. STÖRMER, AND D. GERTHSEN. Capabilities of Analytical Transmission Electron Microscopy for the Analysis of Structural, Chemical and Electronic Properties Exemplified by the $(Ba,Sr)(Co,Fe)O_3$ Material System (Talk). **227th ECS Meeting**, Chicago, USA, May 24th – 28th (2015).

M. MEFFERT, H. STÖRMER, AND D. GERTHSEN. Cation-site determination in $(Ba_{0.5}Sr_{0.5})(Co_{0.8}Fe_{0.2})O_{3-d}$ by exploiting channelling effects in transmission electron microscopy (Poster). **20th International Conference on Solid State Ionics**, Keystone, USA, June 14th – 19th (2015).

M. MEFFERT, L.-S. UNGER, H. STÖRMER, C. NIEDRIG, S. F. WAGNER, E. IVERS-TIFFÉE, AND D. GERTHSEN. Study of Y-doped (Ba,Sr)(Co,Fe)O_{3-d} by analytical transmission electron microscopy (Poster). **20th International Conference on Solid State Ionics**, Keystone, USA, June 14th – 19th (2015).

L.-S. UNGER, M. MEFFERT, H. STÖRMER, S. F. WAGNER, W. MENESKLOU, D. GERTHSEN, AND E. IVERS-TIFFÉE. Nanoscaled $(La_{0.6}Sr_{0.4})CoO_{3-d}$ Functional Layer for Surface Activation of $(Ba_{0.5}Sr_{0.5})(Co_{0.8}Fe_{0.2})O_{3-d}$ (Poster). **20th International Conference on Solid State Ionics**, Keystone, USA, June 14th – 19th (2015).

L.-S. UNGER, M. MEFFERT, S. BAUMANN, H. STÖRMER, W. MENESKLOU, S. F. WAGNER, W. A. MEULENBERG, D. GERTHSEN, AND E. IVERS-TIFFÉE. Effect of Yttrium (Y) doping in $Ba_{0.5}Sr_{0.5}Co_{0.8}Fe_{0.2}O_{3-d}$ (BSCF) (Poster). **14th International Conference of the European Ceramic Society**, Toledo, Spain, June 21st – 25th (2015).

L.-S. UNGER, M. MEFFERT, S. BAUMANN, H. STÖRMER, W. MENESKLOU, S. F. WAGNER, W. A. MEULENBERG, D. GERTHSEN, AND E. IVERS-TIFFÉE. Nanoscaled $La_{0.6}Sr_{0.4}CoO_{3-d}$ Functional Layer for Enhanced Surface Kinetics of $(Ba_{0.5}Sr_{0.5})(Co_{0.8}Fe_{0.2})O_{3-d}$ Oxygen Transport Membranes (OTMs) (Talk). **14th International Conference of the European Ceramic Society**, Toledo, Spain, June 21st – 25th (2015).

M. MEFFERT, H. STÖRMER, AND D. GERTHSEN. Cation distribution in doped $(Ba_{0.5}Sr_{0.5})(Co_{0.8}Fe_{0.2})O_{3-d}$ ceramics using channeling enhanced micoanalysis (Poster). **Microscopy Conference 2015**, Göttingen, Germany, September 6th – 11th (2015).

L. GRÜNEWALD, M. MEFFERT, H. STÖRMER, L.-S. UNGER, S. F. WAGNER, E. IVERS-TIFFÉE, AND D. GERTHSEN. Electron microscopic characterization of Yttrium-doped BSCF ceramics (Poster). **Microscopy Conference 2015**, Göttingen, Germany, September 6th – 11th (2015).

L.-S. UNGER, M. MEFFERT, S. BAUMANN, H. STÖRMER, W. MENESKLOU, S. F. WAGNER, W. A. MEULENBERG, D. GERTHSEN, AND E. IVERS-TIFFÉE. Stabilization of $Ba_{0.5}Sr_{0.5}Co_{0.8}Fe_{0.2}O_{3-\delta}$ (BSCF) by Yttrium (Y) Doping (Poster). **Summer School: Inorganic Membranes for Green Chemical Production and Clean Power Generation** Valencia, Spain, September 23rd – 25th (2015).

L.-S. UNGER, M. MEFFERT, S. BAUMANN, C. NIEDRIG, H. STÖRMER, W. MENESKLOU, S. F. WAGNER, W. A. MEULENBERG, D. GERTHSEN, AND E. IVERS-TIFFÉE. Stabilizing the

High-Performance Cubic Perovskite $Ba_{0.5}Sr_{0.5}Co_{0.8}Fe_{0.2}O_{3-\delta}$ Lattice by Yttrium Doping (Poster). **E-MRS Spring Meeting** Lille, France, May 02nd – 06th (2016).

L.-S. UNGER, M. MEFFERT, V. WILDE, H. STÖRMER, W. MENESKLOU, S. F. WAGNER, D. GERTHSEN, AND E. IVERS-TIFFÉE. Influence of a $La_{0.6}Sr_{0.4}CoO_{3-\delta}$ Functional Layer on $(Ba_{0.5}Sr_{0.5})(Co_{0.8}Fe_{0.2})O_{3-\delta}$ Oxygen Transport Membranes (OTMs) (Talk). **229th ECS Meeting** San Diego, USA, May 29th - June 03rd (2016).

M. MEFFERT, L.-S. UNGER, S. BAUMANN, C. NIEDRIG, H. STÖRMER, W. MENESKLOU, S. F. WAGNER, W. A. MEULENBERG, E. IVERS-TIFFÉE, AND D. GERTHSEN. Stabilization of the cubic perovskite BSCF phase by Y-doping (Talk). **16th European Microscopy Congress** Lyon, France, August 28th - September 02nd (2016).

8 APPENDIX

8.1 Filtering

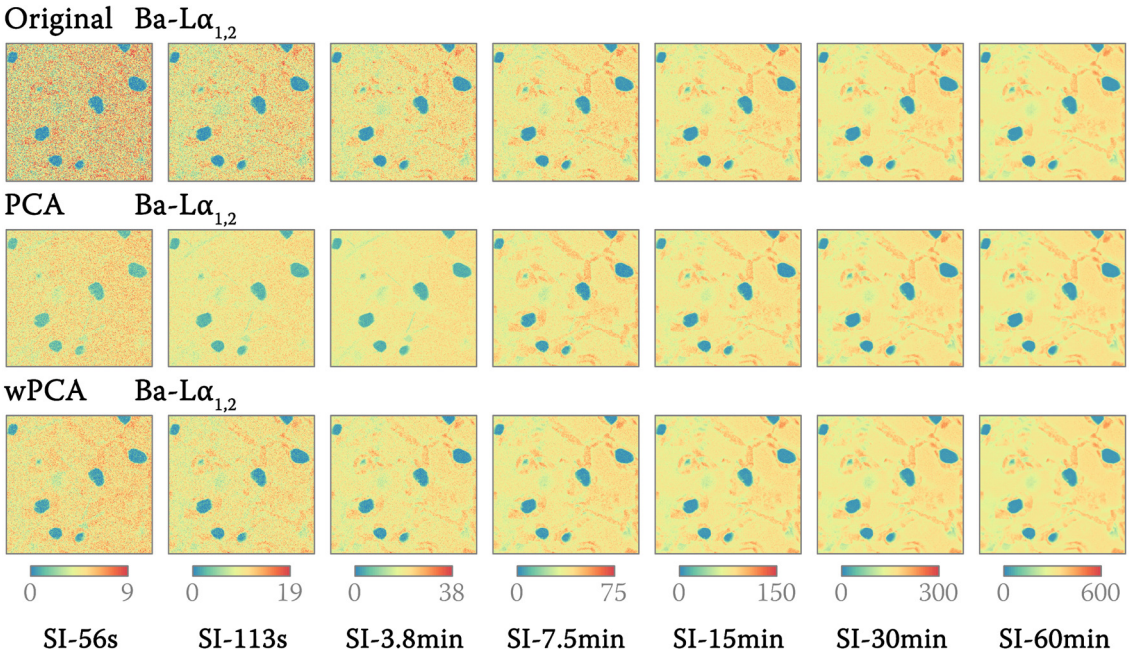

Figure 76. Ba-L$\alpha_{1,2}$ integrated intensity mappings of the original data set, after PCA and wPCA filtering for different effective measurement times. The color scale denotes the number of X-ray counts of the Ba-L$\alpha_{1,2}$ emission line.

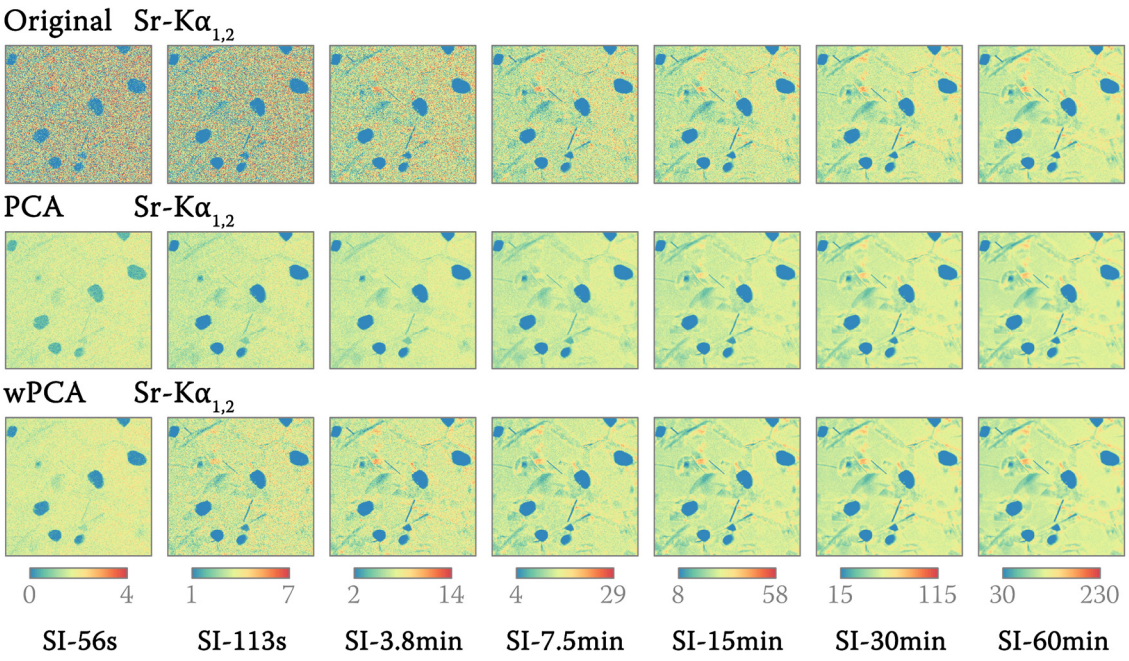

Figure 77. Sr-Kα$_{1,2}$ integrated intensity mappings of the original data set, after PCA and wPCA filtering for different effective measurement times. The color scale denotes the number of X-ray counts of the Sr-Kα$_{1,2}$ emission line.

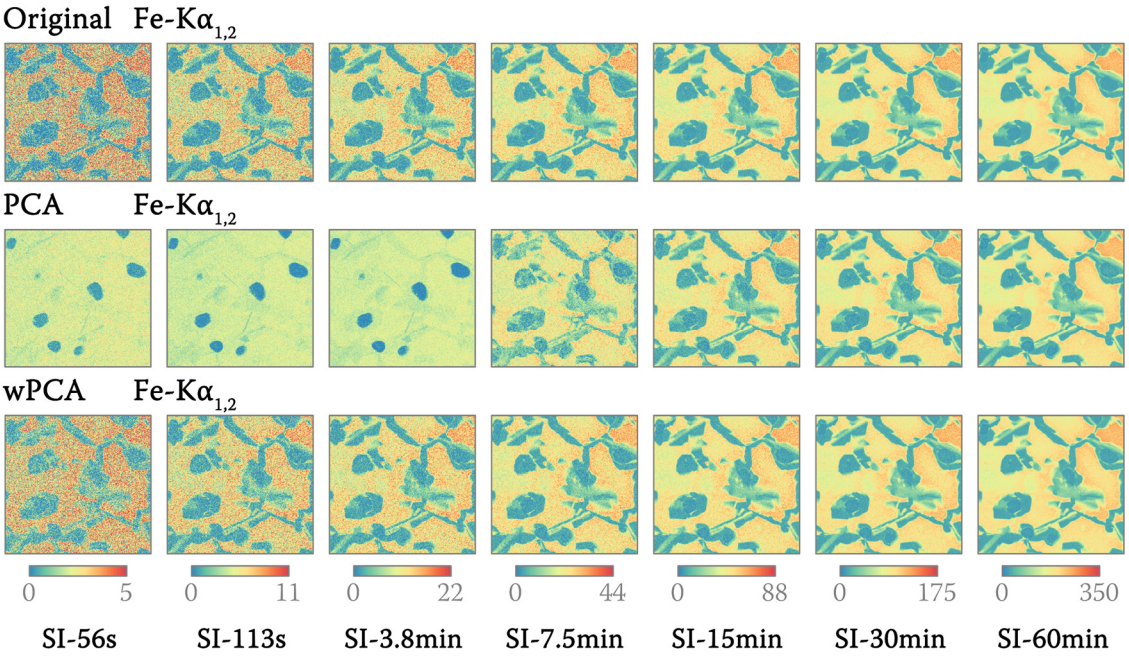

Figure 78. Fe-Kα$_{1,2}$ integrated intensity mappings of the original data set, after PCA and wPCA filtering for different effective measurement times. The color scale denotes the number of X-ray counts of the Fe-Kα$_{1,2}$ emission line.

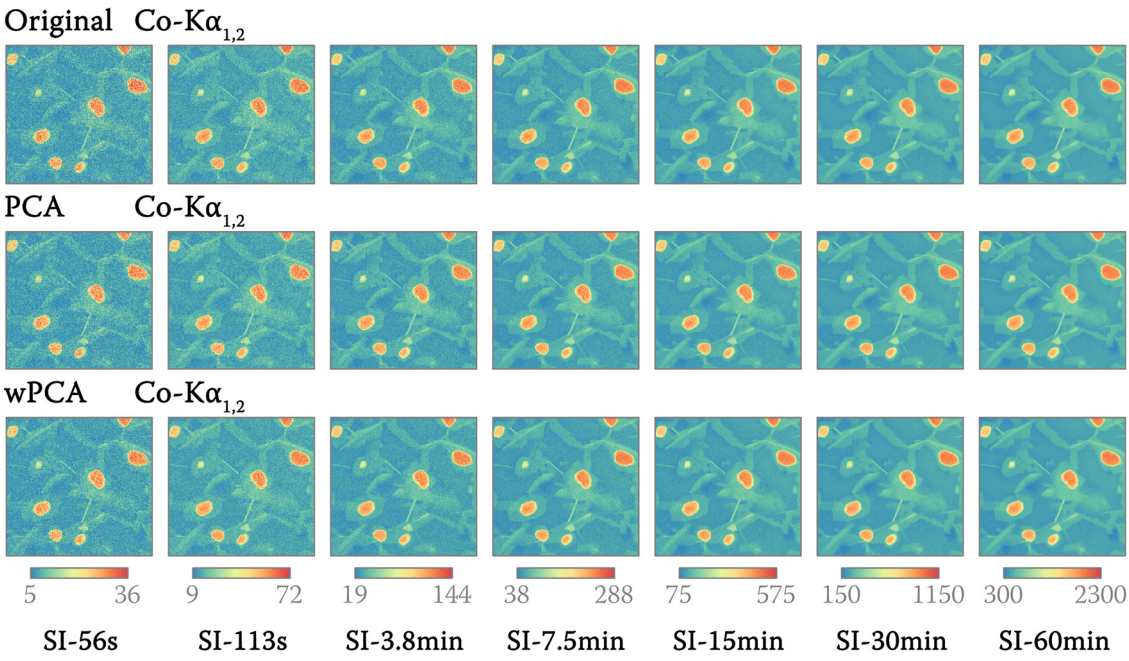

Figure 79. Co-Kα$_{1,2}$ integrated intensity mappings of the original data set, after PCA and wPCA filtering for different effective measurement times. The color scale denotes the number of X-ray counts of the Co-Kα$_{1,2}$ emission line.

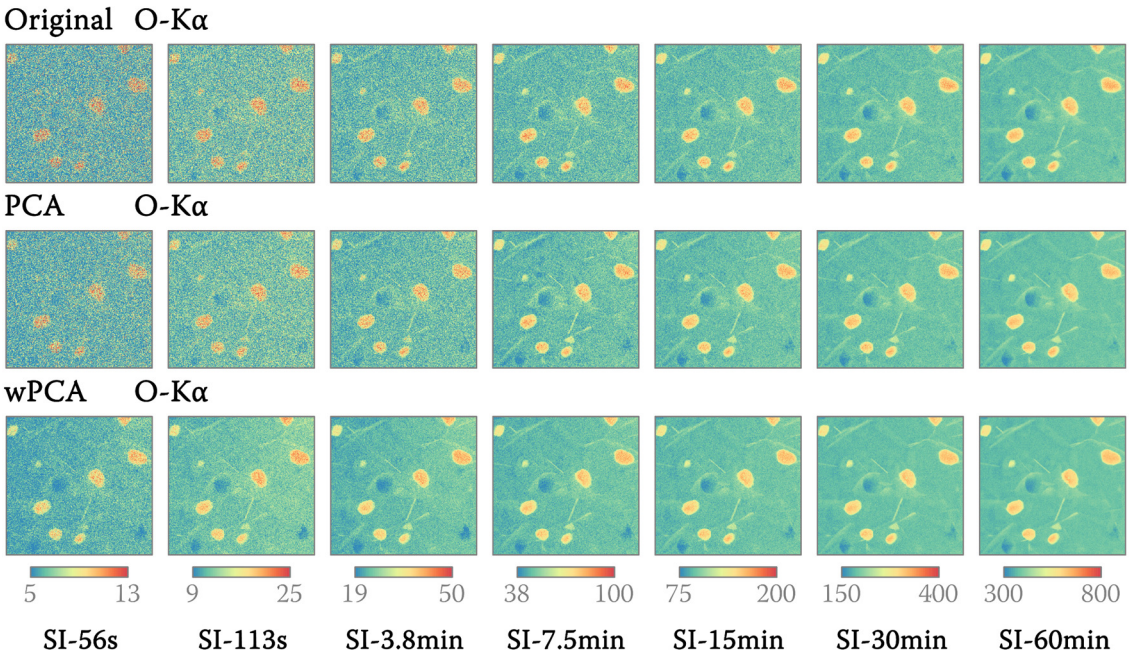

Figure 80. O-Kα integrated intensity mappings of the original data set, after PCA and wPCA filtering for different effective measurement times. The color scale denotes the number of X-ray counts of the O-Kα emission line.

8.2 Grain size determination

sample	fitting parameters		average grain size $\bar{d}$
	mean μ	deviation σ	[μm]
BSCF-1050	1.95	0.37	6.9
BSCF-1070	2.40	0.42	9.1
BSCF-1120	2.79	0.40	14.4
BSCF-1170	4.29	0.42	65.3
BSCF10Y-1070	1.28	0.41	3.3
BSCF10Y-1120	1.81	0.41	5.3
BSCF10Y-1170	2.68	0.55	13.2
BSCF10Y-1220	3.48	0.47	29.6
BSCF*-950	1.35	0.38	3.6
BSCF*-1050	2.61	0.42	11.8
BSCF*-1150	4.56	0.39	80.9
BSCF3Zr*-950	0.97	0.33	2.3
BSCF3Zr*-1050	2.43	0.48	10.3
BSCF3Zr*-1150	4.25	0.40	59.6
$(BS)_{1.05}CF$	2.21	0.56	8.3
$(BS)_{0.95}CF$	1.75	0.38	5.1

Table 11. Overview of fitting parameters and average grain sizes.

8.3 Thickness determination in BSCF using EELS

With increasing sample thickness, the probability for inelastic scattering increases, therefore, giving rise to pronounced features in the low loss region (plasmon peaks) accompanied by a reduction of ZL peak intensity. It has been widely accepted that the ratio between the integrated intensity of the ZL peak I_{ZL} and the integrated intensity of the whole spectrum I_t is connected to the sample thickness t by a logarithmic relation as written in Equation 35.

$$t = \lambda_p \ln \frac{I_t}{I_{ZL}} \tag{35}$$

Here, λ_p corresponds to a material-specific constant for the mean free path for plasmon scattering. It should be noted that λ_p is not only material dependent but also dependent on microscope parameters like beam convergence angle, spectrometer collection angle and, electron energy. λ_p has to be know with a high accuracy to utilize this relation to determine the local sample thickness. However, for most materials λ_p is not known which requires the use of empirical formulas like, e.g. the formula published by MALIS ET AL. [263].

The mean free path for plasmon scattering can be easily derived by measuring samples with known thicknesses. The sample thickness can be derived by other techniques like for example CBED [204]. However, in the case of CBED only the crystalline part is measured and amorphous surface layers, which are included in the EELS technique, are completely neglected. Therefore, another approach was employed within this thesis involving a BSCF wedge sample with known slope. The sample was prepared by ERICH MÜLLER [264] using focused-ion-beam milling techniques. The wedge angle was determined by a side view SE SEM image presented in Figure 81(a). The measured angle angle was 19°. An EELS line scan from the edge of the wedge to a distance of 1500 nm was performed in STEM mode at 300 keV. The beam convergence angle was set to 16.7 mrad. Two line scans were recorded for two different collection angles (40.6 mrad and 6.7 mrad) with 75 scanning points. The two line scans were performed on different regions of the wedge sample to avoid errors induced by contamination. The energy dispersion was set to 0.5 eV per channel giving a spectrum range from 0 to more than 900 eV. I_t was determined by integrating over the whole spectrum. The integration width of the ZL peak was derived from a vacuum spectrum. Here the integration window was defined by the points where the ZL peak reaches 1 % of its maximum intensity. The logarithm of the integrated intensity ratios it depicted in Figure 81(b) as

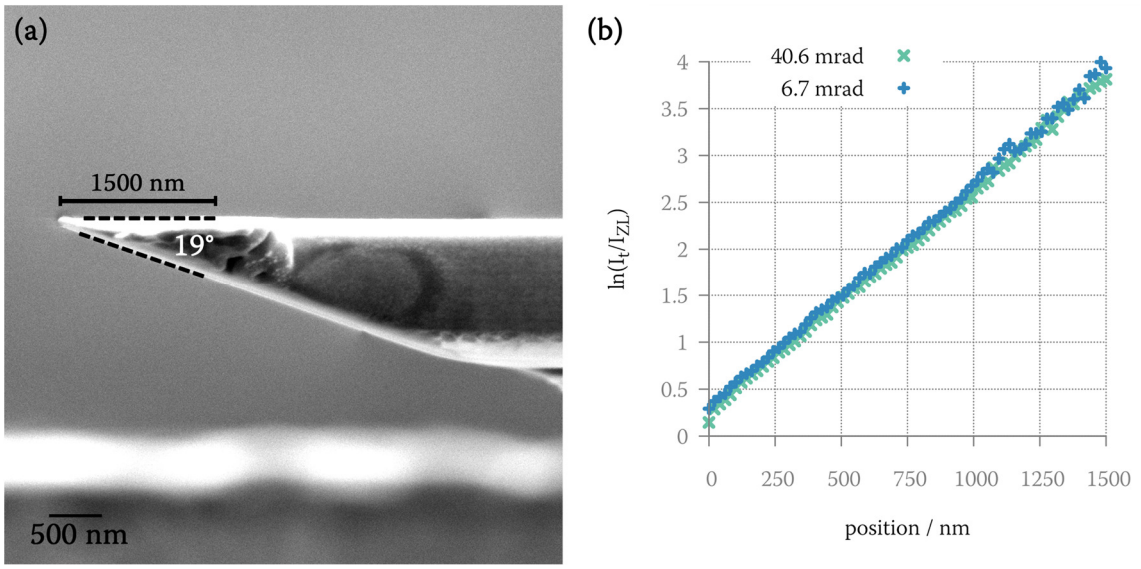

Figure 81. (a) SE SEM side view image of BSCF wedge sample recorded by ERICH MÜLLER [264]. (b) Logarithmic intensity ratio as a function of distance from the edge.

a function of scanning position. For both collection angles, the data show the expected linear behavior even for thick sample regions where the ZL peak almost vanishes. The small offset between both collection angles might be attributed to the different measurement position and, therefore, slightly different starting points with regards to the edge of the wedge. As λ_p only depends on the wedge angle and the slope of $\ln\frac{I_t}{I_{ZL}}$, an arbitrary offset in the curve will not impose any error. For a collection angle of 40.6 mrad and 6.7 mrad a slope of $2.39\times10^{-3}\ nm^{-1}$ (R^2 = 99.9 %) and $2.40\times10^{-3}\ nm^{-1}$ (R^2 = 99.9 %) was obtained by linear regression. A high quality of fit was achieved in both cases with almost identical slopes. Therefore, is can be concluded that the influence of collection angle in BSCF can be neglected within this measurement range. From both collection angles we get a mean free path for plasmon filtering of (144 ± 2) nm. The experimental value can now be compared to the empirical Malis formula. Assuming an average atomic number of 20 for BSCF the Malis formula suggests for a collection angle of 40.6 mrad a λ_p value of about 105 nm which is a quite large deviation compared to the measured value here. However, for a collection angle of 6.7 mrad the Malis formula almost gives the same result as in this experiment with λ_p being 141 nm.

Acknowledgements

I would like to express my special appreciation and thanks to the head of our department Prof. Dr. Dagmar Gerthsen for her excellent guidance and fruitful discussions during the past years. Her expertise greatly contributed to the success of this work. My sincere thanks also go to Prof. Dr.-Ing. Ellen Ivers-Tiffée (IAM-WET, KIT) not only for her role as second reviewer but also her valuable contributions on numerous occasions.

I owe my deepest gratitude to all the members (past and present) of the LEM membrane group, especially Dr.-Ing. Heike Störmer, Dr. Philipp Müller and Virginia Wilde. It is always a joyful activity to work with them. I also acknowledge the strong commitment of the former Bachelor students Lukas Grünewald and Susanne Wachs who contributed valuable insights into the material system.

Special mention and thanks go to Lana Unger, Dr.-Ing. Christian Niedrig and Dr.-Ing. Stefan Wagner (IAM-WET, KIT) for their past and ongoing collaboration. The numerous discussion at several meetings have greatly benefited this work. I also want to thank Prof. Dr. Henny Bouwmeester and Saim Saher (University of Twente) for the successful cooperation and many fruitful meetings. My thanks go to Dr. Stefan Baumann (IEK-1, Forschungszentrum Jülich) for performing the permeation measurements. I am also indebted to Dr. Dirk Fuchs (IFP, KIT) for an interesting side project and also proofreading part of this thesis.

I am particularly grateful for the assistance regarding electron microscopy given by Dr. habil. Reinhard Schneider and Volker Zibat. A very big thanks to Nadejda Firman for her tireless support in sample preparation. I also thank Dr. Erich Müller for providing excellent FIB samples. My sincere thanks to Rita Sauter for managing all the paperwork in the background.

Special mention goes to all participants of the K-Room break, the former LEM Lauffreunde (n.e.V.), the weekly Backstube (go Simon!) and all people contributing to the excellent working atmosphere at the LEM.

A special thanks to my family especially my parents. Words cannot express how grateful I am to my mother and father for their ongoing support. Also big thanks to all of my friends who supported me in writing.

Special thanks to Cheng who made my life much more colorful. 我爱你